Fall 2013

Numerical analyses of long carbon fiber reinforced concrete panels exposed to dynamic loading

Zahra Sadat Tabatabaei

Department: Civil, Architectural and Environmental Engineering

NUMERICAL ANALYSES OF LONG CARBON FIBER REINFORCED CONCRETE PANELS EXPOSED TO DYNAMIC LOADING

by

ZAHRA SADAT TABATABAEI

A DISSERTATION

Presented to the Faculty of the Graduate School of the

MISSOURI UNIVERSITY OF SCIENCE AND TECHNOLOGY

In Partial Fulfillment of the Requirements for the Degree

DOCTOR OF PHILOSOPHY

in

CIVIL ENGINEERING

2013

Approved by:
Jeffery S. Volz, Advisor
John J. Myers
Jason Baird
Victor Birman
K.Chandrashekhara

PUBLICATION DISSERTATION OPTION

This dissertation has been prepared in the style such that the individual sections may be submitted for publication in technical journals and conference proceedings. Pages 24-59, the manuscript entitled "Comparative Impact Behavior of Four Long Carbon Fiber Reinforced Concretes" has been submitted to the journal *Materials and Design*, Elsevier Publishing. Pages 60-83, the manuscript entitled "Numerical Simulation of Impact Tests on Long Carbon Fiber Reinforced Concrete Panels" will be submitted to the *International Journal of Impact Engineering*, Elsevier Publishing, based on the dissertation committee's suggestions. Pages 84-125, the manuscript entitled "Experimental and Numerical Analyses of Long Carbon Fiber Reinforced Concrete Panels Exposed to Blast Loading" were published in the *International Journal of Impact Engineering*, Volume 57, 2013. Pages 126-143, the manuscript entitled "A Comparison between Three Different Blast Methods in LS-DYNA®: LBE, MM-ALE, Coupling of LBE and MM-ALE" was published in the proceedings of the 12th International LS-DYNA® Users Conference, 2012.

A companion paper discussing development of the long carbon fibers is included in the Appendix. The majority of the work that served as the background for this manuscript was completed by other researchers at Missouri S&T, but the author synthesized the results and served as the primary author for this paper. This manuscript entitled "Development of Long Carbon Fiber Reinforced Concrete for Dynamic Strengthening" was accepted for publication in the *Journal of Materials in Civil Engineering*, American Society of Civil Engineers (ASCE).

ABSTRACT

The purpose of this research was to evaluate impact and blast performance of long carbon fiber reinforced concrete experimentally and numerically. Experimental tests were conducted on plain concrete (PC), reinforced concrete, and four different types of long carbon fiber reinforced concrete (LCFRC). The results from each test were then compared to one another. This comparison indicates that adding long carbon fibers to concrete both increases the post-cracking behavior of concrete and decreases the spalls in either an impact or blast test. Among all of the fibers tested, Fiber Type B3 outperformed the other fibers, absorbing more energy during impact. Numerical simulation of a drop weight impact test was then performed on both welded wire reinforced concrete and long carbon fiber reinforced concrete panels. The three-dimensional finite element code LS-DYNA was used for the numerical analyses. Three different, simple input models were used to simulate concrete behavior under impact. As a consequence, both the force time history and deflection time history at failure were obtained for each case. These results were compared together. Then, a series of tests were conducted to compare the blast resistance of panels constructed with either conventional reinforced concrete (RC) or long carbon fiber-reinforced concrete (LCFRC). A finite element model was created in LS-DYNA to replicate both a control panel and an LCFRC panel to observe whether or not the models could predict the observed damage. Each of the LCFRC panels exhibited less material loss and less surface damage than the control panels. The addition of long carbon fibers significantly increased the concrete's blast resistance and significantly reduced the degree of cracking associated with the concrete panels. The results were also compared to the existing damage level chart in UFC 3-340-02.

ACKNOWLEDGMENTS

This is a great opportunity to express my deep and sincere gratitude to my advisor, Dr. Jeffery S. Volz for his continuous guidance, support, and motivation during the last four years. He has taught me a great deal about being direct and staying on point through my research. He has encouraged me to travel multiple times to Michigan Lstc. and certified for using LS-DYNA. I was able to travel to several conferences, providing me with many contacts throughout these conferences. I would also like to thank Dr. Jason Baird, who offered valuable comments for our blast paper. I would like to thank the rest of my committee, my great teachers in different courses I took during my graduate study: Drs. John Myers, Victor Birman, and K.Chandrashekhara. They provided insight in several areas and they taught me a lot in their courses that constantly improved my knowledge and understand about my project.

I should also acknowledge the financial support provided by the Army Research Lab (ARL) and the Leonard Wood Institute (LWI) under Award Nos. W911NF-07-2-0062 and LWI-191-028, respectively. This financial support made it possible for me to conduct this research.

I also need to thank all of my friends and colleagues in civil department for their help and support. My colleagues Benjamin P. Gliha and Darwin “Ish” Keener. There are many people to who have helped me and the list is too exhaustive to show here. I would also like to acknowledge the staff of department, especially John Bullock, Gary Abbott, Jason Cox, Brian Swift, and Karen White. I also grateful for the ideas and help of Dr. Andrea Schokker, Dr. Eric Musselman, and Mr. Andy Coughlin.

I owe my loving thanks to my parents and family members for their encouragement, patience, and understanding throughout my studies abroad. I would like to express my appreciation and thank to my husband for his support, patience, and understanding throughout this time.

TABLE OF CONTENTS

PAPER

LIST OF ILLUSTRATIONS

Page

PAPER I

PAPER II

PAPER III

PAPER IV

LIST OF TABLES

Page

NOMENCLATURE

Symbol	Description
ANFO	Ammonium nitrate/fuel oil
BEC	Blast Effects Computer
COVs	Coefficients of variation
DIF	Dynamic increase factor
DDESB	Department of Defense Explosives Safety Board
D	Deflection
D_{max}	Maximum deflection
E	Input impact energy
E	Internal energy per initial volume
E_F	Impact energy at failure
EOS	Equation of State
E_s	Young's modulus
E_{strain}	Strain energy
E_t	Plastic hardening modulus
f'_c	Compressive strength
f_y	Yield strength
HRWR	High-range water reducer
ICP	Integrated Circuit Piezoelectric
I_{rs}	Residual impact strength ratio
LCFRC	Long carbon fiber reinforced concrete
LBE	LOAD_BLAST_ENHANCED
m	Drop weight mass
MM-ALE	Multi-Material Arbitrary Lagrangian Eulerian
P	Impact load
PC	Plain concrete
P_{max}	Maximum impact force
PS	Pressure sensor
R	Standoff distance

SDAS	Synergy data acquisition system
SSD	Saturated surface dry
V_i	Velocity of drop weight
W_{adj}	Adjusted charge weight
W_c	Steel casing weight
WWR	Welded wire reinforced
X_0	Initial location of the cap
ε_v	Volume strain
δ_{rs}	Residual deflection
γ	Ratio of specific heats
$\Delta\sigma_m$	Maximum failure surfaces
$\Delta\sigma_y$	Yield failure surface
$\Delta\sigma_r$	Residual failure surface
ε_v^p	Plastic volumetric strain

1. INTRODUCTION

1.1. BACKGROUND

Events over the last 10 years, including the bombing of the Murrah Federal Building in Oklahoma City, the 9/11 World Trade Center attacks, and the war in Iraq, have brought the topic of blast and impact resistant materials for structures to the forefront. Technologies that improve concrete's performance under dynamic loading have the potential to save many lives due to the extensive use of reinforced concrete in critical structures. The innovative, long carbon fiber concrete material that formed the basis for this research has numerous applications. It can be used in blast walls, bridge abutments, piers, parapets, building columns, blast resistant facade panels, and more.

The use of long carbon fibers within a concrete matrix can be an economical method to improve blast resistance. These fibers offer distinct advantages over other blast resistant material options. Utilizing long carbon fiber reinforced concrete can increase the capacity of the concrete elements to resist a blast, while reducing secondary fragmentation that results from spalling. This reduction is a critical property of the material; unfortunately fragmentation can lead to substantial damage of both personnel and equipment. Fragmentation is difficult to prevent with current materials. The use of long carbon fibers offers improvement with little to no modification of current design practices, allowing implementation to occur quickly and easily.

Research on the use of fibers to increase the strength of both blast and impact structures has typically been limited to steel fibers and, to a lesser degree, polypropylene fibers. Carbon has many potential benefits over these materials, including its higher strength and modulus as well as its increased durability. Carbon fibers also provide an economical solution, as they are a waste product from the aerospace industry. Short carbon fibers have been used successfully, but they do not provide either the energy dissipation or the spalling resistance provided by long carbon fibers. Long carbon fibers have a tendency to segregate in the mixture and decrease workability thus their limited use in previous studies.

1.2. OBJECTIVES AND SCOPE OF WORK

The ***objectives*** of this study were to model the experimental performance of long carbon fiber reinforced concrete exposed to dynamic loading – both impact and blast – and develop design methodologies for fiber-reinforced concrete. The following scope of work was implemented in an effort to attain these objectives:

Evaluate the influence of long carbon fibers on the dynamic behavior of concrete, including both the blast and impact resistance.

Investigate the behavior of long carbon fiber reinforced concrete under impact loading in LS-DYNA.

Investigate the behavior of long carbon fiber reinforced concrete under blast loading in LS-DYNA.

Develop a spall prediction curve for long carbon fiber reinforced concrete exposed to blast loading.

Compare different concrete models in LS-DYNA to model long carbon fiber reinforced concrete.

1.3. DISSERTATION OUTLINE

This dissertation includes three sections and an appendix. Section 1 gives a brief introduction to the subject area and explains the need for the current research study. The first section also presents the objectives and scope of work of the investigation, as well as a detailed literature review to establish the state-of-the-art on the proposed topic.

Section 2 presents three journal papers and one conference proceeding discussing the analysis and modeling of long carbon fiber reinforced concrete subjected to dynamic loading. The first two papers cover the aspect of impact loading, while the second two papers discuss blast loading.

Section 3 summarized the findings and conclusions of this study and proposed future research.

The appendix contains a companion paper on development of the long carbon fibers used in the current study.

2. LITERATURE REVIEW

2.1. INTRODUCTION

An analysis of both blast and impact loads is considerably different from an analysis of a structure subjected to static loads. Additional factors must be considered when either blast or impact loads are examined, including duration, and the structure's response time. An analysis of blast loads, however, begins in the same manner that an analysis of static loads begins: with the determination of applied loads.

Multiple factors from blast explosions can affect a structure. These factors include an air blast, ground shock, cratering, fire, and impact (from both primary and secondary fragments) [1]. Each of these effects must be analyzed to obtain an accurate assessment of a structure's blast resistance.

An air blast has two effects: a primary effect (the pressure wave impacting the structure) and a secondary effect (the drag loading that occurs as the pressure wave passes around the structure). This study focuses on the primary effect of the air blast. This effect consists of two distinct phases. The initial phase is a positive phase that begins at the peak pressure and decays rapidly. The final phase is a negative phase that is lower in magnitude and longer in duration. Both phases are summarized in Figure 2.1 [2].

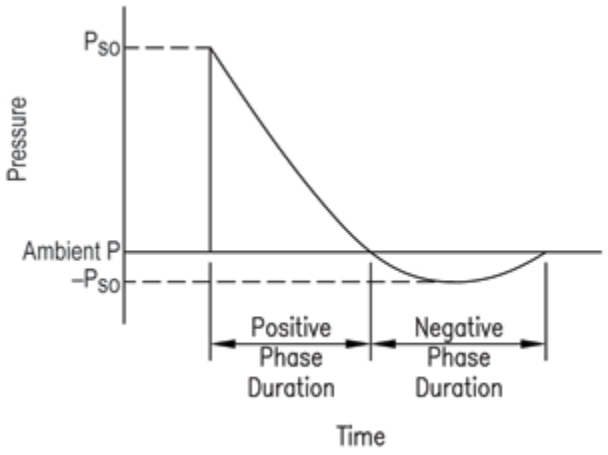

Figure 2.1. Pressure versus Time for Typical Blast Load [2]

The Army published a manual to help both determine the effect an air blast has on a structure as well as design a structure capable of resisting that blast. This manual divides the response of structures into three basic categories. The first includes specimens that are subjected to high pressures (in excess of 100 psi). At these pressures, the load duration is very short (typically around 200 ms) and the specimen is unable to respond at the same rate. As a result, the specimen responds to the loading impulse (the area under the load versus time plot). At lower design pressures (between 10 and 100 psi), the load duration is intermediate, and the structure must respond to both the peak pressure and the impulse. At very low pressure ranges (less than 10 psi), the load duration is long, and the structure responds only to the peak pressure. The specimens in this study were subjected to very high pressures for a short duration so that they would respond to the impulse.

The type of blast load to which the structure is subjected is another important characteristic that must be determined when analyzing a structure. This is a function of the environment around the structural member being analyzed. The member could be subjected to a blast wave that has not been reflected off of any other surfaces (free air burst). It could also be subjected to a more complicated loading history if blast waves that have been reflected off other surfaces also contact the member. The orientation of this member with regard to the blast is also quite important. Any surface that has a perpendicular component to the blast will reflect some of the blast wave. This reflection increases the pressure exerted on that surface.

The properties of the explosive being used are the final aspects that need to be examined. These properties include the distance from the charge to the specimen, the weight of the explosive, the type of explosive being used, and the shape of the explosive charge. The explosive is typically converted into an equivalent weight of TNT when the TM5-1300 is used. The scaled distance is calculated once this conversion is complete. This distance is defined as the distance from the center of the charge to the specimen divided by the cubed root of the weight of the charge. This value is then used in conjunction with graphs correlated to provide pressures and impulses as a function of scaled distance for various charge shapes.

2.2. FIBER REINFORCED CONCRETE EXPOSED TO IMPACT

Seven methods for measuring the impact resistance for fiber reinforced concrete are included in the ACI Committee 544 report, "Measurement of Properties of Fiber Reinforced Concrete" [3]. These methods include a weighted pendulum (Charpy) impact test, a drop-weight test, a constant strain-rate test, a projectile impact test, a split-Hopkinson bar test, an explosive test, and an instrumented pendulum test. The report concludes with a standard test setups for some of the testing types. Impact resistance can be quantified by measuring the energy required to fracture a specimen, the number of blows in a repeated impact test, and the size of damage caused by impact.

Considerable research has been conducted on fiber reinforced concretes subjected to impact. None of this research however, addresses the impact resistance of carbon fiber reinforced concrete. Most studies focus on the effect of steel fibers (Almansa and Canovas [4], Luo et al. [5], Ong et al. [6], Nataraja et al. [7], and Wang et al. [8], among others). The methods used to examine the impact resistance for each varied.

Both Almansa and Canovas [4] as well as Luo et al. [5] used small arms fire to assess the resistance of hooked end steel fibers. To construct the specimens, Alamansa and Canovas [4] used a standard placement technique. Luo et al. used slurry infiltration, a technique that involves placing the fibers into the form and then pouring a fluidized mortar or slurry around the fibers.

Ong et al. [6] used a drop-weight setup to test various volume fractions of both hooked end steel and polymeric fibers. This study tested one-square meter slabs under the impact of a 43 kg mass dropped from 4 m.

Nataraja et al. [7] also used a drop-weight setup to test the capacity of crimped steel fibers. They applied the standard test setup described in ACI 544.2. The specimens used are 15-cm diameter disks that are 6.6-cm thick. Bothe the number of blows to first crack and the number of blows until failure were recorded.

Wang et al. [8] also used a drop-weight setup to examine different volume fractions of polypropylene, hooked steel, and crimped fibers. The specimens in this study were beams. Panels had been used in all previous studies. The drop weight was 60 kg and was dropped from a height of 15 cm. In general, these studies found that increasing the fiber content increased the impact resistance of the specimen. Wang suggested this

increase appeared to have a limit at which the benefit of adding the fibers would be outweighed by the cost of adding additional fibers. In their study, a large jump in impact energy absorbed occurred between 0.5% and 0.75%. Beyond this, any noted increase was small.

Wang et al. [8] indicated that, at a lower fiber content, more of the fibers appeared to break, while at a higher content the fibers pulled out. Pulling the fibers out absorbs more energy and, therefore, when the fiber content becomes high enough to switch to a pull-out failure, the fracture energy increases dramatically. In many cases, it would be desirable to examine the static properties of a material and use this information to predict the behavior of the material under impact loading.

Marar et al. [9] recognized this approach and examined the relationship between impact energy and compression toughness for hooked end steel fibers. Fibers with different aspect ratios were added in varying quantities to high strength concrete. The resulting concrete was tested with the standard ACI 544 test setup to determine the impact energy. This was compared to the compression toughness and determined that the two are logarithmically related. The constants in the equation changed as a function of the aspect ratio of the fibers, though were constant over varying fiber contents.

2.3. FIBER REINFORCED CONCRETE EXPOSED TO BLAST

The following techniques have been proposed for improving the blast resistance of reinforced concrete (RC) slabs: one is strengthening with fiber reinforced polymer (FRP) composites [10] or steel plates on the blasted and/or rear surface of the RC slab; the other technique is employing a fiber reinforced concrete as the slab material .

The concept of using fibers as reinforcement in blast is not new. Fibers were used for structural reinforcement in ancient times. Research on the use of fibers to increase the strength of both blast and impact structures has typically been limited to steel fibers and, to a lesser degree, polypropylene fibers.

Shock tubes may be used to create a short duration shock wave. Magnusson and Hallgren [11] examined air blast loading in a shock tube, and its effect on concrete beams, including some steel fiber reinforced beams. The instrumentation in this study consisted of a pressure gage to measure reflected pressure, deflection gages and

accelerometers at midspan, and load cells placed at the supports. They found that the failure modes of the beams depended on the reinforcement ratio and the presence of fibers. The steel fibers provided increased shear resistance, and resulted in the beams failing in flexure.

The tests conducted by Robins and Calderwod [12] also showed that the inclusion of steel and polypropylene fibers significantly reduces the size and particle velocity of fragments caused by subjecting slabs to explosive loading.

Lan et al. [13] tested a total of 74 specimens using 17 detonation phases. Seven detonations were initiated to test the series of steel fiber reinforced concrete (SFRC) specimens (charge weight for each test varied from 8, 20 or 30 kg). Six detonations were initiated to test the profiled steel sheeting reinforced concrete (PSSRC) specimens and four detonations were initiated to test the slabs and steel–concrete–steel sandwich (SASS) composite panels (charge weight was 100 kg). The stand-off distance for all tests was 5 m. Their results showed that for the same fiber concentration in panels, longer fiber performed better than short fibers in resisting cracking and spalling. However, there is a limit to the fiber length to prevent balling in the concrete mix.

Explosive tests on fiber-reinforced concrete slabs have been carried out by Williamson [14]. He observed that the result of shock loading applied to plain concrete by explosives was to completely disintegrate the slab specimens. A considerable reduction in spall velocity of the fragments was obtained by him when the matrix was reinforced with 1.75% nylon fibers.

In a study carried out by Silva et al. [15], the feasibility of using innovative composite materials to improve the blast resistance capacity of one-way reinforced concrete slabs was examined. Four slabs were strengthened with carbon fiber and steel fiber reinforced polymers, comprising of two slabs retrofitted on a single side and two slabs retrofitted on both sides. Test results indicate that there was no significant increase in blast resistance when the slabs were retrofitted on a single side; however, slabs retrofitted on both sides displayed a significant increase in blast resistance.

2.4. DYNAMIC INCREASE FACTOR

The dynamic increase factor is a way of expressing the increase in a material property (typically either tensile or compressive strength) that results from an increase in the strain rate at which the material is loaded. This increase can be significant, especially at the high strain rates caused by blast and impact testing. Any change in the material properties must be quantified to accurately model the materials responses to these loadings.

A curve was created to define the dynamic increase factor (DIF) for all strain rates. DIF is simply the dynamic strength of the material divided by the static strength of the material. The static strength is determined by loading the specimen at less than 3E-5 strain units per second. Typical strain rates for load types are summarized below in Table 2.1.

Table 2.1. Typical Strain Rates

Type of loading	Strain rate (strain units per second)
Creep	10^{-6} to 10^{-7}
Earthquake	10^{-2} to 10^{-3}
Hard impact	1 to 10
Blast	10^{2} to 10^{3}

In concrete, an increase in ultimate strength is thought to be due to the inertial resistance of the material as it cracks, which results in two changes. First, the specimen will be forced to crack through areas of greater resistance because, in essence, it does not have time to find the weakest path. Next, because these cracks tend to be more discontinuous, a greater amount of cracking is required to cause failure [16].

2.4.1. Concrete in Compression. There has been a significant amount of research completed which examines the effect of loading rate on the compressive properties of concrete [17-19]. Figure 2.2 shows some of the data relating the DIF to

strain rate. The data was collected using a variety of test methods including a split Hopkinson pressure bar, impact testing (including Charpy), and drop weight testing.

The data shown in Figure 2.2 is a summary of unconfined compressive testing. Other tests examined the effect of confinement on the DIF. Schmidt and Cazacu [18] used a split Hopkinson pressure bar to examine confinement. They found that the strain rate sensitivity decreased as the confinement increased. Another variable investigated by Ross et al. [17] was the effect of moisture on the DIF. The results showed the changes in the DIF due to moisture to be minimal.

2.4.2. Concrete in Tension. The DIF of concrete in tension has received less emphasis in the literature than the DIF in compression; however, there is still a significant amount of research available [17, 20]. Figure 2.3 provides a summary of some of the data collected. The figure also shows the bilinear equation (in a log-log plot) that defines the modified CEB (Comité Euro-Internacional du Béton Bulletin) equation.

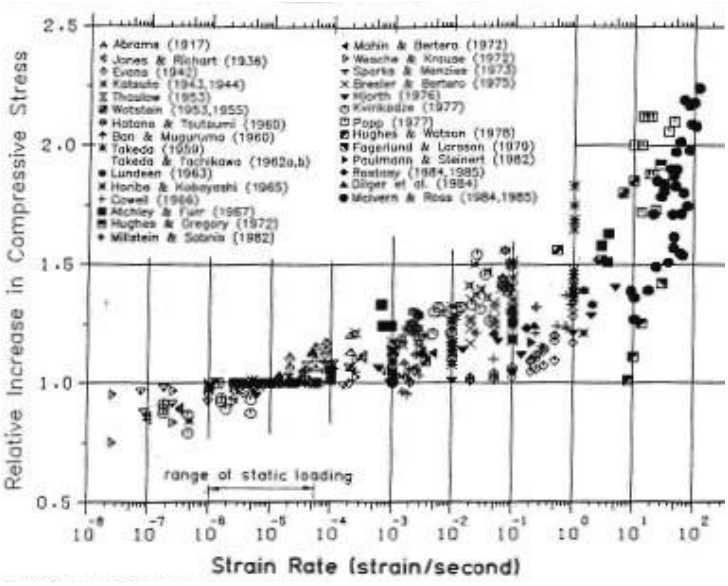

Figure 2.2. DIF for Concrete in Compression

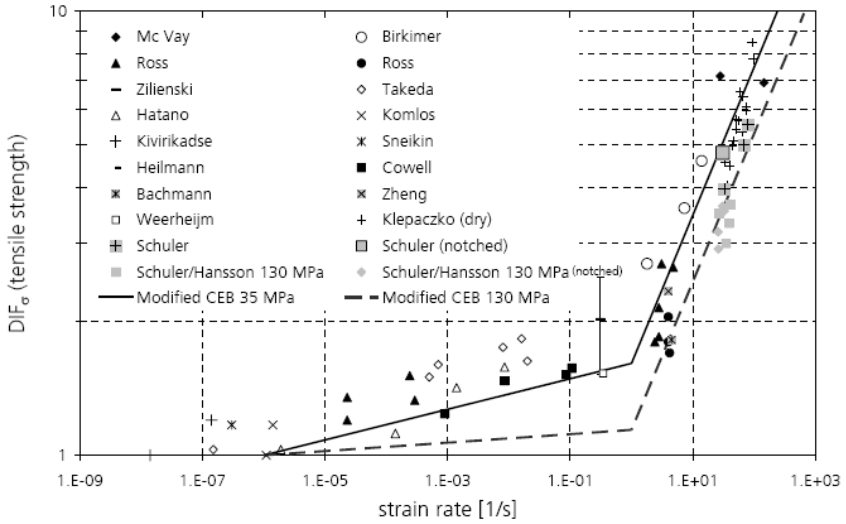

Figure 2.3. DIF for Concrete in Tension

The results shown in Figure 2.3 were obtained using both direct tension and split cylinder testing. Ross et al. [17] tested a variety of configurations including split cylinders and direct tension specimens with both square and saddle shaped notches using a split Hopkinson pressure bar. Suaris and Shah [19] examined the effect of strain rate on steel fiber reinforced concrete. They concluded, "the bond between smooth fibers and the concrete matrix does not appear to be significantly influenced by the strain rate."

2.4.3. Steel Reinforcement. Steel also exhibits strain rate effects, and this must be accounted for within the finite element model. Malvar [21] compiled much of the data dealing with this topic and found that the dynamic increase factor is inversely related to the yield stress of the reinforcement. The equation they developed to calculate the DIF is a function of the yield stress. The equation is shown in Equation 2.1 where ε is the strain rate in seconds^{-1}, and f_y is the yield stress in ksi.

$$DIF = \left(\frac{\varepsilon}{10^{-4}} \right)^{\alpha} \tag{1}$$

where $\alpha = 0.074 - 0.40 * \frac{f_y}{60}$

Alves [22] used the Cowper-Symonds equation to model the rate sensitivity of reinforcing steel. The Cowper-Symonds equation is shown in Equation 2.2. where ε is the strain rate in seconds^{-1}, and c and q are the coefficients. The coefficients Alves used to describe the behavior of mild reinforcing steel were c = 550.43 s^{-1} and q = 3.439.

$$DIF = \left(\frac{\varepsilon}{c}\right)^{\frac{1}{q}} \tag{2}$$

2.5. THE FINITE ELEMENT ANALYSIS TECHNIQUE

2.5.1. The Explicit Finite Element Method (FEM). The explicit FEM was originally developed to solve problems in both wave propagation and impact engineering. It is currently used, however, for many other applications, such as sheet metal forming, underwater simulations, failure analysis, glass forming, metal cutting, pavement design, and earthquake engineering [23]. An implicit FEM becomes expensive when thousands of time steps must be taken to solve a dynamic problem because of the cost of inverting stiffness matrices to solve the large sets of nonlinear equations, especially for models with thousands of degrees of freedom or when nonlinearities are present.

In an explicit FEM, the solution can be achieved without forming a global stiffness matrix. Instead, it is obtained on an element-by-element basis. As a result, the explicit approach can treat large, three-dimensional models (thousands of degrees of freedom) with comparatively modest computer storage requirements. Other advantages include the easy implementation and accurate treatment of general nonlinearities. The explicit method is conditionally stable, however, requiring small time steps to be used. For stable computations, the time step is selected by the computer code such that, for undamped problems [24]:

$$\Delta t \leq \frac{l}{c_w} \tag{3}$$

where l is related to the smallest element size and c_w is its fastest wave speed (the speed at which stress waves travel in the element). The physical interpretation of this

condition for linear displacement elements is that Δt must be small enough that information does not propagate across more than one element in a time step. Thus this could result in excessive simulation times as the level of discretization increases.

2.5.2. The Finite Element Approximation. Three steps are required to complete a FEM analysis: 1) domain discretization, 2) local approximation, and 3) bothe the assemblage and solution of the global matrix equation. The domain discretization involves dividing the deformable body occupying a spatial domain (V) into a finite number of internal, contiguous elements of regular shapes defined by a fixed number of nodes (N_{nod}). For linear elasticity, the domain (V) can be described by the following equations [25]:

$$\varepsilon_{ij} = \frac{1}{2}\left(\frac{\partial u_i}{\partial x_j} + \frac{\partial u_j}{\partial x_i}\right) \quad \text{strain-displacement (kinematic) equations} \tag{4}$$

$$\sigma_{ij} = D^e_{ijkl}\varepsilon_{kl} \quad \text{stress-strain (constitutive) equations} \tag{5}$$

$$\frac{\partial \sigma_{ij}}{\partial x_j} + \bar{b}_i = 0 \quad \text{equilibrium (static) equations} \tag{6}$$

Where u_i is the displacement vector, ε_{ij} is the column matrix of the strain components, σ_{ij} is the column matrix of the stress components, $\bar{b}_i$ is the vector of the body forces, and D^e_{ijkl} is the elastic material stiffness matrix.

In the standard displacement version of the FEM, the displacement components are approximated as linear combinations of suitably chosen interpolation –or shape– functions $N_I(x)$, where $I = 1, 2, \ldots N_{nod}$, and x is the vector of Cartesian components x_1, x_2, and x_3. A typical property of the FE shape functions is that each of them is associated with one of N_{nod} nodes. The value of the I-th shape function is equal to one at node number I and zero at all other nodes. The displacement approximation is defined as

$$u_i(x) = \sum_{I=1}^{N_{nod}} N_I(x) d_{Ii} \qquad \text{i=1, 2, 3} \tag{7}$$

where d_{Ii} are the unknown displacement parameters. In matrix notation, the approximation in (7) is rewritten as

$$u(x) = N(x)d \tag{8}$$

Similarly, the kinematic (4) provides an approximation of the strains,

$$\varepsilon(x) = \partial u(x) = \partial N(x)d = B(x)d \tag{9}$$

Where $B = \partial N$ is the strain-displacement matrix – or the B-matrix – containing the derivatives of the shape function with respect to the spatial coordinates.

Substituting the strain approximation into (9), the constitutive (5), produces the stress approximation

$$\sigma(x) = D_e(x)\varepsilon(x) = D_e(x)B(x)d \tag{10}$$

Where the argument x at D_e explicitly marks that the elastic properties may be position-dependent.

Although approximations of displacements, strains, and stresses satisfy both the kinematic and constitutive equations exactly, the static differential equations of equilibrium (4-6), in general, cannot be satisfied exactly at every point of the body (i.e., in a strong sense, because the adopted approximations depend only on a finite number of unknown displacement parameters). The static equations directly are not used directly. Instead, they are replaced by the principle of virtual work, which leads into the weak form of the equilibrium equations. This weak form introduces an arbitrary matrix of virtual displacement parameters (δd) in its integral-based equality.

Taking into account that neither d nor δd are functions of the spatial coordinates and, as such, can be taken out of the virtual work equations integrals. The weak form of the equilibrium equations can be written as

$$d^T K_e^T \delta d = f_{ext}^T \delta d \tag{11}$$

where

$$K_e = \int_V B^T(x) D_e(x) B(x) dV \tag{12}$$

is the (global) elastic stiffness matrix and

$$f_{ext} = \int_V N^T(x) \bar{b} dV \tag{13}$$

is the (equivalent) external force vector. Equation 9 is satisfied for δd if and only if

$$f_{ext} = K_e d \tag{14}$$

These are the discretized equations of equilibrium from which we can compute the unknown displacement parameters.

2.5.3. Central Difference Scheme for Explicit Time Integration. As previously stated, in an explicit FEM, the solution can be achieved without forming a global stiffness matrix. LS-DYNA uses the central-difference method, which is characteristic of explicit methods for direct time integration [24, 25]. In this method, the solution is determined in terms of both previous (before current time step t_n) elastic displacements and time derivatives of these displacements. This method allows us to obtain the finite element solution using the following equations (without damping):

$$\dot{u}_{t\,n+\frac{1}{2}} = \dot{u}_{t\,n-\frac{1}{2}} + \Delta t_n M^{-1}(f_{ext,t_n} - \int_V B^T \sigma_{t_n} dV) \tag{15}$$

$$u_{t\,n+1} = u_{t\,n} + \Delta t_{n+\frac{1}{2}} \dot{u}_{t\,n+\frac{1}{2}} \tag{16}$$

where f_{ext,t_n} is the vector of applied forces associated with the boundary conditions and body forces at time step t_n, M is the mass matrix, and $\int_V B^T \sigma_{t_n} dV$ is the internal force vector.

Both the velocities and the displacements are updated at each time step. In general, implicit methods have the form

$$u_{t\,n+1} = f(\dot{u}_{t\,n+1} + \ddot{u}_{t\,n+1}, \dot{u}_{t\,n}, ...) \tag{17}$$

and, therefore, a computation of the current nodal displacements requires knowledge of the time derivatives from $u_{t\,n+1}$, which are unknown. Consequently, simultaneous equations must be solved to compute the current displacements. In contrast, explicit methods have the form

$$u_{t\,n+1} = f(u_{t\,n}, \dot{u}_{t\,n}, \ddot{u}_{t\,n}, u_{t\,n-1}, ...) \tag{18}$$

and, therefore, current nodal displacements can be determined in terms of completely historical information. This information consists of both displacements and time derivatives of displacements at previous time steps. If a diagonal mass matrix is used, (15) is a system of linear algebraic equations, and a solution is obtained without solving simultaneous equations. Once displacements are updated, strains can be computed that are then used to determine both stresses and, eventually, nodal forces.

2.6. FINITE ELEMENT ANALYSIS OF FIBER REINFORCED CONCRETE

Using a numerical simulation tool is motivated by the high cost of undertaking impact and blast tests and the ease of changing material properties. Hence, it is possible to study the influence of different parameters, such as fracture energy, which depends on the volume fraction of added fibers, and different impact and blast conditions. However, in order to make simulations an effective tool in these kinds of studies, the fiber-reinforced concrete has to be homogenized and modeled as one material instead of modeling each of the discrete fibers and their bond to the surrounding concrete.

In recent decades, several codes have been developed to model impact and explosion such as ABAQUS, ANSYS, AUTODYN, ELFEN, and LS-DYNA. Also, various material models of different types of concrete have been proposed for impact and blast analysis [26-29]. Most of them are dedicated to high-strength and steel-reinforced brittle concrete structures under transient dynamic loadings [28]. In such models, damage accumulation, strain-hardening, and strain rate are considered [29]. In some others, an equation of state (EOS) is also included [27]. A major drawback, however, is that many of them require too many parameters, some of which have no physical meaning, and cannot be determined by conventional material tests.

In another numerical study, Teng et al. [26] employed a simple elastoplastic material model and the LS-DYNA code to model the non-linear softening behavior of fiber reinforced concrete (FRC) with 1, 1.5 and 2% steel fibers. They also carried out a number of preliminary mechanical tests such as uniaxial compression and split tests to obtain the material properties and non-linear stress-strain curve of steel fiber-reinforced concrete (SFRC). They compared the numerically predicted residual velocity of projectiles and the cavity diameters of concrete targets with the test results.

Agardh and Laine [27] performed a numerical simulation of FRC under high velocity impact loading using the LS-DYNA code. The results of their finite element simulation model, such as the velocity of projectiles after penetration and diameters of craters, were in fairly good agreement with actual test results.

Farnam et al. [30] tested high-performance-fiber-reinforced concrete (HPFRC) panels by drop projectiles up to an impact at which failure occurs. The combination of SOIL_CONCRETE material model with the MAT_ADD_EROSION option allowed for

efficient simulation of HPFRC. However, direct shear tests are then required to obtain an accurate value of ultimate shear strain for the MAT_ADD_EROSION option.

N. Kishi et al. [31] analyzed the impact-resistant behavior of reinforced concrete slabs with various types of support conditions. They assumed simple constitutive models for each material in LS-DYNA. The stress-strain relationship of concrete was defined by using a bilinear model in compression and a linear cut-off model in tension. The stress-strain relationship of reinforcing steel was defined by using a bilinear isotropic hardening model.

Numerical simulations were carried out by Alavi Nia [32] using LS-DYNA. Nia found that a Winfrith concrete material model associated with the ADD_EROSION option and maximum principal strain was an appropriate model for simulating FRC behavior under impact loading.

Zhao et al. [33], employed LS–DYNA to investigate the damage mechanism and dynamic responses of reinforced concrete (RC) containment subjected to internal blast loading. A fluid-structure coupling algorithm and multi-material model were adopted in this study.

Wright et al. [34] focused on identifying a carbon fiber based composite material that offered an optimum combination of structural performance, blast protection and low cost through an integrated combination of numerical modeling and experimental assessment. They performed a small scale test to provide valuable experimental data for model validation. The finite element codes AUTODYN and LS-DYNA were used to predict the blast response of the composites. The blast load was initially represented using load curves which were derived for a range of C4 explosive charge weights in AUTODYN. The difference between material models used in LS-DYNA and AUTODYN and the subsequent results were presented and discussed.

Coughlin et al. [35] used LS-DYNA to model one fiber reinforced concrete barrier and a control barrier to see if the analytical results would match the results of experimental testing. The charge center and equivalent weight of TNT used to apply the blast load to the models was defined using the *LOAD_BLAST function in LS-DYNA. The selected steel material model was a bilinear stress strain curve including strain rate effects. A triaxial damage model, the Continuous Surface Cap Model (CSCM), was used

to model concrete in the barriers. The CFRC barrier model used the same material parameters as the control concrete, but the fracture energy parameters for tension and shear were modified to match the results of previous uniaxial tensile tests. This model showed reasonably good agreement for barrier damage patterns when compared with blast test results for both a traditional and fiber-reinforced concrete specimen.

Ganchai et al. [36] presented results that compared numerical simulation results to the experimental responses of concrete panels subjected to blast loading. LS-DYNA was used in the numerical analysis for blast load and Concrete Damage Model Release 3 was used to define the concrete's material properties. In this study, the results indicated that the maximum deflection obtained from LS-DYNA was 17% less than the experimental values.

Hao et al. [37] conducted a study on the dynamic behavior of both reinforced concrete slabs and the factors that influence behavior (i.e, the concrete strength ratio, slab thickness, and the steel reinforcement ratio when subjected to blast loading). An analysis was performed using LS-DYNA, and numerical analysis, principles for a blast resistant design were proposed, such as increasing the slab thickness, which is preferred over concrete strength enhancement to improve the behavior of RC slabs subjected to blast loading.

Broadhouse [38] presented theoretical information on the Winfrith Concrete Model. He also described both the various input parameters in the model and the effect of strain rate enhancement. In the latter part of his paper, Broadhouse [18] also described the methodology to output cracks in LS-DYNA. Broadhouse [18] provided enough information to use the Winfrith Concrete Model, with its crack plotting capability, to study the behavior of concrete under various load and stress conditions.

Sangi et al. [39] compared the behavior of reinforced concrete slabs analyzed to both the Winfrith Concrete Model and the Concrete Damage Model Release 3 when subjected to drop weights. Impact tests were done on the following six reinforced concrete slabs: four slabs were 30 in. square (775 mm square) and 3 inch (76 mm) thick and two were 91 in. square (2320 mm square) and 6 inch (150 mm) thick. The results obtained from the experimental output were compared with the two models from LS-DYNA. In this study, the damage pattern obtained from the Winfrith Concrete Model

was in agreement with the experiment performed. Additionally, the impact force histories obtained from the experiment were in agreement with both models. Thus, they suggested the use of these two models for finite element studies on reinforced concrete slabs.

Xu et al. [40] presented a numerical simulation study on concrete spallation of reinforced concrete slabs under various blast loading and structural conditions. The Pseudo Tensor concrete material model [24] was employed, taking into account the strain rate effect. The erosion technique was adopted to model the spallation process. The principal tensile strain was adopted as the criteria for erosion in the numerical simulation. Here, the simulation results (using the erosion criterion mentioned above for concrete spallation) demonstrated a consistent comparison with relevant experimental observations.

REFERENCES

[1] Battat, Brigitte, Application of Structural Materials for Protection From Explosions – A State of the Art Report, Advanced Materials and Processes Technology (AMPT-21), New York, January 2001.

[2] Unified Facilities Criteria (UFC) 3-340-02, "Structures to Resist the Effects of Accidental Explosions," Washington D.C., U.S. Department of Defense; 2008. p. 50-70.

[3] ACI Committee 544, 1996, "State-of-the-Art Report on Fiber Reinforced Concrete (ACI 544.1R-96) (Reapproved 2002)," American Concrete Institute, Farmington Hills, MI.

[4] EM. Almansa and MF. Canovas, "Behavior of Normal and Steel Fiber-Reinforced Concrete under Impact of Small Projectiles," *Cement and Concrete Research*, vol. 29, no. 11, Nov. 1999, pp. 1807-1814.

[5] X. Luo, W. Sun, and SYN. Chan, "Characteristics of High-Performance Steel Fiber-Reinforced Concrete Subject to High Velocity Impact," *Cement and Concrete Research*, vol. 30, no. 6, June 2000, pp. 907-914.

[6] KCG. Ong, M. Basheerkan, P. Paramasivam, "Resistance of Fiber Concrete Slabs to Low Velocity Projectile Impact," *Cement and Concrete Composites*, vol.21, no. 5-6, Oct 1999, pp 391-401.

[7] MC. Nataraja, N. Dhang, and AP. Gupta, "Statistical Variations in Impact Resistance of Steel Fiber-Reinforced Concrete Subjected to Drop Weight Test," *Cement and Concrete Research*, vol. 29, no. 7, July 1999, pp 989-995.

[8] N. Wang, S. Mindess, and K. Ko, "Fiber Reinforced Concrete Beams under Impact Loading," *Cement and Concrete Research*, vol. 26, no. 3, March 1996, pp 363-376.

[9] K. Marar, O. Eren, and T. Celik, "Relationship between Impact Energy and Compression Toughness Energy of High-Strength Fiber-Reinforced Concrete," *Materials Letters*, vol. 47, No. 4-5, Feb 2001, pp 297-304.

[10] K.M. Mosalam, A.S. Mosallam, "Nonlinear Transient Analysis of Reinforced Concrete Slabs Subjected to Blast Loading and Retrofitted with CFRP Composites." Composites Part B: Engineering, 2001, 32(8), 623–636.

[11] J. Magnusson, and M. Hallgre, "Reinforced High Strength Concrete Beams Subjected to Air Blast Loading," *Structures and Materials*, 15, *Structures Under Shock and Impact* VIII, 2004, p 53-62.

[12] P.J. Robins, and R.W. Calderwod, "Explosive Testing of Fiber Reinforced Concrete," 1978, 76-78.

[13] S. Lan, T. Lok, and L. Heng, "Composite Structural Panels Subjected to Explosive Loading," *Construction and Building Material*, 2005, 19(5), 387-395.

[14] G.R. Williamson, "Response of Fibrous Reinforced Concrete to Explosive Loading" Technical Report 2-48 (US Army Corps of Engineers, Ohio, USA - River Division Laboratories), 1996.

[15] P.F. Silva, and B. Lu, "Improving the Blast Resistance Capacity of RC Slabs with Innovative Composite Materials," *Composites Part B: Engineering*, 2007, 38(5-6), 523-534.

[16] PH. Bischoff, and SH. Perry, "Compressive Behavior of Concrete at High Strain Rates," *Materials and Structures*, vol. 24, No. 144, Nov, 1991, p 425-4.

[17] C.A. Ross, J.W. Tedesco, and S.T. Kuennen, "Effects of Strain Rate on Concrete Strength," *ACI Materials Journal*, vol. 92, no. 1, Jan-Feb, 1995, p 37-47.

[18] Schmidt, M.J., and Cazacu, O., "Behavior of Cementitious Materials for High-Strain Rate Conditions, *Journal De Physique*. IV : JP, vol. 134, 2006, pp 1119-1124.

[19] Suaris, Wimal, and S.P. Shah, "Strain-Rate Effects in Fiber-Reinforced Concrete Subjected to Impact and Impulsive Loading," *Composites*, vol. 13, no. 2, April 1982, pp153-159.

[20] H. Schuler, and H. Hansson, "Fracture Behavior of High Performance Concrete Investigated with a Hopkinson Bar," *Proceedings - 8th International Conference on Mechanical and Physical Behaviour of Materials under Dyanmic Loading*, EURODYMAT 2006, p 1145-1151.

[21] L. Malvar, and Javier, "Review of Static and Dynamic Properties of Steel Reinforcing Bars," *ACI Materials Journal*, vol. 95, No. 5, Sep-Oct, 1998, p 609-616.

[22] M. Alves, "Material Constitutive Law for Large Strains and Strain Rates," *Journal of Engineering Mechanics*, vol. 126, no. 2, February 2000, pp 215-218.

[23] Livermore Software Technology Corporation, "LS-DYNA Keyword User's Manual," Version 970, April 2003.

[24] Livermore Software Technology Corporation, "LS-DYNA Theoretical Manual, May1998.

[25] J.N. Reddy, "An Introduction to the Finite Element Method," McGraw-Hill Education - 2006 - Hardback - 766 pages - ISBN 0072466855

[26] Teng T-L, Chu Y-A, Chang F-A, Shen B-C, Cheng D-S., "Development and validation of numerical model of steel fiber reinforced concrete for high-velocity impact," *Computer Material Science*, 2008; 42 :90-99.

[27] L. Agardh and L. Laine, "3D FE-Simulation of High Velocity Fragment Perforation of Reinforced Concrete Slabs," *International Journal of Impact Engineering*, 1999; 22(4):911–22.

[28] C.Y. Tham, "Reinforced concrete perforation and penetration simulation using AUTODYN-3D." Finite Element Analysis Design, 2005, 41, 1401–10.

[29] T.J. Holmquist, GR. Johnson, and WH. Cook, "A Computational Constitutive Model for Concrete Subjected to Larger Strains, High Strain Rates, and High Pressure, *Proceedings of the 14th International Symposium on Ballistics*, 1993, 591–600.

[30] Y. Farnam, S. Mohammadi, and M. Shekarchi, "Experimental and Numerical Investigations of Low Velocity Impact Behavior of High-Performance Fiber-Reinforced Cement Based Composite," *International Journal of Impact Engineering*, 2010, 37(2), 220–229.

[31] N. Kishi, Y. Kurihashi, S. Ghadimi khasraghy, H. Miami, "Numerical Simulation of Impact Response Behavior of Rectangular Reinforced Concrete Slabs under Falling-Weight Impact Loading," Applied Mechanics and Materials, 2011, 82, 266-271.

[32] Alavi, Nia , M. Hedayatian, M. Nili, and V. Afrough Sabet, "An Experimental and Numerical Study on How Steel and Polypropylene Fibers affect the Impact Resistance in Fiber-Reinforced Concrete," International Journal of Impact Engineering, 2012, 46, 62-73.

[33] Zhao, C.F., Chen, J.Y., Wang, Y., and Lu, S.J. , "Damage Mechanism And Response of Reinforced Concrete Containment Structure under Internal Blast Loading," Theoretical and Applied Fracture Mechanics, 2012, 61, 12–20.

[34] Wright, A., French, M., "The Response of Carbon Fiber Composites to Blast Loading Via the Europa CAFV Programme," *Journal of Material Science*, 2008, 43, 6619-6629.

[35] Coughlin, A.M., Musselman E.S., Schokker A.J., and Linzell D.G., "Behavior of Portable Fiber Reinforced Concrete Vehicle Barriers Subject to Blasts from Contact Charges," *International Journal of Impact Engineering*, 2010, 37(5), 521-529.

[36] G. Tanapornraweekit, "Modeling of a Reinforced Concrete Panel Subjected to Blast Load by Explicit Non-linear FE Code," *In Proceedings of AEES Conference*, 2007.

[37] D.U.Hao, L.Z., "Numerical Analysis of Dynamic Behavior of RC Slabs under Blast Loading," Transactions of Tianjin University, 2008. 15(1): p. 61-64.

[38] B. Broadhouse, and G. Attwood, "Finite Element Analysis of the Impact Response of Reinforced Concrete Structures uUsing Dyna3D," Proceedings of Structural Mechanics in Reactor Technology, University of Stuttgart Germany Elsevier Science Publishing. 1993.

[39] A. Sangi, and I. May, "High-Mass, Low-Velocity Impacts on Reinforced Concrete Slabs," In proceeding . 7th European LSDYNA Conference, 2009, Dynamore GMBH.

[40] K. Xu, and Y. Lu, "Numerical Simulation Study of Spallation in Reinforced Concrete Plates Subjected to Blast Loading," *Computers & Structures*, 2006. 84(5-6): p. 431-438.

PAPER

I. COMPARATIVE IMPACT BEHAVIOR OF FOUR LONG CARBON FIBER REINFORCED CONCRETES

Zahra S. Tabatabaei, Jeffery S. Volz, Benjamin P. Gliha, Darwin I. Keener

ABSTRACT

The addition of long carbon fibers (fibers more than 10 mm in length) to traditional reinforced concrete is proposed as a method to improve the impact spalling resistance of concrete. A series of experimental tests were conducted to compare the impact resistance of plain concrete (PC), steel reinforced concrete, and four different types of long carbon fiber reinforced concrete (LCFRC) panels. The plain and conventional steel reinforced concrete panels served as control specimens. Of the four types of long carbon fibers tested in this study, the first fiber type consisted of an epoxy-impregnated, bidirectional weave (Type A), while the remaining types consisted of fiber tow with three different variations of a polypropylene support system (Type B). To determine the properties and performance of the LCFRC, experimental testing included a drop weight impact test of the panels as well as a standard ASTM test method for flexural performance of fiber-reinforced concrete. The results from each test in terms of impact energy, time histories of impact load and deflection, strain energy, failure crack pattern, and flexural properties were then compared to one another. This comparison indicated that adding long carbon fibers to concrete increases the post-cracking behavior of the concrete and decreases fragmentation during an impact test. Of the four fibers tested, Fiber Type B3 exhibited the highest performance, absorbing more energy during impact. This result is most likely related to the unique shape of this type of fiber in comparison to the others, which allowed more extensive wetting of the fiber with cement paste and thus improved bond to the cementitious matrix.

Keywords: Long carbon fiber concrete; Impact test; Experimental study

1. Introduction

Considerable research has been conducted on fiber reinforced concretes subjected to impact. The majority of these studies dealt with the effect of steel fibers [1-12]. The methods used to examine the impact resistance for each varied. Both Almansa and Canovas [1] as well as Luo et al. [6] used small arms fire to assess the resistance of hooked end steel fibers. Ong et al. [3] used a drop weight setup to test various volume fractions of both hooked end steel fibers and polymeric fibers. Nataraja et al. [2] also used a drop weight setup to test the capacity of crimped steel fibers. Wang et al. [7] used a drop weight setup to examine different volume fractions of polypropylene, hooked steel, and crimped fibers.

In general, these studies found that increasing the fiber content increased the impact resistance of the specimen. Wang et al. [7] indicated, however, that this increase appears to have a limit at which the benefit of adding the fibers outweighs the cost. They indicated that, at the lower fiber content, more of the fibers appeared to break. At the higher fiber content, the fibers pulled out. Pulling the fibers out absorbs more energy. Therefore, when the fiber content becomes high enough to switch to a pull out failure, the fracture energy increases dramatically.

Adding fibers to concrete increases its ductility, tensile strength, flexural strength, and resistance against both dynamic and impact loads [13,14]. Furthermore, adding fibers reduces the possibility of spalling and scabbing failures, prevents crack propagation, and extends the softening region in the concrete matrix [15]. Success, however, is highly dependent on the type of fiber used, both the size and the properties of the fibers, the volume fraction added, and the properties of the concrete matrix. Longer fibers are known to need more energy for pull out [16]. Research in the area of fibers more than 30 mm in length, however, is virtually nonexistent. Because fibers used in this present research (100 mm long) were more than three times as long as other researched fibers, they are referred to here as long fibers. Carbon fibers possess many potential benefits over other fibers, including a higher strength, higher modulus, and increased durability. Carbon fibers also offer an economical benefit as they can be used as a waste product from the aerospace industry.

Long carbon fibers have not been previously used because they tend to both segregate mixtures and decrease workability. A proprietary coating was applied to the fiber yarn to form a stiff tape and overcome these problems. This coating allows the fibers to be added directly into the concrete mixer, where they evenly distribute through the mixture [15,17-19].

The objectives of this study were as follows:

Investigate the comparative behavior of four different types of long carbon fibers on the impact resistance of concrete

Find a relationship between impact energy and panel deformation

Investigate the failure mode of long carbon fiber reinforced concrete

Experimental Overview

The experimental program included both an impact test and additional tests to determine the mechanical properties of long carbon fiber reinforced concrete (LCFRC).

2. Experimental overview

2.1. Materials and mixture proportions

The materials used were Type I Portland cement, natural sand fine aggregate, and crushed limestone coarse aggregates measuring no more than 19 mm. The mixture proportion was as follows: 0.78 units of cement by weight to 1 unit of sand and 1 unit of coarse aggregate, with a water-to-cement ratio of 0.38. A high-range water reducer (HRWR) was added to improve the workability of the fiber concrete mixes. Table 1 defines the matrix mixture proportion used for all of the panels.

Four types of long carbon fibers were tested in this study. The first fiber, referred to as Fiber Type A, was a 3K (K refers to thousands of filaments in a strand), plain weave, 40 % epoxy fiber. The second fiber, referred to as Fiber Type B, consists of a 48K carbon fiber tow with a polypropylene support system. Three variations of Fiber Type B were tested. They are referred to as B1, B2, and B3. These fibers differed in their polypropylene support system. In Fiber Type B1, the carbon fiber tow was twined around a polypropylene backbone. In Fiber Type B2, the polypropylene was placed around the carbon fiber tow, forming a jacket that provided necessary fiber resiliency. A heat

treatment process partially bonded the carbon fibers to the polypropylene jacket. Fiber Type B3 consisted of carbon fiber tow twined around a stiffer polypropylene backbone. In Fiber Type B3, the tow and backbone were weaved together with cotton string. The weaving allowed for additional stability, kept the fiber from breaking apart during mixing, and allowed the cement paste to thoroughly coat the carbon fiber tow. The mechanical properties of the fibers are given in Table 2. A photograph of each fiber type is shown in Fig. 1.

2.2. Specimen dimensions and material properties

A total of six sets of falling-weight impact tests were conducted. These six sets of tests consisted of two conventional plain concrete (PC) panels, two welded wire reinforced (WWR) concrete panels, two panels for Fiber Types A1 and B1, and four panels for Fiber Types B2 and B3. Panels without fibers were used as control panels (reference panels). All specimen panels measured 1220-mm square in plan, with a thickness of 50 mm. Details of both the WWR concrete panel's cross section and the reinforcement layout are given in Fig. 2. Specimen properties are listed in Table 3.

Three 150 × 300 mm cylinders were cast for each concrete batch to determine the compressive strength of the mixture. The concrete compressive strength (f'c) was between 49.8 and 54 MPa. This difference was due to differences in casting time for each series of experiments. The yield strength (fy) of the reinforcing bars was 407 MPa.

The LCFRC panels are denoted by fiber type (i.e., A1, B1, B2, and B3). The subsequent number is the number of the test conducted on that type of panel (i.e., A1-1 is panel type A1, trial 1). Panels without fibers are identified with an abbreviation of the panel's type (PC or WWR) with the subsequent test number, (i.e., WWR-1).

2.3. Specimen production, casting, and curing

All dry components (cement and sand) were first pre-mixed together in the mixing machine for a few minutes. Approximately half of the liquid (water and super plasticizer) was added to the dry mixture. Once the dry components were fully mixed with the liquid, in the case of the LCFRC panels, fibers were added manually during

mixing. Care was taken to avoid balling of the fibers. After sufficient mixing, the remaining liquid was added to the mixture.

Sixteen panels were cast and cured at 23 ± 5°C a minimum of 28 days prior to testing. Each panel was subjected to a seven-day moist cure using both wet burlap and plastic, followed by 21 days under ambient air conditions.

2.4. Impact tests

Falling-weight impact tests were conducted by dropping a 70 mm diameter, 23 kg steel rod from a prescribed height onto the midspan of a panel using the impact test apparatus, as shown in Fig. 3. All panels were simply supported on all four sides. A 13-mm-thick section of neoprene with the same diameter as the rod was affixed to the bottom of the rod. This neoprene reduced the amount of vibration after impact with the load cell. To ensure impact occurred perpendicular to the specimen, the drop weight was guided through a 4.5 m section of PVC pipe to prevent rotation. The drop weight can drop freely onto the test specimen along this pipe. The drop weight was held in position prior to each drop by a manually operated pulley system. The effect of friction between the impacting mass and the guide system is considered negligible and thus was neglected in this study.

The dynamic load cell was centered on the panel to measure the load imparted on the panel by the drop weight. This load cell consisted of four individual dynamic load cells built by PCB Piezotronics, each capable of measuring up to 89 kN in compression under dynamic load. Using machined steel discs, a combined load cell was constructed that could measure up to 359 kN of force. A 25-mm-thick neoprene square was placed under the load cell to reduce excessive vibration after impact.

To measure deflection, a linear motion potentiometer with a 50-mm-stroke was secured under the panel, as shown in Fig. 3. This potentiometer was installed with an initial deflection of 13 mm to measure panel rebound.

The test protocol involved increasing drop heights until the specimen failed. Each series began with a drop height of 75 mm. The drop height increased by 75 mm for

subsequent drops until a drop height of 600 mm was reached. From 600 mm until failure, the drop height increased by 150 mm each time.

2.5. Flexural tests

Flexural tests were performed according to ASTM: C1609 to determine the flexural properties of the long carbon fiber reinforced concrete. The beams measured 150×150×500 mm with a span length of 450 mm (Fig.4.). Load and deflection data were collected electronically at a frequency of 5 Hz. These beams contained identical fiber sizes for each type of fiber: 100×6 mm for type A and 100 mm for type B. Three specimens were tested in each series. Net deflection values, for both data acquisition and rate control, were obtained at the mid-span and mid-height of the beams. Flexural toughness was calculated using toughness values (T_{150}^{D}), defined as the area under the load-deflection curve up to a net deflection of 1/150 of the span length.

3. Results and discussion

3.1. Impact energy

The drop height was recorded when the first crack was observed and at failure (see Table 4). Occurrence of the first crack was based on visual observation. Ultimate failure was determined based on the drop height required to sufficiently open the crack, thus fracturing the panel. In terms of first crack occurrence, the B3 series outperformed the other panels, followed closely by the WWR series. In terms of failure, Panels B3-3 and B3-4 outperformed the other panels, failing at higher drop heights. Again, the WWR panels followed closely behind the B3 series. Panel B3-4 (1.5% fiber) achieved the highest failure height of 3.66 m.

The impact energy is an important parameter in the evaluation of the mechanical properties of LCFRC panels under impact loads. The impact energy absorbed by the panels was computed based on both the weight of the rod and its velocity at the instant it struck the panel [20]. Equation (1) was used to calculate impact energy at both the appearance of the first crack and at failure:

$$E = \sum_{i=1}^{N} \frac{1}{2} m v_i^2 \quad (1)$$

where m = drop weight mass, v_i = velocity of drop weight at contact with the panel, and N= number of drops.

The impact energy absorbed by the LCFRC panels both at the appearance of the first crack and at failure was compared with that of the reference specimens (see Table 4). In terms of energy absorbed at first crack, the LCFRC panels absorbed more energy than the control panels. The B2 specimens were the only exception. Of the four types of fibers considered, the B3 specimens absorbed the highest amount of energy before the first crack appeared. The highest impact energy absorbed was 0.28 kJ (content 1%, B3). However, the input impact energy for initiating the first crack was not appreciably related to the fiber content and it did not change considerably by increasing the fiber volume fraction in the B series of tests. The impact energy at failure (EF) ranged from 0.09 and 0.83 kJ, with the B3 specimens outperformed all of the other panels. The B3 specimens outperformed the PC, WWR, LCFRC-B1, and LCRFC-B2 panels by a factor of 10, 1.2, 1.9, and 4, respectively. Increasing the fiber volume fraction from 1% to 1.5% in the B3 series increased the input impact energy at failure by approximately 70%, an appreciable change.

In terms of absorbed energy, some panels had less impact resistance than the control panels before the initiation of first crack, while at failure all of the panels had considerably higher impact resistance than the control panels. After first crack, because of the interlocking between fibers, the energy for failure increases for the LCFRC panels in comparison to the reference specimens. Residual impact strength ratio is a parameter showing the interlocking and post-cracking behavior of the fiber-reinforced concrete during impact. The residual impact strength ratio was calculated for all the panels using equation (2) [20].

$$I_{rs} = \left[\frac{\text{Energy absorbed at ultimate failure}}{\text{Energy absorbed at initiation of first crack}} \right] \quad (2)$$

Residual impact strength translates into the ability to absorb more energy under dynamic loads. For the control panels, initiation of first crack and failure occurred simultaneously, and thus the residual impact strength ratio is equal to 1.0 for these specimens (sudden failure). A value greater than 1.0 indicates reserve post-cracking strength and ductility. The panels with fibers showed substantial improvement in the residual impact strength, with ratios ranging from 1.9 (B3-2) to 5.8 (B3-3). The WWR series also showed significant residual impact strength with ratios of 5.5 (WWR-1) and 6.6 (WWR-2).

The maximum impact force (P_{max}), maximum deflection (D_{max}), and residual deflection (δ_{rs}) are also listed in Table 4. The impact force is a function of drop height and the ability of the panel to absorb energy. The highest impact force captured was for the B3 and WWR series of specimens, with maximum values of 74 kN for specimen B3-4 and 88 kN for specimen WWR-2. However, the B3-4 specimen was able to absorb more energy as the corresponding drop height was 3.66 m for B3-4 and only 3.05 m for WWR-2. For the B3 series, an increase in fiber percentage from 1% to 1.5% resulted in a 50% increase in average impact force with a corresponding 60% increase in drop height at failure. For the same increase in fiber percentage for the B2 series, the increase in average impact force at failure was only 20%.

Fig. 5 shows the relationship between input impact energy (E) and maximum deflection (D_{max}). It also illustrates the relationship between input impact energy (E) and residual deflection (δ_{rs}). Both the maximum and the residual deflections of the panels in the same series tended to increase proportionally as the input impact energy increased. Both the slope of the regression line and the R^2 values for all panels are shown in Fig. 5. From these relationships, the following conclusions are drawn:

The residual and maximum deflections of the LCFRC panels are linearly proportional to the input impact energy (E). There is not any acceptable trend for residual deflection and input impact energy for B2 series.

For all the LCFRC panels, the inclinations of the regression lines depend on the fiber properties and percentage of the fibers.

The residual and maximum deflection of the WWR panels is polynomial proportional to the input impact energy (by degree of 2).

No trend exists for the plain concrete panel due to the sudden failure of this panel.

3.2. Time histories of impact load and deflection

Figure 6 shows the time histories of both the impact load (P) and the deflection (D) for all of the panels at failure. In this figure, all the graphs were adjusted to the same start time axis for comparison purposes. All of the panels' impact load-time histories illustrate a rapid increase in the load, giving rise to the maximum load in a very short time. The impact duration of the load-time histories was between 3.2 and 7 milliseconds. The duration of the load-time histories at failure for the LCFRC panels was around 4 milliseconds for all of the fibers. The peak of the initial pulse-like waveform increased as the drop height (initial velocity) increased. The duration of the initial pulse-like waveform was approximately the same for the same series of panels regardless of the drop height. There was approximately a 0.15 milliseconds time lag between the initial rise of the impact load and the maximum midspan deflection. The maximum midspan deflection increased as the drop height increased. Additionally, the duration of deflection-time histories increased as the drop height increased. Multiple contacts between the panels and the projectile were characterized by the occurrence of multiple peaks. These peaks were referred to as 'secondary peaks' in the observed load history. The WWR panel resisted a higher load for a longer duration time than any of the other panels. An increase in both peak load and deflection was generally observed when fibers were added. This observation indicates a ductile response against impact with less damage caused to the panels.

3.3. Strain energy

The strain energy developed in the panels to dissipate the impact energy is among the important parameters in the evaluation of the mechanical properties of LCFRC under impact loads. This energy is calculated by the integration of the load-deflection curves (see Fig. 7) as shown in equation (3):

$$E_{strain} = \int P d\delta \quad (3)$$

In comparing the three fiber types, the B3 fibers showed increased ductility, higher peak deflection, and lower residual deflection, which increased further with the change from 1% to 1.5%. Although the WWR series failed at higher drop heights than the A, B1 and B2 fibers, the shape of the load-displacement curves indicates lower strain energy with a pronounced lower initial portion followed by a sharp peak. The shape of the curves for all of the LCFRC panels is very similar, with each showing a broad zone (wider portion) of strain energy development. The B3 fibers at 1.5% outperformed all of the other panels in terms of energy absorption as shown by the broader load-displacement curve. The majority of energy absorption for the fiber-reinforced panels is due to fiber pullout during impact.

The input potential energy imparted into the panels is a function of drop hammer's mass, the height from which it was dropped, and acceleration due to gravity. The ratio of the strain energy to the input potential energy was determined for each drop height for all the panels. The variations of this ratio and strain energy as a function of drop height are shown in Fig. 8. For all of the specimens, strain energy increased with increasing drop height. The B2 series did not perform very well, with the very short line on the graph indicating much lower ductility than the other LCFRC panels. The slope of strain energy to the height line is very steep for the B3 series, which shows mitigation of high impact loads through fiber pullout and post-cracking strength. The strain energy of the B3 panels, either volume fraction, is higher than all other panels. This result indicates that the B3 panels are more ductile, and can thus absorb more dynamic energy, than the other panels, including the WWR series.

3.4. Failure crack patterns

Qualitative analysis of impact damage is an important measure of panel performance [21]. Both plain concrete (PC) panels failed with similar cracking patterns, as shown in Fig. 9, with about four cracks spreading directly from the center of the panel to the outside edge in the middle of each side. The sudden failure exhibited by these

panels was expected. This failure is the reason why reinforcement, either mild steel and/or fibers, is necessary in the concrete mixture.

All of the reinforced panels, either WWR or fibers, displayed similar crack patterns. The cracking initiated at the center of the panels and spread toward each edge. However, in comparison to the control (PC) panels, the cracking for the reinforced panels exhibited a more tortuous path between the panel center and the panel edges, which translated into more energy absorption during impact. The B2 and B3 series show the increase in tortuosity of the cracking as the fiber percentage is increased from 1% to 1.5%. The cracks become much more irregular and often end up closer to the panel corners, resulting in a longer crack length and corresponding increase in energy absorbed during impact. In comparing the WWR and fiber-reinforced panels, the crack edge is also different. The fiber panels have a much more irregular crack edge as the failure needs to follow the weakest path through the cementitious matrix. This irregularity also translates into more energy absorption during impact. In addition to the more tortuous path for the cracking, the fiber-reinforced panels absorbed more energy during impact due to fiber pullout along the failure crack and the ability of the fibers to maintain post-cracking continuity (see Fig. 10). The B2 and WWR panels were the only series to include both punching shear cracks near the panel middle and spreading cracks from the panel center of the outside edges. The WWR panels also displayed a higher degree of damage in terms of both spalling (fragmentation) and amount of cracking compared to the fiber-reinforced panels.

3.5. Flexural properties

The effect of fiber type and volume on energy absorption was calculated using toughness values based on ASTM: C1609. The load–displacement curves for all the fibers discussed in this study are shown in Figs 11-13, and the flexural toughness is given in Table 5.

Specimens with 1.5% fiber showed higher energy absorption capacity (toughness) than 1% fiber. Increasing the fiber percentage from 1% to 1.5% resulted in an approximately 60% increase in toughness of the B3 specimens and a 20% increase in the

B2 specimens. Increasing the fiber percentage increased the toughness value of the B3 series more than the B2 series. This increase could be related to the stiff skeleton and stability from weaving a backbone into the tow. This combination of weaving and backbone allows a greater amount of cement paste to coat the fibers, resulting in improved pull out resistance. As a result, the B3 series experienced a greater increase in capacity when the fiber percentage was increased from 1% to 1.5%. In comparing the toughness values, the B3 specimens performed better than all of the other types of fibers, which is consistent with the impact test results. Fig. 14 shows the shapes of the fractured cross-sections after flexural tests of the beam. The shape of the pulled-out fibers was visible in the cross-sections of all the fibers. Beams with fiber B3 required more energy for pull out resulting in higher toughness values and increased absorbed energy during the flexural tests.

3.6. Comparison of test results with previous research

There are several test methods that evaluate the impact strength of fiber reinforced concrete, such as the drop-weight test proposed by the American Concrete Institute (ACI) committee 544 [22]. There is not one specific standard impact test and there is not enough statistical data on the variation of existing results. Most of the impact tests conducted on fiber reinforced concrete have only been concerned with obtaining qualitative data and have not yielded basic material properties that can be used in design. In general, these studies found that increasing the fiber content increased the impact resistance of the specimens [1-5]. In this section, the test results are compared with studies performed on fiber reinforced concrete under different types of impact loading.

Bindiganavile et al. [11] performed both static and impact flexural tests on four types of fibers: straight polyolefin fiber, two lengths of a sinusoidally deformed polypropylene fiber, and a steel fiber with flattened ends. It was observed that among the three polymeric fibers tested, the longer of the two deformed polypropylene fibers was the most promising under impact loading and the efficiency of polymeric fibers as concrete reinforcement increases substantially under impact loading. However, they found that the efficiency of steel fibers decreases under impact loads. The importance of

using longer fibers to improve impact resistance of concrete was the aim of the current study. Suitable length, shape and form of fibers has affect on impact performance as revealed by both the current research and Bindiganavile's study.

In another study by Xu et al. [12], results from drop-weight tests of plain concrete and different types of steel and synthetic fiber reinforced concrete specimens were studied. The test results demonstrated that concrete specimens reinforced with a new spiral II steel fiber performed the best among seven types of fiber reinforced concrete specimens in resisting the impact loading in terms of ultimate strength, post-failure strength and the energy absorption.

In a study done by Ramakrishna et al. [20] the impact behavior of cement mortar slabs reinforced with four natural fibers, coir, sisal, jute, and hibiscus cannebinus were investigated. Four different fiber contents (0.5%, 1.0%, 1.5% and 2.5%) and three fiber lengths (20mm, 30mm and 40mm) were considered. The results obtained showed that of the four fibers, coir fiber reinforced mortar slab specimens had the best performance based on the set of chosen indicators, i.e. the impact resistance, residual impact strength ratio (Irs), impact crack-resistance ratio and the condition of fiber at ultimate failure. Most of these sets of indicators were very similar to the current study. In the Ramakrishna study, the residual impact strength (I_{rs}) of all natural fiber reinforced slab specimens ranged from 1.87 to 3.91 while in the current study this number varies from 1.9 to 5.8. Coir fiber reinforced slab specimens exhibited fiber pull out failure, whears all other types of fiber reinforced specimens exhibited fiber fracture at ultimate failure. In the current study, fiber pull out was the failure mode of fibers in all the cases investigated.

4. Conclusions

The following conclusions can be drawn from this study on the behavior of long carbon fiber reinforced concrete under drop-weight impact testing:

The strain energy of the four different fibers considered in this study are found to be 4-20 times higher than that of plain concrete and 1.5 times higher than that of WWR concrete panels. This increase in strain energy is due to fiber pull out during impact.

The cracking edge of fiber-reinforced panels is more irregular as the failure surface needs to follow the weakest path through the fiber-cementitious matrix and thus absorbs more energy.

The panels with fibers showed substantial improvement in the residual impact strength (I_{rs}), with ratios ranging from 1.9 to 5.8. The fiber type B3-3 has the highest residual impact strength ratio among the various types of long carbon fibers. This high value was because fiber type B3 consisted of carbon fiber tow twined around a stiff polypropylene backbone and weaved together with cotton string. The weaving allowed for additional stability and energy absorption during impact.

The residual and maximum deflection of the LCFRC panels is linearly proportional to the input impact energy. For all the LCFRC panels, the inclinations of the regression lines depend of the fiber properties and percentage of the fibers. The residual and maximum deflection of the WWR panels is polynomial proportional to the input impact energy by a degree of 2.

Fiber B3 showed increased toughness in flexural tests compared with the other types of fibers. Increasing the fiber percentage had a greater effect on the B3 series compared to the B2 series. This increase could be related to the stiff skeleton and stability from weaving a backbone into the tow. This combination allows enhanced coating of the fibers within the cementitious matrix allowing increased pull out resistance. As a result, increasing the fiber percentage from 1% to 1.5% had a greater effect on the B3 series compared to the B2 series.

Acknowledgements

The authors gratefully acknowledge the financial support provided by the U.S. Army Research Lab (ARL) and the Leonard Wood Institute (LWI) under Award Nos. W911NF-07-2-0062 and LWI-191-028, respectively. The conclusions and opinions expressed in this paper are those of the authors and do not necessarily reflect the official views or policies of the ARL and LWI. The authors also are grateful for the ideas and help of Dr. Eric Musselman, Assistant Professor, Villanova University, Dr. Andrea Schokker, Professor and Executive Vice Chancellor for Academic Affairs, University of Minnesota Duluth, and Pro-Perma Engineered Coatings for supplying Fiber Types B1, B2, and B3.

References

[1] Almansa EM, Canovas MF, "Behavior of Normal and Steel Fiber-Reinforced Concrete under Impact of Small Projectiles," *Cement Concrete Research,* 1999, 29: 1807-1814.

[2] Nataraja MC, Dhang N, Gupta AP, "Statistical Variations In Impact Resistance Of Steel Fiber-Reinforced Concrete Subjected To Drop Weight Test," *Cement Concrete Research,* 1999, 29:989-995.

[3] Ong KCG, Basheerkhan M, Paramasivam P, "Resistance of Fiber Concrete Slabs to Low Velocity Projectile Impact," *Cement Concrete Research,* 1999, 21: 391-401.

[4] Yan H, Sun W, Chen H., "The Effect of Silica Fume and Steel Fiber on the Dynamic Mechanical Performance of High-Strength Concrete," *Cement Concrete Research,* 1999, 29 :423-426.

[5] Banthia N, Mindess S, Trottier J., "Impact Resistance of Steel Fiber Reinforced Concrete," *ACI Material Journal,* 1996.

[6] Luo X, Sun W, Chan SYN., "Characteristics of High-Performance Steel Fiber-Reinforced Concrete Subject to High Velocity Impact," *Cement Concrete Research,* 2000, 30 907-914.

[7] Wang N, Mindess S, Ko K., "Fiber Reinforced Concrete Beams Under Impact Loading," *Cement Concrete Research,* 1996; 26 :363-376.

[8] Teng T-L, Chu Y-A, Chang F-A, Shen B-C, Cheng D-S., "Development and validation of numerical model of steel fiber reinforced concrete for high-velocity impact," *Computer Material Science,* 2008; 42 :90-99.

[9] Nyström U, Gylltoft K., "Comparative Numerical Studies of Projectile Impacts on Plain and Steel-Fiber Reinforced Concrete," *International Journal of Impact Engineers,* 2011; 38:95-105.

[10] Xu Z, Hao H, Li HN., "Dynamic Tensile Behavior of Fiber Reinforced Concrete With Spiral Fibers," *Material Design,* 2012; 42: 72–88.

[11] Löfgren I., "Fiber-Reinforced Concrete for Industrial Construction - A Fracture Mechanics Approach to Material Testing and Structural Analysis," Chalmers University of Technology, Chalmers University of Technology 2005.

[12] Zhou X, Ghaffar SH, Dong W, Oladiran O, Fan M., "Fracture and Impact Properties of Short Discrete Fiber-Reinforced Cementitious Composites," *Mater Des,* 2013; 49: 35–47

[13] Musselman E, University TPS., "Characterizing Blast And Impact Resistance of Long Carbon Fiber Reinforced Concrete," Pennsylvania State University,2007

[14] Schokker AJ, Moser EJ., "Impact Resistance of Long Fiber Concrete," Paper presented at the 33rd Annual Conference of the Canadian Society for Civil Engineering, Canada 2005.

[15] Gliha BP., "Long Carbon Fiber Reinforced Concrete for Impact and Blast Protection," Missouri University of Science and Technology 2011.

[16] Keener DI., "Blast and Impact Resistance of "Long" Carbon Fiber Reinforced Concrete," Missouri University of Science and Technology 2012.

[17] Tabatabaei ZS, Volz JS, Gliha BP, and Keener DI., "Development of Long Carbon Fiber Reinforced Concrete for Dynamic Strengthening," *ASCE Material Journal,* 2013.

[18] Ramakrishna G, Sundararajan T., "Impact Strength of a Few Natural Fiber Reinforced Cement Mortar Slabs: A Comparative Study," *Cem Concr Comp* 2005; 27 :547-553.

[19] Tabatabaei ZS, Volz JS, Baird J, Gliha BP, and Keener DI., "Experimental and Numerical Analyses of Long Carbon Fiber Reinforced Concrete Panels Exposed to Blast Loading," *International Journal of Impact Engineers*, 2013; 57: 70-80.

[20] Ramakrishna G, Sundararajan T. Impact strength of a few natural fiber reinforced cement mortar slabs: a comparative study. *Cem Concr Comp* 2005; 27:547-553.

[21] Tabatabaei ZS, Volz JS, Baird J, Gliha BP, and Keener DI. Experimental and numerical analyses of long carbon fiber reinforced concrete panels exposed to blast loading *International Journal of Impact Engineers*, 2013; 57: 70-80

[22] American Concrete Institute (ACI) Committee 544. (2001). "Report on fiber reinforced concrete." ACI, Detroit

Table 1. Panel Concrete Mixture Designs

IDs	Concrete Mixture (kg/m^3)
Portland Cement (Type I)	605
Fine Aggregate [a]	783
Coarse Aggregate [a,c]	783
Water	230
Water Reducing Admixture[b]	32.5 milliliters per 45 kg of cement

[a] Weights at saturated surface dry (SSD) condition

[b] High range water reducer (HRWR) was Gelenium 3030

[c] 19 mm maximum aggregate size

Table 2. Properties of the Fibers Used

Properties	Value	
Fiber type	Type A	Type B
Tensile strength (MPa)	586-675	4137
Tensile modulus (GPa)	57.9-59.9	242
Elongation (%)	1.6	1.5
Density (g/cc)	1.76	1.81
Fiber diameter (microns)	6.9	7.2
Carbon content (%)	92	95
Yield (m/kg)	230	270
Fiber Length (mm)	10	10
Alkali, Acid & Salt Resistance	High	High
Electrical Resistivity	0.00175 ohm-cm	0.00155 ohm-cm

Table 3. Specimen Properties

Specimen	PC		WWR		A1		B1		B2				B3			
Trial	1	2	1	2	1	2	1	2	1	2	3	4	1	2	3	4
Volume fraction of fiber (%)	-	-	-	-	1.5	1.5	1	1	1	1	1.5	1.5	1	1	1.5	1.5
Compressive strength of concrete, f'c (MPa)	52.8	52.8	54	54	51	51	52	52	49.8	49.8	53	53	51.2	51.2	51.6	51.6

*Note: Panels were cast in pairs, so the same concrete was used for each pair

Table 4. Maximum Dynamic Response Values of Panels at both Cracking and Failure

Specimen	First Crack			Failure						Residual
	Impact velocity	Falling height	Input impact energy	Impact velocity	Falling height	Input impact energy	Maximum impact force	Maximum deflection	Residual deflection	impact strength
	V_{cr}, m/s	h_{cr}, m	E_{cr}, kJ	V_F, m/s	h_F, m	E_F, KJ	$P_{max\ F}$, kN	D_{max}, mm	δ_{rs}, mm	I_{rs}
PC-1	2.7	0.38	0.09	2.7	0.38	0.086	28	3.8	2.8	1.0
PC-2	3.0	0.46	0.10	3.0	0.46	0.104	32	5.6	0.0	1.0
WWR-1	3.5	0.61	0.14	8.1	3.35	0.756	58	22.8	2.1	5.5
WWR-2	3.0	0.46	0.10	7.7	3.05	0.688	88	19.3	0.8	6.6
A-1	3.5	0.61	0.14	6.2	1.98	0.447	53	12.1	3.8	3.2
A-2	3.5	0.61	0.14	6.2	1.98	0.447	50	9.5	2.5	3.2
B1-1	3.5	0.61	0.14	6.2	1.98	0.447	58	13.3	9.0	3.2
B1-2	3.9	0.76	0.17	5.7	1.68	0.379	58	13.2	7.6	2.2
B2-1	2.4	0.30	0.07	4.2	0.91	0.205	45	10.7	7.4	3.0
B2-2	2.4	0.30	0.07	5.2	1.37	0.309	35	16.6	13.5	4.6
B2-3	2.4	0.30	0.07	4.9	1.22	0.275	50	10.2	6.3	4.1
B2-4	2.1	0.23	0.05	4.9	1.22	0.275	42	11.1	6.7	5.3
B3-1	3.9	0.76	0.17	6.5	2.13	0.480	53	18.5	7.0	2.8
B3-2	4.9	1.22	0.28	6.7	2.29	0.516	36	15.2	3.8	1.9
B3-3	3.5	0.61	0.14	8.3	3.51	0.792	65	29.7	2.7	5.8
B3-4	4.2	0.91	0.21	8.5	3.66	0.825	74	20.1	3.0	4.0

Table 5. Average Response Quantities for Flexural Behavior

	Peak load (kN)	Toughness (N-m)
Fiber A-1.5%	33	52
Fiber B-1%	43	77
Fiber B2-1%	37	98
Fiber B2-1.5%	34	120
Fiber B3-1%	40	250
Fiber B3-1.5%	39	389

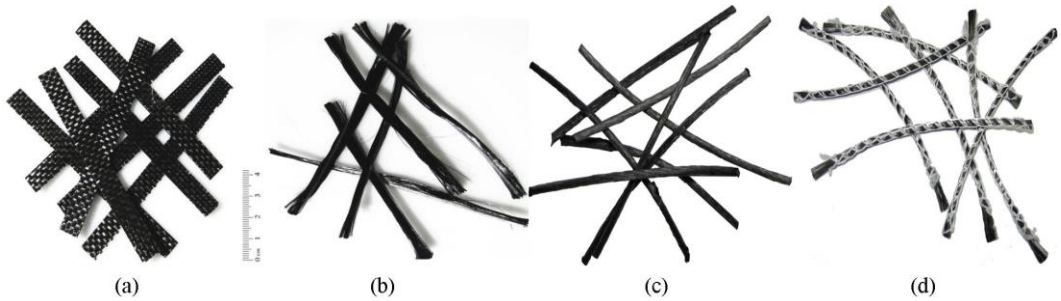

Figure 1. Four Different Types of Fibers; a) Fiber Type A, b) Fiber Type B1, c) Fiber Type B2, d) Fiber Type B3

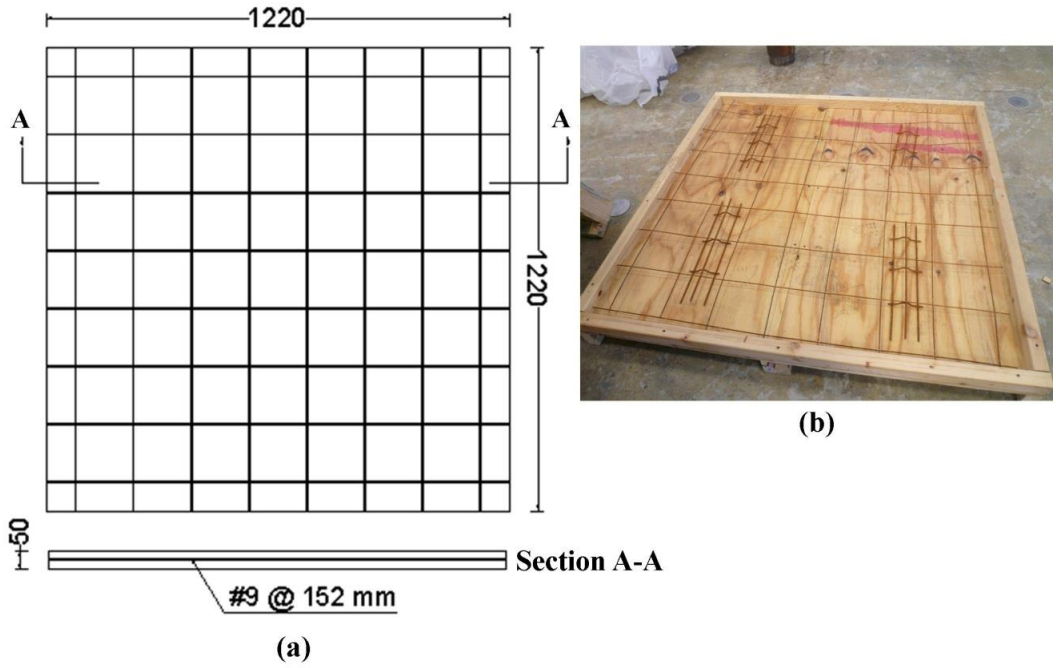

Figure 2. Details of WWR Concrete Panels (a) Cross Section of Panels; and (b) Reinforcement Layout of Panels (Unit: mm)

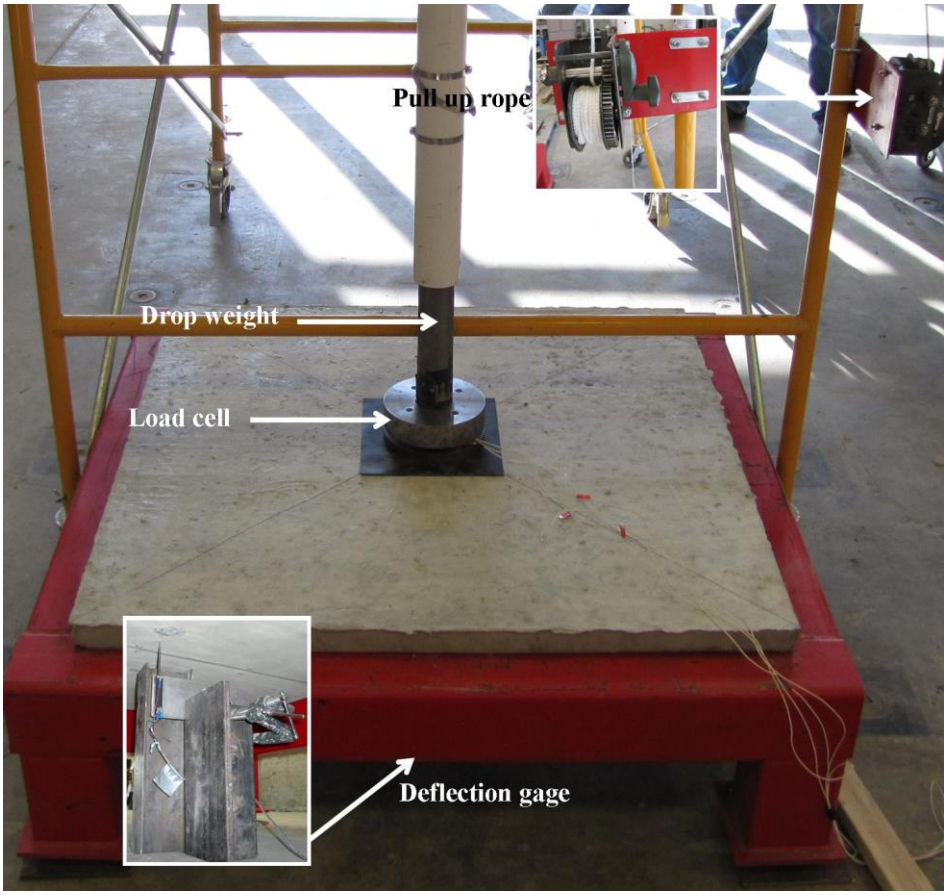

Figure 3. Impact Test Apparatus

Figure 4. Flexural Strength Test Setup

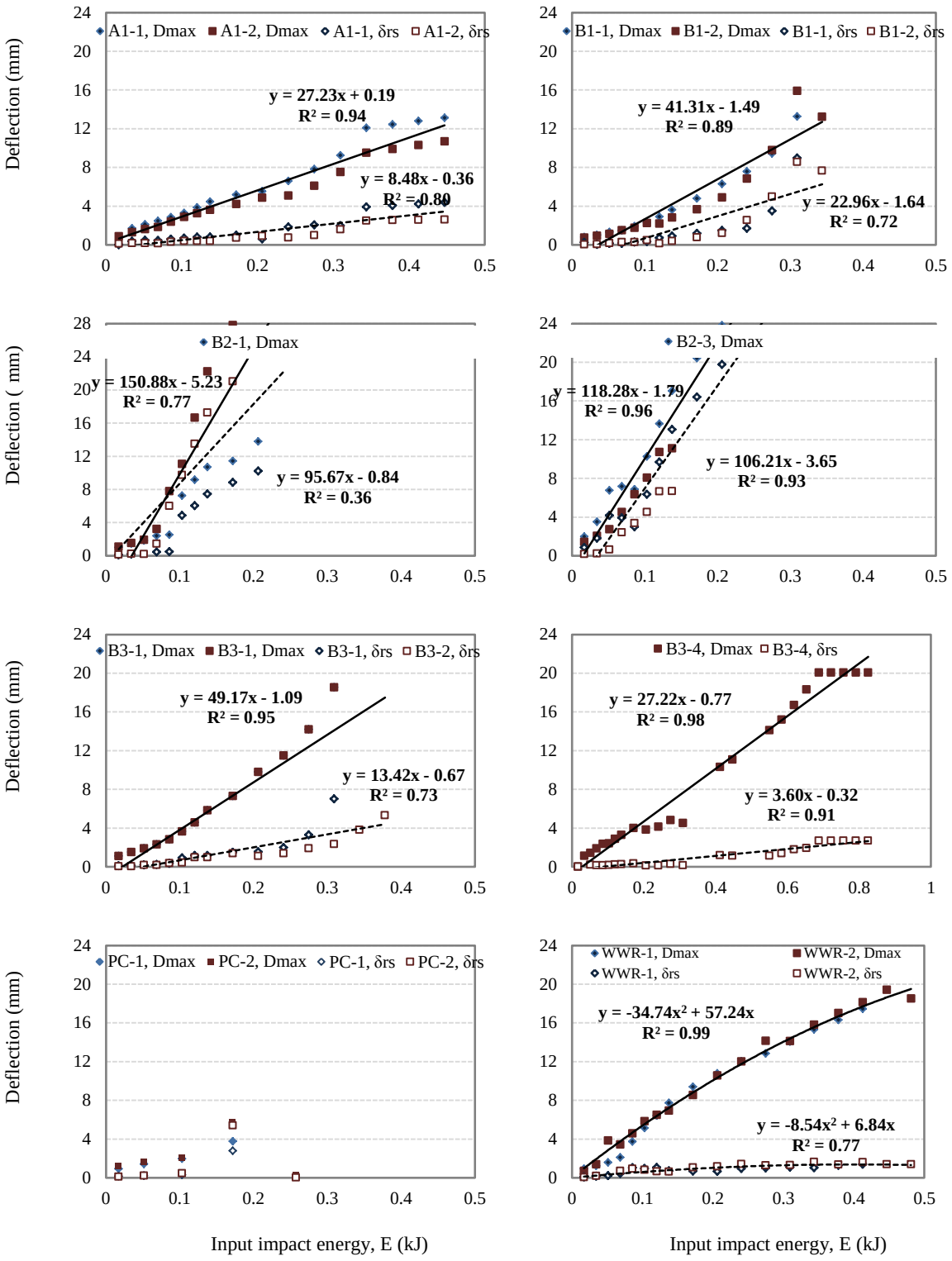

Figure 5. Relationships between Both the Input Impact Energy (E) and Maximum Deflection (D_{max}) as well as the Input Impact Energy (E) and the Residual Deflection (δ_{rs}) for all of the Panels

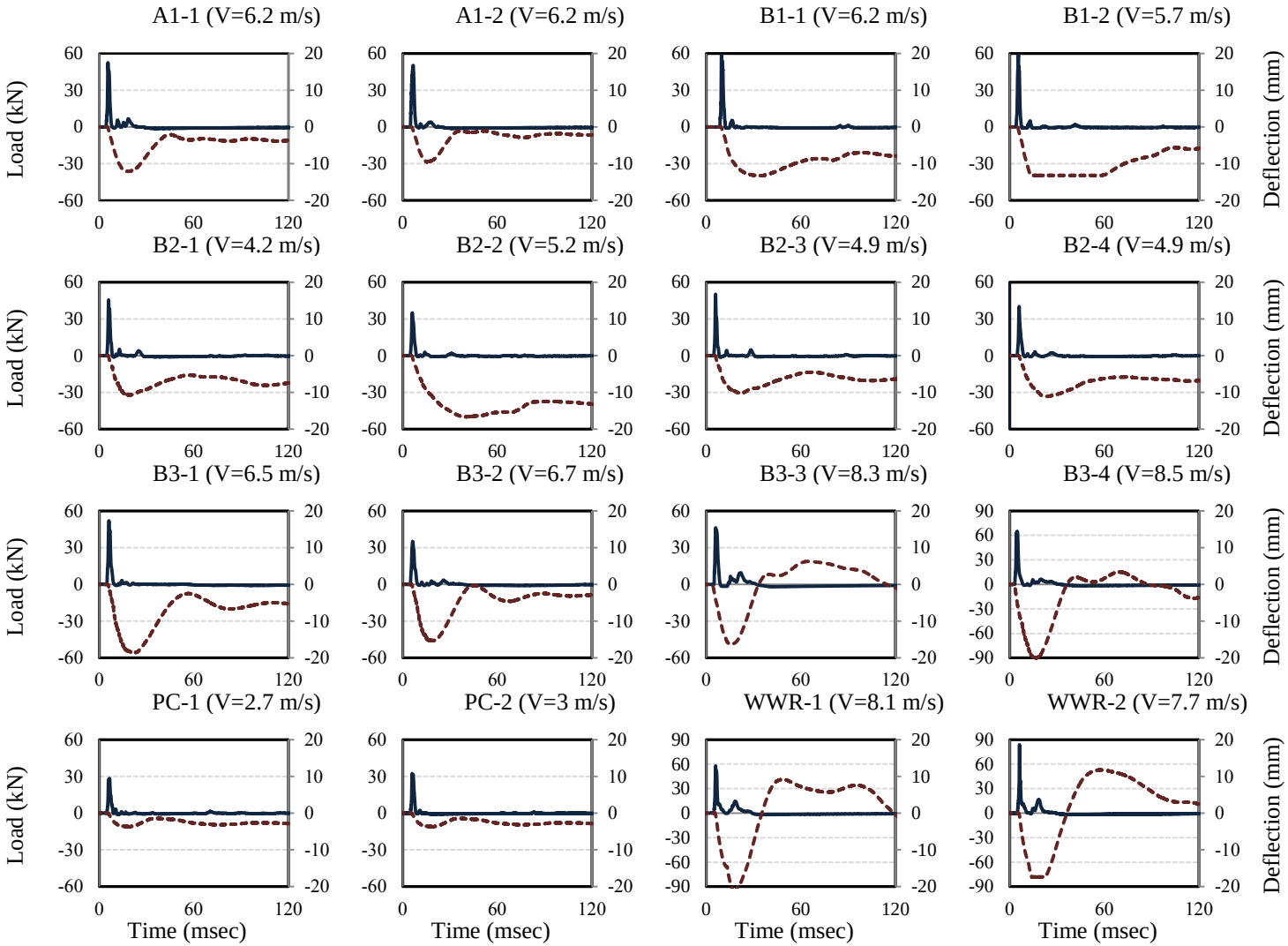

Figure 6. Impact Load and Deflection Time History for all Specimens

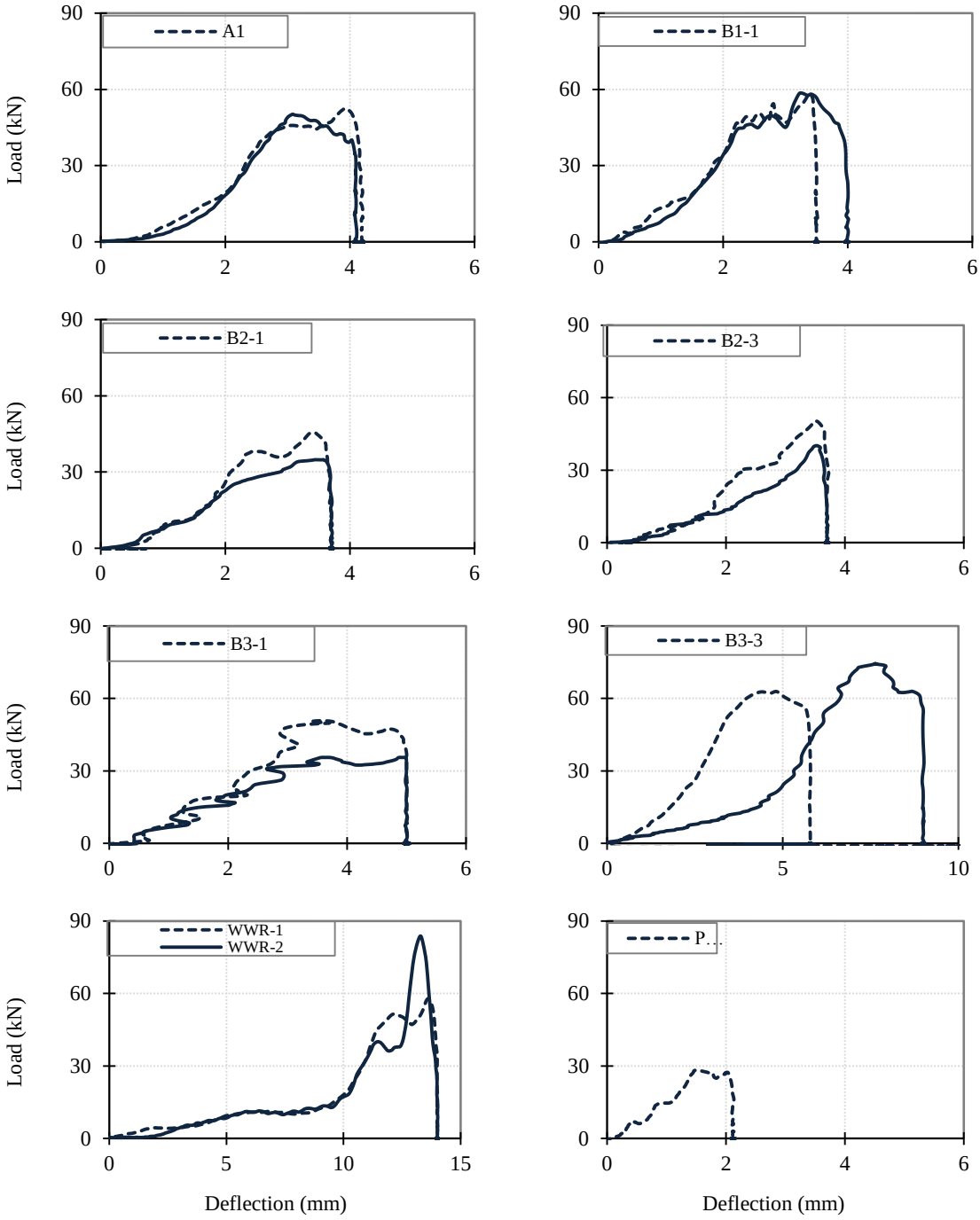

Figure 7. Load-Displacement Relationship for all Specimens

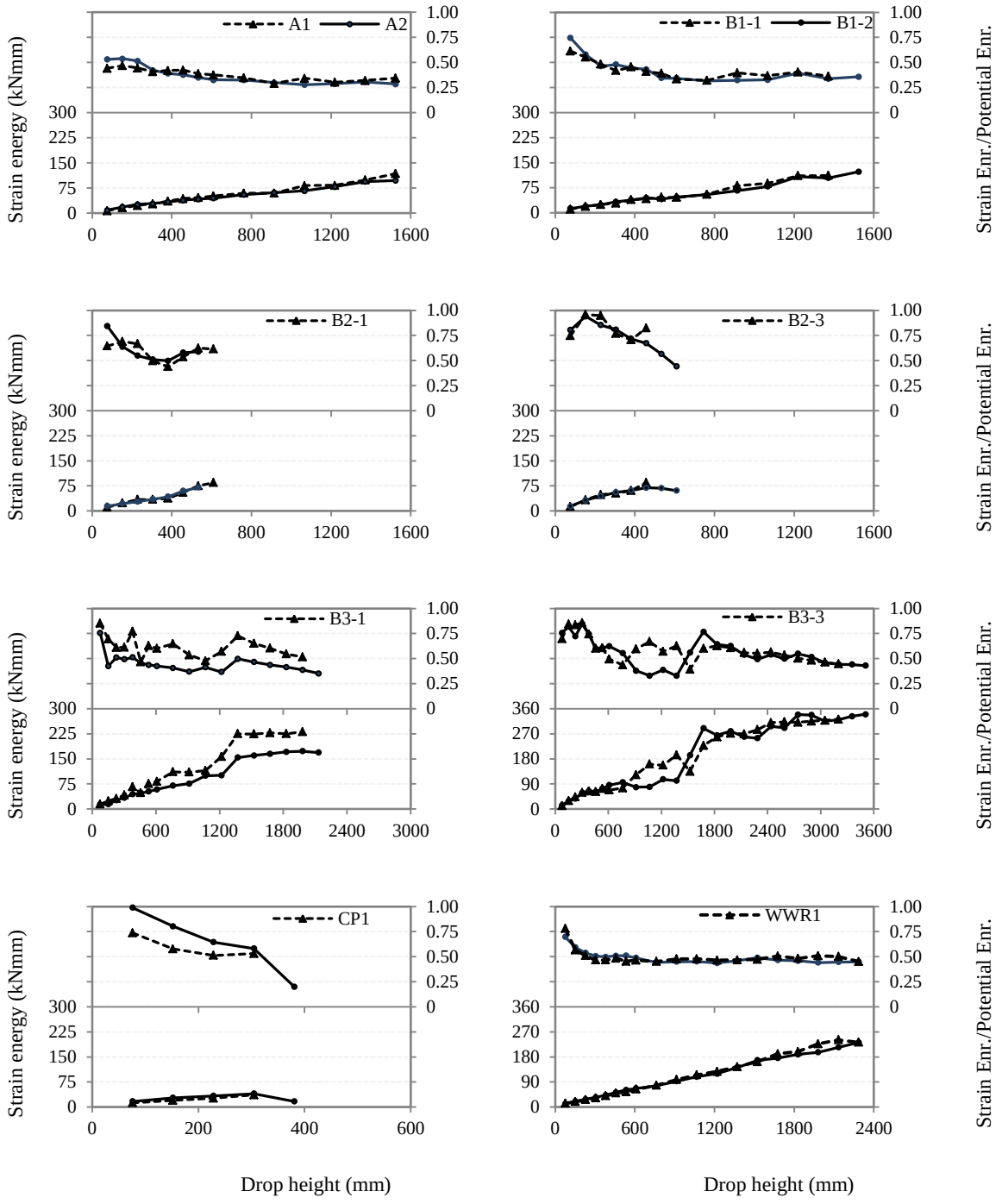

Figure 8. Effect of Drop Height on the Strain Energy and Ratio of Strain Energy to the Input Potential Energy for all the Specimens

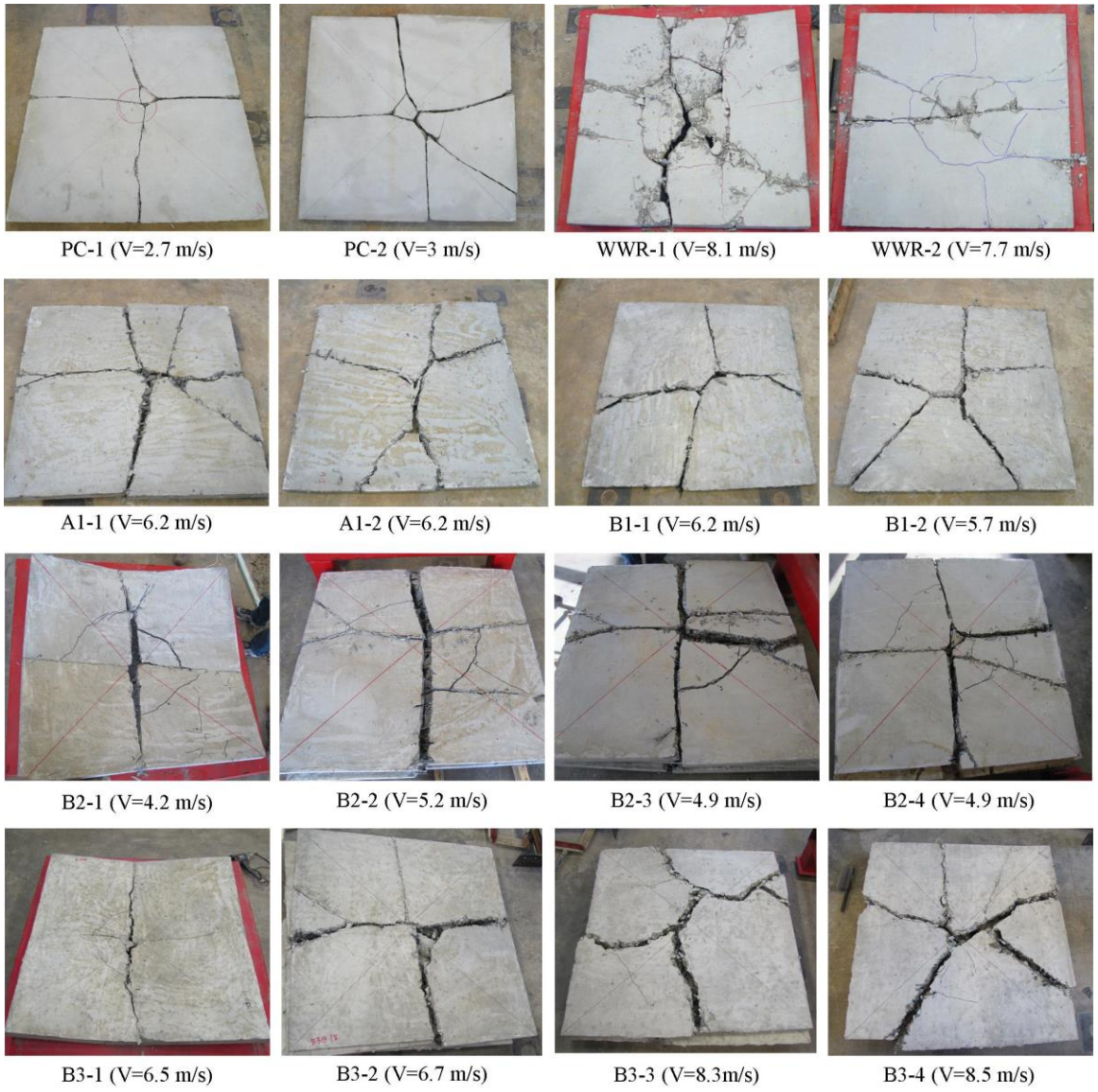

Figure 9. Failure Crack Patterns in all the Panels

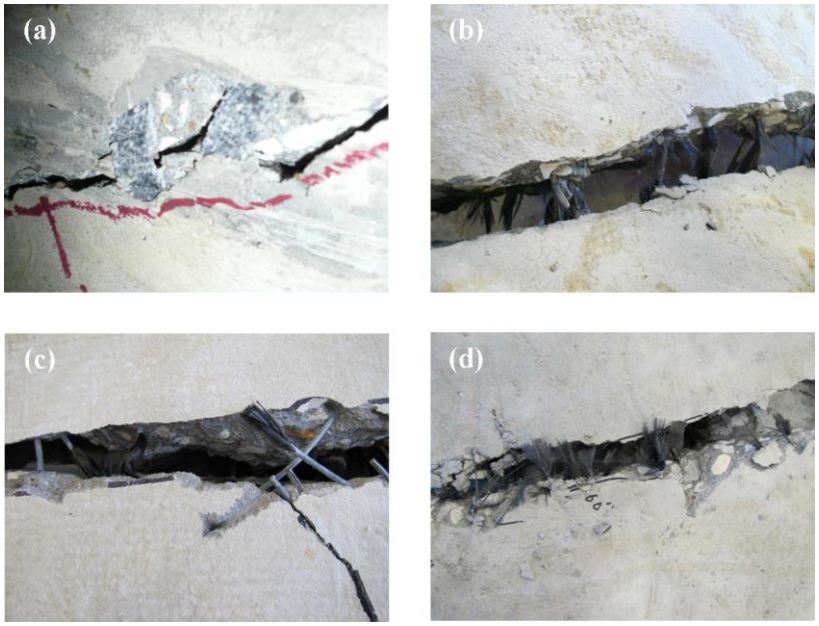

Figure 10. Bridging of Fibers: (a) Fiber A, (b) Fiber B1, (c) Fiber B2, and (d) Fiber B3

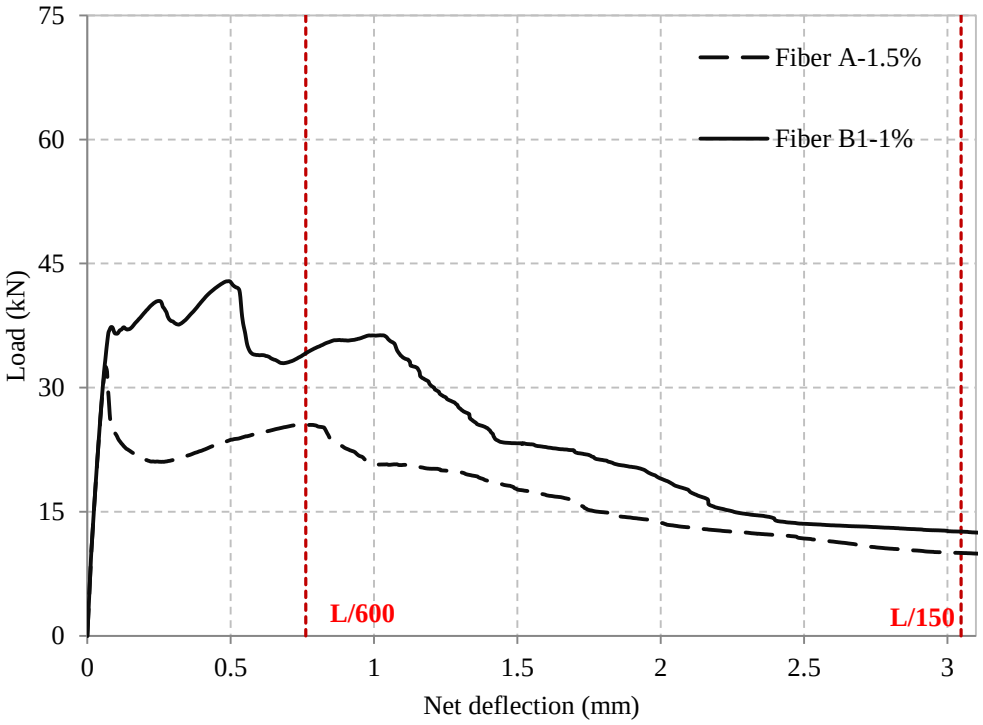

Figure 11. Load Deflection Response Curves for Fiber Type A and B1

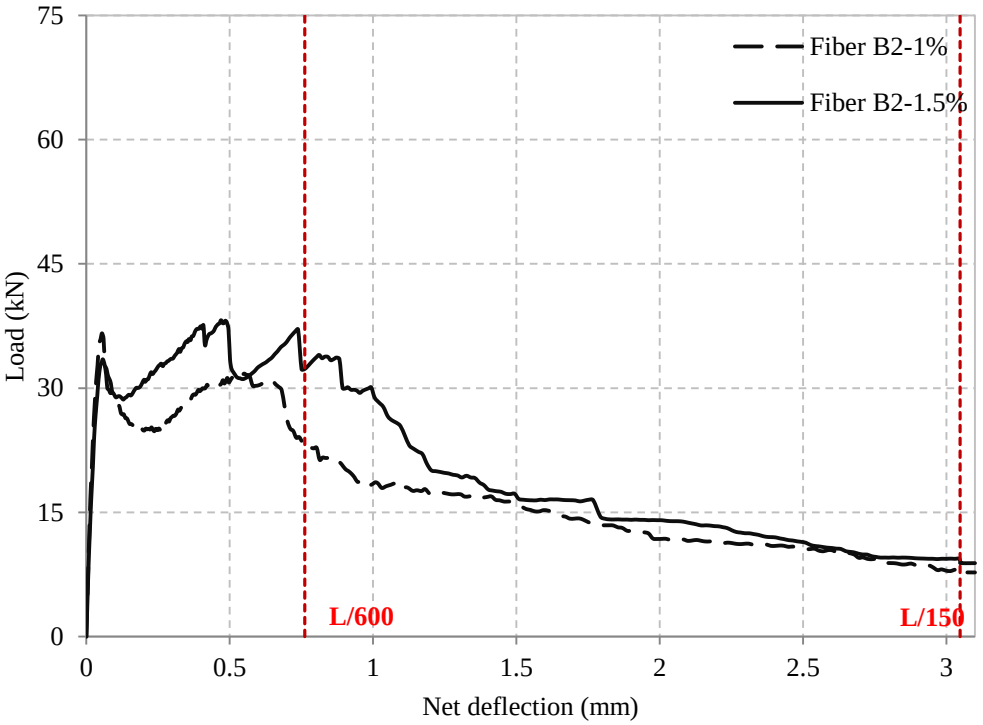

Figure 12. Load Deflection Response Curves for Fiber Type B2

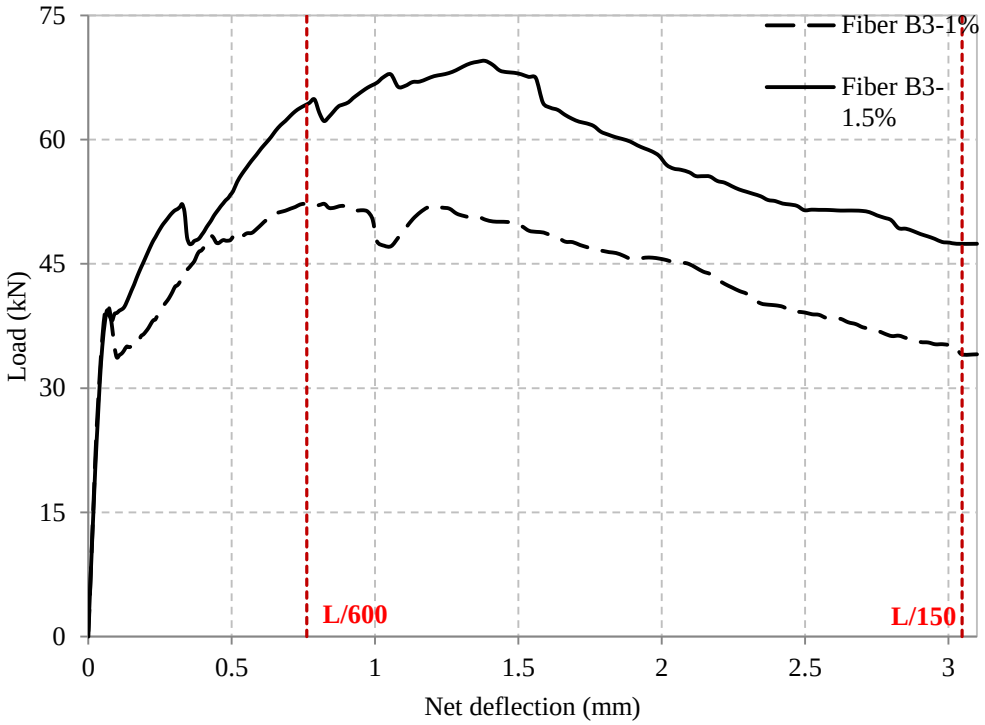

Figure 13. Load Deflection Response Curves for Fiber Type B3

Figure 14. Fracture Surface of Fiber Reinforced Concrete after Flexural Tests

II. NUMERICAL SIMULATION OF IMPACT TESTS ON LONG CARBON FIBER REINFORCED CONCRETE PANELS

Zahra S. Tabatabaei, Jeffery S. Volz, Benjamin P. Gliha, Darwin I. Keener

Abstract

This paper presents numerical simulations of drop weight impact test performed on both welded wire reinforced concrete and long carbon fiber reinforced concrete (LCFRC) panels. The three-dimensional finite element code LS-DYNA® was used for the numerical analyses. Three different, simple input models were used to simulate concrete behavior under impact. As a consequence, both the force time history and deflection time history at failure were obtained for each case. These results were compared. These results and error analysis indicate a favorable agreement between the numerical results and the experimental data. Thus, this present model with Mat_159 in LS-DYNA can provide a reliable prediction of the damage characteristics for both types of panel.

1. Introduction

Concrete is the primary material for protective structures. By adding fibers to the cement mixtures, ductility, tensile strength, flexural strength and resistance of concrete against dynamic loading increases. Dynamic loading, however, can cause tremendous casualties and expensive property loss. Damage from dynamic loading (either blast or impact) is, in general, a topic of interest to researchers across various fields. A number of in-depth studies have examined the impact behavior of reinforced concrete structures (Agardh et al. 1999; Schwer et al. 1999; Alavi Nia et al. 2012; Remennikov et al. 2011).

Agardh et al. (1999) used LS-DYNA finite element (FE) codes to explain the performance of fiber concrete against projectiles with a high velocity. Schwer et al. (1999) both developed and improved numeric computational techniques for simulating the penetration and perforation of concrete slabs and steel plate. These specimens were targeted by obliquely impacting large, deformable projectiles. Alavi Nia et al. (2012) compared the impact loading results from LS-DYNA simulations of both plain concrete and fiber reinforced concrete with experimental testing data. Mat_84 in LS-DYNA, with the maximum principle strain as the failure criterion, was used to model concrete behavior in this study. Remennikov et al. (2011) used Mat_159 in LS-DYNA to simulate concrete in drop hammer test conditions. The predicted impact forces, deformation histories, and failure modes were found to be in good agreement with the experimental results.

This paper presents three-dimensional FE modeling techniques for both welded wire reinforced (WWR) concrete panels and long carbon fiber reinforced concrete (LCFRC) panels under impact loading conditions using LS-DYNA (2010). A numerical validation was performed by comparing with experimental data using three pre-defined concrete material models in LS-DYNA.

The purpose of this paper is to study both the model capabilities and limitations so that these material models may be used as an alternative to expensive field testing for dynamic loading.

2. Experimental Test Description

In this study, experimental tests for reinforced concrete panels impacted by a falling weight were used to validate the FE models (Tabatabaei et al. 2013). Concrete panels were impacted by a 23 kg steel rod dropped from increasing heights until each panel failed (see Fig.1). A 13 mm thick section of neoprene was affixed to the bottom of the rod. The neoprene and the rod shared the same diameter. The panels measured 1220 mm square in plan with a thickness of 50 mm. When the panels were reinforced, 152×152 – MW9×MW9 welded wire reinforcing placed at mid-depth was used. When the panels contained fibers, 100 mm long carbon fibers were added to the mixture at a dosage rate of 1% by volume. The compressive strength of the concrete measured 52 MPa. The yield strength of the reinforcement measured 410 MPa. A linear motion potentiometer was secured under the panel to measure deflection. The load applied on the panel was measured with a dynamic load cell centered on the panel. A 3.5 mm thick neoprene square was placed under the load cell to reduce excessive vibration after impact (Tabatabaei et al. 2013).

3. Numerical Simulation

3.1. Finite Element Model

The three-dimensional finite element code LS-DYNA is used globally to analyze the response of structures to dynamic loading. It was used in this study because of its proven effectiveness in geometric modeling and impact analysis.

Due to two axes of symmetry, only one-quarter of the panel (including both the falling weight and the support) was modeled for numerical analysis (Fig.2). The mesh aspect ratio was 1. In total, approximately 177,000 nodal points and 154,000 elements were used to model each test.

A restart analysis was performed to model periodic impact loading. The results at the end of each impact were assumed as the input state for the next impact analysis. The projectile struck the panel at different velocities (increasing drop height). A 5% partial loss of projectile energy was assumed for each strike.

All nodes located at the corners of the slab on the top of the rigid support were fixed to model boundary conditions. This restraint was similar to the actual test apparatus constraints, thus allowing the panel to rotate about its own longitudinal axis without being able to translate.

The algorithm CONTACT_AUTOMATIC_ SURFACE _TO_SURFACE in LS-DYNA was used to model all contacts within the model. A penalty-based method was used to handle the contact/impact phenomena. In line with the theoretical manual of LS-DYNA (2006), each slave node was examined for penetration through the master surface at every time step (cycle) when the penalty method was applied. This algorithm automatically generated both slave and master surfaces. When penetration was found for the parts in contact, a nominal interface spring was used to apply force proportional to the penetration depth of these interfaces, eliminating penetration (2006). Interface stiffness was computed as a function of the bulk modulus, volume, and face area of the elements on the contact surface.

Reinforcement elements were coupled to the concrete element with CONSTRAINED_LAGRANGE_IN_SOLID. Here the slave set for the reinforcement elements was coupled to the master set for concrete elements.

3.2. Material Modeling

3.2.1. Reinforcement

Beam elements (a 2-node Hughes-Liu beam element formulation with 2×2 Gauss quadrature integration) were used to model steel reinforcing bars. A plastic kinematic model was chosen to consider the effects of both isotropic and kinematic beam element hardening (2006). The plastic hardening modulus, E_t, was assumed to be 1% of the elastic modulus, Es (Young's modulus). Density, modulus of elasticity, and Poison's ratio were assumed to be equal to 7800 kg/m^3, 210 GPa, and 0.3, respectively. The strain rate was accounted for using the Cowper and Symonds model [8]. This model scales the yield stress with the factor

$$1+\left(\frac{\dot{\varepsilon}}{C}\right)^{\frac{1}{P}} \quad (1)$$

where $\dot{\varepsilon}$ is the strain rate and both c and p represent the strain rate parameters. For this model, c=40 and p=5 was used according to the findings in Reference 9 (1993).

3.2.2. Load Cell, Support, and Rod

MAT_RIGID (MAT_020) was used from the LS-DYNA material library to model the loading cell, support, and rod. Both Young's modulus and Poisson's ratio of steel material were used for the rigid material in the numerical simulation.

3.2.3. Neoprene

Two pieces of neoprene, the one at the bottom of the rod and the one below the load cell were also modeled as they were present during the experimental test. One section of neoprene was glued to the steel rod. The contact interfaces between the neoprene and the steel rod were modeled with the algorithm *CONTACT_SURFACE_TO_SURFACE_TIEBREAK. Here the neoprene was allowed to slip while separation was prohibited. A viscoelastic material for neoprene was chosen from the LS-DYNA library (see Table1).

3.2.4. Concrete Panel

Two different types of concrete materials needed to be modeled for this research program: welded wire reinforced concrete and fiber-reinforced concrete panels. For both, the material parameters were generated automatically in LS-DYNA from three simple input concrete models. The method for creating a material model capable of describing the fiber-reinforced concrete presented many challenges. When fibers are added to the concrete, they become activated as soon as the matrix cracks. Fibers start to be pulled out, leading to an increased shear-transfer capacity. To model the fiber reinforced concrete,

the parameters generated after one run (describing fracture energy toughness in both tension and shear) were modified according to previous uniaxial tensile tests (Ottosen et al. 1997; Coughlin et al. 2010).

Eight node solid hexahedron elements with a single integration point were used to represent the concrete. A mesh size of 5 mm was found in the convergence study to be appropriate for the concrete panels. Each concrete panel was modeled using constant stress solid elements to avoid both the negative volume effect and error termination.

LS-DYNA (version 971) has several concrete material models. In this study, three materials in LS-DYNA, namely:

Material type 72 (MAT_CONCRETE_DAMAGE_REL3)

Material type 84 (MAT_WINFRITH_CONCRETE)

Material type 159 (MAT_CSC_CONCRETE)

were used to simulate the concrete.

3.2.4.1 Material type 72R3

This material is the third release of a Karagozian and Case (K&C) concrete model (Malvar et al. 1997). It is a plasticity-based model that uses three shear failure surfaces, including both damage and a strain-rate effect (Malvar et al. 1997). In this model, the stress tensor is expressed as the sum of the hydrostatic stress tensor (changes the concrete volume) and the deviatoric stress tensor (controls shape deformation).

The compaction model is a multi-linear approximation in internal energy for the hydrostatic stress tensor. Pressure is defined by Eq. (2).

$$p = C(\varepsilon_v) + \gamma T(\varepsilon_v)E \tag{2}$$

where E is the internal energy per initial volume and γ is the ratio of specific heats. The volume strain (ε_v) is given by the natural logarithm of the relative volume. This model contained an elastic path from the hydrostatic tension cut-off (Zhao et al. 2013) (see Fig. 3). Tensor failure occurs when tension stress is greater than the hydrostatic tension cut-off. When the volumetric strain exceeds the elastic limit, compaction occurs and the concrete becomes a granular type of material. The bulk unloading modulus is a function of volumetric strain. Unloading occurs from the

unloading bulk modulus to the pressure cut-off. Reloading always follows the unloading path to the point where unloading began; it continues on the loading path (Malvar et al. 1997). Fig. 3 shows pressure versus volumetric strain curve for equation of state form 8 with compaction. In the compacted state, the bulk unloading modulus depends on the volumetric strain.

The deviatoric stresses are limited by three independent surfaces (Fig. 4). These surfaces were defined by the following eight parameters in Eqs. (3-5).

$$\Delta\sigma_{\mathrm{m}} = \mathrm{a}_0 + \frac{P}{a_1 + a_2 P} \tag{3}$$

$$\Delta\sigma_{\mathrm{y}} = \mathrm{a}_{0\mathrm{y}} + \frac{P}{a_{1y} + a_{2y} P} \tag{4}$$

$$\Delta\sigma_{\mathrm{r}} = \frac{P}{a_{1f} + a_{2f} P} \tag{5}$$

where $\Delta\sigma_{\mathrm{m}}$ denotes the maximum failure surfaces, $\Delta\sigma_{\mathrm{y}}$ denotes the yield failure surface, and $\Delta\sigma_{\mathrm{r}}$ denotes the residual failure surface.

Inputs for the Concrete Damage Model Release 3 generated parameters based solely on a uniaxial compressive strength value (Schwer et al. 2005). The remaining parameters were taken as zero, allowing the model to generate damage function values on its own.

3.2.4.2 Material type 084

The Winfrith concrete model is a smeared crack, smeared rebar model applied to an 8-noded, single integration point, continuum element only. It is based upon the so called four parameter model proposed by Ottosen (1975):

$$Y(I_1, J_2, J_3) = aJ_2 + \lambda\sqrt{J_2} + bI_1 - 1 \tag{6}$$

with

$$\lambda = \begin{cases} k_1 \cos\left[\frac{1}{3}\cos^{-1}(k_2 \cos(3\theta))\right] \cos(3\theta) \geq 0 \\ k_1 \cos\left[\frac{\pi}{3} - \frac{1}{3}\cos^{-1}(-k_2 \cos(3\theta))\right] \cos(3\theta) \geq 0 \end{cases} \tag{7}$$

$$\cos(3\theta) = \frac{3\sqrt{3}}{2}\frac{J_3}{J_2^{3/2}} \tag{8}$$

The four parameters (i.e, a, b, k1 and k_2) are functions of the ratio of tensile strength to compressive strength $(\frac{f_t}{f_c'})$. They are determined from uniaxial compression tests (correspondingly, $(\theta = 60^0)$ degree), uniaxial tension tests $(\theta = 0^0)$, biaxial compression tests $(\theta = 0^0)$, and triaxial compression tests $(\theta = 60^0)$.

This material requires slightly more input than just the unconfined compressive strength of concrete to be quantified as a simple input. Additional inputs (i.e., tangent modulus, tensile strength and, fracture energy) can be provided via an empirical formula.

3.2.4.3 Material type 159

This model combines the shear (failure) surface with a hardening-compaction surface (cap) using a multiplicative formulation (see Fig. 5). The yield function is defined in terms of three stress invariants as in Eq. (9).

$$Y(I_1, J_2, J_3) = J_2 - \Re(J_3)^2 F_f^2(I_1) F_c(I_1, \kappa) \tag{9}$$

Where $F_f(I_1)$ is the shear failure surface, $F_c(I_1, \kappa)$ is the hardening cap (with κ defined as the cap hardening parameter), and $\Re(J_3)$ is the Rubin three-invariant reduction factor. The multiplicative form allows the cap and shear surfaces to be combined both continuously and smoothly at their intersection.

The shear failure surface $F_f(I_1)$ is defined as in Eq. (10)

$$F_f(I_1) = \alpha - \lambda \exp^{-\beta I_1} + \theta I_1 \tag{10}$$

The material constants α, β, δ, and θ are determined from triaxial compression test data. The cap hardening surface is expressed as in Eq. (11).

$$F_c(I_1, \kappa) = \begin{cases} 1 - \dfrac{(I_1 - L(\kappa))^2}{(X(\kappa) - L(\kappa))^2} & I_1 \geq L(\kappa) \\ 1 & I_1 \leq L(\kappa) \end{cases} \tag{11}$$

With

$$L(\kappa) = \begin{cases} \kappa & \kappa \geq \kappa_0 \\ \kappa_0 & \kappa \leq \kappa_0 \end{cases} \tag{12}$$

$$X(\kappa) = L(\kappa) + RF_f(I_1) \tag{13}$$

Eq. (11) describes the ellipse (or cap) for $I_1 \geq L(\kappa)$. The shear failure surface intersects the cap at $I_1 = L(\kappa)$. When the shear surface and the cap initially intersect (before the cap either expands or shrinks), k_0 is the value of I_1. The cap expands when plastic volume compaction occurs, and the cap shrinks when plastic volume dilation occurs. The motion of the cap is controlled by the hardening rule specified by Eq. (14).

$$\varepsilon_v^p = W\left[1 - \exp^{(-D_1(X - X_0) - D_2(X - X_0)^2}\right] \tag{14}$$

where ε_v^p is the plastic volumetric strain, W is the maximum plastic volumetric strain, and X_0 is the initial location of the cap when $\kappa = \kappa_0$. The five parameters (X_0, R, W, D_1 and D_2) were determined from hydrostatic compression and uniaxial strain tests.

For this model, the three inputs required to generate the default parameters were the unconfined compressive strength, the aggregate size, and the units used in the finite element model Hallquist (2006).

4. Numerical Results and Discussion

The transient dynamic numerical study of two types of panels was conducted to identify the observed failure modes in all of the numerical tests. A comparison was also made to validate the results of the numerical simulation with the experimental results.

4.1. Comparison of Computed Deflection with Experimental Results

The displacement results using three different models were computed and compared with the experimental values (see Fig. 6). In experimental test, for the WWR panels, residual deflection after a few rebounds was 2 mm. The maximum midspan deflection of the WWR panel was 22 mm. For the LCFRC panels, residual deflection was 2.2 mm and maximum midspan deflection was 13 mm.

When compared to the experimental results, all three models overestimated the residual deflection and underestimated maximum deflection by different percentages. The deflections obtained from the CSCM (MAT_159) and the Concrete Damage Model Release 3 (MAT_72) was lower than the experimental deflection by 4 mm and 2 mm respectively for the WWR panels. These numbers were 3 mm and 0.5 mm for the LCFRC panels. The Winfrith model (MAT_84) underestimated the maximum displacement by 35% for the WWR panels. The Winfrith model (MAT_84) had the largest difference with the experimental results compared to the other two models, while MAT_72 had the closest agreement to the test results.

4.2. Comparison of Computed Force with Experimental Results

The predicted load time histories of the concrete panels were compared to the experimental results in Fig. 7. In the experimental test, for the WWR panels, load duration was about 6 msec and maximum applied load on the panel was 88 kN. For the LCFRC panels, these numbers were 4 msec and 55 kN.

The CSCM (MAT_159) and the Concrete Damage Model Release 3 (MAT_72) had a very good estimation of the maximum applied force on the panels, within 1 kN and 5 kN for the WWR and LCFRC panels, respectively. The Winfrith model (MAT_84) underestimated the maximum force by 26% for the WWR panels and 18% for the LCFRC panels. Load duration for all three models was less than the experimental results. The duration for the CSCM, the Concrete Damage Model, and the Winfrith model for the WWR panel was 4 msec, 3 msec, and 2 msec, respectively. These numbers for the LCFRC panel models were 5 msec, 4 msec, and 3 msec, respectively. The area below the load time was less than the experimental results for all the concrete models, which is also the reason why there was less deflection from the numerical results in comparison to the experimental values.

Multiple contacts between the panels and the projectile were characterized by the occurrence of multiple peaks. These peaks were referred to as secondary peaks in the observed load history. The only concrete model which could not show these secondary peaks was Concrete Damage Model Release 3 (MAT_72).

4.3. Error Analysis of the Results

A quantities error analysis was performed to facilitate the comparison of simulation results to experimental data. The root mean square error (RMSE) of the FE simulation results with respect to the experimental data is given by Eq. (15).

$$RMSE = \sqrt{\frac{\sum_{i=1}^{N} (f_{i-FEA} - f_{i-EXP})^2}{N}} \tag{15}$$

where N is the total number of data points, and f_{i_FEA} and f_{i_Exp} are the force or deflection values obtained from the FE analysis and experimental data, respectively, at the i^{th} data point. In general, the smaller the values of RMSE, the better match is between FE results and the experimental data. The differences with the respective test data referred to the error of the FE results. Error for two types of panels (WWR and LCFRC) by using three different simple input concrete are shown in Table 2. Mat_159 has the least error with experimental results.

5. Conclusions

An extensive study was conducted on the dynamic response of the WWR and LCFRC panels under impact from a falling weight. Three different simple input concrete models in LS-DYNA were used to predict the behavior of these panels. Two concrete models namely, the CSCM and the Concrete Damage Model, predicted force and displacement time history of impact closer to the experimental results than the Winfrith model. In general, after error analysis of the results, there was reasonable correlation with the test results and numerical results.

Acknowledgements

The authors gratefully acknowledge the financial support provided by the U.S. Army Research Lab (ARL) and the Leonard Wood Institute (LWI) under Award Nos. W911NF-07-2-0062 and LWI-191-028, respectively. The conclusions and opinions expressed in this paper are those of the authors and do not necessarily reflect the official views or policies of the ARL and LWI. The authors also are grateful for the ideas and help of Dr. Eric Musselman, Assistant Professor, Villanova University, Dr. Andrea Schokker, Professor and Executive Vice Chancellor for Academic Affairs, University of Minnesota Duluth, and Pro-Perma Engineered Coatings for supplying fibers.

References

[1] L. Agardh and L. Laine. 3D FE-Simulation of High Velocity Fragment Perforation Of Reinforced Concrete Slabs. *International Journal of Impact Engineering*, 1999; 22(4):911–22.

[2] LE. Schewr and J. Day, "Computational Techniques for Penetration of Concrete and Steel Targets by Oblique Impact of Deformable Projectiles," Nucl Eng Des 1991, 125:215–38.

[3] M. Alavi Nia, M. Hedayatian, V. Nili, and Afrough Sabet, "An Experimental And Numerical Study On How Steel And Polypropylene Fibers Affect The Impact Resistance In Fiber-Reinforced Concrete," *International Journal of Impact Engineering*.

[4] AM. Remennikov, SY. Kong, and B. Uy, "Response of Foam- and Concrete-Filled Square Steel Tubes under Low-Velocity Impact Loading," *ASCE Material Journal*.

[5] JO. Hallquist, "LS-DYNA Keyword User's Manual," version 971, vol. 1. *Livermore Software Technology Corporation (LSTC),* 2010.

[6] Z.S. Tabatabaei, JS. Volz, DI. Keener, and BP. Gliha, "Comparative Impact Behavior of Four Long Carbon Fiber Reinforced Concretes," *Materials and Design Journal*, 2013.

[7] Hallquist JO. LS-DYNA theory manual. Livermore Software Technology Corporation (LSTC); 2006.

[8] GR. Cowper and PS. Symonds, "Strain-Hardening and Strain-Rate Effects in the Impact Loading of Cantilever beams," Report to Brown Univ. Providence RI. United States; 1957.

[9] PPM. Lemmen and AW. Vredeveldt, "Application of Explicit Finite Element Method in Ship Collision Analysis," TNO, Report 93-CMC-R1153, 1993.

[10] LJ. Malvar, JE. Crawford, JW. Wesevich, and D. Simons, "A Plasticity Concrete Material Model for DYNA 3D," International Journal of Impact Engineering 1997; 19 (9-10): 847-73.

[11] L. Schwer and LJ. Malvar, "Simplified Concrete Modeling With *MAT_CONCRETE_DAMAGE_REL3," LS-DYNA, H-I-49-60, Bamberg; 2005.

[12] NS. Ottosen, "Failure and Elasticity of Concrete," RISO-M1810, July 1975.

[13] AM. Coughlin, ES. Musselman, AJ. Schokker, and DG. Linzell, "Behavior of Portable Fiber Reinforced Concrete Vehicle Barriers Subject to Blasts from Contact Charges," Int J Impact Eng 2010;37:521-9.

[14] ZS. Tabatabaei, JS. Volz, J. Baird, BP. Gliha, and DI. Keener, "Experimental and Numerical Analyses of Long Carbon Fiber Reinforced Concrete Panels Exposed to Blast Loading," Int J Impact Eng 2013; 57: 70-80.

[15] YD. Murray, "Users Manual for LS-DYNA Concrete Material Model 159," Report No. FHWA-HRT-05-062. Washington, DC: Federal Highway Administration; 2007. p. 20.

Table 1. Viscoelastic Material Properties

	Neoprene
Mass density (kg/m^3)	960
Bulk modulus, K_0 (MPa)	78.5
Short-term modulus, G_0 (MPa)	8.3
Long-term modulus, G (MPa)	1.8
Decay constant, (sec^{-1})	530

Table 2. Error Analysis of the Experimental and Numerical Simulations

Model	WWR		LCFRC	
	Deflection	Force	Deflection	Force
Mat_72	7.3	10.7	3.9	16.7
Mat_84	7.5	11.2	5.1	12.9
Mat_159	7.2	10.8	2.1	10.2

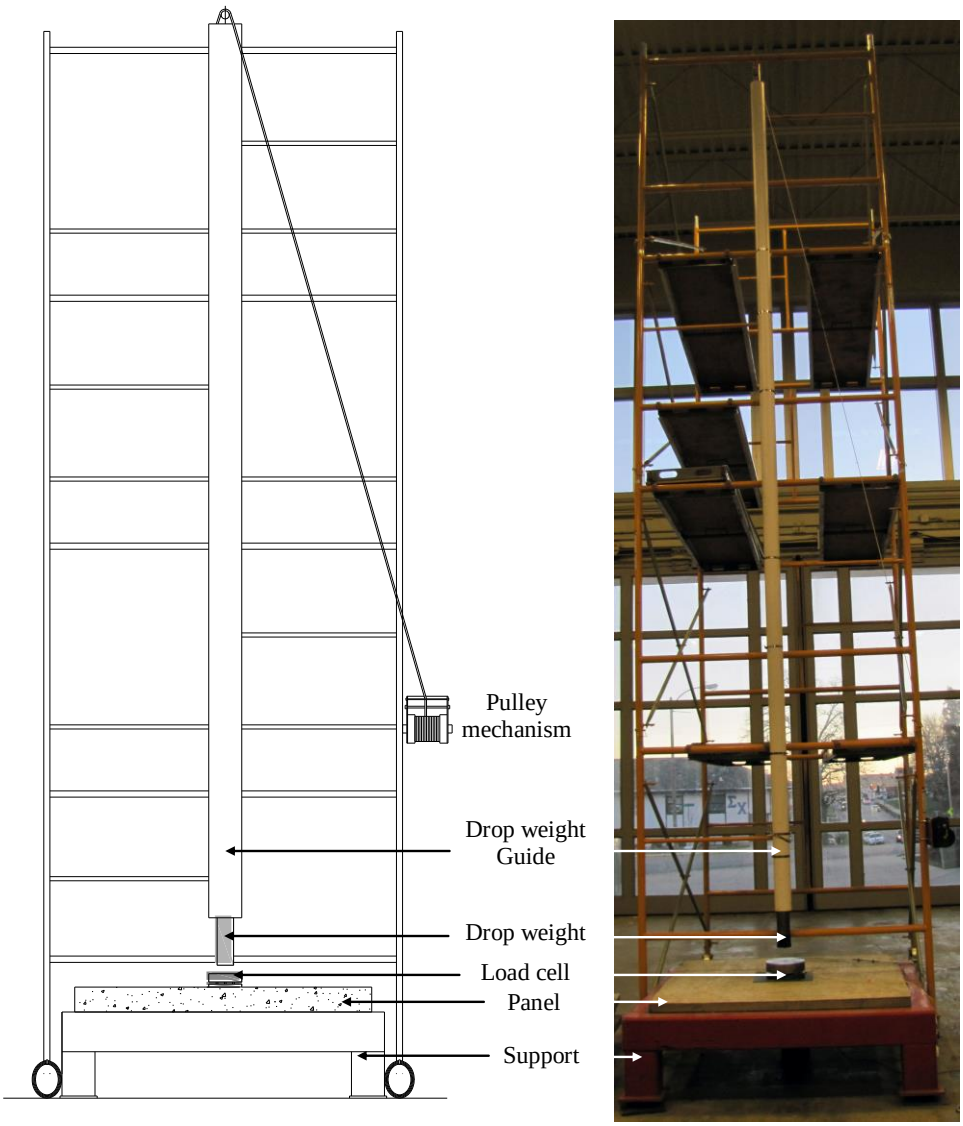

Figure 1. Test Setup

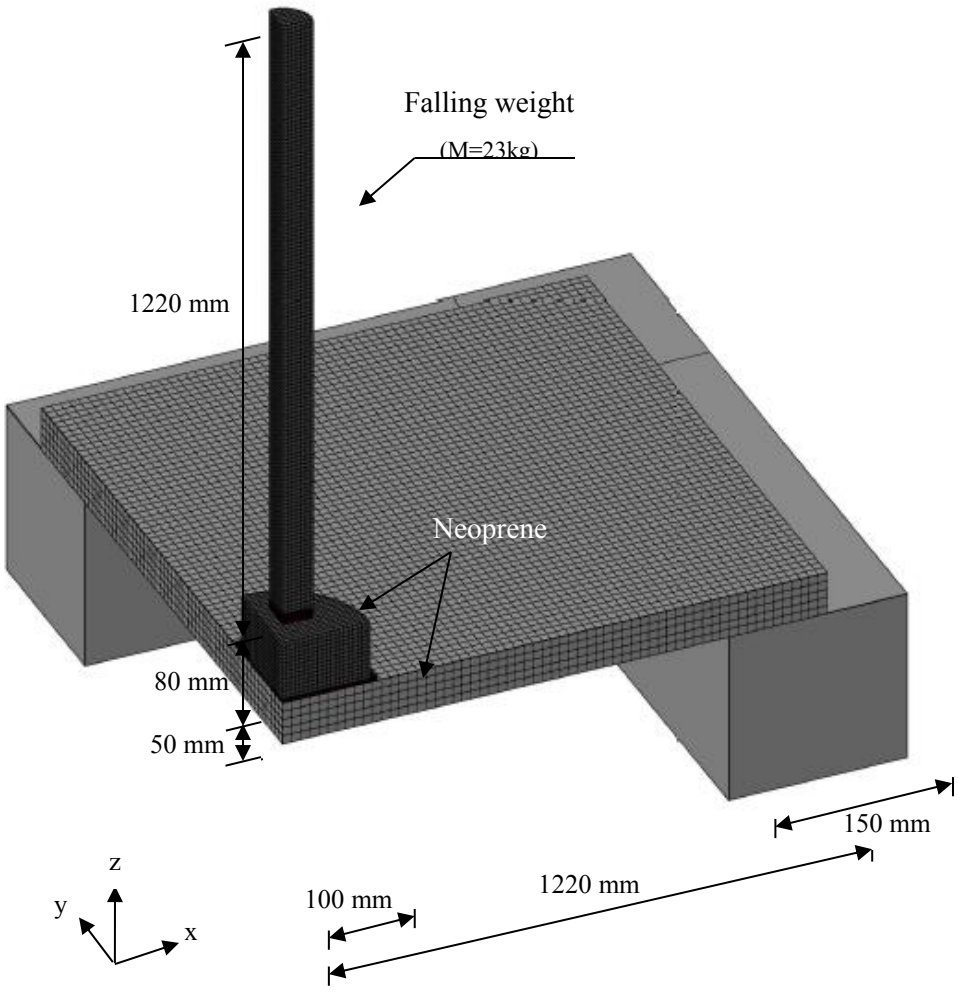

Figure 2. Finite Element Mesh Scheme for Panel

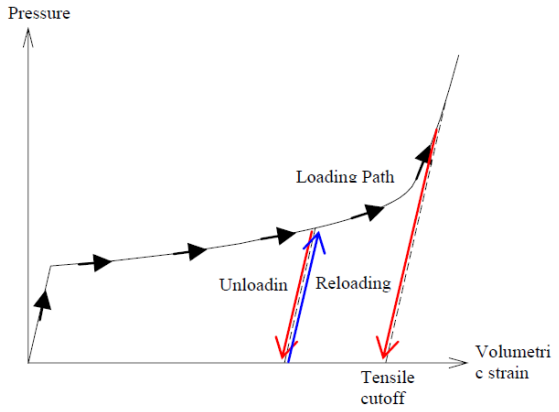

Figure 3. Pressure Versus Volumetric Strain Curve

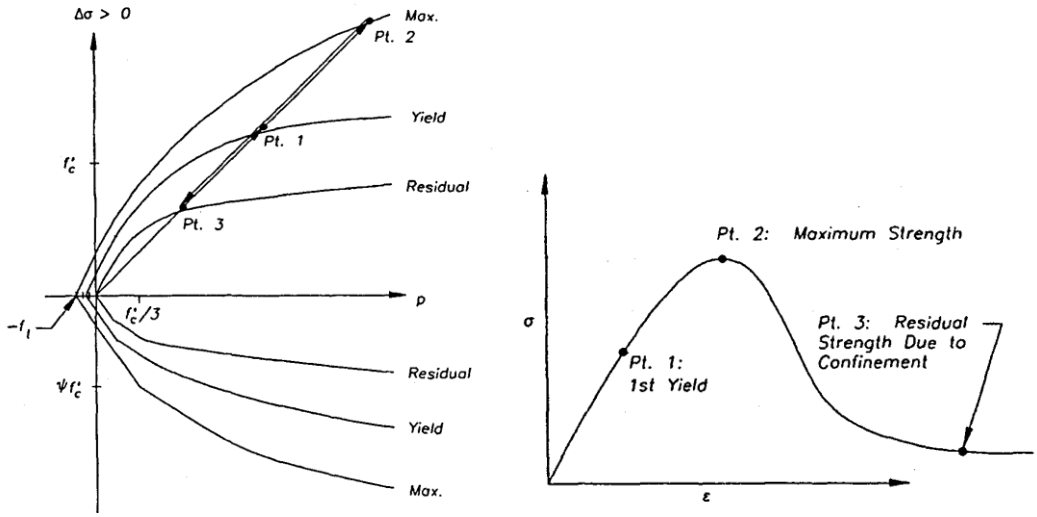

(a) (b)

Figure 4. Strength Model for Concrete (Schwer et al. 2005): (a) Failure Surface in Concrete Material Model and (b) Concrete Constitute Model

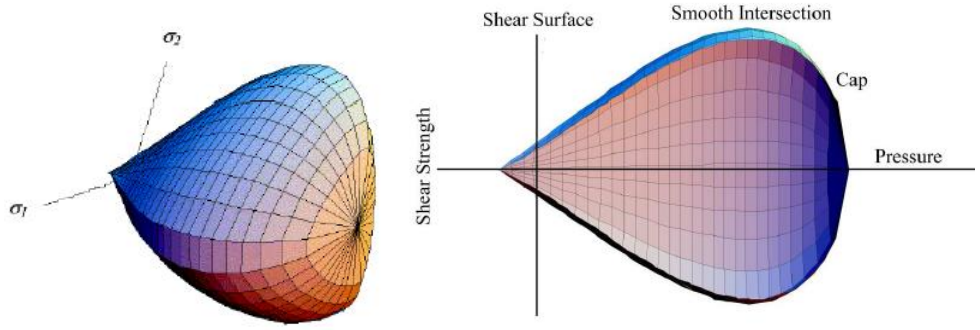

(a) Three-Dimensional (b) Two-Dimensional in the Meridional Plane

Figure 5. General Shape of the Yield Surface in Mat_159 Model (Murray, 2007).

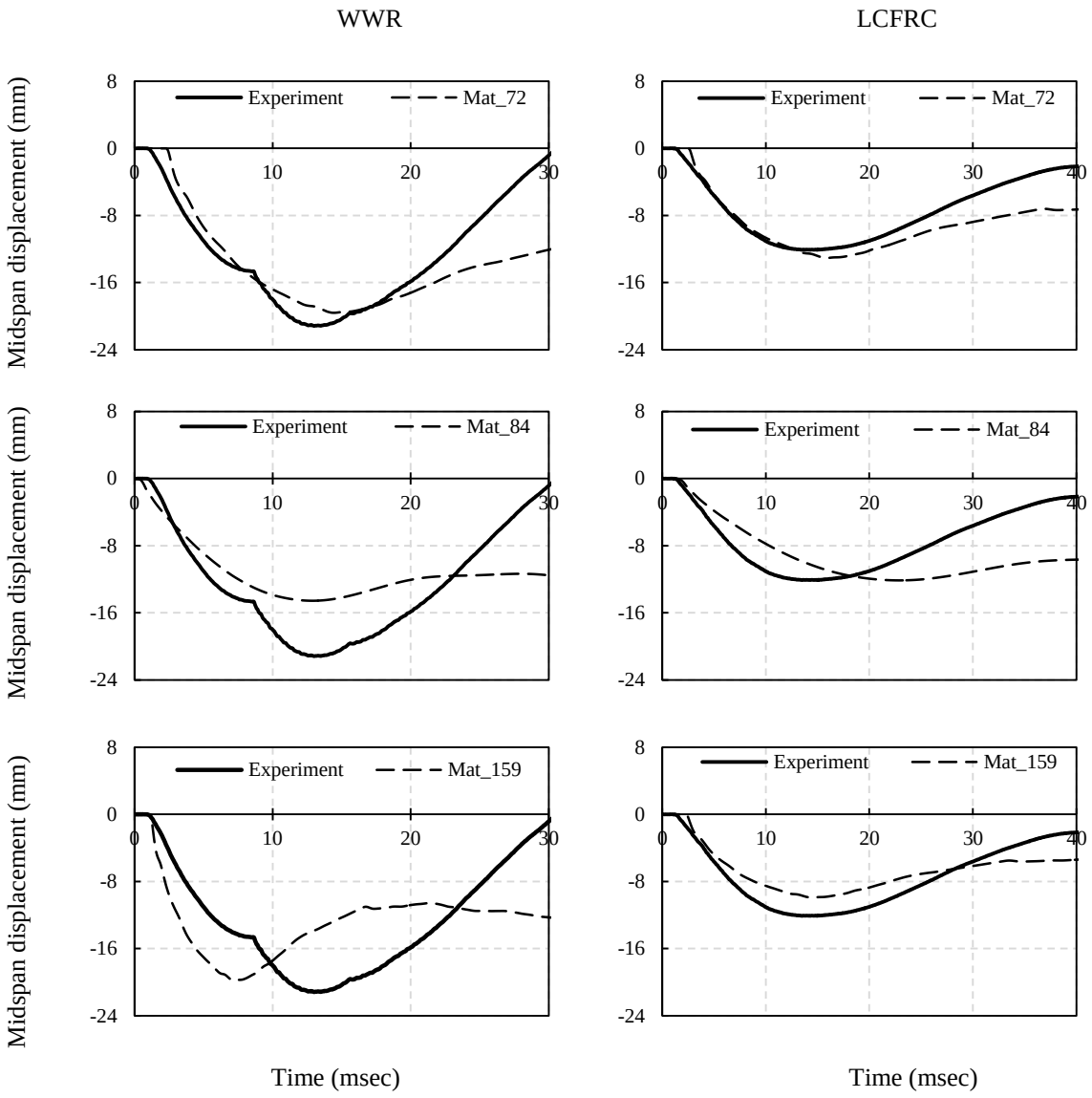

Figure 6. Deflection Comparison for Different Concrete Material Models

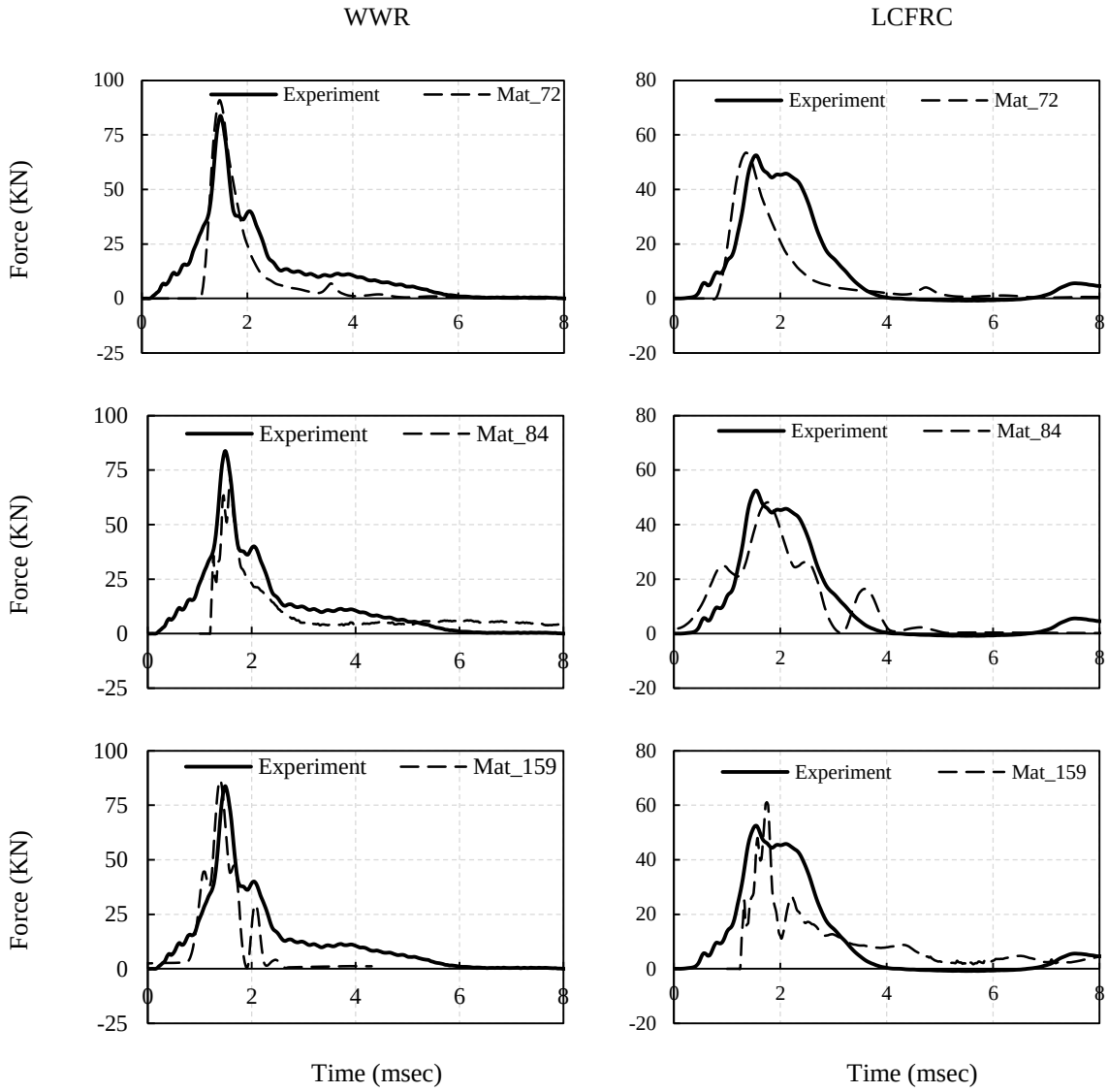

Figure 7. Force Comparison for Different Concrete Material Models

III. EXPERIMENTAL AND NUMERICAL ANALYSES OF LONG CARBON FIBER REINFORCED CONCRETE PANELS EXPOSED TO BLAST LOADING

Zahra S. Tabatabaei, Jeffery S. Volz, Jason Baird, Benjamin P. Gliha, Darwin I. Keener

ABSTRACT

The addition of long carbon fibers to traditional reinforced concrete is proposed as a method to improve the blast spalling resistance of concrete. A series of tests was conducted to compare the blast resistance of panels constructed with either conventional reinforced concrete (RC) or long carbon fiber-reinforced concrete (LCFRC). Conventional reinforced concrete panels were tested as control specimens. Pressure sensors measured both the free-field incident pressure and the reflected pressure for each panel. Furthermore, a finite element model was created in LS-DYNA to replicate both a control panel and an LCFRC panel to observe whether or not the models could predict the observed damage. Each of the LCFRC panels exhibited less material loss and less surface damage than the control panels. The addition of long carbon fibers significantly increased the concrete's blast resistance and significantly reduced the degree of cracking associated with the concrete panels. The results were also compared to the existing damage level chart (UFC 3-340-02). A comparison of the results indicates that the finite element modeling approach adopted in this study provides an adequate representation of both RC and LCFRC experimental responses. The results can be used in blast modeling with a reasonable degree of accuracy.

1. Introduction

Events over the last 10 years, including the Oklahoma City bombing, the 9/11 World Trade Center attacks, and the war in Iraq, have brought the topic of structural blast and impact resistant materials to the forefront. Due to the extensive use of reinforced concrete in critical structures, technologies that improve the performance of concrete under dynamic loading have the potential to save many lives.

The concept of using fibers as reinforcement is not new. Fibers were used for structural reinforcement in ancient times. Research on the use of fibers to increase the strength of both blast and impact structures has typically been limited to steel fibers and, to a lesser degree, polypropylene fibers [1-8]. Carbon fibers, however, possess many potential benefits over other fibers, including higher strength and stiffness, as well as increased durability. Carbon fibers also offer an economical benefit as 22 they are readily available as a waste product from the aerospace industry [9, 10].

Short carbon fibers have been successfully used within 23 concrete mixtures [11]. However, research in the area of carbon fibers more than 30 mm in length is virtually nonexistent. Because fibers used in this present research (100 mm long) are more than twice as long as other researched fibers, they are referred to here as long fibers.

Long carbon fibers have not been previously used because they tend to segregate within the mixtures and decrease workability. A proprietary coating is applied to the fiber yarn to form a stiff tape that overcomes these problems. This coating allows the fibers to be added directly into the concrete mixer, where they evenly distribute throughout the material. The concrete mixture to which the fibers are added has been established in previous work [12, 13]. This project examined the properties of this material, focusing on the blast resistance.

The use of long carbon fibers within a concrete matrix can be an economical option for improving blast resistance with distinct advantages over other blast-resistant material options. The long carbon fibers will also reduce secondary fragmentation by improving the spalling resistance of the concrete, a critical property for protecting personnel and equipment during a blast and difficult to prevent with current materials. With the use of long carbon fibers, these improvements come with little to no

modification of current design practices, allowing implementation to occur quickly and easily.

Two types of long carbon fibers were investigated in this study and are referred to as Fiber Type A and Fiber Type B. Fiber Type A is a 3K (K refers to thousands of filaments in a strand), plain weave, 40% epoxy, preimpregnated fabric. This fiber has an optimized application of 100 _ 10 mm fibers, at a dosage rate of 1.5% by volume, and a curing cycle of 121 _C for 45 min. Fiber Type B is a twined, 48K, polypropylene backbone carbon fiber with an optimized application of 100 mm long fibers and a dosage rate of 1% by volume [14]. Figure 1 is a photograph of both fiber types.

The goal of this study was to compare the blast resistance of long carbon fiber reinforced concrete (LCFRC) panels with traditional reinforced concrete (RC). The panels' responses were compared in terms of both the loss of mass and the extent of surface damage. Additionally, the panel response was simulated numerically using the finite element code LS-DYNA [15]. Successful damage prediction using numerical methods allowed the concrete panels to be assessed further without the need for full-scale blast testing.

2. Experimental procedure & results

2.1. Specimen design & specifications

Seven panels were tested to determine their responses to blast loading: three conventional reinforced concrete control panels (CP), two reinforced concrete panels containing long carbon fiber Type A (LCFRC-A), and two reinforced concrete panels containing long carbon fiber Type B (LCFRC-B). All of the panels measured 1830 × 1830 mm with a thickness of 165 mm.

All panels were constructed using identical concrete mixtures and steel reinforcement. The panels were designed in accordance with UFC 3-340-02 [16] for a charge weight of 34 kg of TNT at a standoff distance of 1675mm and zero angle of incidence. Details of both the steel reinforcement design and layout are illustrated in Figure 2. The flexural and shear designs assumed a Type II cross section based on the scaled distance of the charge, which represented an intermediate-range blast [16]. Since the calculated response time of the structure was significantly greater than the duration of

load, the panels were designed for the impulse generated by the blast with a yield line analysis to determine the panel resistance at a maximum support rotation of 2°. The shear design was based on an unlaced reinforced slab for both diagonal tension and direct shear and ignored any beneficial effect of the fibers. Based on the scaled distance and the use of a grid system of top and bottom flexural reinforcement, UFC 3-340-02 allows shear reinforcement in the form of single leg stirrups at alternate bar intersections in both directions. For the charge weight, standoff distance, and slab thickness selected for the test panels, the spall and breach parameters of UFC 3-340-02 indicated a strong likelihood of spalling. Furthermore, the McVay [17] prediction curves indicated the likelihood of severe spalling.

Mix proportions for the specimens are given in Table 1. Carbon fibers were added at 1.5% and 1% by volume for Types A and B, respectively. A high-range water reducer (HRWR) was added to the mix to maintain consistency and workability after the fibers were added to the concrete. Properties for the specimens are listed in Table 2, which includes the compressive strength at time of testing, which varied from 28 to 30 days after casting. The compressive strength values represent the average of three replicate 150 × 300 mm cylindrical test specimens. The yield strength of the reinforcing steel was 407 MPa.

2.2. Blast test setup & procedure

The blast test setup is shown in Figure 3. The panels were supported along all four sides by a frame constructed from high strength steel tube sections filled with concrete. Ammonium nitrate/fuel oil (ANFO) was chosen for the explosive charge because it is easier and less expensive to produce and procure than TNT. Because it is also harder to detect, terrorists tend to prefer ANFO (e.g., Murray Federal Building, Oklahoma City, 1995). The charge used for the testing consisted of 38.5 kg of ANFO with four 0.45-kg pentolite boosters, corresponding to a net equivalent weight (NEW) of 34 kg of TNT (TNT equivalent weight factor 0.83 for ANFO [18] and 1.11 for Pentolite [manufacturer]). The charge was centered above each panel using prefabricated cardboard tubes (Sonotubes), which allowed refinements during the test procedure by adjusting the standoff distance.

The sensor setup is also shown in Figure 3. Pressure transducers referred to as PS1, PS2, and PS3 were placed at the specimen's center as well as 430 mm and 860 mm away from the center, respectively. These distances were at approximately 1/3 and 2/3 of the diagonal distance from the center to the corner of the panel. Two free-field incident pressure sensors referred to as FPS1 and FPS2 were placed at a distance of 7420 mm from the center of the panel. General purpose ICP (Integrated Circuit Piezoelectric) sensors, each rated up to 69 MPa with a usable range up to 103 MPa, were used to record the reflected pressure (PS1, PS2, and PS3). Pressure sensors rated up to 3.5 MPa were used for the free-field measurements (FPS1 and FPS2).

The blast testing was conducted in a two-step process at Test Range 27D, located at Fort Leonard Wood, Missouri. In the preliminary test stage, two control panels were subjected to the 34 kg NEW TNT charge at standoff distances of 1065 mm and 1370 mm, respectively, corresponding to previous ConWep [19] analyses.

Preliminary blasts produced shockwaves that spalled the concrete extensively, debonding much of the reinforcement without any readable data. Because pressures greatly exceeded the capacity of the sensors, all of the panel sensors were damaged and the synergy data acquisition system (SDAS) failed to record the free field incident pressures. Thus, for the main test stage, a standoff distance of 1675mmwas selected. The specimens used for both the preliminary and main tests, with corresponding blast explosive charges, are summarized in Table 3.

3. Blast test results

3.1. Calculated vs. measured blast parameters

In 1984, Kingery and Bulmash [20] developed curves for the description of different air blast parameters using data compiled from their original 1966 report. The original report was based on air blast data taken on four large (5-500 ton) TNT events conducted in Canada between 1959 and 1964. The parameters are presented in double logarithmic diagrams, with the scaled distance Z as abscissa, as well as polynomial equations. These diagrams and equations are commonly used by researchers and designers to evaluate air blast phenomena. The equations are also implemented in

different computer programs that can be used for the calculation of air blast wave values (e.g., ConWep).

The Blast Effects Computer (BEC) is an open source available on the Internet through the Department of Defense Explosives Safety Board (DDESB). The BEC is a macro-rich Microsoft Excel spreadsheet originally released as a circular slide rule by the DDESB in 1978 [21]. The BEC spreadsheet is optimized for air blast predictions and includes modifications that account for type of weapon and atmospheric conditions such as height above sea level. The BEC calculates these blast effects from a detonation of either ammunition or explosives stored either above ground or in earth covered magazines [21].

Both the maximum free-field incident pressures and positive phase impulses from both ConWep and the BEC were calculated for comparison with the test data, which is shown in Table 4. The experimental values represent the average of the two free-field pressure sensors, as both sensors recorded very similar readings. In examining the data, ConWep underpredicted the free-field incident pressure and significantly overpredicted the impulse, while the BEC significantly underpredicted the free-field incident pressure and underpredicted the impulse. Except for Panel LCFRCB1, the experimental results were within 9% of the ConWep calculated free-field pressures but exceeded the BEC results by over two times. In terms of impulse, the experimental results fell between the ConWep and BEC values, although they were closer to the BEC results, varying from 3% to 18% of the BEC calculated impulse. The ConWep calculated impulse exceeded the test results by 31-40%.

The significant difference between the ConWep and experimental impulses may have been due to using ANFO as the primary explosive. ConWep uses a TNT equivalent in its calculations, and compared to TNT, ANFO produces a larger number of moles of product gas per unit mass of reactants, performing more work on the target. Furthermore, several researchers, e.g., [18, 22-26], have identified noticeable differences between ConWep predicted values and those measured during blast testing. It is also important to note that the Kingery-Bulmash blast parameter equations used in ConWep are based on a best fit of the data available from the early 1960s, and researchers have noted that there is

a level of uncertainty in using simplified models to predict complex phenomena such as blast loading, e.g., [27].

Figures 4, 5, and 6 depict the measured free-field pressures at sensor FPS1 for Panels CP-3, LCFRC-A1 and LCFRC-B2. Also included in the figures are the ConWep predicted values for comparison. In all three cases, the experimental values peak at a slightly larger pressure than predicted by ConWep but decay at a much higher rate, resulting in lower positive impulse values compared with ConWep. The experimental results also show the negative phase typical of a blast event.

3.2. Visual observation of damage

Visual observation of the panels confirmed the superior performance of the LCFRC panels (Figures 7-11). Figure 7 reveals the extensive damage experienced by both faces of the control panel, which was predicted by both the UFC 3-340-02 [16] and McVay [17] spall and breach parameters. The top face of the panel displays the traditional X-shaped yield line pattern consistent with a concrete panel, supported on four sides, exposed to a blast wave. Sufficient damage was inflicted on the top face, exposing the top layer of steel reinforcement in some areas. The bottom face of the panel also experienced severe damage. Most of the bottom layer of reinforcement was exposed. Large sections of concrete are missing from the panel. Origination of the blast wave is readily apparent. The most significant damage occurred in the center. Less damage occurred at distances further from the center.

Figure 8 reveals the damage experienced by Panel No. 1 for Fiber Type A. The top face of the panel experienced significantly less damage than the control panel. Some carbon fibers were exposed, a result, primarily, of the small amount of concrete paste bonded to the top of the fibers that cracked off during the blast. In addition, a very small amount of concrete (concrete paste plus aggregate) spalled off the top face of the panel. The yield line pattern can also be seen. The full "X," however, as displayed on the top face of the control panel, did not fully develop on the top face of this panel. Essentially, significantly less cracking occurred in this panel when compared to the control panel. Panel No. 2 for Fiber Type A performed just as well as, if not better than Panel No. 1 and, thus, significantly better than the control panel, as shown in Figure 9.

The Fiber Type B panels performed slightly better than the Fiber Type A panels and, thus, significantly better than the control panel. As revealed in Figures 10 and 11, the Fiber Type B panels showed slightly less spalling and cracking on all surfaces when compared to the Fiber Type A panels. As with the Fiber Type A panels, the Fiber Type B panels performed exceptionally well under the blast loading when compared to the control panel.

3.3. Physical measurement of damage

The weights of the panels, both before and after each blast test, were recorded to quantify the amount of damage sustained during the blast. Figure 12 compares the weight loss percentages for each panel. In terms of the amount of material lost during the blast, the fiber-concrete composite panels outperformed the non-fiber concrete panel (control) by nearly a factor of 10. This significant reduction in weight loss for the fiber concrete composite panels translates into a substantial decrease in harmful, flying debris in a blast event.

The panels were also evaluated with regard to the extent of damage on each face as a percentage of the surface area. These results are plotted in Figure 13. Again, the fiber- concrete composite panels significantly outperformed the control panel.

3.4. Comparison of test data with UFC 3-340-02 and Mcvay spall and breach parameters

Both UFC 3-340-02 [16] and McVay [17] contain spall and breach prediction curves for reinforced concrete slabs subjected to high explosive bursts. The prediction curves are shown in Figure 14 for UFC-340-02 and in Figures 15 and 16 for McVay. The experimental results are also plotted in each of the figures. In Figure 14, the test results are clustered together as the only difference in the spall parameter, shown as Equation (1), [28] is the concrete compressive strength, which varied slightly between panels.

$$\psi = R^{0.926} f_c^{'0.266} W_{adj}^{-0.353} \left(\frac{W_{adj}}{W_{adj} + W_c}\right)^{0.333} \quad (1)$$

where R is the standoff distance (feet), f_c is the concrete compressive strength (psi), W_{adj} is the adjusted charge weight (lb), and W_c is the steel casing weight (lb).

In Figures 15 and 16, the test results are plotted as a single value as the scaled thickness and scaled range are identical for all the panels. Based on these prediction curves, all of the panels should have experienced spalling (Figures 14 and 15) or severe spalling (Figure 16). The control panels experienced severe spalling, as shown in Figure 7, while the fiber-reinforced panels experienced minimal to no damage, as shown in Figures 8, 9, 10, and 11. Based on the McVay damage classification system, the fiber-reinforced panels would be classified as either no damage or, at most, threshold spalling.

4. Finite element modeling and development of fiber reinforced concrete spall prediction curve

The short duration of both blast loading and response, in addition to the destructive result of the testing, limits the opportunity for a thorough understanding of structural responses. Furthermore, full-scale explosive tests are too expensive to be used to examine every important parameter. Use of advanced computer modeling is essential to understand the behavior of structures subjected to a blast. In this regard, numerical simulations were conducted using a general-purpose finite element program, LS-DYNA 971 software. This software is a powerful FEA tool for modeling the high strain rate behavior of a number of engineering materials, such as concrete and steel [29]. As LS-DYNA is based on explicit numerical methods, it is well-suited for analyzing dynamic problems associated with large deformation, blasts, and wave propagation.

4.1. Model description

The panels were discretized using a Lagrangian mesh rigid material was used, to represent the support under the panel edges. A contact was specified between the panel and the supports with a coefficient friction of 0.3. Hourglass control was applied to avoid zero energy modes. Both gravity loads and bond slip between the concrete and steel reinforcement were neglected in the simulation due to the short simulation durations and very high blast pressures. Rebar was incorporated into the concrete mesh via the CONSTRAINED_LAGRANGE_IN_SOLID command. Elements erode when damage exceeds 0.99 and the maximum principle strain exceeds 1.

The blast shock wave was modeled using the extension of the empirical blast model, which appears in Version 971-R4 as *LOAD_BLAST_ ENHANCED (LBH). The

top face of the model was defined to receive pressure from the blast load. From this information, the air blast function calculates the appropriate pressure to be applied on this surface. In this algorithm [30], LS-DYNA looks up tables of information to determine pressure for a given cube root scaling value (not time). The algorithm implements Friedlander's equation to find the rate of decay for the pressure. Friedlander's equation uses the current model time, time to arrival, and duration time along with a decay coefficient to calculate the drop in pressure over time. The negative phase is presented in the simulation by using LBE with NEGPHS =0: negative dictated by the Friedlander equation. Based on the pressure measurements obtained during the blast testing, the charge weight was adjusted in LS-DYNA to obtain the same impulse as that experienced by the test specimens. The decision to modify the charge weight to obtain the same impulse was based on the fact that for this high-intensity, short duration blast, the impulse governs the response of the panels.

4.2. Model materials

The concrete for this study was modeled as solid elements using the MAT_CSCM_CONCRETE (MAT_159), which was implemented to LS-DYNA version 971. The MAT_159 model [31] can simulate concrete behavior during blast loads when the material experiences large strains, high strain rates, and high pressure [32]. The advantage of the MAT_CSCM_CONCRETE model is that this model is based on a single user input parameter, i.e., the unconfined compressive strength. Because the unconfined compressive strength can be derived easily from simple experiments, the present concrete model is very useful, particularly when the known concrete properties are limited. As most of the concrete's properties are related to the unconfined compressive strength, the remaining model parameters are generated automatically using a built-in algorithm associated with this material model and can be modified by the user if needed. Two different types of concrete materials needed to be modeled for this research program: the control concrete and the fiber-reinforced concrete. For both the fiber and the control concrete, material parameters were generated automatically in LS-DYNA from the target concrete compressive strength of 52 MPa. The method for creating a material model capable of describing the fiber-reinforced concrete involved presented many challenges. The parameters generated after one run of MAT_159, which

described fracture energy toughness in both tension and shear, were modified based on previous uniaxial tensile tests [33].

A piecewise linear plasticity model was implemented for the reinforcing bars in the numerical simulation, which is suitable for modeling the behavior of isotropic nonlinear hardening materials. This model also takes into account the effect of strain rate on material strength. Default strain rate parameters that were used correspond to values given in the European CEB code [34]. The steel yield stress and ultimate strength were 475 and 750 MPa, respectively, according to ASTM A615 [35].

4.3. Analytical results

Finite element model results indicate more spalling occurred in the control panel when compared to the LCFRC model. Figure 17 compares the plastic strain on the top surface of the control (CP-3) with the fiber-reinforced (LCFRC-B1) specimens. The LCFRC-B1 contains fewer areas in which the plastic strain is higher than that found in the control specimens, indicating that the LCFRC model provides a better distribution of both stresses and strains than the control.

Both the top and the bottom surfaces of both modeled panels were compared with the surfaces of actual damaged panels to validate the model. The damaged area was defined as the locations where the outside elements had eroded. The border between the remaining outside elements and the area of damage is illustrated in Figure 18 for CP-3 and in Figure 19 for LCFRC-B1.

Table 5 presents a comparison of the surface damage both measured experimentally and predicted analytically for both the control panel and the LCFRC panel. The percentage difference between the analytical and experimental panel was, 1.1% for LCFRC-B1 panel. This difference was at 23.2% for control panel.

Though close-range blasts can be difficult to model, these relatively simple three-dimensional models constructed in LS-DYNA using simple geometry, readily available material models, and empirically derived blast loads were shown to predict sustained damage to a panel with reasonable accuracy. While the developed models are not exact, they are simple enough to implement and can be utilized when blast testing is not a feasible option to test an LCFRC panel’s performance.

4.4. Fiber-reinforced concrete spall prediction curve

Based on this study, the existing spall and breach prediction curves do not accurately reflect the response of fiber-reinforced concrete. As a result, a parametric study was completed for the fiber-reinforced concrete using the finite element models previously developed. The parametric study examined panel thickness, standoff distance, and charge weight. The resulting spall prediction curve for fiber-reinforced concrete is plotted in Figure 20 using the same parameters as the UFC-340-02 diagram (Figure 14). The curve is described by the following equation:

$$\frac{h}{R} = \frac{1}{a + b\psi^{2.5} + c\psi^{0.5}} \begin{cases} a = -0.0404 \\ b = 0.0191 \\ c = 0.1925 \end{cases} \quad (2)$$

5. Conclusions

A series of blast tests has been carried out to investigate the blast resistance of reinforced concrete panels with and without long carbon fibers. Comparison of weight loss of panels shows that the addition of long carbon fibers, either Type A or Type B, significantly increased the spalling resistance of the concrete. The fiber-concrete composite panels outperformed the non-fiber concrete panel (control) by nearly a factor of 10, in terms of the amount of material lost during the blast. The long carbon fibers also significantly reduced the degree of cracking associated with the concrete panels. This decreased cracking correlates to a significant increase in blast resistance for structures constructed with the fiber-reinforced concrete.

Evaluation of surface damage shows that a significant decrease in damage occurred in the concrete of the fiber-reinforced panels. This reduction fell within a range of 75-89%. This improvement over conventional concrete would significantly reduce the lethality of a blast for personnel located behind a wall constructed with fiber-reinforced concrete.

LS-DYNA successfully modeled the response of long carbon fiber-reinforced concrete exposed to blast loading. A significant finding of this study is that use of Material Model 159 (Continuous Surface Cap Model), with an increase in fracture energy

for both tension and shear, more accurately describes the response of the LCFRC. This approach allows finite element modeling as an attractive alternative when full-scale blast testing is not feasible.

Based on the finite element modeling, a parametric study was performed to develop a spall prediction curve for fiber-reinforced concrete panels.

Acknowledgments

The authors gratefully acknowledge the financial support provided by the Army Research Lab (ARL) and the Leonard Wood Institute (LWI) under Award Nos. W911NF-07-2-0062 and LWI-191-028, respectively. The conclusions and opinions expressed in this paper are those of the authors and do not necessarily reflect the official views or policies of ARL and LWI. The authors are also grateful for the ideas and help of Dr. Eric Musselman, Assistant Professor at the University of Minnesota, and Mr. Andy Coughlin at Hinman Consulting Engineers, Inc.

References

[1] C. Wu, DJ. Oehlers, M. Rebentrost, J. Leach, AS. Whittaker, "Blast Testing Of Ultrahigh Performance Fiber And FRP-Retrofitted Concrete Slabs," *Eng Struct* 2009; 31:2060-9.

.

[2] KK. Antoniades, TN. Salonikios, and AJ. Kappos, "Evaluation of Hysteretic Response and Strength Of Repaired R/C Walls Strengthened With Frps," *Eng Struct* 2007; 29:2158-71.

.

[3] VC. Rougier and BM. Luccioni, "Numerical Assessment of FRP Retrofitting Systems For Reinforced Concrete Elements," Eng Struct 2007; 29:1664-75.

[4] GJ. Ha, YY. Kim, and CG. Cho, "Groove and Embedding Techniques Using CFRP Trapezoidal Bars For Strengthening Of Concrete Structures," *Eng Struct* 2008; 30:1067-78.

.

[5] EM. Almansa, MF. Canovas, "Behavior of Normal and Steel Fiber-Reinforced Concrete Under Impact Of Small Projectiles," *Cement Concr Res* 1999;29:1807-14.

.

[6] X. Luo, W. Sun, and SYN. Chan, "Characteristics of High-Performance Steel Fiber Reinforced Concrete Subject to High Velocity Impact," *Cement Concr Res* 2000;30:907-14.

[7] H. Masuya, M. Yamamoto, M. Toyama, and Y. Kajikawa, "Experimental Study on The Perforation of Steel Fiber Reinforced Concrete Slab by Impact," *Struct Mater* 2000;8:205-14.

.

[8] Suaris, and SP. Shah, "Strain Rate Effects in Fiber Reinforced Concrete Subjected to Impact and Impulsive Loading," *Composites* 1982;2:153-9.

.

[9] ES. Musselman ES, "Characterizing Blast and Impact Resistance of Long Carbon Fiber Reinforced Concrete," Doctoral thesis, Department of Civil and Environmental Engineering, Pennsylvania State University; 2007.

[10] EJ. Moser and AJ. Schokker, "Assessment of Long Carbon Fiber Concrete for Impact Resistance," Ogden Technologies, Inc.; 2005.

.

[11] ACI Committee 544. Report On Fiber Reinforced Concrete. Farmington Hills, MI: American Concrete Institute; 2002. p. 66.

.

[12] AJ. Schokker and ES. Musselman, "Safetcrete Blast Testing Evaluation," Ogden Technologies, Inc., Mid-Atlantic Universities Transportation Center (MAUTC); 2006. p. 44.

[13] ZS. Tabatabaei ZS, JS. Volz, BP. Gliha, and DI. Keener, "Development of Long Carbon Fiber Reinforced Concrete For Dynamic Strengthening," *ASCE Mater J* 2012. http://dx.doi.org/10.1061/(ASCE)MT.1943-5533.0000692.

[14] BP. Gliha, "Long Carbon Fiber Reinforced Concrete For Impact And Blast Protection," MS thesis, Department of Civil and Environmental Engineering, Missouri University of Science and Technology; 2011.

[15] LSTC. LS-DYNA Keyword User's Manual Version 9.71. California: Livermore Software Technology Corporation; July 2006. p. 154.

.

[16] Unified Facilities Criteria (UFC) 3-340-02. Structures to Resist the Effects of Accidental Explosions, Washington D.C.: U.S. Department of Defense; 2008. p. 50-70.

[17] MK. McVay, "Spall Damage Of Concrete Structures," Technical report SL-88-22.Waterways Experiment Station, Vicksburg, MS: US Army Corps of Engineers; 1988. p. 431.

[18] MM. Swisdak and JM. Ward, "The New DDESB Blast Effects Computer," Minutes of the 28th DoD explosives safety seminar; Aug. 1998.

.

[19] DW. Hyde, "Fundamental Of Protective Design For Conventional Weapons, CONWEP (Conventional Weapons Effects)," TM5-855-1. Vicksburg, MS: United States Army Waterway Experiment Station; 1992. p. 1-31.

[20] CN. Kingery and G. Bulmash, "Airblast Parameters From TNT Spherical Air Burst And Hemispherical Surface Burst," ARBRL-TR-02555. Aberdeen Proving Ground, Maryland, USA: US Army Armament Research and Development Center, BRL; 1984. p. 124.

[21] MM. Swisdak, "DDESB Blast Effects Computer Version 6, User's Manual And Documentation," DDESB technical paper No 17, revision 1; May 2005.

[22] JT. Baylot and DD. Rickman DD, "Uncertainties In Blast Loads On Structures," Proceedings of the 2007 structures congress: new horizons and better practices. Long Beach, CA: American Society of Civil Engineers; May 2007. 10 p. http://dx.doi.org/10.1061/40946(248)4.

[23] RS. Browning, "Resistance of Multi-Wythe Insulated Masonry Walls Subjected To Impulse Loads," MS thesis, Auburn University, Auburn; 2008.

[24] SR. Samuels, "Blast Resistant Glazing Tests," MS thesis, Texas Tech University, Lubbock; 2002.

[25] MM. Swisdak, “Simplified Kingery Airblast Calculations,” Proceedings of the 26th DoD explosives safety seminar. Indian Head, MD: Naval Surface Warfare Center; August 2002. PN.

[26] D. Bogosian, J. Ferritto, and Y. Shi, “Measuring Uncertainty and Conservatism In Simplified Blast Models,” Proceedings of the 30th explosives safety seminar. Atlanta, GA: Department of Defense; August 2002.

[27] J. Dewey, “The Shape of the Blast Wave: Studies of the Friedlander Equation,” MABS 21, Israel; 2010. p. 22.

[28] KA. Marchand, S. Woodson, and T. Knight, “Revisiting Concrete Spall And Breach Prediction Curves: Strain Rate (Scale Effect) And Impulse (Pulse Length And Charge Shape) Considerations.”

[29] MA. Crisfied MA and J. Wills, “Analysis of R/C Panels using Different Concrete Models,” *J Eng Mech* 1989; 115.

[30] Randers-Pehrson, Bannister, “Air Blast Loading Model For DYNA 2D and DYNA 3D,” Aberdeen Proving Ground, MD: Army Research Laboratory, ARL-TR-310; 1997. p. 49.

[31] YD. Murray, “Users Manual For LS-DYNA Concrete Material Model 159,” Report No. FHWA-HRT-05-062. Washington, DC: Federal Highway Administration; 2007. p. 20.

[32] Suaris Wimal and SP. Shah, “Strain-Rate Effects in Fiber-Reinforced Concrete Subjected to Impact and Impulsive Loading,” *Composites* 1982; 13:153-9.

[33] AM. Coughlin, ES. Musselman, AJ. Schokker, and DG. Linzell DG, “Behavior of Portable Fiber Reinforced Concrete Vehicle Barriers Subject to Blasts from Contact Charges,” *Int J Impact Eng* 2010; 37:521-9.

[34] Comité euro-international du béton. CEB-FIP Model Code 1990 Design Code. London: T. Telford; 1993. p.437.

[35] LJ. Malvar, “Review of Static And Dynamic Properties of Steel Reinforcing Bars,” *ACI Mater J* 1998; 95:609-16.

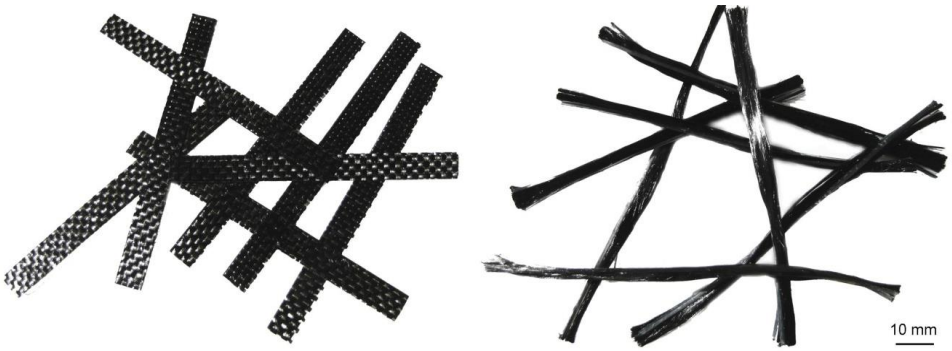

Figure 1. Fiber Type A (Left) and Fiber Type B (Right)

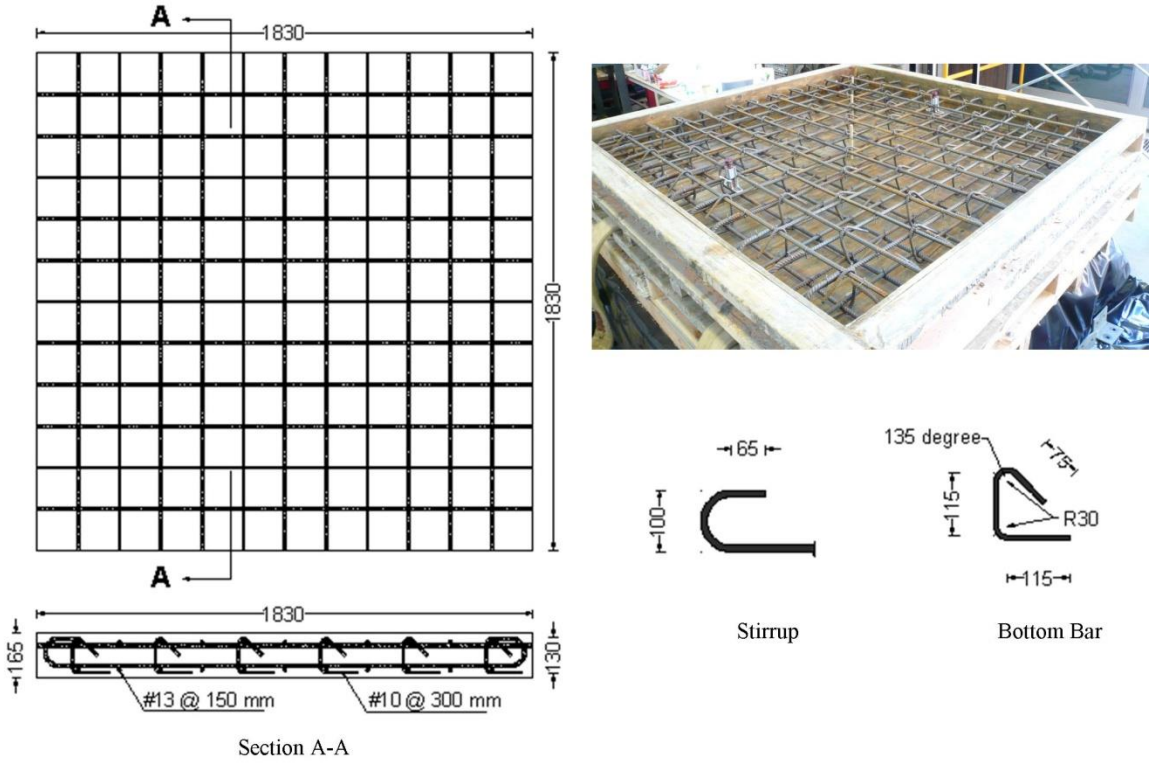

Figure 2. Test Specimen Geometry and Reinforcement Details (Units: mm)

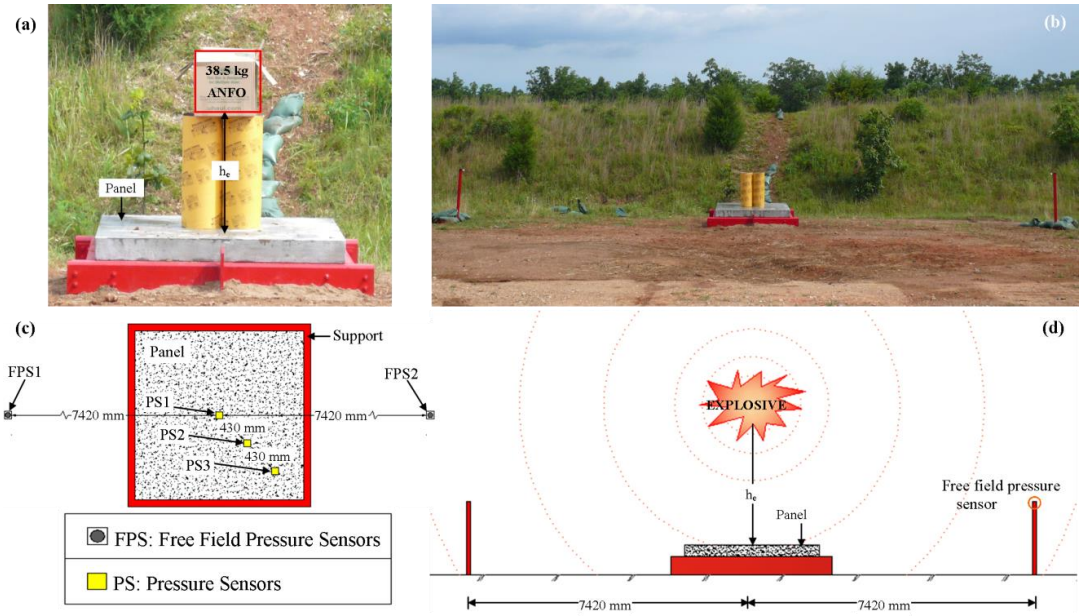

Figure 3. Blast Test Setup and Sensor Locations

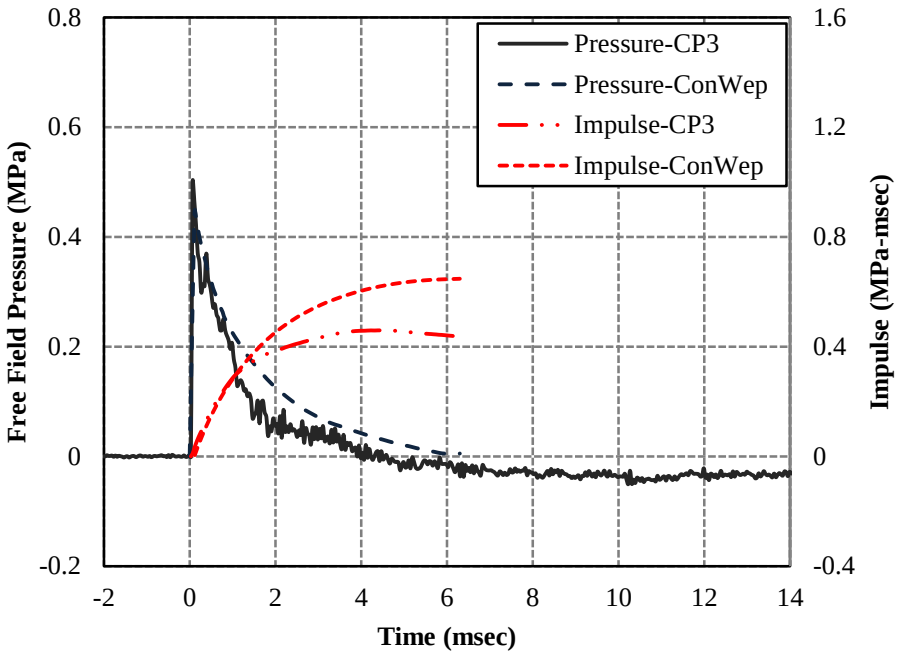

Figure 4. Time History of Free-Field Incident Pressure and Specific Impulse on CP-3 by Experiment and ConWep at FPS1

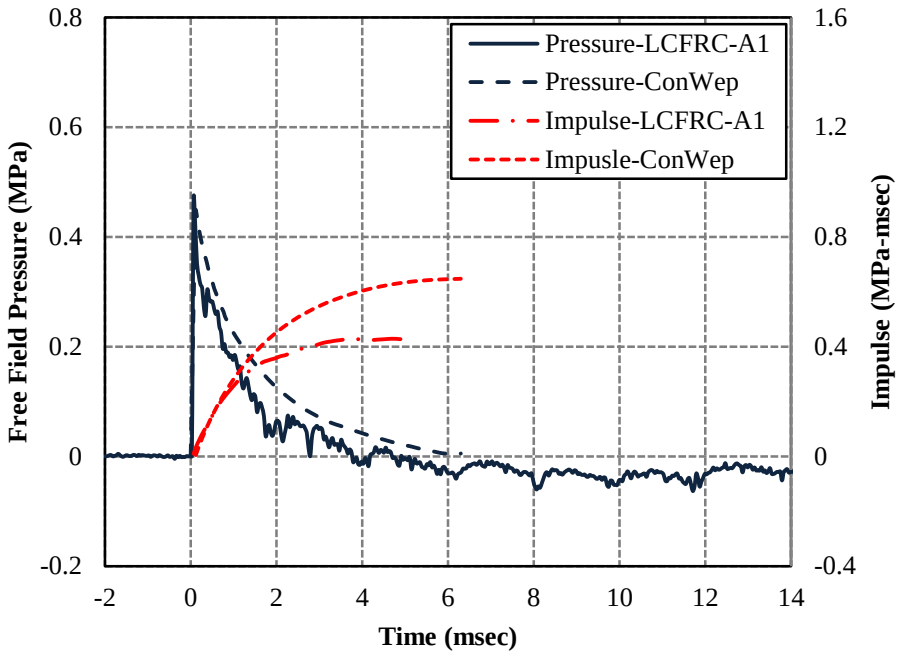

Figure 5. Time History of Free-Field Incident Pressure and Specific Impulse on LCFRC-A1 by Experiment and ConWep at FPS1

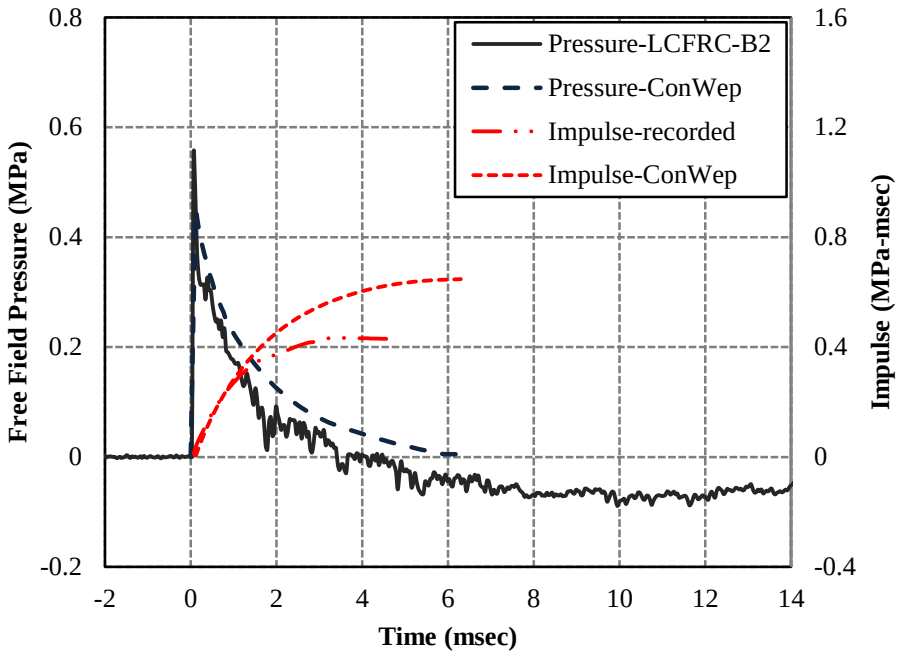

Figure 6. Time History of Free-Field Incident Pressure and Specific Impulse on LCFRC-B2 by Experiment and ConWep at FPS1

a b c

Figure 7. Control Panel No. 3 after Test: Top (a), Bottom (b), and Side (c)

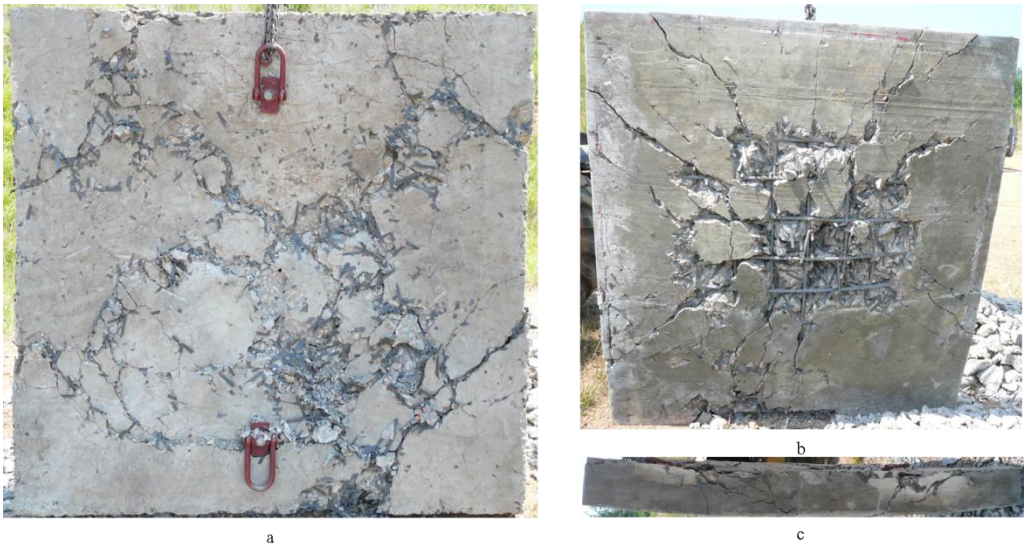

Figure 8. Fiber Type A, Panel No. 1 after Test: Top (a), Bottom (b), and Side (c)

Figure 9. Fiber Type A, Panel No. 2 after Test: Top (a), Bottom (b), and Side (c)

Figure 10. Fiber Type B, Panel No. 1 after Test: Top (a), Bottom (b), and Side (c)

Figure 11. Fiber Type B, Panel No. 2 after Test: Top (a), Bottom (b), and Side (c)

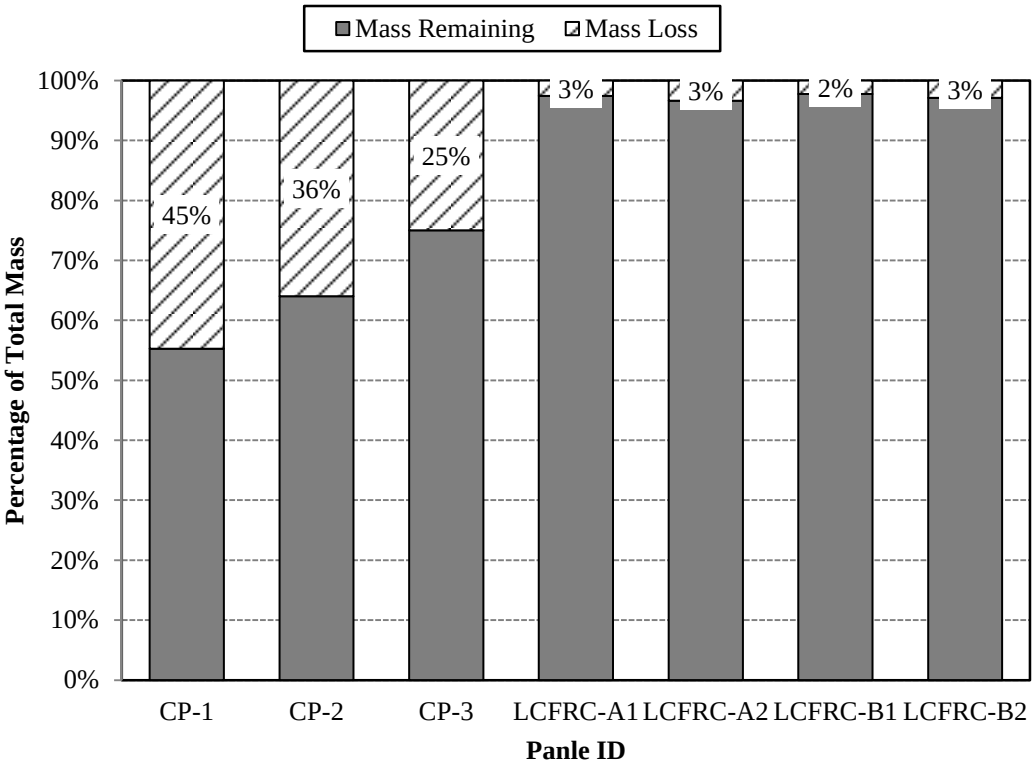

Figure 12. Comparison of Panels' Weight Loss due to Blast Loading

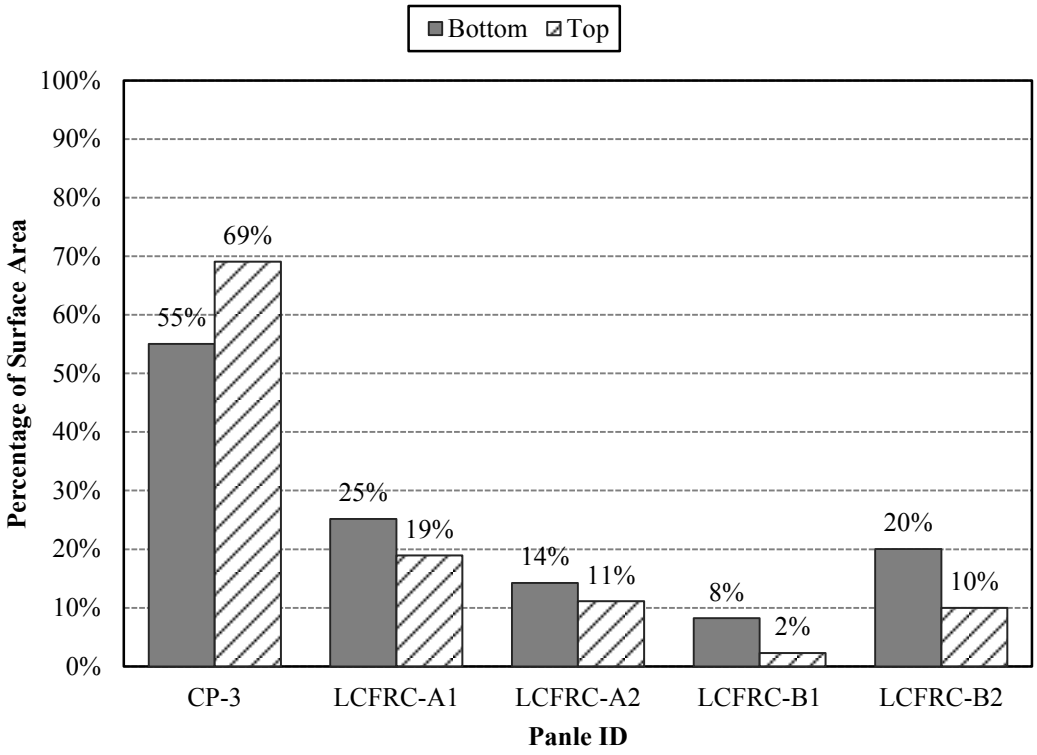

Figure 13. Surface Damage of Front and Back Faces of Panels

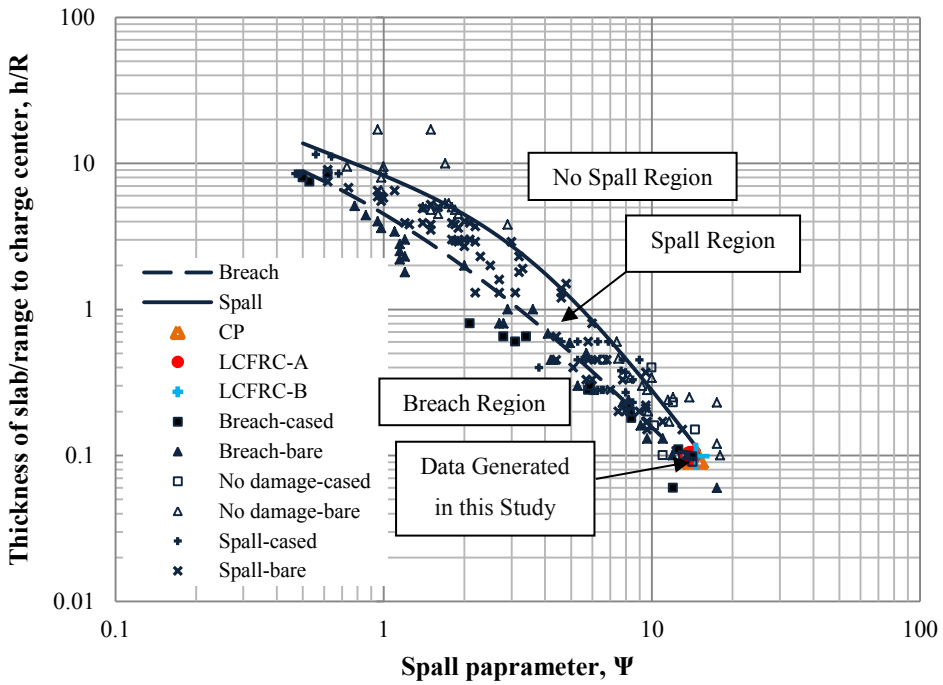

Figure 14. Threshold Spall and Breach Curves for Slabs Subjected to High-Explosive Bursts in Air [16]

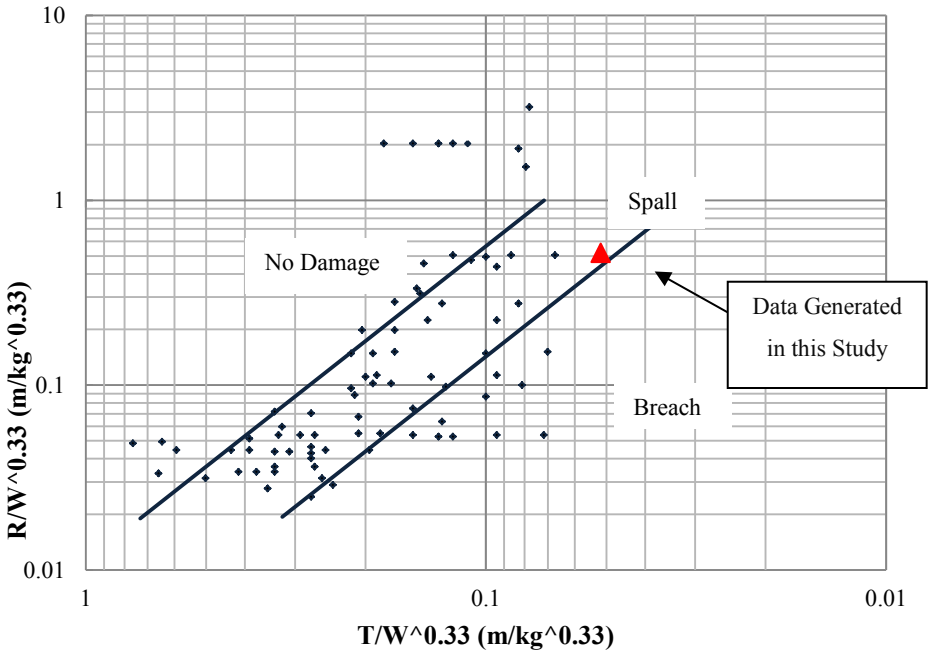

Figure 15. Log-Log Prediction Curves for Damage to Concrete Panels [17]

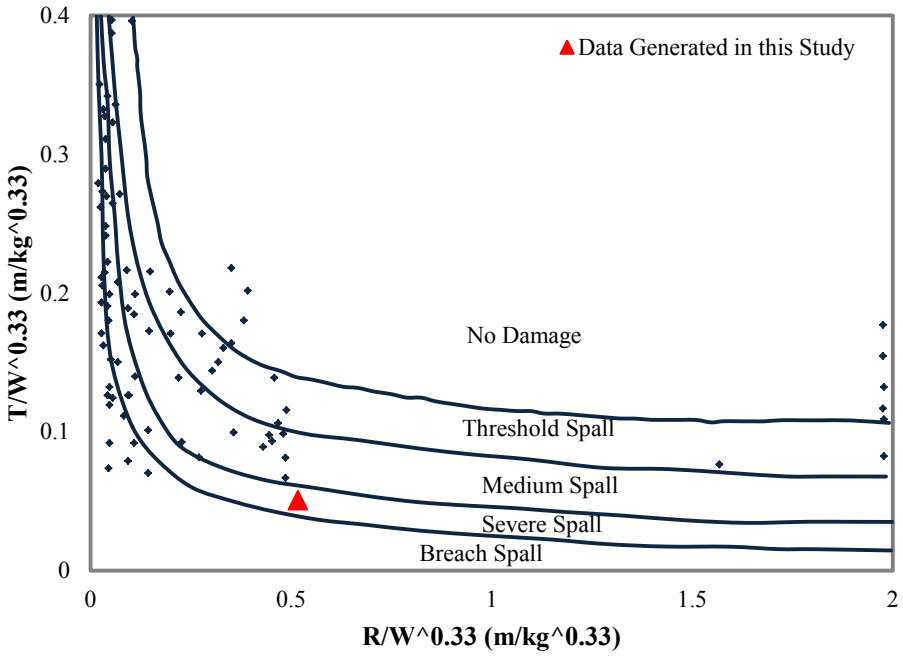

Figure 16. Prediction Curves for Damage to Concrete Panels [17]

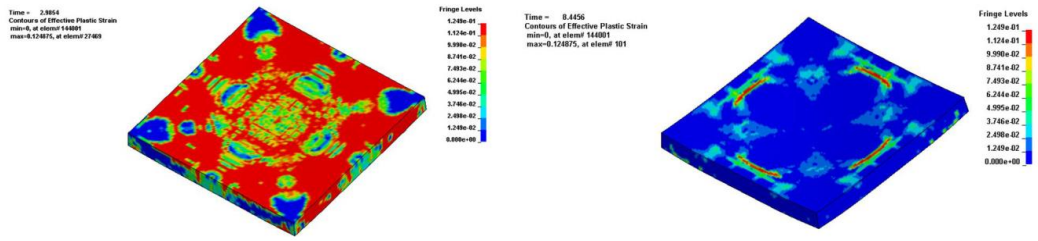

Figure 17. Top Surface Plastic Strain: CP-3 (Left) and LCFRC-B1 (Right)

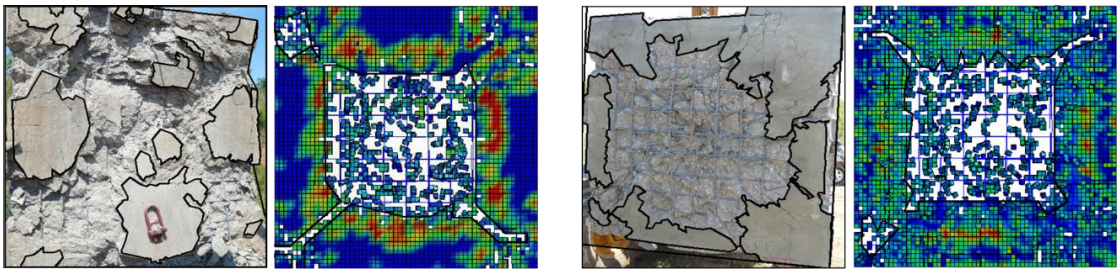

Figure 18. Comparison of Surface Damage from Analytical and Experimental Studies, CP-3; Top Surface (Left) and Bottom Surface (Right)

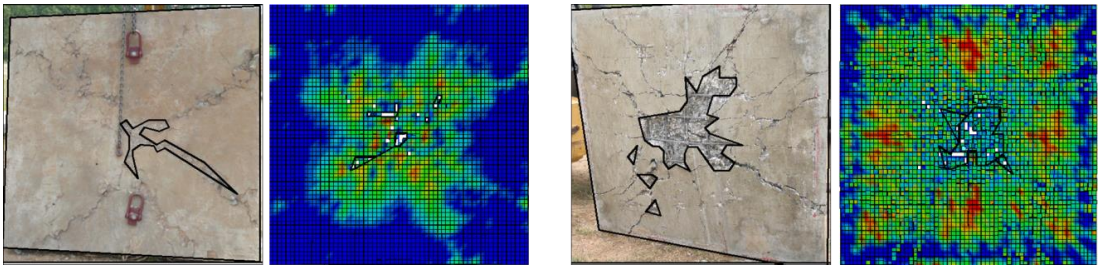

Figure 19. Comparison of Surface Damage from Analytical and Experimental Studies, LCFRC-B1; Top Surface (Left) and Bottom Surface (Right)

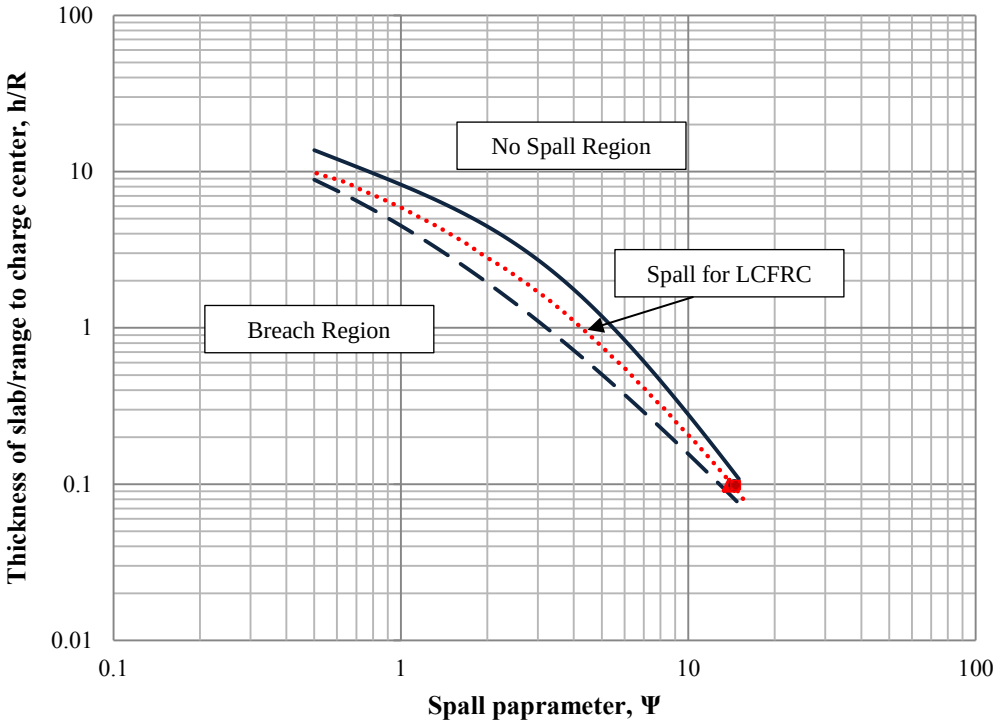

Figure 20. Spall Prediction Curve for Long Fiber-Reinforced Concrete

Table 1. Panel's Concrete Mixture Designs

IDs	Concrete Mixture (kg/m^3)
Portland Cement (Type I)	605
Fine Aggregate [a]	783
Coarse Aggregate [a,c]	783
Water	230
Water Reducing Admixture[b]	32.5 milliliters per 45 kg of cement

[a] Weights at saturated surface dry (SSD) condition

[b] High range water reducer (HRWR) was Gelenium 3030

[c] 19 mm maximum aggregate size

Table 2. List of the Specimens' Properties

Specimen	CP	LCFRC-A	LCFRC-B
Volume Fraction of Fiber (%)	-	1.5	1
Compressive Strength of Concrete, f'_c (MPa)	52	44.6	53.8

* Note: Panels were cast in pairs, so the same concrete was used for each pair

Table 3. Panel Test Matrix

Test Specimen	Trials	Standoff Distance h_e (mm)
Preliminary Test (34 Kg NEW TNT)		
CP-1[a]	1	1065
CP-2[a]	1	1370
Main Test (34 Kg NEW TNT)		
CP-3[a]	1	1675
LCFRC-A[b]	2	1675
LCFRC-B[c]	2	1675

[a] Control Panel

[b] Long Carbon Fiber-Reinforced Concrete - Fiber Type A

[c] Long Carbon Fiber-Reinforced Concrete - Fiber Type B

Table 4. Experimental and Analytical Incident Free-Field Pressure and Impulse for Panels

Blast Test	Incident free-field pressure (MPa)			Impulse (MPa-ms)		
	Experimental	Analytical		Experimental	Analytical	
		ConWep	BEC		ConWep	BEC
CP-3	0.50	0.46	0.22	0.47	0.68	0.40
LCFRC-A1	0.47	0.46	0.22	0.44	0.68	0.40
LCFRC-A2	0.49	0.46	0.22	0.45	0.68	0.40
LCFRC-B1	0.55	0.46	0.22	0.46	0.68	0.40
LCFRC-B2	0.45	0.46	0.22	0.41	0.68	0.40

Table 5. Comparison of Surface Damage from Experimental and Analytical Studies

Test specimen	Face	% of surface damage	
		Experimental	Analytical
CP-3	Top	69.1%	31.6%
	Bottom	55.0%	33.1%
LCFRC-B1	Top	2.3%	0.5%
	Bottom	8.2%	1.8%

IV. A COMPARISON BETWEEN THREE DIFFERENT BLAST METHODS IN LS-DYNA®: LBE, MM-ALE, COUPLING OF LBE AND MM-ALE

Zahra S. Tabatabaei, Jeffery S. Volz

Abstract

A previous experimental test was modeled in LS-DYNA®. Three different methods of simulation were performed. These methods are empirical blast method, arbitrary Lagrangian Eulerian (ALE) method, and coupling of Lagrangian and ALE method. Free field pressure history recorded from the experimental test was compared with the first method. Peak pressures for all these three methods were compared together and discussion of the results is provided.

Introduction

During recent years, several promising finite element solutions have been presented for determining the response of structures subjected to blast loading. For simulating structures subjected to blast loads, three different methods of analysis are available in LS-DYNA. First, a purely Lagrangian approach, where the air blast pressure is computed empirically with ConWep [1] data, referred to as LOAD_BLAST_ENHANCED (LBE). This pressure is directly applied to Lagrangian elements of the structure. Second, the Multi-Material Arbitrary Lagrangian Eulerian (MM-ALE) method, where the explosive as well as the air are explicitly modeled. An initial charge is detonated within an air domain and impulse transferred through contact algorithms. Third, LBE and MM-ALE coupling. An available experimental test is modeled with all three methods to determine the most accurate approach. For each model, problem description, input deck is provided in detail, for LBE case comparison with experimental results is provided.

Test Description

A test model based on the previous work of Tabatabaei and Volz [2] was used as the basis for the comparison of various air blast simulation techniques. The charge weight for this testing was 38.5 kg of ANFO with four, 0.45-kg pentolite boosters which had a net equivalent weight (NEW) of 36 kg of TNT. The charge was centered 168 centimeters over the 184 cm by 184 cm concrete panel. The panel contained steel reinforcement based on U.S. Army TM5-1300 [3], now UFC 3-340-02 [4]. Two types of blast pressures, the free-field incident pressure and the reflected pressure, were measured. The free-field incident pressure and the reflected pressure on the concrete specimens were measured at standoff distances of 742 cm and 168 cm, respectively, from the center of the explosive charge. The reflected pressure transducers on the specimen were placed at the specimen's center, referred as Sensor A. The free field pressure sensor was referred as Sensor B. The primary response quantity used for comparing the simulation results is the peak pressure at these two different sensors.

Figure 1 shows the geometric axis and blast epicenters for all the models. In order to reduce computational time and allow for high mesh refinement, constraints were

imposed normal to the x-z and y-z planes such that 1/4 of the blast was considered. A finite element model of concrete panel is developed using Lagrangian solid elements. The model used for Concrete is the CSCM in LS-DYNA.

*MAT_PIESWISE_LINEAR_PLASTICITY in beam element was used to model rebar in concrete. This model represents steel reinforcement behavior, with plastic deformation, strain rate effects and failure. The *CONSTRAINED_LAGRANGE_IN_SOLID formulation implemented in LS-DYNA was used to model interface between concrete and rebar (CTYPE=2).

Method 1: Purely Lagrangian Approach

A segment surface in the top face of the plate is defined to apply blast load using CONWEP blast function, LOAD_BLAST_ENHANCED. This method is based on a vast amount of experimental data implemented to LS DYNA. The implementation is based on a report by Randers-Pehrson and Bannister [1997]. This feature includes enhancements for treating reflected waves, moving warheads and multiple blast sources.

Three different mesh densities corresponding to element sizes of 5×5 mm and 10×10 mm and 20×20mm. In *LOAD_BLAST_ENHANCED option there are four different types of blast sources. Three of these subroutines s are presented and used in this paper. Subroutine 1 is a hemispherical surface burst in which charge is located on or very near the ground surface. Subroutine 2 is a spherical free-air burst in which there is no amplification of the initial shock wave due to interaction with the ground surface. Subroutine 4 is an air burst with ground reflection in which initial shock wave impinges on the ground surface and is reinforced by the reflected wave to produce a Mach front.

Comparison of calculated results for three of blast cases and three mesh sizes considered is presented in Table 1. The peak reflected overpressure generated in the middle point of the panel for hemispherical charge was 24% and 47% more than Spepherical charge and Airburst with ground reflection, respectively (5mm mesh). Example time histories of the reflected pressure calculated for all types of blast charge, 5 × 5 mm element size are presented in Figure 2. Figure 3 shows an example of time histories of the reflected pressure for different mesh sizes (Blast 2).

This approach is the only method which free field pressure at Sensor B was recorded and compared with experimental results. Due to long distance of Sensor B from the panel, for the other two methods (ALE and Coupling) it was too CPU time intensive to calculate pressure at Sensor B. Comparison between recorded free field pressure at Sensor B and calculated pressure in LS-DYNA are presented in Figure 4.

Figure 4 shows that for blast type 2 (default in LS-DYNA), LBE method underestimates peak pressure and impulse at this sensor. The difference between the calculated and measured reflected pressure readings may have been caused by using ANFO as the primary explosive, as opposed to ConWep's use of a TNT equivalent in its calculations. ANFO produces a larger number of moles of product gas per unit mass of the reactants, which expands during and after the process of the chemical reaction performing more work on the target.

To find out the correct amount of TNT which shows the same amount of peak pressure and impulse as experimental test, different amount of TNT were modeled in LS-DYNA. Results of this work are presented in Figure 5. This figure shows that there is different relationship between the increase of TNT with increase in the amount of impulse and peak pressure. Due to this difference two different conversion factors should be used for peak pressure and impulse of ANFO to TNT.

Method 2: ALE Approach

In this method, Lagrangian and ALE solution were combined in the same model and the fluid-structure interaction (FSI) handled by a coupling algorithm. The background air mesh configuration was chosen as cubic. The cube consists of two materials, air and TNT. The *ALE_MULTI_MATERIAL_GROUP defines the two materials. The explosive (TNT) is defined using *MAT_HIGH_EXPLOSIVE_BURN, which controls the explosive's detonation characteristics. For TNT, a JONES_WILKINS_LEE (JWL) EOS is used. The JWL EOS defines the pressure as a function of the relative volume, V, and initial energy per initial volume, E, such that

$$P = A\left(1-\frac{\omega}{R_1 V}\right)\exp(-R_1 V) + B\left(1-\frac{\omega}{R_2 \omega}\right)\exp(-R_2 V) + \frac{\omega}{V}E \qquad (1)$$

The parameters A, B, R_1, and R_2 are constants pertaining to the explosive are shown in Table 2. The *INITIAL_VOLUME_FRACTION_GEOMETRY card defines the initial distribution of air and TNT. It also defines where the TNT is placed, and its initial shape. Initial detonation defines where and when the detonation starts.

*MAT_NULL is used to model the air. The linear polynomial EOS is linear in internal energy per unit initial volume, E. The pressure used is given by:

$$P = C_0 + C_1\mu + C_2\mu^2 + C_3\mu^3 + (C_4 + C_5\mu + C_6\mu^2)E \quad (2)$$

Where C_0, C_1, C_2, C_3, C_4, C_5, and C_6 are constants and $\mu = \frac{\rho}{\rho_0} - 1$ with $\frac{\rho}{\rho_0}$ the ratio of current density to initial density. All the parameters used for this method are given in Table 2. A monotonic, second order accurate Van-Leer and Half-Shift Index advection scheme is used for material transport. The *CONSTRAINED_LAGRANGE_IN_SOLID keycard is used to couple the air domain (Master) to the plate (Slave). Since Lagrangian slave side of this model comprised of solids which may be eroded (concrete) due to material failure criteria, CTYPE was set to 5. An appropriate degree of refinement for the ALE mesh is partially dictated by the geometric characteristics of the Lagrangian parts. A reasonable goal is to have the ALE elements be nearly the same size as the Lagrangian elements where coupling is to take place.

Method 3: Coupling the Empirical Blast Load to ALE

In this method, the size of background mesh is reduced and covers only 8 cm on top of the panel and 4 cm around the panel. Explosive is not modeled in this method. A single element of background mesh towards explosive, referred to as the ambient layer, is receiving information from the blast Subroutine s (Figure 7). All the parameters and definitions of air and EOS is identical to Method 2, the only difference is that the ambient layer will be activated by setting AET=5 in *SECTION_SOLID and this segment is identified with *LOAD_BLAST_SEGMENT [5, 6]. Figure 7 shows time sequence of pressure fringes of wave propagating from the ambient layer into the concrete panel.

Results

All the simulations for this study were run using single precision SMP-DYNA 5.0. Table 3 contains comparison of model size and the statistics on the CPU time for these models. The MM-ALE model took approximately twice as long for completion than the Coupling method and 21 times more than Lagrangian simulation. The Coupling method model took 10 times more than LBE method for completion. Peak pressure at Sensor A for all the models are summarized in Table 4. The experimentally measured pressure at Sensor A was 150 MPa.

Conclusions

This paper presented three different methods for blast modeling in LS-DYNA and compared the results with experimentally measured test data. The LBE method underestimates peak pressure and impulse of blast at Sensor B. LBE method shows smaller peak pressure in comparison to ALE and Coupled method. Coupled method shows very close results to ALE method while using considerably less CPU time. All three methods underestimate blast pressure at Sensor A.

References

[1] D. Hyde, "User's Guide for Microcomputer Programs ConWep and FUNPRO Applications of TM5-855-1: Fundamentals of Protective Design for Conventional Weapons, U.S. Army Engineers Waterways Experimentation Station, 1988.

[2] Z.S. Tabatabaei and J.S. Volz, "Experimental and Numerical Analyses of Long Carbon Fiber-Reinforced Concrete Panels Exposed to Blast Loading," *International Journal of Impact Engineering*, Under Review.

[3] United States Army, TM5-1300: Structures to Resist the Effects of Accidental Explosions, 1990.

[4] Unified Facilities Criteria (UFC) 3-340-02: Structures to Resist the Effects of Accidental Explosions, U.S. Department of Defense, 2008.

[5] United States Army, TM5-1300: Structures to Resist the Effects of Accidental Explosions, 1990.

[6] T. Slavik, "A Coupling of Empirical Explosive Blast Loads to ALE Air Domains in LS-DYNA," *7th European LS-DYNA Conferences* Salzburg Austria, 2009.

[7] L. Schwer, "A Brief Introduction to Coupling Load Blast Enhanced with Multi-Material ALE: The Best of Both Worlds for Air Blast Simulation," Bamberg 2010.

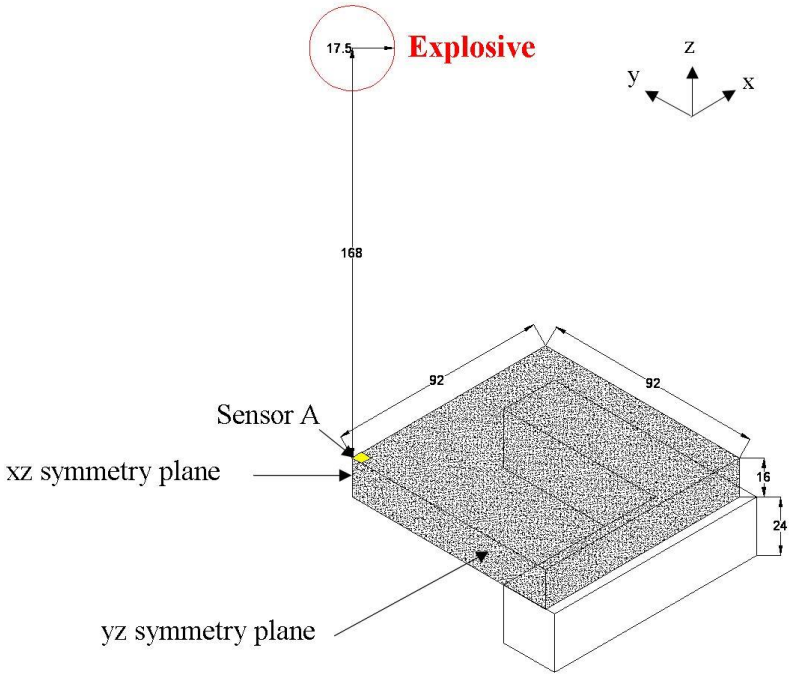

Figure 1. Test Setup

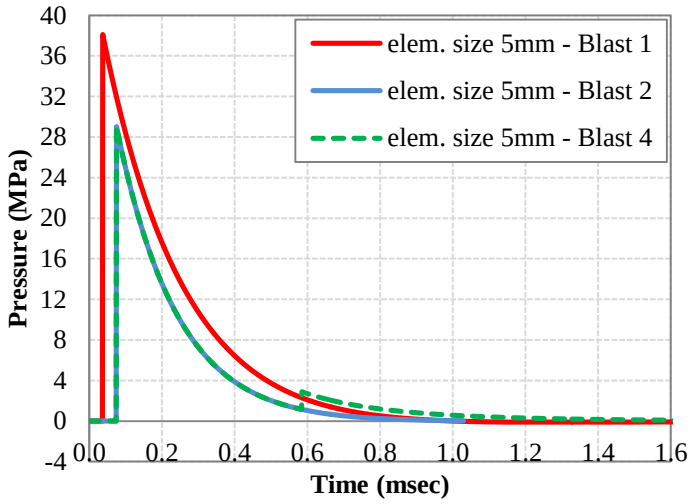

Figure 2. Time Histories of Reflected Pressure for Different Type of Charge for 5 mm Mesh Density

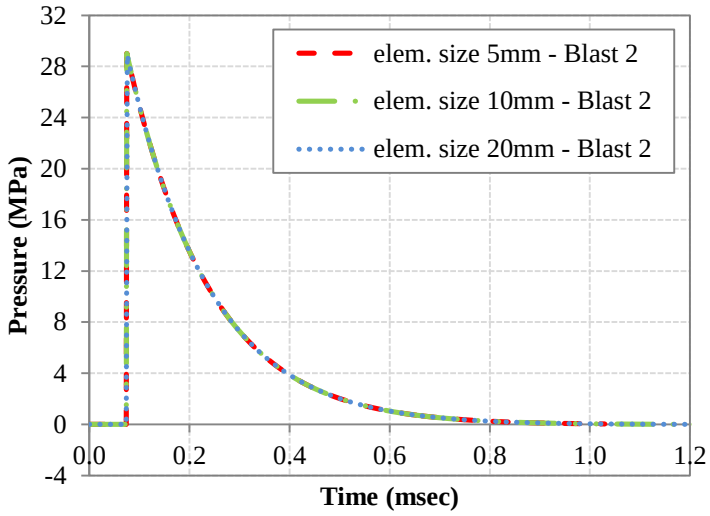

Figure 3. Time Histories of Reflected Pressure for Spherical Charge for Different Mesh Densities

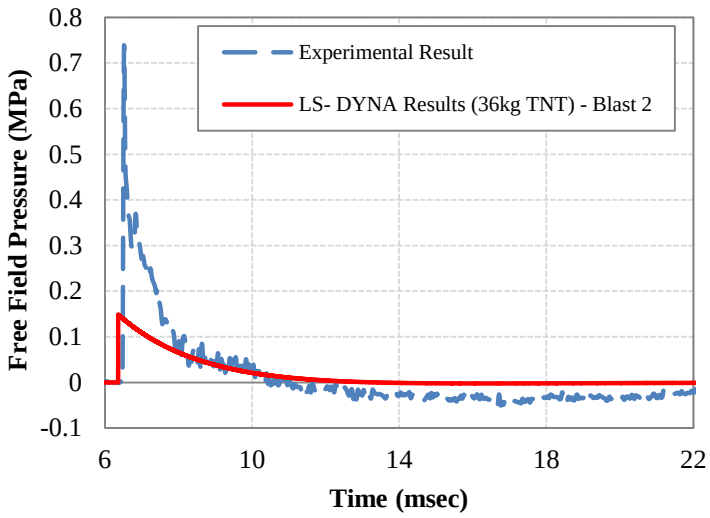

Figure 4. Comparison of Reflected Pressure Histories in Sensor B with LBE Method and Experimental Results

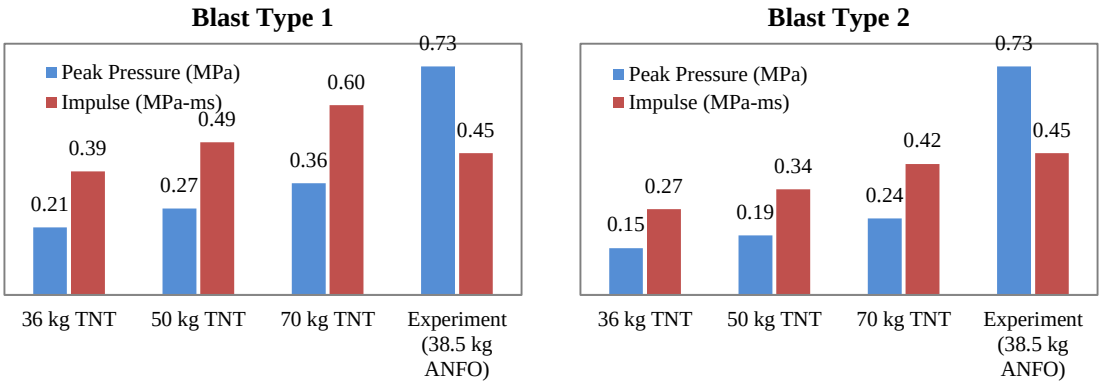

Figure 5. Comparison of Peak Pressure and Impulse of Different Amount of TNT

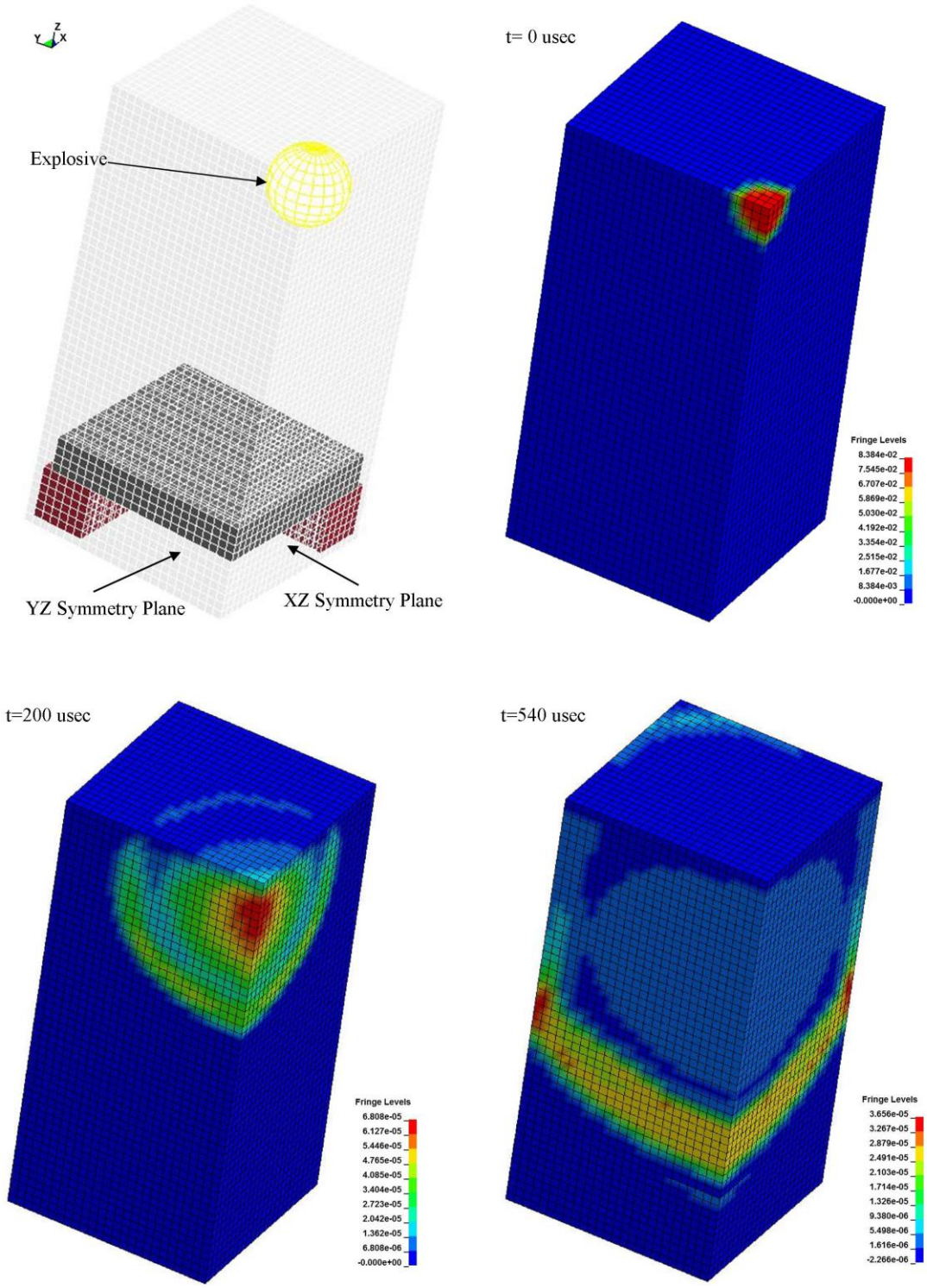

Figure 6. Time Sequence of Pressure Fringes Showing Wave Propagating from the Explosive Source

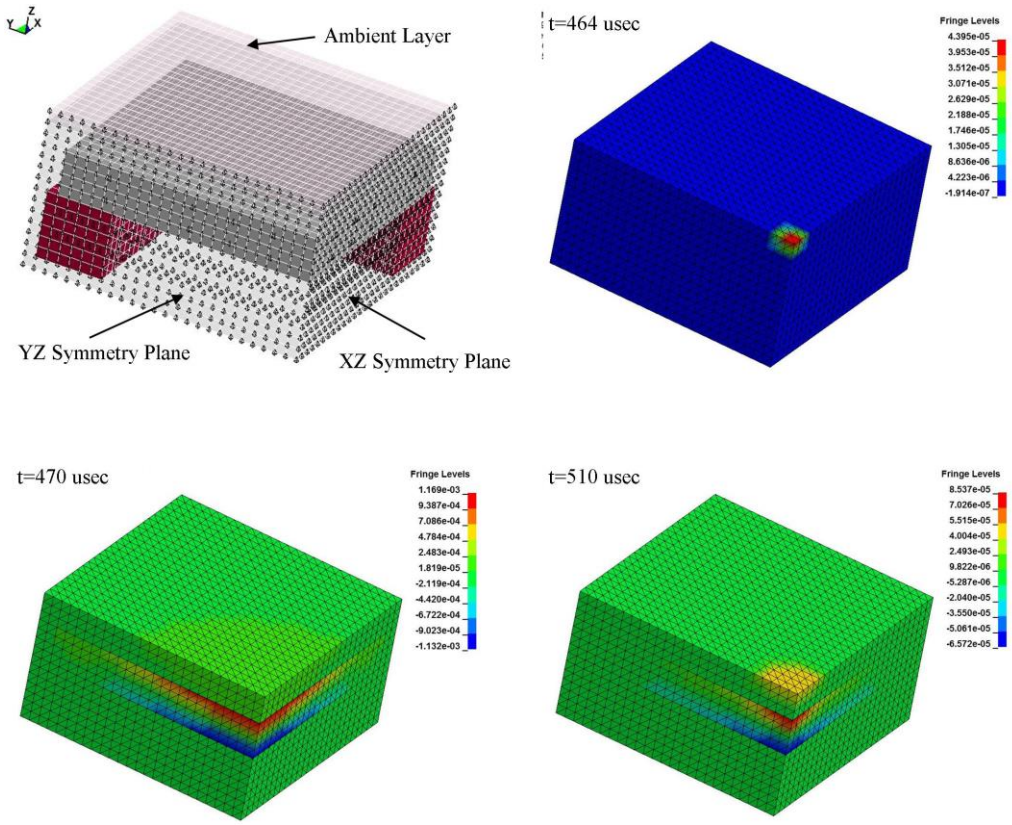

Figure 7. Time Sequence of Pressure Fringes Showing Wave Propagating from the Ambient Layer

Table 1. Comparison of Peak Reflected Pressure and Impulse for Empirical Blast Loads

Different Type of Blast Source	Peak Pressure (MPa)	Impulse (MPa-msec)
EQ1. Hemispherical Charge		
element size 5 x 5 mm	38.1	7.65
element size 10 x 10 mm	37.58	7.71
element size 20 x 20 mm	37.93	7.63
EQ2. Spherical Charge - No Amplification		
element size 5 x 5 mm	29.02	4.68
element size 10 x 10 mm	29.02	4.68
element size 20 x 20 mm	28.85	4.67
EQ4. Air Burst with Ground Reflection		
element size 5 x 5 mm	20.02	5.28
element size 10 x 10 mm	28.16	5.26
element size 20 x 20 mm	28.85	5.27

Table 2. ALE Material Property and EOS Input Data

Material	Unit (cm, g, μs)								
TNT	*MAT_HIGH_EXPLOSIVE_BURN								
	RO	D	PCJ						
	1.63	0.693	0.21						
	*EOS_JWL								
	A	B	R_1	R_2	OMEG	E_0	V_0		
	3.71	3.23E-02	4.15	0.95	0.3	4.30E-02	1		
Air	*MAT_NULL								
	RO	PC	MU						
	1.23E-03	-1.00E+05	0						
	*EOS_LINEAR_POLYNOMIAL								
	C_0	C_1	C_2	C_3	C_4	C_5	C_6	E_0	V_0
	0	0	0	0	0.4	0.4	0	2.58E-06	1

Table 3. Statistics on Three Blast Models

	LBE	MM-ALE	Coupling
No. of elements	4179	37856	12930
Initial time step	6.06E-04	6.06E-04	6.06E-04
Total CPU time	02:13:35	84:40:03	41:42:00
Element processing time (% of total CPU time)	77.22	87.87	76.9
Contact algorithm (% of total CPU time)	19.14	12.06	22.9

Table 4. Comparison of Results For all Three Blast Modeling

	Peak Pressure (MPa)
LBE Method	29
ALE Method	71
Coupled Method	55

SECTION

3. SUMMARY, DISCUSSION, CONCLUSIONS, AND RECOMMENDATIONS

3.1. SUMMARY OF RESEARCH WORK

The purpose of this research was to evaluate impact and blast performance of long carbon fiber reinforced concrete experimentally and numerically. Experimental tests were conducted on plain concrete (PC), reinforced concrete, and four different types of long carbon fiber reinforced concrete (LCFRC). The results from each test were then compared to one another. This comparison indicates that adding long carbon fibers to concrete both increases the post-cracking behavior of concrete and decreases the spalls in either an impact or blast test. Among all of the fibers tested, Fiber Type B3 outperformed the other fibers, absorbing more energy during impact.

Numerical simulations of a drop weight impact test were then performed on both welded wire reinforced concrete and long carbon fiber reinforced concrete panels. The three-dimensional finite element code LS-DYNA was used for the numerical analyses. Three different, simple input models were used to simulate concrete behavior under impact. As a consequence, both the force time history and deflection time history at failure were obtained for each case. These results were compared together.

Then, a series of tests were conducted to compare the blast resistance of panels constructed with either conventional reinforced concrete (RC) or long carbon fiber-reinforced concrete (LCFRC). Conventional reinforced concrete panels were tested as control specimens. Pressure sensors measured both the free-field incident pressure and the reflected pressure for each panel. Furthermore, a finite element model was created in LS-DYNA to replicate both a control panel and an LCFRC panel to observe whether or not the models could predict the observed damage. Each of the LCFRC panels exhibited less material loss and less surface damage than the control panels. The addition of long carbon fibers significantly increased the concrete’s blast resistance and significantly reduced the degree of cracking associated with the concrete panels. The results were also compared to the existing damage level chart (UFC 3-340-02).

Three different methods of simulation were performed to model experimental blast tests. These methods were an empirical blast method, arbitrary Lagrangian Eulerian (ALE) method, and coupling of Lagrangian and ALE method. Free field pressure history recorded from the experimental test was compared with the first method. Peak pressure for all these three methods were compared together and discussion of results was provided.

3.2. DISCUSSION

The primary difference between the current study and those performed in the past involves the length of the fibers used within the fiber-reinforced concrete. In the past, fibers have been limited in length due to the problems of dispersion and balling (agglomeration). The long fibers used in the current study contained either a special coating or weaving technique to develop the necessary resiliency to overcome these two problems and allow their use in reinforced concrete. The resulting material possessed increased ductility, tensile strength, flexural strength, and dynamic resistance. However, short steel, polypropylene, carbon, and other fiber types also increase the values of these same material properties when used in concrete. So the question becomes why do we need the increased fiber length and how does it benefit the resulting fiber-reinforced concrete more than conventional short fibers.

First, the benefit of the increased fiber length lies in the random nature of adding fibers to concrete combined with the three-dimensional nature of a structural element. The process of using fibers in concrete involves adding the fibers directly to the concrete during the mixing process. The fibers than distribute randomly in the concrete, which is then subsequently placed, consolidated, finished, and cured. As a result, even if the fibers are distributed uniformly within the fiber-reinforced concrete, their orientation is completely random, and this random orientation within a particular element (e.g., panel, beam, wall) results in a very complex behavior. For instance, consider a simplified comparison between two 2-in.-long fibers and one 4-in.-long fiber. Both have the same fiber volume, and the two 2-in.-long fibers have the same combined pull out strength as one 4-in.-long fiber. However, if within the first element, the two 2-in.-long fibers are aligned end-to-end, then a crack can form directly between them, negating their benefit.

Whereas within the second element, the 4-in.-long fiber can occur in the same place as the two end-to-end 2-in.-long fibers, and the crack cannot pass through the same location as in the first element without engaging the 4-in. fiber. This is a simplified explanation of a complex phenomenon, but the theory holds as you examine two fiber-reinforced concrete elements with multiple fibers, one with short fibers and one with long fibers, with both elements having the same fiber volume. Any potential crack must follow a longer path to avoid the longer fibers. In the extreme, very, very short fibers would be relatively easy for a crack to avoid, and would thus add very little resistance to the material.

This behavior was evident in both the static flexural tests and the impact and blast tests. For the static flexural tests, the same volume of fibers behaved much differently depending on the fiber length (i.e., 2-in.-long fibers vs. 4-in.-long fibers). The concrete that contained the longer carbon fibers had significantly increased toughness as a result of the failure crack taking a more tortuous path through the material to find the weakest plane. This longer path translated into increased fracture energy, resulting in increased flexural resistance and toughness. This behavior was even more evident in the impact and blast tests where the fiber-reinforced concrete revealed very irregular crack surfaces, which translated into significantly improved energy absorption and corresponding dynamic resistance.

The second benefit of the longer fibers involved their “ductility effect”. When placed in concrete, fibers resist forces through failing in either fracture or pull out. Because of the brittle nature of most fibers, if the fibers fracture, they add resistance to the material but the failure mechanism of the fiber-reinforced concrete is still brittle. However, if the fibers can pull out of the cementitious matrix prior to fracture, they provide pseudo ductility to the fiber-reinforced concrete, resulting in a failure mode that is much more ductile in nature, and thus able to absorb more energy compared to when the fibers fracture. However, the fibers must pull out in a controlled manner to increase this pseudo ductility. If they pull out too quickly, the effect will be minimized. The fibers need to pull out progressively with increases in load. The long fibers used in this study performed, in general, in this manner. There were noticeable differences in pull out behavior between the different fiber types tested, yet where the fibers had a more staged

pull out behavior, the resulting fiber-reinforced concrete exhibited a more ductile failure mode, with a corresponding increase in toughness. Also, the longer fibers used in this study allowed a longer plateau of this pseudo ductility compared to the short fibers. This pseudo ductility was most evident in the blast testing phase where the long fiber-reinforced concrete exhibited a tremendous increase in energy absorption.

Finally, the longer fibers provide a "net" within the concrete to reduce spalling of the material when exposed to dynamic loads, particularly blast. The fibers can be thought of as a net within the concrete that holds the material together even after suffering significant failure. In this way, the longer the fibers, the better. A perfect system would have fibers that extend continuously throughout the concrete to provide a true net that would hold the spalled pieces of concrete together and keep the failed element in one piece, preventing any spalling. This type of behavior is critical in a blast event where secondary fragmentation (spalling) adds to the lethality of a blast. If the fiber-reinforced concrete can contain all of the spalling, it is a much safer material in a blast. Unfortunately, it is not yet possible to have the fibers run continuously through the fiber-reinforced concrete due to constructability issues. However, the long fibers used in this study showed significant improvement in resisting this secondary fragmentation compared with conventional short fibers.

3.3. CONCLUSIONS

This section summarizes the conclusions from both the experimental and analytical studies of impact and blast resistance of long carbon fiber reinforced concrete. With regard to impact behavior, the following conclusions are presented:

- The strain energy of the four different fibers considered in this study were found to be 4-20 times higher than that of plain concrete and 1.5 times higher than that of WWR concrete panels. This increase in strain energy is due to fiber pull out during impact.
- The cracking edge of fiber-reinforced panels is more irregular as the failure surface needs to follow the weakest path through the fiber-cementitious matrix and thus absorbs more energy.

- The panels with fibers showed substantial improvement in the residual impact strength (I_{rs}), with ratios ranging from 1.9 to 5.8. Fiber type B3-3 had the highest residual impact strength ratio among the various types of long carbon fibers. This higher value was because fiber type B3 consisted of carbon fiber tow twined around a stiff polypropylene backbone and weaved together with cotton string. The weaving allowed for additional stability and energy absorption during impact.
- The residual and maximum deflection of the LCFRC panels was linearly proportional to the input impact energy. For all the LCFRC panels, the inclinations of the regression lines depended on the fiber properties and percentage of the fibers. The residual and maximum deflection of the WWR panels was polynomial proportional to the input impact energy by a degree of 2.
- Fiber B3 showed increased toughness in flexural tests compared with the other types of fibers. Increasing the fiber percentage had a greater effect on the B3 series compared to the B2 series. This increase could be related to the stiff skeleton and stability from weaving a backbone into the tow. This combination allows enhanced coating of the fibers within the cementitious matrix allowing increased pull out resistance. As a result, increasing the fiber percentage from 1% to 1.5% had a greater effect on the B3 series compared to the B2 series.

With regard to blast behavior, the following conclusions are presented:

- Comparison of weight loss of panels showed that the addition of long carbon fibers, either Type A or Type B, significantly increased the spalling resistance of the concrete.
- The fiber-concrete composite panels outperformed the non-fiber concrete panel (control) by nearly a factor of 10, in terms of the amount of material lost during the blast.
- The long carbon fibers also significantly reduced the degree of cracking associated with the concrete panels. This decreased cracking correlates to a

significant increase in blast resistance for structures constructed with the fiber-reinforced concrete.

- Evaluation of surface damage shows that a significant decrease in damage occurred in the concrete of the fiber-reinforced panels. This reduction fell within a range of 75-89%. This improvement over conventional concrete would significantly reduce the lethality of a blast for personnel located behind a wall constructed with fiber-reinforced concrete.
- LS-DYNA successfully modeled the response of long carbon fiber-reinforced concrete exposed to blast loading.
- A significant finding of this study is that use of Material Model 159 (Continuous Surface Cap Model), with an increase in fracture energy for both tension and shear, more accurately describes the response of the LCFRC.
- Based on the finite element modeling, a parametric study was performed to develop a spall prediction curve for fiber-reinforced concrete panels.
- Between three different methods of modeling blast in LS-DYNA, LBE method underestimated peak pressure and impulse of blast at the free field sensor. The LBE method shows smaller peak pressure in comparison to ALE and Coupled method. Coupled method shows very close results to ALE method while using considerably less CPU time. All three methods underestimate blast pressure at the reflected pressure sensor.
- The only time the LBE method should not be used in blast modeling is when there is shadowing (there is an object between explosive and target). In this study, the explosive was on top of the panel without any shadowing and the LBE method modeled the blast accurately.

3.4. RECOMMENDATIONS

Based on the conclusions stated in the previous section, the following recommendations for future research were developed:

- Model long carbon fibers in concrete discretely to see if results match more closely with experimental test data.

- Compare long carbon fiber reinforced concrete panel behavior with steel fiber reinforced concrete or different type of fiber reinforced concrete.
- Investigate the impact and blast behavior of long carbon fiber reinforced concrete beams.
- Investigate the shear behavior of long carbon fiber reinforced concrete.

APPENDIX A.
DEVELOPMENT OF LONG CARBON FIBER REINFORCED CONCRETE FOR DYNAMIC STRENGTHENING

V. DEVELOPMENT OF LONG CARBON FIBER REINFORCED CONCRETE FOR DYNAMIC STRENGTHENING

Zahra S. Tabatabaei, Jeffery S. Volz, Benjamin P. Gliha, Darwin I. Keener

Abstract

This paper discusses the development and testing of long carbon fibers – fibers 75 mm long or longer – to improve the resistance of reinforced concrete to dynamic loading, such as blasts and impact. In the past, attempts to use long fibers in concrete have failed due to both balling (agglomeration) and poor dispersion of the fibers. In the present study, two types of long carbon fibers were developed and optimized for their use in reinforced concrete. The resulting long carbon fiber reinforced concrete (LCFRC) was subsequently evaluated through impact and blast testing. Full-scale blast testing revealed that these fibers significantly increased the concrete spalling resistance. In terms of the amount of material lost during the blast, LCFRC panels outperformed non-fiber concrete panels by nearly a factor of 10. This significant reduction in weight loss for the LCFRC panels translates into a substantial decrease in harmful, flying debris in a blast event, and a corresponding reduction in blast lethality.

Introduction

Improving both the blast and the impact resistance of reinforced concrete by adding fibers has attracted considerable research interest over the last 30 years (Almansa and Cánovas 1999; Luo et al. 2000; Suaris and Shah 1982). Most of this research has traditionally focused on short steel, polyethylene (PE), and polypropylene fibers, ranging in length from 38 mm to 51 mm and in diameter from 0.1 mm to 0.5 mm (ACI Committee 544 2001). Research in the area of carbon fibers, particularly long carbon fibers, is virtually nonexistent.

In the past, attempts to use long fibers - fibers measuring either 75 mm in length or longer - in concrete have failed due to both balling (agglomeration) and poor dispersion of the fibers. Despite these failures, long carbon fibers offer two potential levels of improvement to both the blast and impact resistance of a concrete element (Musselman 2007). First, long carbon fibers absorb more energy through pullout during the pressure wave, or impact, improving the overall resistance of the concrete element. Second, the fibers significantly diminish secondary fragmentation, thus reducing one of the leading causes of damage to surrounding personnel and materials (Musselman 2007).

The problems of both balling and dispersion must be resolved in order to capitalize on the benefits of long carbon fibers. One way to resolve this issue is to coat the carbon fibers in order to enhance the stiffness of the carbon graphite yarn and thus reduce the potential for balling. Long carbon fibers coated with a proprietary acrylic blend developed by Ogden Technologies, Inc., were previously used in reinforced concrete (Ogden 2008). However, these fibers created a concrete mixture that was difficult to place and resulted in a moderately non-uniform fiber dispersion.

In addition to acrylic coatings, thermoset plastics offer the greatest potential for coating the carbon graphite yarn in terms of both resilience and dispersion within the concrete matrix. Specifically, epoxies, polyesters, polyurethanes, silicones, and vinyl esters offer ease of use and can be formulated with application-specific properties (Rosato and Rosato 2004). Of these, epoxies offer the highest performance in terms of strength, chemical resistance, corrosion resistance, and dimensional stability. Costing less than epoxies, polyesters offer very good strength, chemical resistance, and a wide choice of resins. Both polyurethanes and polyureas generally are considered high-performance

thermoset resins and offer high impact strength, toughness, and resistance to abrasion. Silicones, which use silicon-based rather than carbon-based fibers as the backbone of the polymer, offer the potential for increased lubricity, or sliding, of the fibers to prevent balling. Finally, vinyl esters combine the best features of both epoxy and polyester resins, generally at a lower cost (Rosato and Rosato 2004). Epoxy, polyester, and vinyl ester were used in this research as initial resins for coating the fibers.

In this study, a preliminary coating was developed for both carbon fiber tow and carbon fiber fabric. Two fibers were then developed and will subsequently be referred to as "Fiber Type A" and "Fiber Type B." Different dimensions of these two fibers were then tested to determine the optimum size for use in concrete. Following the basic tests of Fiber Types A and B, the fibers were used to enhance concrete panels under both impacts and blasts. In all cases, long carbon fiber reinforced concrete (LCFRC) was applied without incident and outperformed panels without fibers.

Preliminary Coating Development

Both carbon fiber tow and carbon fiber fabric were investigated as potential fiber reinforcement for concrete. The tow represents the traditional fiber shape used in concrete. Its long, thin shape offers both less flow resistance and potentially improved distribution within the concrete. The carbon fiber fabric offers both a stiffening effect of the weave for improved resiliency as well as a two-dimensional effect, depending on the widths selected.

Fiber Resiliency

Initially, formulations for epoxy, polyester, and vinyle ester low-viscosity resins were developed at Missouri University of Science and Technology. These low-viscosity coatings were chosen for their ease of application. The coatings were then applied to a polyacrylonitrile (PAN-based), commercial grade, 12K carbon fiber tow. The 12K tow was chosen both because it is the most common tow size in the industry and because it fulfills the material strength requirements of the application.

The coatings were tested on a 12K carbon fiber tow from two different manufacturers. The first product (Product A) contained 1% epoxy-compatible sizing. The

second product (Product B) included both sized (1.1%) and unsized samples. The unsized fibers were very difficult to work with as they resisted the coatings; they began to fray and separate during the coating process. All subsequent work used only sized carbon fiber tows. Table 5.1 shows the typical fiber properties for these two products. The actual properties of individual lots will vary within specified limits.

To prepare the carbon fibers for coating, lengths of tow were secured in a wooden frame measuring approximately 460 mm wide by 610 mm long, as shown in Figure 5.1(a). After their installation in the frame, sets of fibers were coated with the three initial resins (epoxy, polyester, and vinyl ester) using a fine-bristle paintbrush. The tows were then cured under ambient indoor conditions. Once these polymers set, the fibers were removed from the frame, visually inspected, and cut to the desired lengths. Figure 5.1(b) is an example of a set of coated carbon fibers, in this case, epoxy.

A forensic investigation of the coated fibers indicated several problems. The most significant problem was a lack of uniform coating. The thickness of the coating noticeably varied along the length of each fiber. In some instances, the fiber had from very little to no coating at all. When a portion of the tow containing excessive resin was flexed, it would fracture before reaching a 70° angle. When a portion of the fiber containing too little resin was flexed, it neither resisted bending nor returned to its original orientation. The coatings, particularly the epoxy, also showed signs of incomplete curing, often remaining slightly tacky to the touch.

Figure 5.2 is a cross-section of an epoxy-coated fiber at 400X magnification. The circles are the individual carbon filaments, and the jagged edge on the right side of the image is the boundary between the fiber coating and the slide mounting epoxy. The epoxy fiber coating dominates the cross-section, covering nearly 80%, and indicating an excessive amount of material. Excessive coating results in a very brittle material with little to no resiliency. While the carbon fibers are extremely supple, the epoxy coating is very rigid. Thus, maintaining a balanced carbon fiber to epoxy ratio is required to arrive at the necessary fiber resiliency. This finding occurred with both the polyester and the vinyl ester resins as well.

Based on these initial results, the viscosity of the resins was reduced, and the amount of catalyst was increased. Subsequent fibers possessed a more uniform coating

with only a slight amount of residual tackiness. This improved the resiliency of the fibers. The carbon fiber to resin ratio remained low, however, with the resin accounting for between 60% and 70% of the cross section. Urethane, silicone, and soy-based coatings also were developed, but with similar results. The resin application method appeared to be more critical than the resin type.

Carbon fiber fabric was also investigated as a potential material to provide fiber reinforcement for concrete. The initial product selected (Product C), shown in Figure 5.3, is a commercial grade, unidirectional, carbon fiber fabric. This fabric is characterized by longitudinal sections of 12K tow separated by a distance of approximately 1.5 mm. The fabric was stitched together with intermittent plastic thread.

The coating process for the carbon fabric was identical to that used for the carbon tow. To prepare the carbon fabric for coating, the 458 mm wide fabric was stretched between two sets of rollers and clamped into a wooden frame. Once secure, the fabric was wrapped with masking tape at locations slightly beyond the outside edges of the frame and cut to length. The fabric was then coated with the revised epoxy formulation using a fine bristle paintbrush. Only epoxy was applied because preliminary findings suggested the application method was more critical than the resin type. After curing under ambient conditions, the fabric was removed from the frame, visually inspected, separated into individual tows, and cut to the desired lengths.

A forensic investigation of the coated fabric fibers revealed an improved resin distribution. This result can most likely be attributed to the shape of the carbon fibers within the fabric, namely, their arrangement in a strip much wider than the thickness. This rectangular shape of the tow cross section resulted in a more uniform resin distribution. The resulting fabric fibers were substantially more resilient than the carbon tow fibers, although they would still snap if flexed in a tight radius. Cross sections of the fiber viewed at 400X magnification confirmed the relatively low carbon fiber-to-resin ratio. However, the fabric fiber cross section noticeably improved the fiber's behavior when compared with the individual tow fibers.

A balance exists between lubricity of the coated fiber to improve dispersibility and bonding of the coated fiber to the concrete matrix. A delicate balancing act also exists between pullout and breaking of the coated fibers when subjected to load. During

either a blast or impact, fibers absorb the greatest amount of energy during pullout. The amount of energy absorbed is directly related to the degree of bond created. If the bond is too weak, the fibers will pull out easily with little benefit to the concrete. If the bond is too strong, the fibers will fracture brittlely. Balance must be maintained in order to improve performance.

Epoxy, polyester, and vinyl ester coated fibers underwent comparative bond tests in a cementitious matrix. To reduce the number of variables, only the carbon fibers from Product A (fiber aspect ratio of 100) were used to examine each of these three resin types. To compare fibers, epoxy-coated Products B (fiber aspect ratio of 90) and C (fiber aspect ratios of 20 and 200) were also tested. Preparing the specimens involved casting an individual fiber within a cementitious grout. Grout was chosen over concrete in order to limit the variability caused by the addition of a coarse aggregate. The grout consisted of one part Portland cement and three parts fine aggregate (sand), with a water-to-cement ratio of 0.50. The plastic forms measured 50 mm in diameter, and the coated fibers were embedded to a depth of 50 mm. A frame maintained the fibers at both the correct depth and location within the grout as it cured.

All specimens were placed in a curing chamber for 28 days following casting. Both the test setup and a typical bond test specimen are displayed in Figure 5.4. All tests were performed on an Instron 4469 machine with a loading rate of 1.27 mm per minute. A neoprene pad placed between the top of the grout and the test fixture provided uniform bearing and reduced any bending of the strand. Based on recommendations from several fiber manufacturers, the strand was anchored to the test fixture with neoprene pads placed within the machine grips. Sandpaper glued to the inside face of the neoprene prevented the fibers from pulling out of the grip prematurely during the test. The bond test continued until the fiber either fractured or pulled out of the grout.

Test results are depicted in Table 5.2. The epoxy-coated strands registered the highest average bond strength, while the vinyl ester revealed the lowest. In fact, the vinyl ester had a tendency to debond from the carbon fiber during loading. This resulted in the fiber pulling out of the coating rather than the mortar. Bond strengths were also extremely low. In terms of types of failures, both the epoxy and polyester coatings

exhibited both fracture and pullout failures. The majority of these failures fell into the latter group.

In general, the bond test results exhibited significant variability, with coefficients of variation (COVs) near 50%. A significant part of this variability was the result of the coating process, which remained inconsistent. This fact is evident by comparing the epoxy-coated fibers from Products A and B with those from Product C. As previously discussed, the Product C fabric fibers revealed improved resin distribution compared to the carbon tow fibers. As a result, the Product C fibers were more consistent, with a COV of only 14.3%. The test setup also added to the variability, as it was particularly difficult to grip the fibers without them failing prematurely in the grips. Some of the tests had to be repeated because of the fibers slipping from the grips, while others had to be discounted because of premature failure within the grip region.

Nonetheless, the comparative bond test results provided much useful information. In general, the epoxy coating performed very well, followed closely by the polyester resin, while the vinyl ester performed very poorly. In terms of fiber type, the Product C fabric fibers performed exceptionally well in terms of both the average bond strength, 2242 versus 157 N, and the variability of test data, with a COV of only 14.3 %. This significantly higher bond strength is likely the result of more of the carbon filaments coming into contact with the mortar. The Product C fabric fibers had, overall, a very flat, rectangular cross-section, a result of them being constructed from a fabric rather than a tow. The difference in bond performance between the epoxy-coated versions of Products A and B is not statistically significant due to the high variability in the test results, meaning they performed equally.

Industrial Manufacturing Phase

The next step in the research study involved moving from the laboratory to a full-scale industrial production. This step was necessary for two reasons. First, laboratory production of coated carbon fibers could not, in a reasonable period of time, generate the quantity necessary for all of the testing involved in this research project. Second, in order to move effectively from the laboratory to large-scale production, the fibers that are tested must be produced through an actual industrial process.

Fabric Fiber: Fiber Type A

The first fiber developed for industrial production was based on the fabric fibers from Product C. This fabric-based fiber mapped well with the conclusions drawn from the preliminary coating design phase. Improving these fibers required a resin application method that would result in a more uniform polymer throughout both the fiber length and cross-section. Improvement also required a much higher carbon fiber-to-resin ratio. An epoxy-based resin was finally chosen as it offered the highest degree of bond strength. Also, in general, epoxies are stronger and more flexible than polyester resins.

Preimpregnated (prepreg) carbon fiber fabrics were chosen as a possible solution based on the conclusions drawn from the preliminary design phase. Prepreg fabrics are formed with the resin installed and are partially cured during the manufacturing phase. Thus, these fabrics have the added benefit of precise flow control during the impregnating process. When subsequently cured at elevated temperatures, the resin completes the thermosetting process. The thermoset polymer resin chosen was a controlled-flow, low-viscosity epoxy with a dynamic viscosity of 4500 centipoise. These characteristics result in precise control during the impregnating process. The mechanical properties of the prepreg carbon fiber can be found in Table 5.3.

A 3K, plain weave fabric manufactured from commercial grade carbon fiber was chosen for this study. The plain weave, formed by interlocking perpendicular tows, offers a greater stiffening effect than a unidirectional fabric, such as the Product C fabric used in the preliminary design phase. A 40% resin content offered the highest carbon fiber-to-resin ratio possible with the prepreg.

Initially, the 3K, plain weave fabric was cured for two hours at 177° C, the temperature recommended by the manufacture. In order to investigate both potential fiber aspect ratios and fiber volumes, the cured fabric was sectioned into different lengths and widths. These sizes measured 50 mm, 100 mm, and 150 mm in length and 6 mm, 9 mm, and 12 mm in width. A photograph of the fibers (Fiber Type A) is shown in Figure 5.5(a).

Twined Fiber: Fiber Type B

The second fiber developed for industrial production was based both on a carbon fiber tow and a unique manufacturing process. This manufacturing process involves a

twinning of the fiber. Thus, Fiber Type B consisted of a carbon fiber tow twined around a polypropylene fiber core. This core served as a stiff backbone to the fiber. During the manufacturing process, a light coating of thermally-activated epoxy was applied to the polypropylene. This was followed by a twinning of the carbon fiber around this core structure. A subsequent heat treatment process partially bonded the carbon fiber to the polypropylene. After curing, the fiber was sectioned to the desired lengths. Arriving at the necessary resiliency, however, also required a larger tow size. After several trial runs, a 48K tow was chosen to twine into fibers for testing rather than the 12K tow used during the preliminary coating design phase. The finished product is shown in Figure 5.5(b). The end result was a more traditional concrete fiber shape, although appreciably longer in length, with significantly improved resiliency.

Preliminary Concrete Mix Design

In general, adding fibers to concrete reduces the workability of the mixture. For the long carbon fibers developed in this research project, the effect was amplified significantly. The increased surface area of the fibers required significantly more paste than a standard concrete mix. There is a practical limit, however, on the amount of paste that can be used in a concrete mix, as excessive paste leads to increased shrinkage. In contrast, lower coarse aggregate content increases workability. The combination of increased paste content and decreased coarse aggregate content should result in a mix with sufficient workability for the long carbon fibers. Based on this information, the mix design was developed, and the proportions are shown in Table 5.4. Both the fresh and hardened property tests of this base (control) concrete mix (without any fibers) are presented in Table 5.5. The compressive and flexural strength values in Table 5.5 represent an average of three replicate specimens.

Optimization of Fiber Type A Mix

Fiber Type A, the fabric fiber alternative, offered one significant advantage over Fiber Type B. Fiber Type A could be tailored to this specific application by varying not only the fiber length and volume but also the aspect ratio. To investigate this potential, the cured fabric was cut into both lengths of 50 mm, 100 mm, and 150 mm and widths of

6 mm, 9 mm, and 12 mm. The following sections discuss both the testing performed on both fiber curing cycles (initial and final) and the resulting optimized Fiber Type A solution.

Initial Cure Fibers

The first variable investigated involved the fiber volume, or fiber fraction. This variable is calculated as the ratio of the volume of fibers to the total volume of the material, expressed as a percentage. The optimal solution would use the highest fiber volume possible that still allows the concrete to be placed and consolidated into a form containing conventional reinforcing steel. As previously noted, as the amount of fiber increases, the workability decreases.

A valuable test method to evaluate the workability of fiber-reinforced concrete is ASTM C995 (ASTM 2001). This test evaluates the time required for the fiber-concrete sample to flow out of an inverted traditional slump cone after placing a standard vibrator into the mix. Using a constant fiber dimension, 100×6 mm, the fiber percentage was varied and the ASTM flow cone test was performed. The results are shown in Figure 5.6(a). As expected, as the fiber percentage increased, the flow time increased. This rate of increase was approximately 10 seconds for each 0.5% of additional fibers.

A series of flexural strength tests were also performed on the fiber reinforced concrete. This concrete contained identical fiber sizes (100×6 mm) though the fiber percentages varied. The test procedure followed ASTM C78/C78M (ASTM 2010). The beams measured 150×150×600 mm with a span length of 450 mm. Test results are shown in Figure 5.6(b). As expected, as the fiber percentage increased, the flexural strength increased. The flexural strength peaked, however, at a fiber volume of 1.5%. This peak was most likely due to either the fibers beginning to interfere with each other at the higher percentage, or the fact that the number of fibers crossing the critical stress region did not increase between 1.5 and 2% due to the inherent random distribution of the fibers in the concrete.

A series of flexural performance tests were performed in accordance with ASTM C1609/C1609M (ASTM 2010). The beams measured 150×150×500 mm with a span length of 450 mm. Load and deflection data were collected electronically at a frequency

of 5 Hz. These beams contained identical fiber sizes (100×6 mm) with three fiber volume contents (1%, 1.5%, and 2%). Three specimens were tested in each series. Net deflection values, for both data acquisition and rate control, were obtained at the mid-span and mid-height of the beams (see Figure 5.7). The effect of fiber volume on energy absorption was calculated using toughness values (T_{150}^{D}), defined as the area under the load-deflection curve up to a net deflection of 1/150 of the span length (see Table 5.6). Specimens with 1.5% fiber showed higher energy absorption capacity (toughness) than 1% fiber. Toughness of specimens was almost the same for 1.5% and 2% fibers.

Based on the combination of workability, flexural strength, and toughness, a fiber volume of 1.5% was chosen for subsequent testing on both fiber dimensions and aspect ratios. The 1.5% fiber volume resulted in the highest flexural strength and toughness as well as producing a reasonable level of workability.

The second variable investigated involved both the fiber dimensions and the aspect ratios. To study this effect, the fiber dimensions were varied. In addition, both the flow rate and the flexural strength were evaluated at a constant fiber volume of 1.5%. As previously mentioned, the key to optimizing the fiber dimensions is choosing a balance between workability and strength. In terms of workability, the results indicated that a considerable variation in flow time occurred, ranging from 11.6 seconds to 30 seconds. These results also indicated that, for each fiber length, the highest aspect ratio (length/width) resulted in the lowest flow time (see Figure 5.8(a)). Flexural strength, however, showed a much smaller variation between the different fiber sizes, averaging 6.56 MPa with a COV of only 7.5%, as shown in Figure 5.8(b). The 100×6 fibers recorded the highest flexural strength, 7.29 MPa. They resulted, however, in a flow time nearly twice that of the 100×9 fibers. Those fibers had a flexural strength only 9% less than the 100×6 fibers. Based on these test results, the optimal solution for Fiber Type A was a 100×9 mm fiber at a dosage rate of 1.5% by volume.

Final Cure Fibers

Initial testing of fiber reinforced beams revealed the fibers' slightly brittle behavior. Thus, several alternative curing cycles were performed on the prepreg. 93° C for 45 minutes was eventually established. The result was a fiber with significantly

improved resiliency. The development of all subsequent fiber reinforced concrete utilized fibers from this alternative curing cycle.

Workability was controlled more by fiber volume and fiber dimensions, so the research team only tested the revised cure fibers for flexural strength. The results for fiber dimensions of 50×9, 100×9, 100×12, and 150×9 are displayed in Figure 5.9. This revised cure resulted in a fabric that was unable to be sectioned into 6 mm wide fibers with any degree of consistency. The plot in Figure 5.9 also contains the results for a control set of specimens containing no fibers. This value was added because the compressive strength of the concrete for these tests averaged 48.3 MPa when compared to 51 MPa for the specimens in the initial cure section.

These tests indicated that the 100×9 fibers demonstrated the highest flexural strength. Consequently, even with the alternative curing cycle, the optimal solution for Fiber Type A remained a 100×9 mm fiber at a dosage rate of 1.5% by volume. The resiliency of the fiber, however, improved significantly with the new curing cycle.

Optimization of Fiber Type B Mix

Fiber Type B, the traditional fiber, could be tailored to the specific application by varying both the fiber length and volume. To investigate this potential, the twined carbon fiber was sectioned into lengths of 50 mm, 100 mm, and 150 mm. Preliminary concrete mix tests indicated that the 50 mm fibers did not disperse uniformly throughout the concrete. These fibers were too light to mix uniformly with the other constituents and tended to form into bunches within the samples. The 100 mm and 150 mm fibers did mix well, distributing in a fairly random and uniform manner. The 150 mm fibers did not mix well, however, with samples that contained a 150×150 mm reinforcement mesh. The 150 mm long fibers tended to wrap around the reinforcement at several locations, while the 100 mm long fibers did not. As a result of these mix tests, the 100 mm long fiber was chosen for subsequent testing.

The next variable investigated involved the fiber volume. With a fiber length of 100 mm, the fiber percentage was varied and the ASTM flow cone test was performed at fiber volumes of 1%, 1.5%, and 2%. Unfortunately, Fiber Type B had a more pronounced effect on workability than Fiber Type A. At a fiber volume dosage of 2%, the flow cone

test could not be completed on the fiber concrete. Consequently, a fiber volume dosage rate of 1.25% was also tested. The results for the flow cone tests are presented in Figure 9.10(a). As expected, as the fiber percentage increased, the flow time increased. Unexpectedly, however, the time increased exponentially, indicating a substantial effect of increased fiber volume on workability.

A series of flexural strength tests based on ASTM C78/C78M (ASTM 2010) were also performed on fiber reinforced concrete containing 100 mm long fibers at fiber volumes of 1%, 1.25%, and 1.5%. The results are shown in Figure 9.10(b). The results, however, did not follow the expected outcome of increased strength for increased fiber percentage. Rather, these results were very nearly identical for each fiber volume, differing by less than 5%. This indicated no additional benefit in terms of flexural strength beyond 1% fiber volume.

A series of flexural performance tests based on ASTM C1609/C1609M (ASTM 2010) were performed on fiber reinforced concrete containing 100 mm long fibers at volumes of 1%, 1.25%, and 1.5%. The results are shown in Figure 5.11 and Table 5.6. In comparing the toughness values, the 1% and 1.25% fiber fractions were nearly identical, with the 1.5% dosage experiencing a lower value most likely due to the significantly decreased workability of that mix and difficulty in forming the specimens. Also, the toughness of Fiber Type B was considerably higher than Fiber Type A.

Based on the combination of workability, flexural strength, and toughness, a fiber length of 100 mm and fiber volume of 1% was chosen for subsequent testing.

Application Examples of LCFRC

The purpose of this task was to evaluate both the spalling, or secondary fragmentation resistance, and the overall dynamic resistance of LCFRC as compared to conventional reinforced concrete (Gliha 2011). These applications were tested in two parts: impact tests and blast tests.

Impact Tests

The drop weight impact tests included a total of eight specimens, each measuring 1220 mm×1220 mm in plan, with a thickness of 50 mm, and simply supported on all four

sides. The specimens included two plain concrete panels (PC) (i.e., no reinforcement or fibers), two panels reinforced with 152×152 – MW9×MW9 welded wire reinforcing (WWR) placed at mid-depth, two panels reinforced with 100×9 mm Fiber Type A (LCFRC-A) at a dosage rate of 1.5% by volume, and two panels reinforced with 100 mm long Fiber Type B (LCFRC-B) at a dosage rate of 1% by volume. The plain concrete and WWR reinforced panels served as comparison panels.

The test protocol involved dropping a 22.7 kg guided steel cylinder from increasing heights until the specimen failed. Each series of test began with a drop height of 75 mm. The drop height increased by 75 mm for subsequent drops until a drop height of 600 mm was reached. From 600 mm until failure, the drop height increased by 150 mm each time. Both the height at which cracking first occurred and the height at which failure occurred were recorded (Tabatabaei et al. 2012).

Panels were compared with each other in terms of first visible cracking, failure height, and failure morphology. The results of the impact testing are summarized in Table 5.7. Although the LCFRC exhibited a higher average cracking height, the WWR panels outperformed the LCFRC in failure height. As expected, the plain concrete panels did not exhibit any visual cracking prior to failure. The LCFRC panels clearly outperformed the plain concrete panels, with the former panels failing at over four times the height of the latter. Figure 5.12 reveals the failure morphology for each panel type. The plain concrete panels failed with four relatively straight cracks emanating from the sides, while the cracking pattern for the fiber panels was much more tortuous, which resulted in more energy absorption and thus higher capacity.

Although the WWR panels failed at a greater height than the LCFRC panels, they displayed significantly more damage, both in terms of spalling and the extent of cracking. The noticeably improved behavior of the LCFRC panels over the WWR panels can be attributed to the increased amount of energy that the fibers absorbed during impact, through pullout, and the ability of the fibers to maintain post-cracking continuity. Both of these attributes should significantly improve the blast resistance of the LCFRC. The results of the impact tests suggested that a hybrid system that utilized both long carbon fibers and mild reinforcement would provide the highest degree of failure and spalling resistance.

Blast Tests

The blast tests included a total of seven specimens, each measuring 1830 mm×1830 mm in plan, with a thickness of 165 mm, and simply supported on all four sides. The specimens included three panels with steel reinforcement alone, two panels with steel reinforcement and 100×9 mm Fiber Type A at a dosage rate of 1.5% by volume, and two panels with steel reinforcement and 100 mm long Fiber Type B at a dosage rate of 1% by volume. The panels without carbon fibers served as comparison panels. All seven specimens contained the exact same steel reinforcement layout, the design of which was based on UFC 3-340-02 (2008). Flexural reinforcement consisted of top and bottom mats of #13 bars spaced at 152 mm on center. Due to the lack of distance to develop the bottom reinforcing steel for flexure, 180-degree hooks were required. For shear, #10 bars were placed at every other intersection of the mat #13 bars, with the top having a 135-degree bend and the bottom having a 90-degree bend.

The test protocol involved exposure to a charge of 38.6 kg of ammonium nitrate/fuel oil (ANFO) and boosters, corresponding to a net equivalent weight (NEW) of 34 kg of TNT (TNT equivalent weight factor 0.83 (BEC, 1978), at a stand-off distance of 1700 mm above the center of the panel. Pressure sensors were placed 7600 mm from the charge to determine the free-field pressure and to verify the complete detonation of the explosives.

The performance of the panels was evaluated through both physical measurements and visual observations. The data recorded for each test included the panel weights both before and after each blast test, in addition to permanent deformation. Both the weight loss and permanent deformation were used to quantify the amount of damage during the blast. Table 5.8 contains these physical data measurements. The permanent deformation of Control Panel No. 3 (CP-3) could not be measured reliably due to the extensive damage experienced by this panel.

In terms of the amount of material lost during the blast, the fiber concrete composite panels outperformed the non-fiber concrete panel (control) by a factor of nearly 10. This significant reduction in weight loss for the fiber concrete composite panels translates into a substantial decrease in harmful, flying debris during a blast event.

Visual observations of the panels confirmed the superior performance of the fiber concrete composite panels. Figure 5.13(a) reveals the extensive damage experienced by the control panel. The top face of the panel displays the traditional X-shaped yield line pattern consistent with exposure of a concrete panel to a blast wave and supported on four sides. Sufficient damage was done to the top face to expose the top layer of steel reinforcement in some areas. Figure 5.13(b) reveals the damage experienced by the Fiber Type A panel. The top face of the panel experienced significantly less damage than the control panel. There are carbon fibers exposed, but that is primarily a result of the small amount of concrete paste that was bonded to the top of the fibers that cracked off during the blast. There is also a very small amount of concrete (concrete paste plus aggregate) that spalled off the top face of the panel. Also, the yield line pattern can be seen, but the full "X," as displayed on the top face of the control panel, did not fully develop on the top face of this panel. In other words, there was significantly less cracking in this panel as compared to the control panel. Approximately 44 full squares of reinforcement were exposed by the blast on the bottom face of the control panel as compared to approximately 11 on the fiber panel. This represents a 75% reduction in the amount of large projectiles produced by the blast.

The Fiber Type B panels performed slightly better than the Fiber Type A panels, and thus significantly better than the control panel. As revealed in Figure 13(c), the Fiber Type B panels showed slightly less spalling and degree of cracking as compared to the Fiber Type A panels. As with the Fiber Type A panels, the Fiber Type B panels performed exceptionally under the blast loading as compared to the control panel.

Conclusions

The present experimental analysis was conducted in order to develop coatings that would allow the use of long carbon fibers within conventional reinforced concrete. Based on the results of this research study, the following conclusions and recommendations are presented:

- For Fiber Type A, the optimal application is a 100×9 mm fiber at a dosage rate of 1.5% by volume, using the curing cycle of 93° C for 45 minutes.

For Fiber Type B, the optimal application is a 100 mm long fiber at a dosage rate of 1% by volume.

- For Fiber Type A, the 3K, plain weave, 40% epoxy prepreg will significantly improve the spalling resistance of conventional reinforced concrete. Fiber Type A is easier to place and consolidate than Fiber Type B but is considerably more expensive (approximately 3 times).
- For Fiber Type B, the twined, 48K, polypropylene backbone carbon fiber offers the most cost effective method for significantly improving the spalling resistance of conventional reinforced concrete. Fiber Type B can be modified from its current configuration in order to markedly improve both its workability and its consolidation performance. Preliminary testing indicates that potential modifications include tighter windings and/or the application of an epoxy or other polymer at the cut ends to maintain the integrity of the individual fibers during the harsh concrete mixing and placing operations.

Acknowledgements

The authors gratefully acknowledge the financial support provided by both the U.S. Army Research Lab (ARL) and the Leonard Wood Institute (LWI) under Award Nos. W911NF-07-2-0062 and LWI-191-028, respectively. The conclusions and opinions expressed in this paper are those of the authors and do not necessarily reflect the official views or policies of either ARL or LWI. The authors are also grateful for the ideas and assistance of Drs. Eric Musselman and Andrea Schokker, University of Minnesota Duluth, and Mr. Michael Koenigstein, Pro-Perma Engineered Coatings.

References

[1] ACI Committee 544 (2001). Report on fiber reinforced concrete, American Concrete Institute.

[2] ASTM C 995 "Test Method for Time of Flow of Fiber Reinforced Concrete through Inverted Slump Cone," 482–483, American Society for Testing and Materials, Philadelphia, PA, 2001.

[3] ASTM C 78/C 78M, "Standard Test Method for Flexural Strength of Concrete (Using Simple Beam with Third Point Loading)," American Society for Testing and Materials, Philadelphia, PA, 2010.

[4] ASTM C1609/C1609M, "Standard Test Method for Flexural Performance of Fiber-Reinforced Concrete (Using Beam With Third-Point Loading)," American Society for Testing and Materials, PA, 2010.

[5] BEC, "Department of Defense Explosives Safety Board Blast Effects Computer," GPO, 1978.

[6] Gliha, B. , "Long Carbon Fiber Reinforced Concrete for Impact and Blast Protection," M.S. thesis, Missouri University of Science and Technology, Rolla, MO, 2011.

[7] Luo, X., Sun, W., and Chan, S. Y. N., "Characteristics of High-Performance Steel Fiber-Reinforced Concrete Subject to High Velocity Impact," *Cement and Concrete Research*, 30(6), 907-914, 2000.

[8] Malvar, L. J., "Review of Static and Dynamic Properties of Steel Reinforcing Bars," *Materials Journal*, 95(5), 609-616, 1998.

[9] Musselman, E., "Characterizing Blast and Impact Resistance of Long Carbon Fiber Reinforced Concrete," Ph.D. Dissertation, The Pennsylvania State University, State College, PA, 2007.

[10] Ogden, J. H., "Concrete Reinforced with Acrylic Coated Carbon Fibers," 2008.

[11] Rosato, D. V., Rosato, D.V., and Rosato, M. V., "Plastic Product Material and Process Selection Handbook," Elsevier, 2004.

[12] Suaris, W., and Shah, S. P., "Strain-Rate Effects in Fiber-Reinforced Concrete Subjected to Impact and Impulsive Loading," *Composites*, 13(2), 153-159, 1982.

[13] Tabatabaei, Z. S., Volz, J.S., Gliha, B. P., and Keener, D. I., "Experimental and Numerical Analyses of Long Carbon Fiber-Reinforced Concrete Panels Exposed to Blast Loading," *Int J Impact Eng,* in press, 2012.

[14] UFC 3-340-02, "Structures to Resist the Effects of Accidental Explosions," UFC 3-340-02, Washington, DC, 2008.

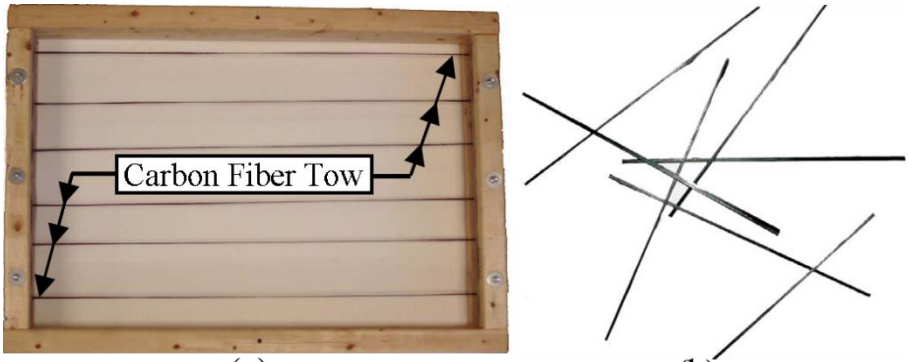

Figure 1. (a) Frame for Securing Carbon Fiber Tow Prior to Coating (b) and Wet Layup Epoxy Coated Fibers

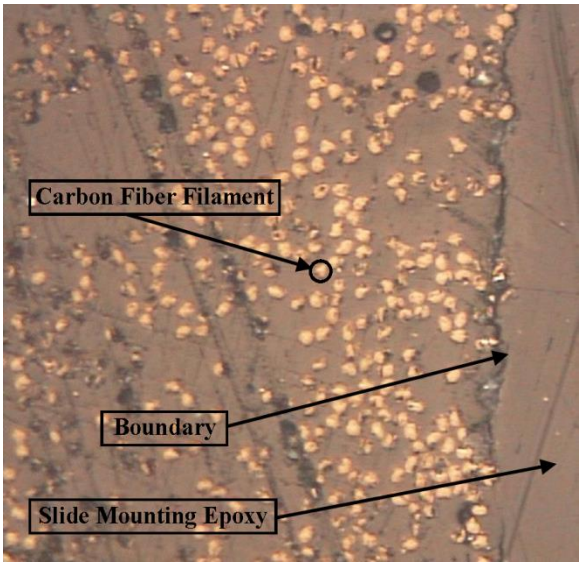

Figure 2. Epoxy-Coated Carbon Fiber Cross-Section at 400X Magnification

Figure 3. Unidirectional Carbon Fiber Fabric (Product C)

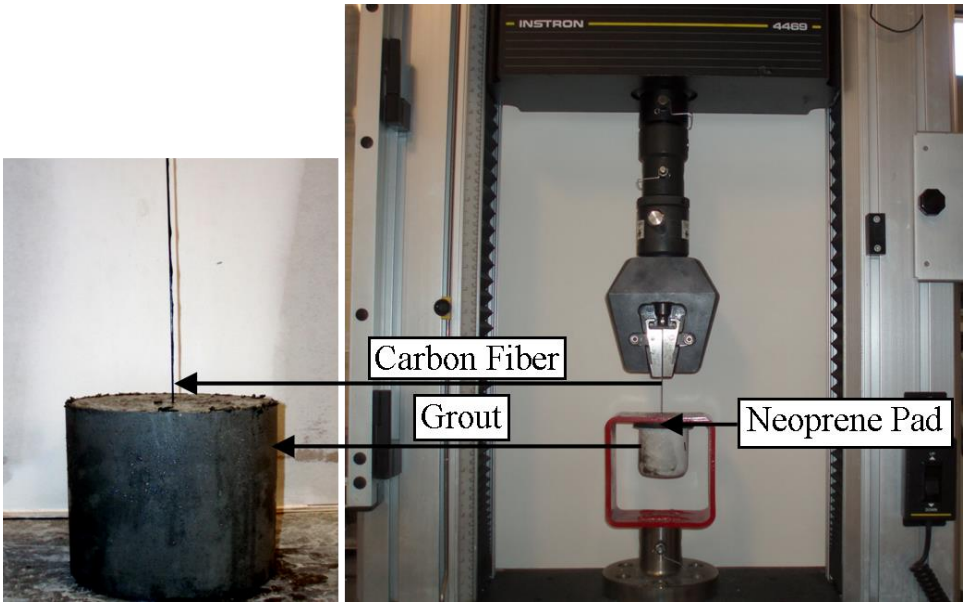

Figure 4. Bond Test Setup

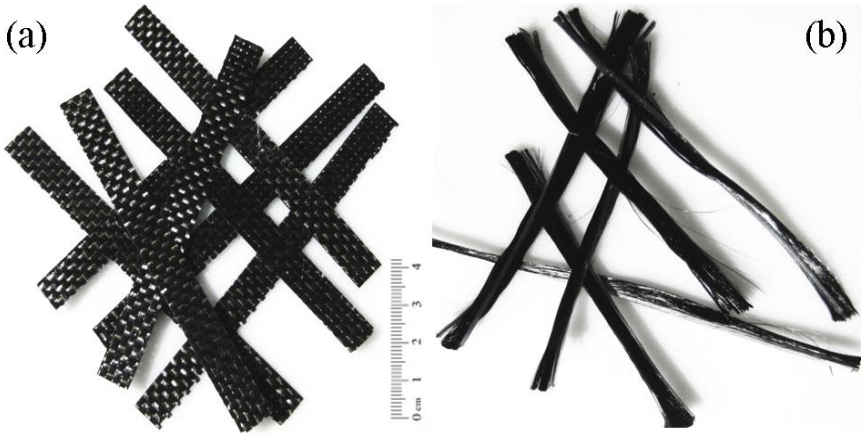

Figure 5. (a) Fiber Type A, (b) Fiber Type B

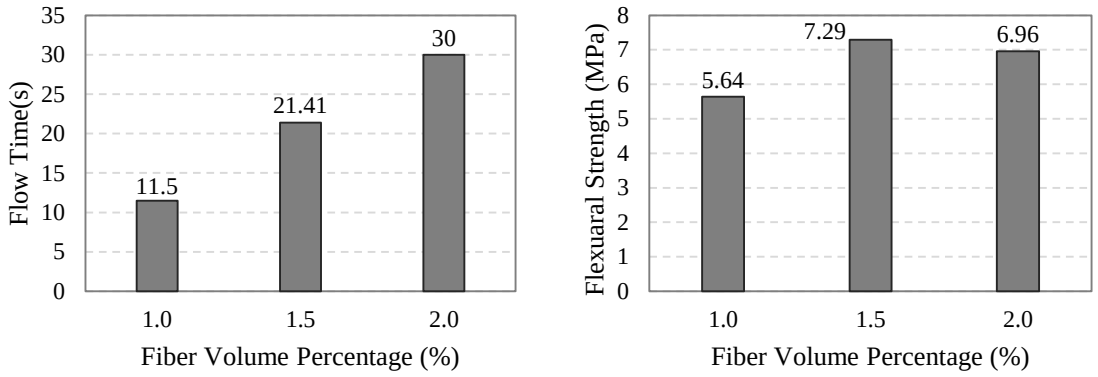

(a) (b)

Figure 6. Fiber Type A (100×6 mm); (A) Flow Cone Test Results, (B) Flexural Strength Test Results

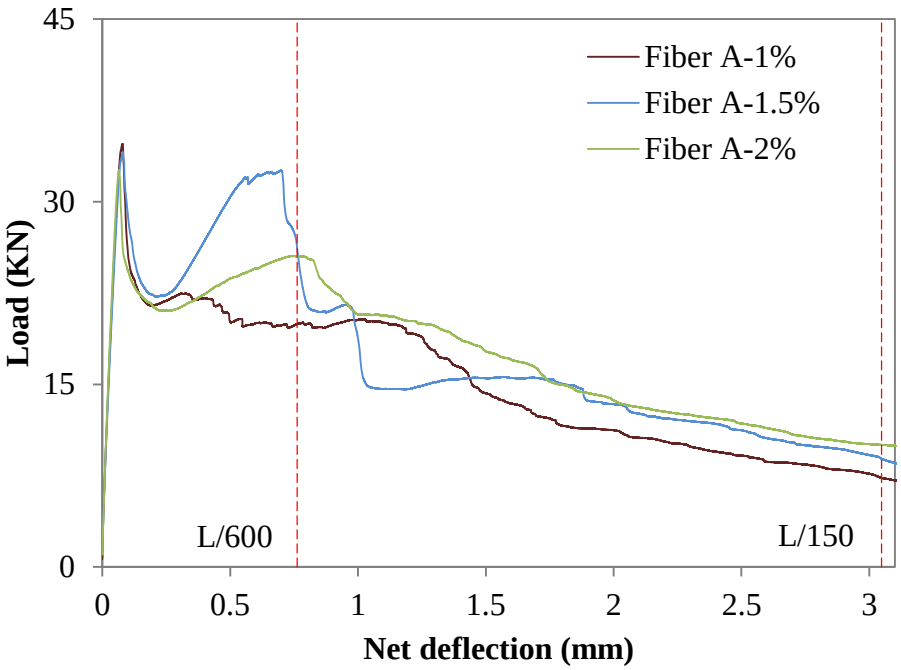

Figure 7. Load-Deflection Response Curves of LCFRC-Fiber Type A

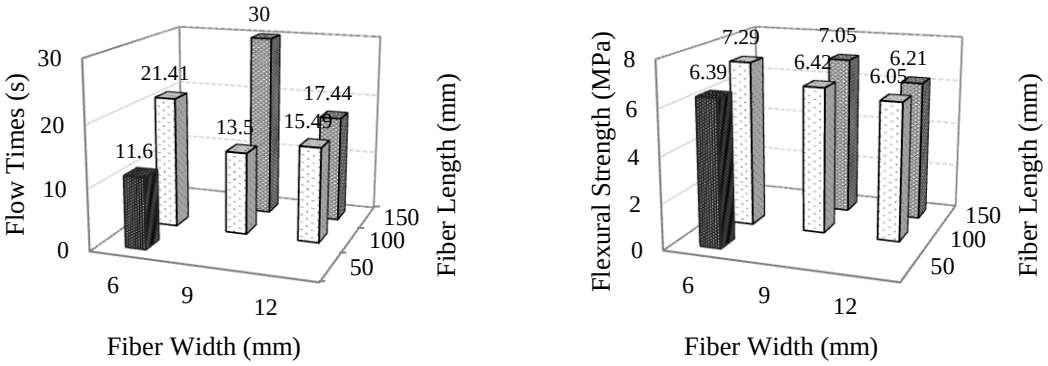

(a) (b)

Figure 8. Fiber Type A (1.5% Fiber Volume); (a) Flow Cone Test Results, (b) Flexural Strength Test Results

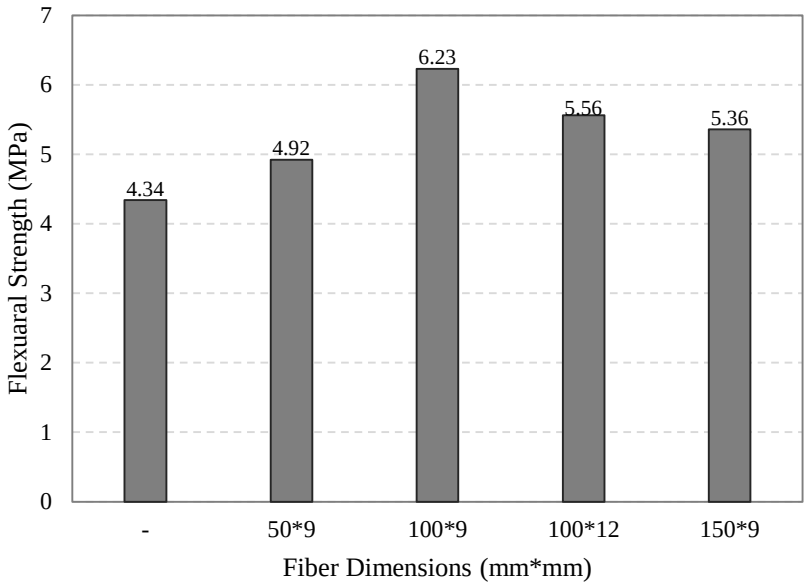

Figure 9. Flexural Strength Test Results for Fiber Type A, Modified Cure

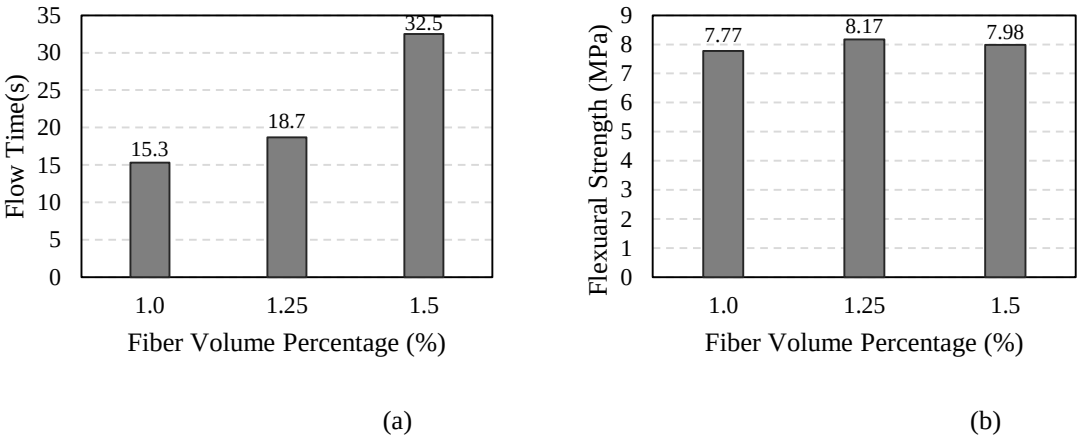

(a) (b)

Figure 10. Fiber Type B (100-mm-long); (a) Flow Cone Test Results, (b) Flexural Strength Test Results

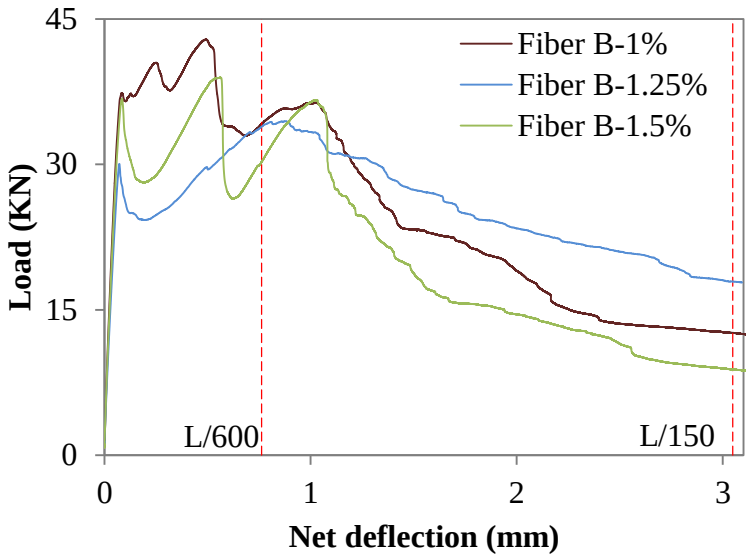

Figure 11. Load-Deflection Response Curves of LCFRC-Fiber Type B

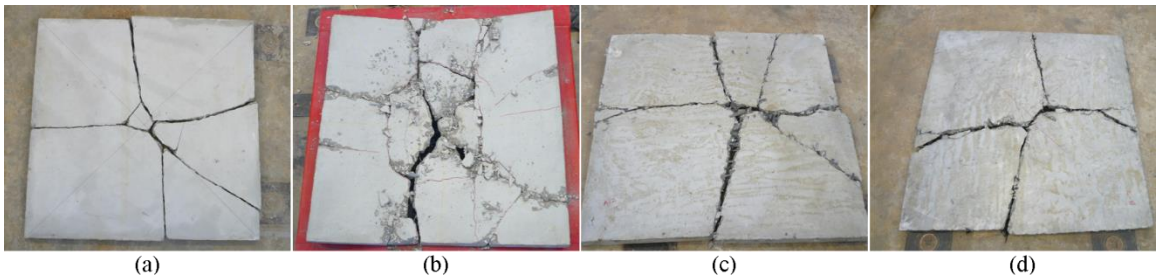

Figure 12. Crack Patterns in all the Panels; (a) Plain Concrete Panel, (b) Welded Wire Reinforced Panel, (c) Panel with Carbon Fiber Type A, (d) Panel with Carbon Fiber Type B

Figure 13. Failure Pattern of Panels after Blast: (a) Welded Wire Reinforced Concrete Panel, (b) Panel with Long Carbon Fiber Type A, (c) Panel with Long Carbon Fiber Type B

Table 1. Typical Fiber Properties for Products A and B

Typical Fiber Properties	Units	Product A	Product B
Tensile Strength	GPa	3.75	4.39
Tensile Modulus	GPa	231	231
Ultimate Elongation		1.60%	1.80%
Density	g/cm^3	1.76	1.78
Weight/Length*	g/m	0.792	0.8
Approximate Yield*	m/g	1.26	1.25
Filament Diameter	microns	7	6.9
Carbon Content		92%	94%

* (For 12 K) K refers to 1000s of filaments in a strand

Table 2. Comparative Bond Test Results

Fiber Type	Coating Type	Carbon Fiber Bond Strength (N)			Failure Mode
		Test Value	Average	COV	Fracture (F), Pullout (P)
Product A	Epoxy	1446	925	48.70%	F
		658			P
		672			P
	Polyester	867	784	41.30%	P
		1059			F
		427			P
	Vinyl Ester	142	157	98.90%	P
		142			P
		40			P
		418			P
		40			P
Product B	Epoxy	1032	704	51.30%	P
		418			P
		325			P
		516			F
		254			P
		996			F
		947			P
		1148			F
Product C	Epoxy	1913	2242	14.30%	P
		2553			F
		2260			P

Table 3. Mechanical Properties of Preimpregnated Carbon Fiber

Mechanical Properties	Strength (MPa)	Modulus (GPa)
Tensile	703-786	59.9-62.0
Compressive	751-820	55.1-57.9

Table 4. Fresh and Hardened Properties of Concrete Mix

Property	Test Result
Slump (mm)	230
Density (kg/m^3)	2291
Compressive Strength (MPa)	51
Flexural Strength (MPa)	5.5

Table 5. Concrete Mixture Designs

Material	Concrete Mixture (kg/m^3)
Portland Cement (Type I)	605
Fine Aggregate [a]	783
Coarse Aggregate [a,c]	783
Water	230
Water Reducing Admixture[b]	32.5 milliliters per 45 kg of cement

[a] Weights at saturated surface dry (SSD) condition

[b] High range water reducer (HRWR) was Gelenium 3030

[c] 19 mm maximum aggregate size

Table 6. Average Response Quantities for Flexural Behavior of LCFRC

	Peak load (KN)	Toughness (N-m)
Fiber A-1%	34.7	45.9
Fiber A-1.5%	32.6	52.2
Fiber A-2%	34	53
Fiber B-1%	42.8	76.5
Fiber B-1.25%	34.5	78.4
Fiber B-1.5%	38.1	64

Table 7. Drop-Weight Impact Test Results

IDs	Cracking Height (mm)	Failure Height (mm)
PC No.1	381	381
PC No.2	457	457
WWR No.1	610	3353
WWR No.2	457	3048
LCFRC-A - 1	610	1981
LCFRC-A - 2	610	1981
LCFRC-B - 1	610	1981
LCFRC-B - 2	762	1676

Table 8. Physical Measurements of Blast Test Panels

IDs	Permanent Deformation (mm)	Weight (kg.)			Weight Loss
		Before	After	Loss	
CP-3	-	1417.5	1064	354	25%
LCFRC-A - 1	12.7	1417.5	1370	48	3%
LCFRC-A - 2	11.4	1428.8	1393	36	3%
LCFRC-B - 1	10.2	1428.8	1397	32	2%
LCFRC-B - 2	12.7	1415.2	1374	41	3%

APPENDIX B.
IMPACT TESTING RESULTS

This appendix includes the results of the impact test. For each specimen all of the force and displacement vs. time graphs were plotted for each drop height. The graphs start at the first drop height for each panel and continue up to the point at which the linear motion potentiometer was removed from underneath the panel.

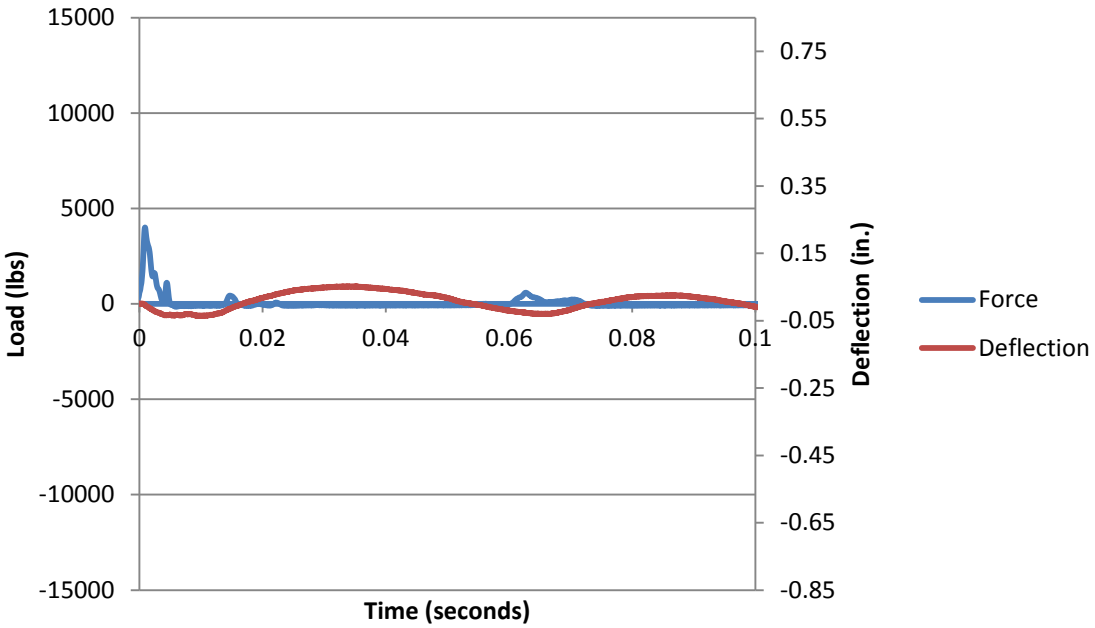

Figure B.1. Force and deflection vs. time for Plain Concrete 1 at 3 inches

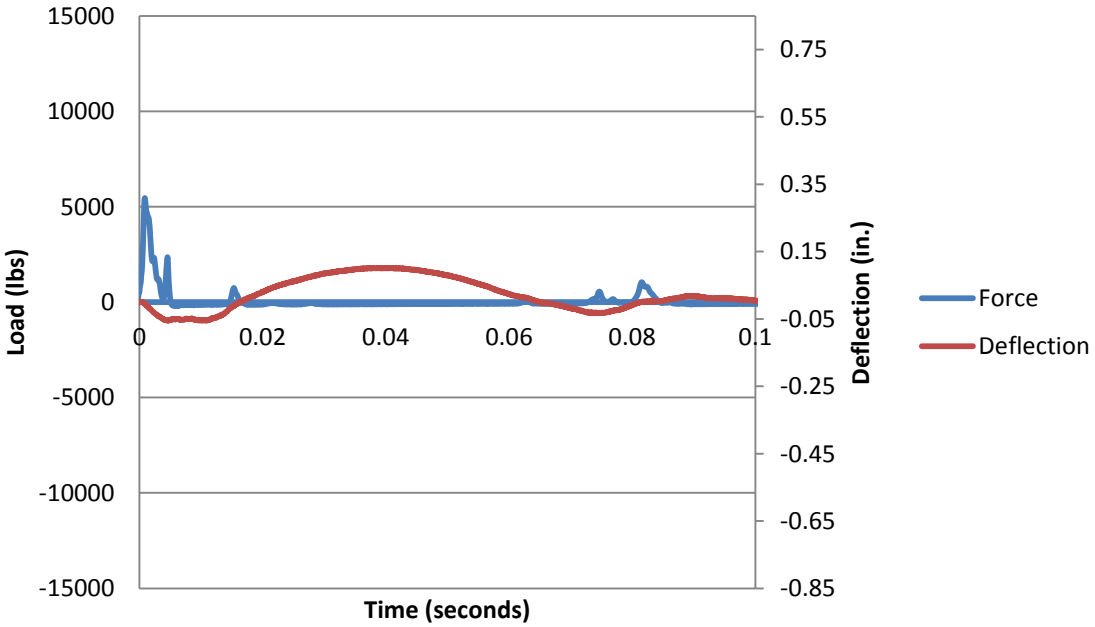

Figure B.2. Force and deflection vs. time for Plain Concrete 1 at 6 inches

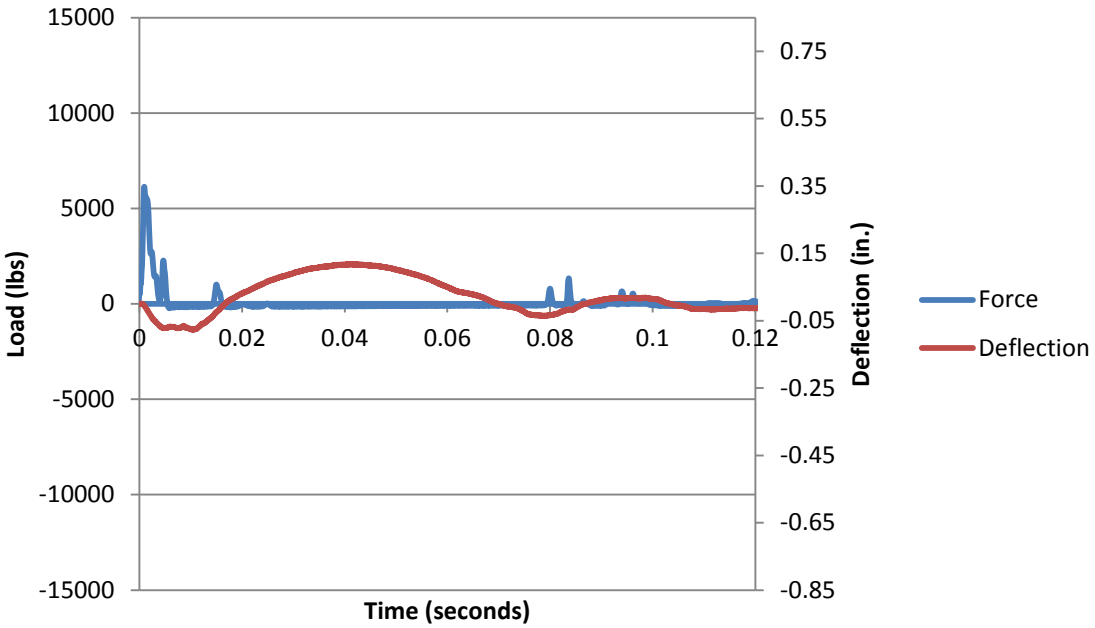

Figure B.3. Force and deflection vs. time for Plain Concrete 1 at 9 inches

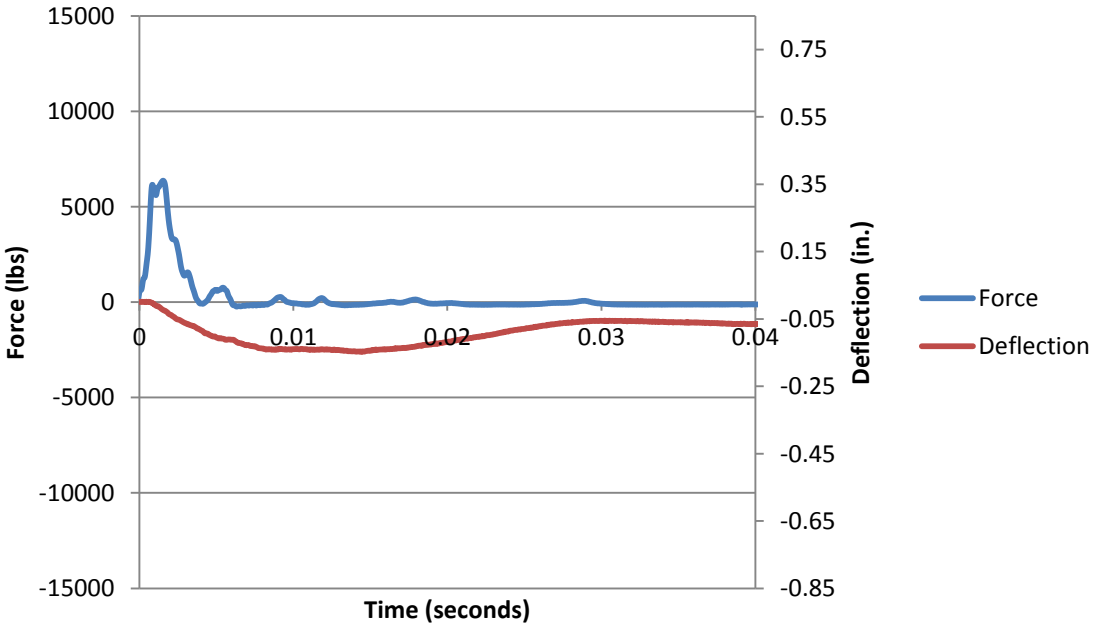

Figure B.4. Force and deflection vs. time for Plain Concrete 1 at 12 inches

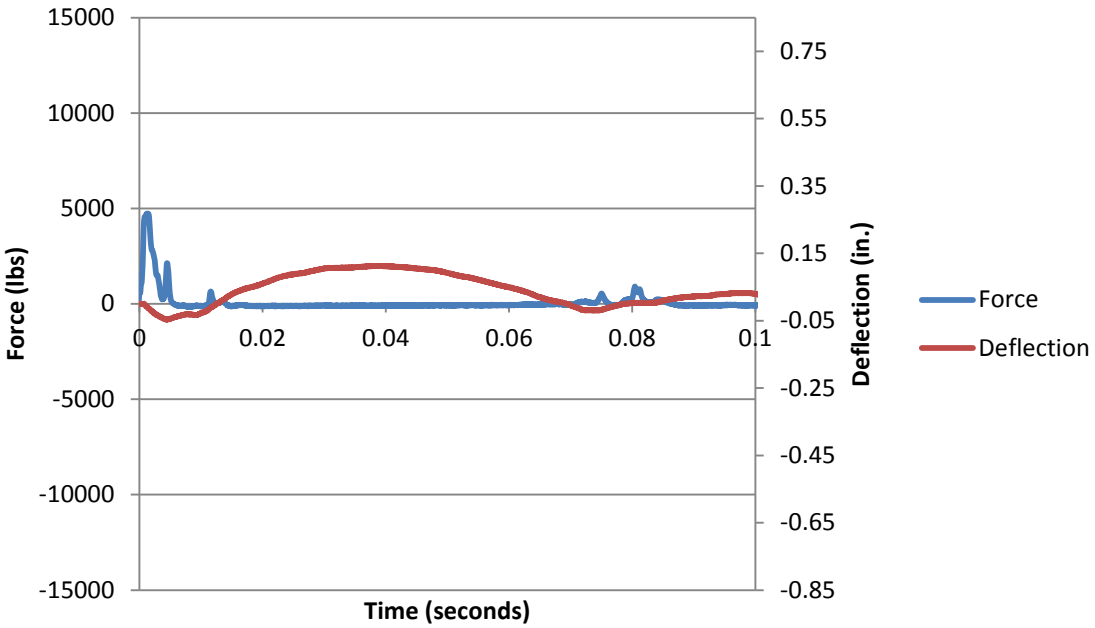

Figure B.5. Force and deflection vs. time for Plain Concrete 2 at 3 inches

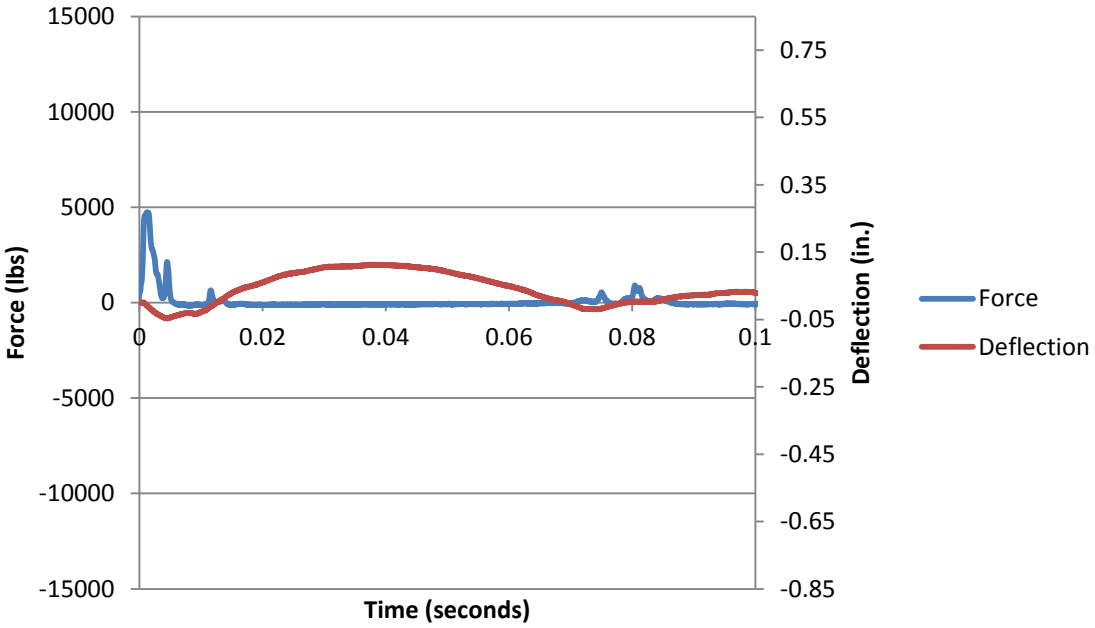

Figure B.6. Force and deflection vs. time for Plain Concrete 2 at 6 inches

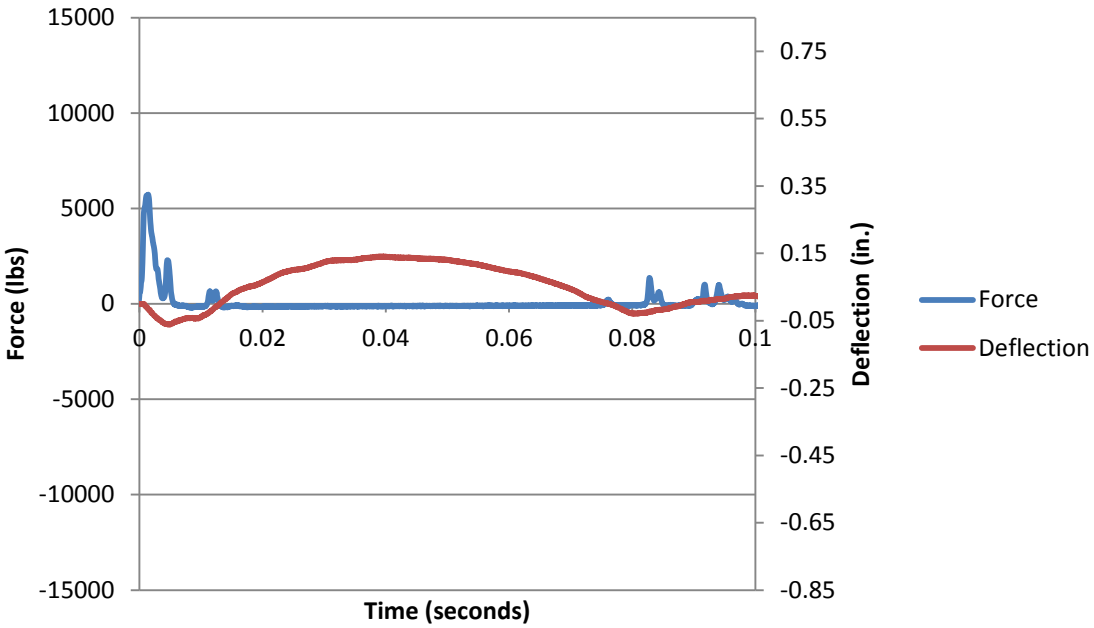

Figure B.7. Force and deflection vs. time for Plain Concrete 2 at 9 inches

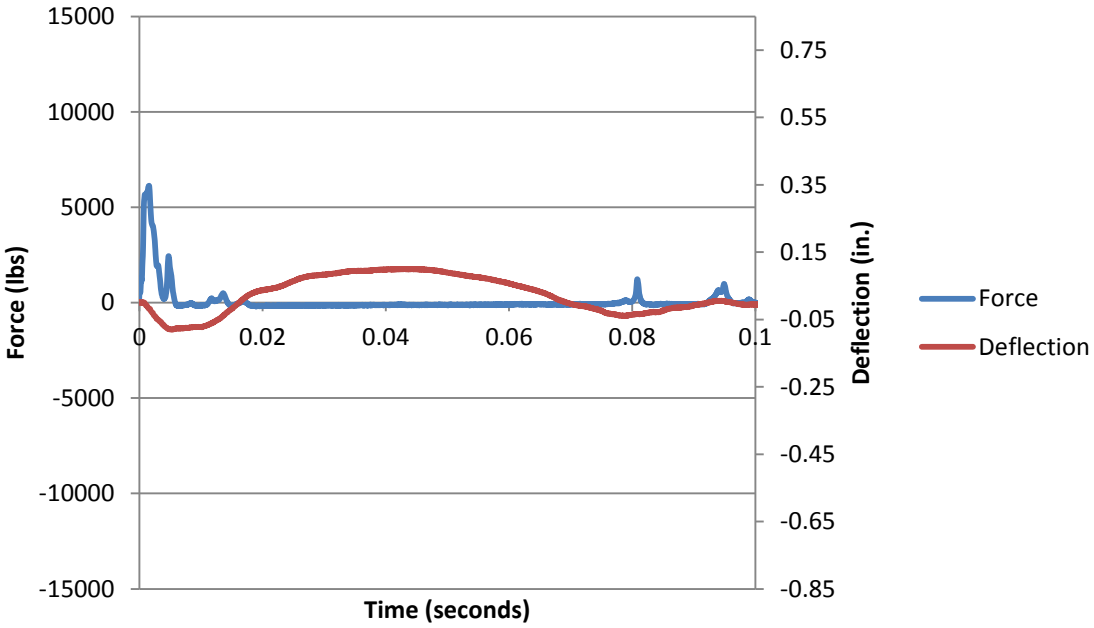

Figure B.8. Force and deflection vs. time for Plain Concrete 2 at 12 inches

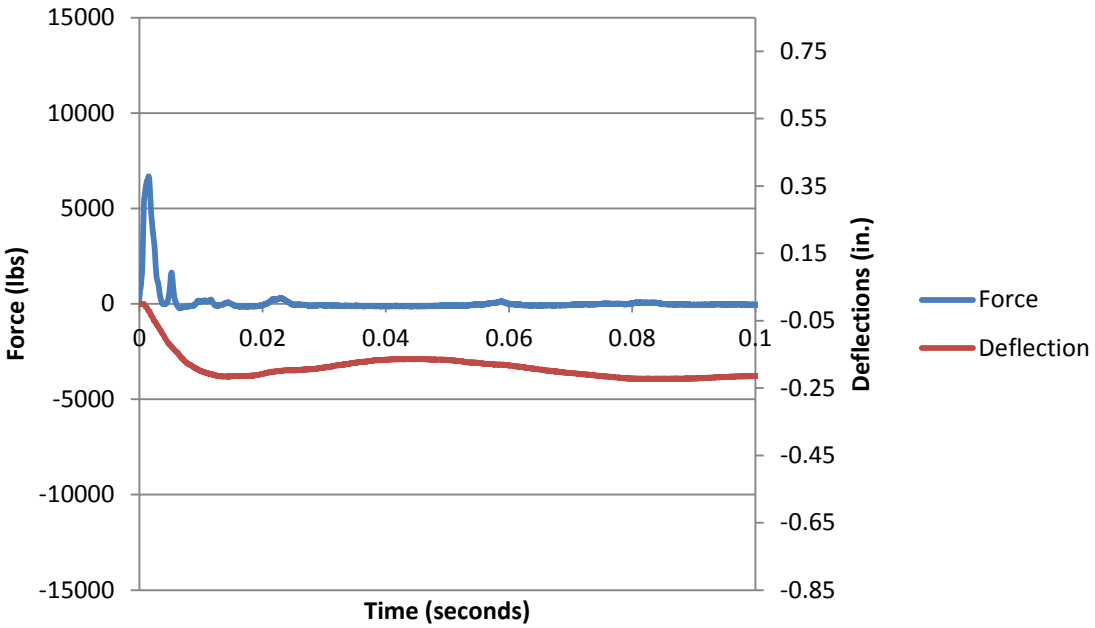

Figure B.9. Force and deflection vs. time for Plain Concrete 2 at 15 inches

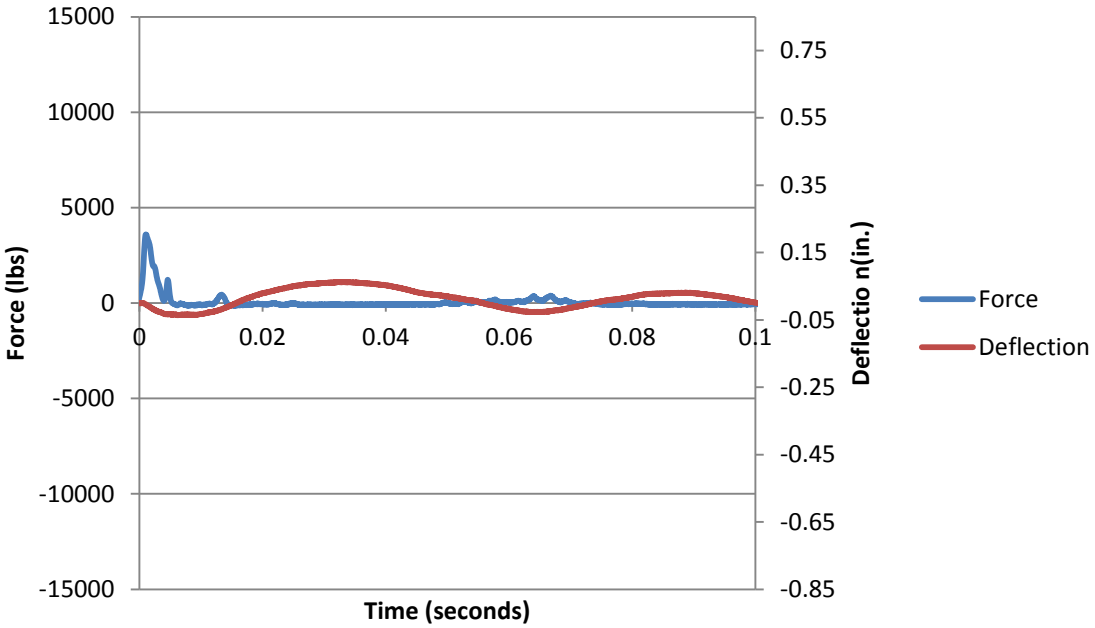

Figure B.10. Force and deflection vs. time for WWR 1 at 3 inches

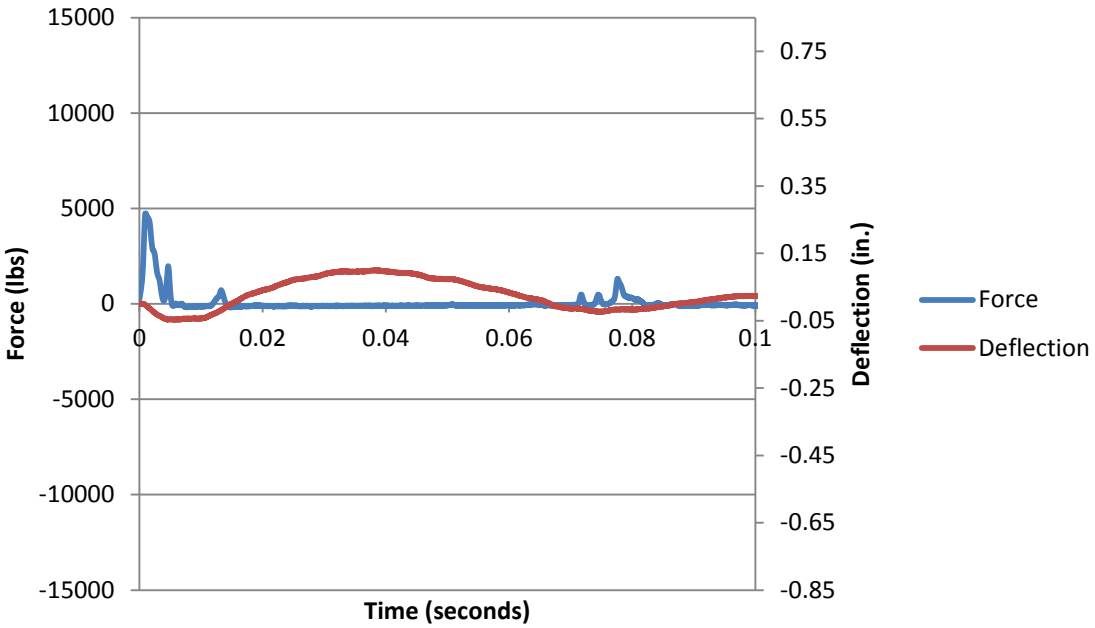

Figure B.11. Force and deflection vs. time for WWR 1 at 6 inches

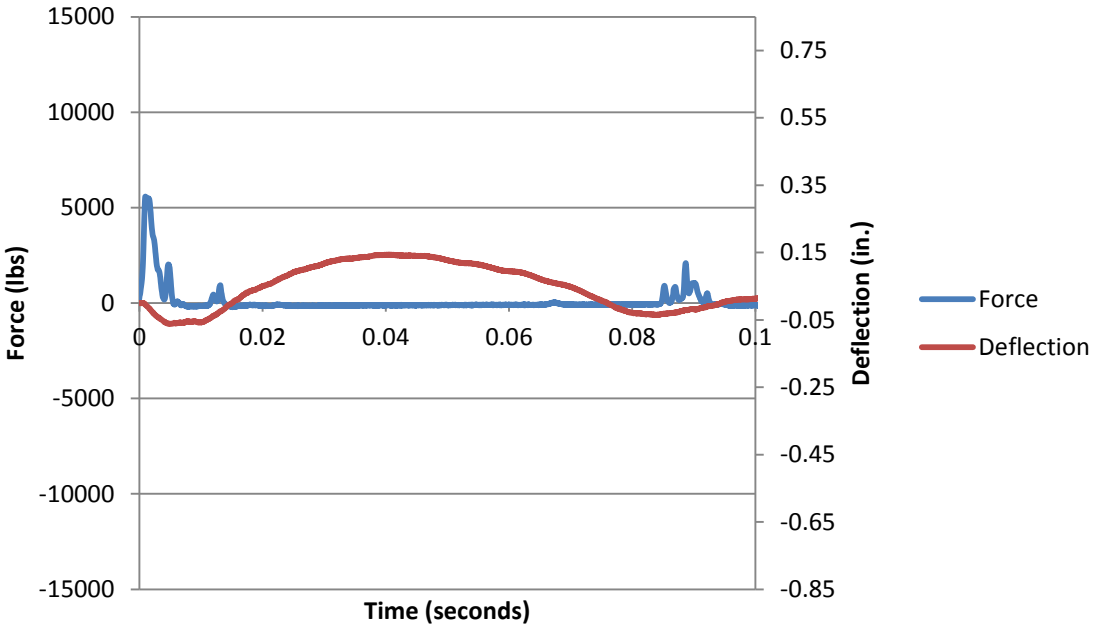

Figure B.12. Force and deflection vs. time for WWR 1 at 9 inches

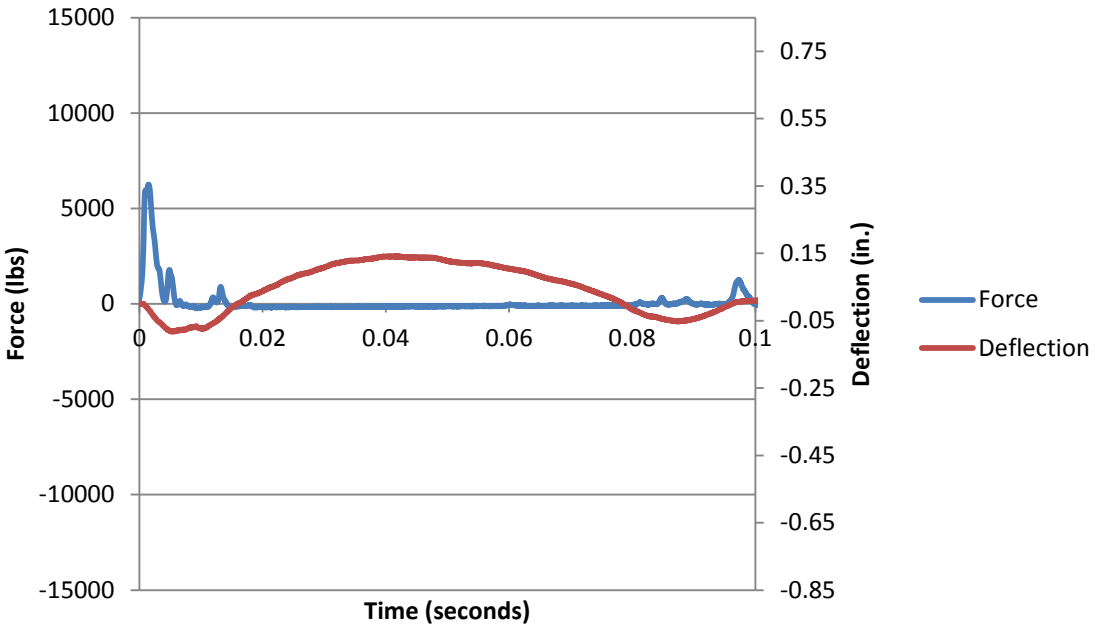

Figure B.13. Force and deflection vs. time for WWR 1 at 12 inches

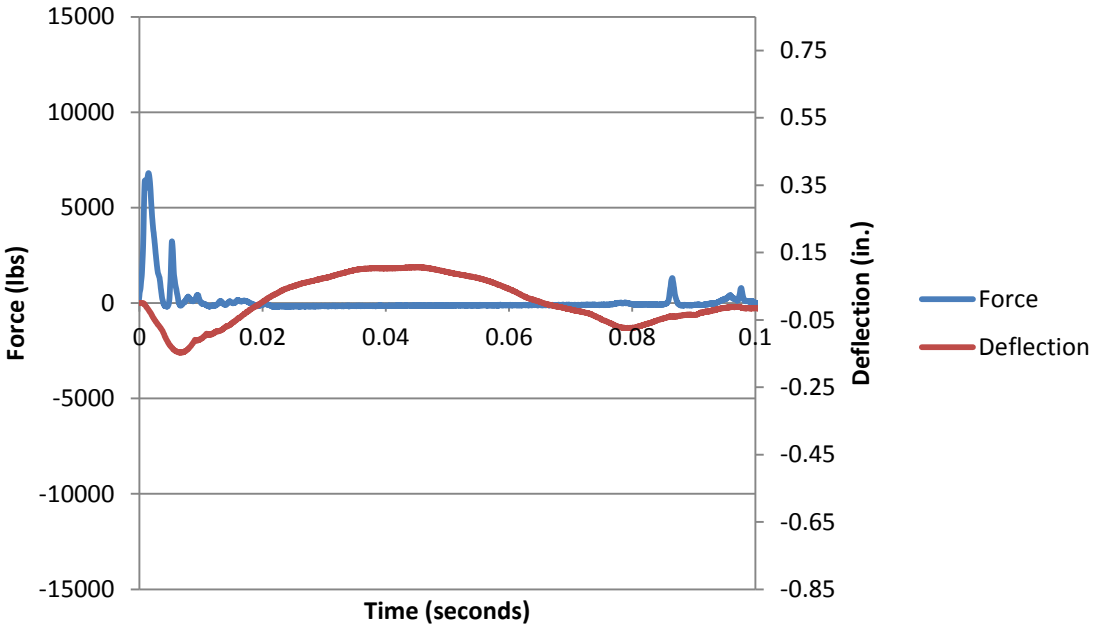

Figure B.14. Force and deflection vs. time for WWR 1 at 15 inches

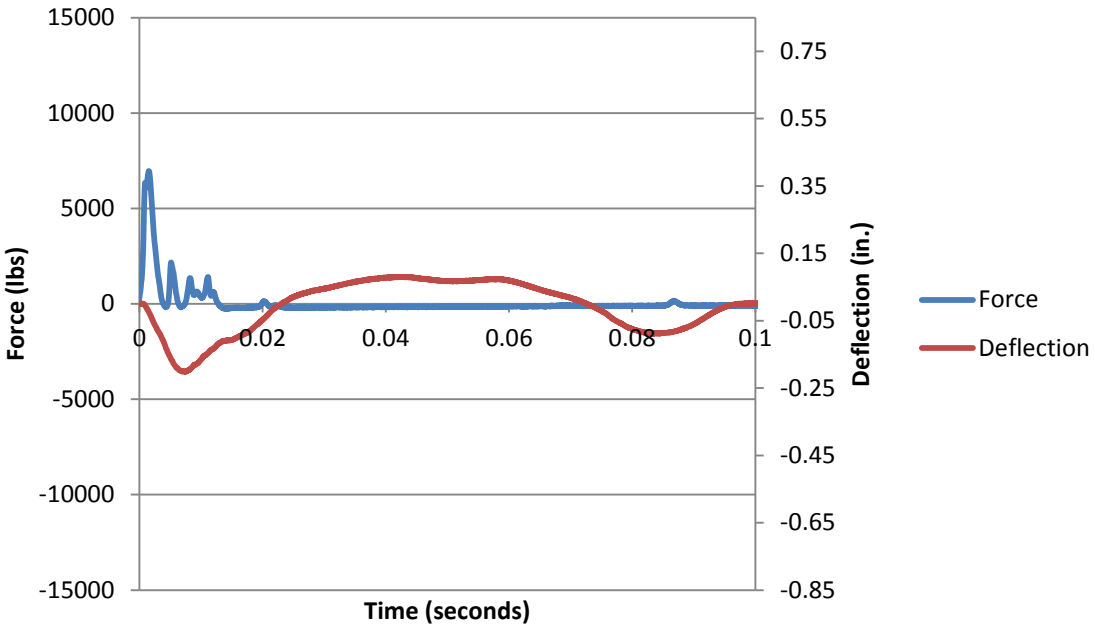

Figure B.15. Force and deflection vs. time for WWR 1 at 18 inches

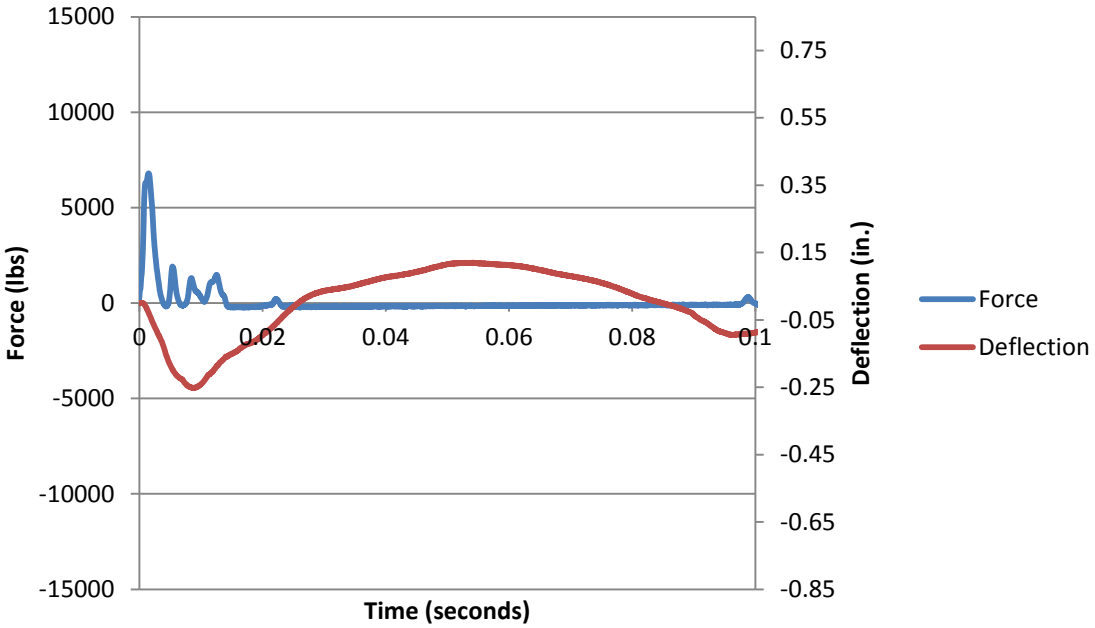

Figure B.16. Force and deflection vs. time for WWR 1 at 21 inches

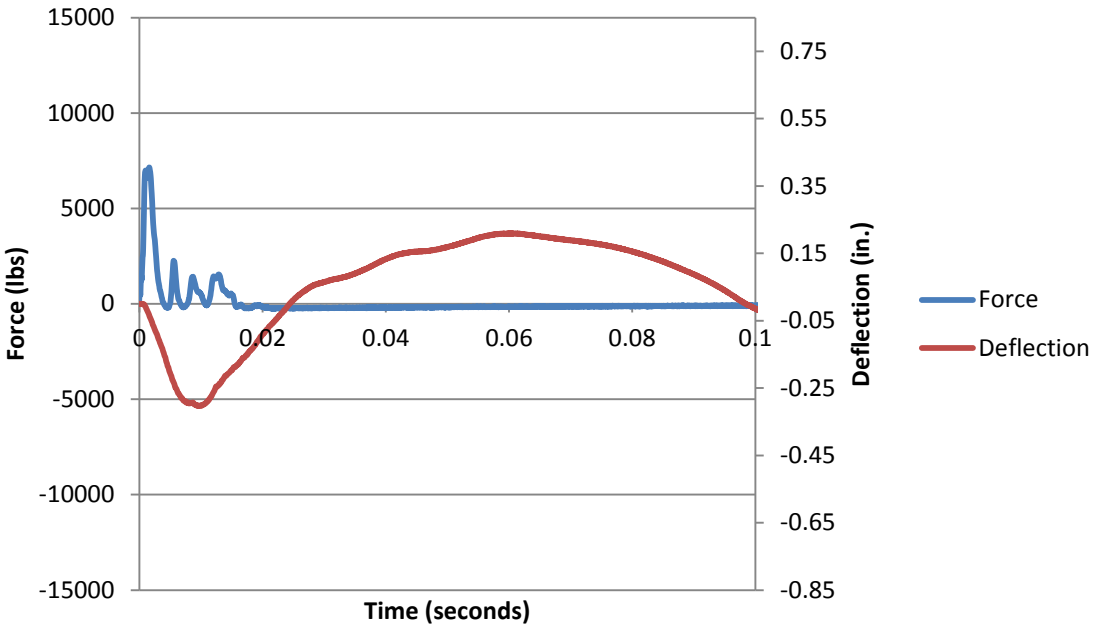

Figure B.17. Force and deflection vs. time for WWR 1 at 24 inches

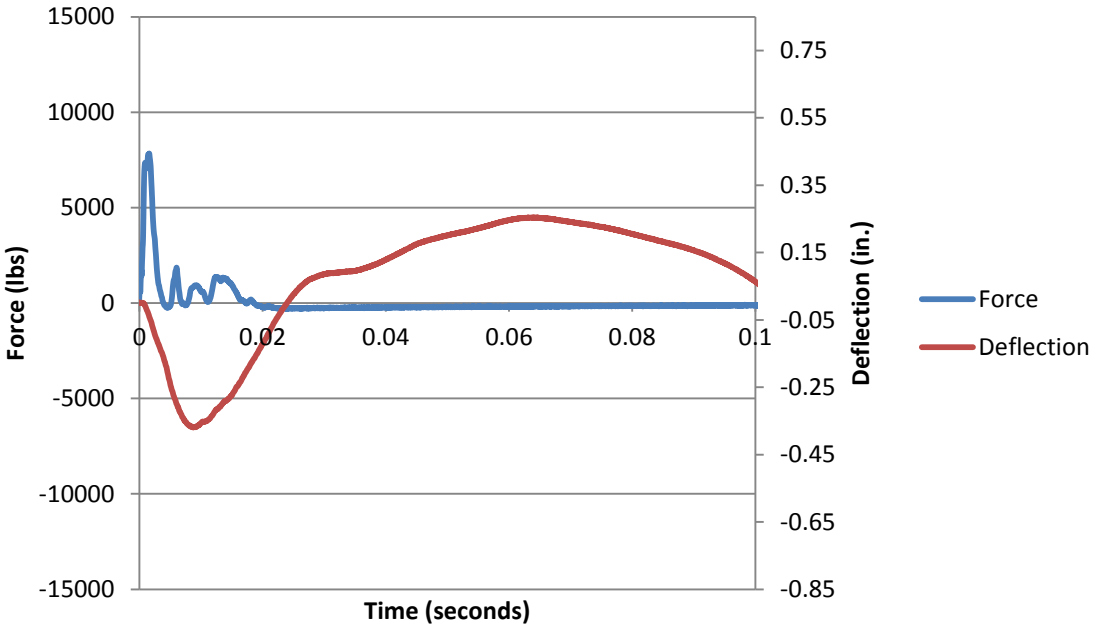

Figure B.18. Force and deflection vs. time for WWR 1 at 30 inches

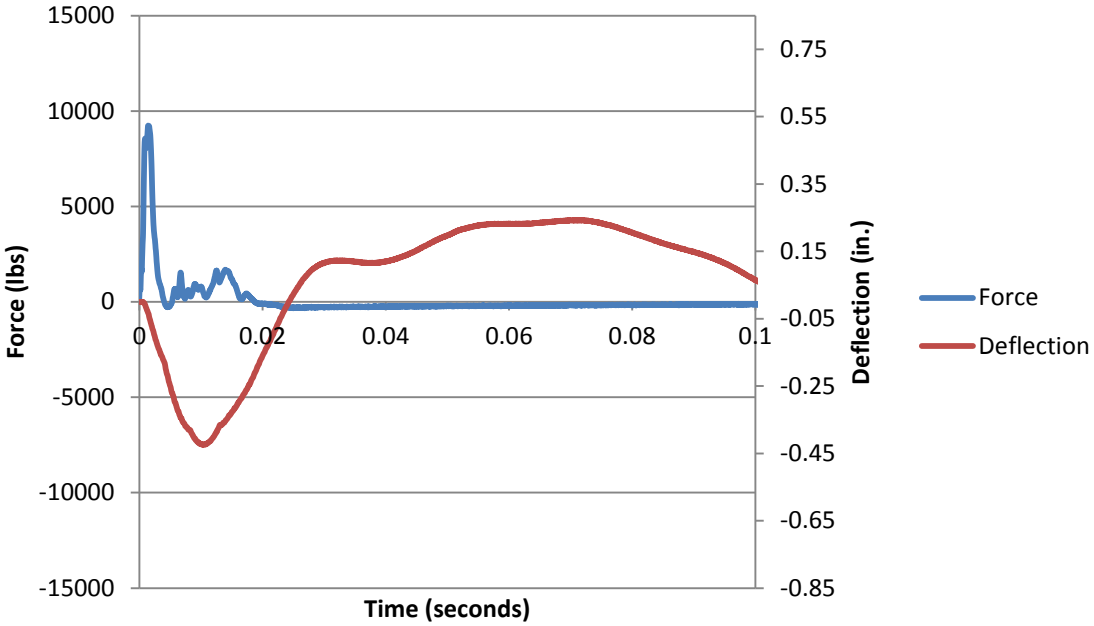

Figure B.19. Force and deflection vs. time for WWR 1 at 36 inches

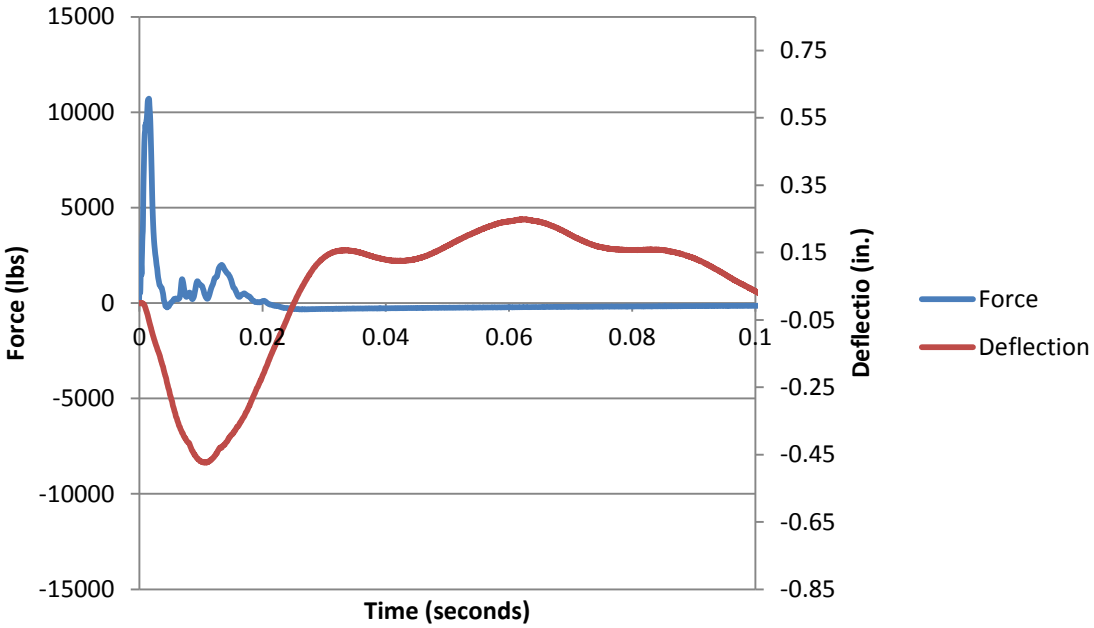

Figure B.20. Force and deflection vs. time for WWR 1 at 42 inches

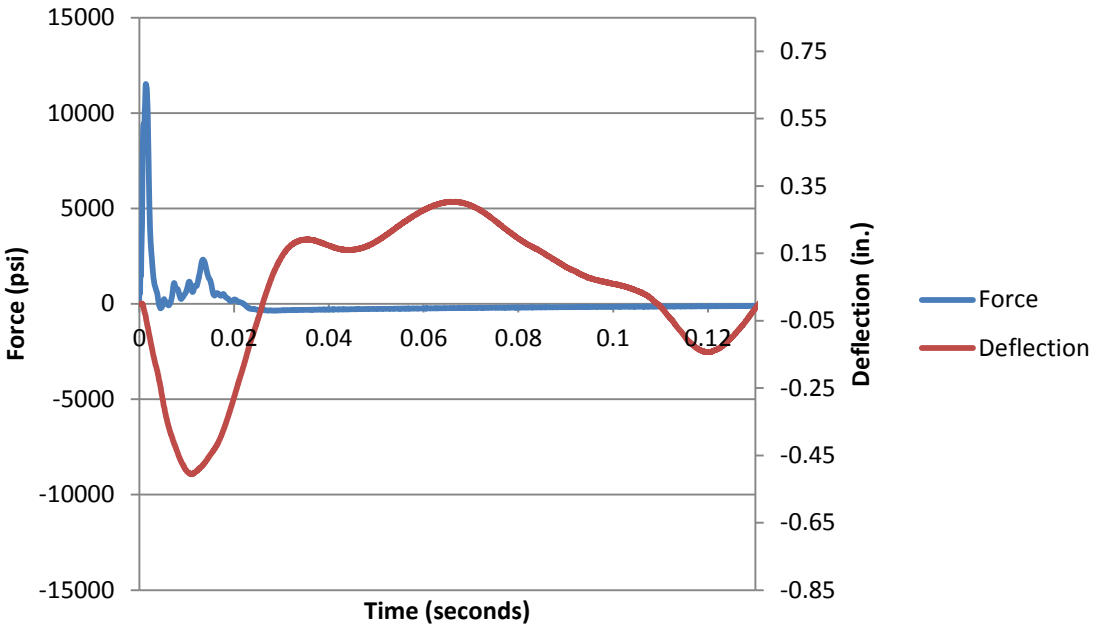

Figure B.21. Force and deflection vs. time for WWR 1 at 48 inches

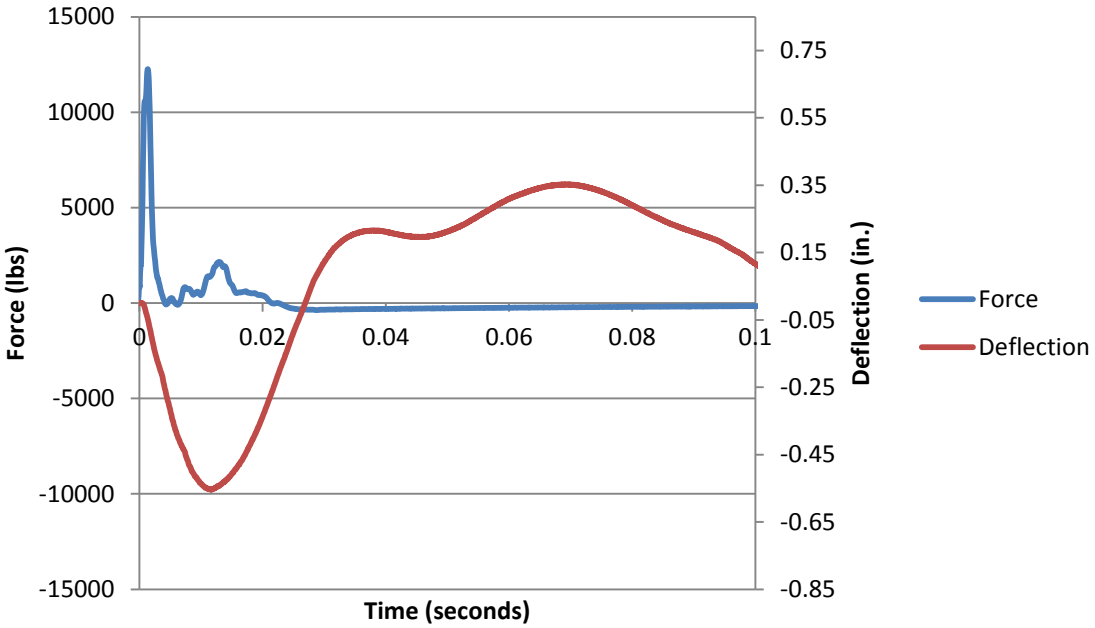

Figure B.22. Force and deflection vs. time for WWR 1 at 54 inches

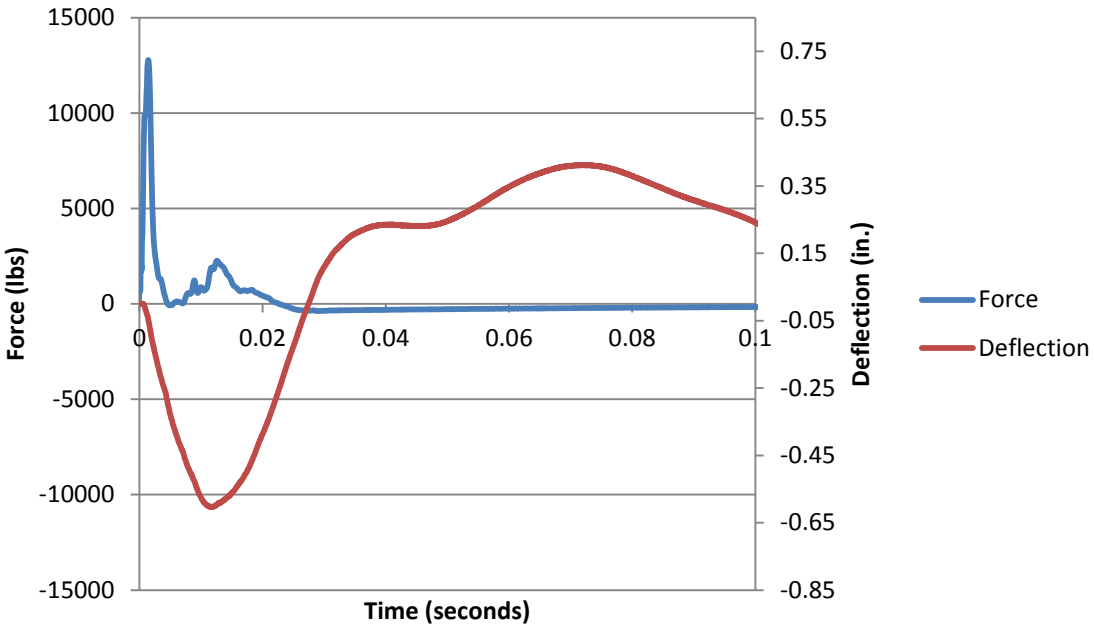

Figure B.23. Force and deflection vs. time for WWR 1 at 60 inches

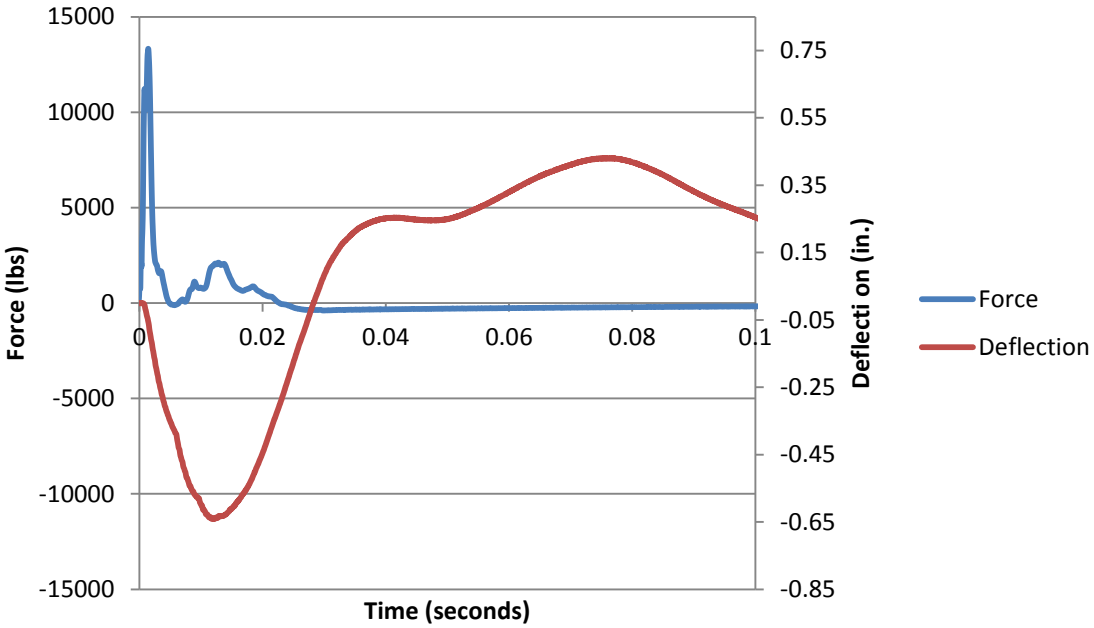

Figure B.24. Force and deflection vs. time for WWR 1 at 66 inches

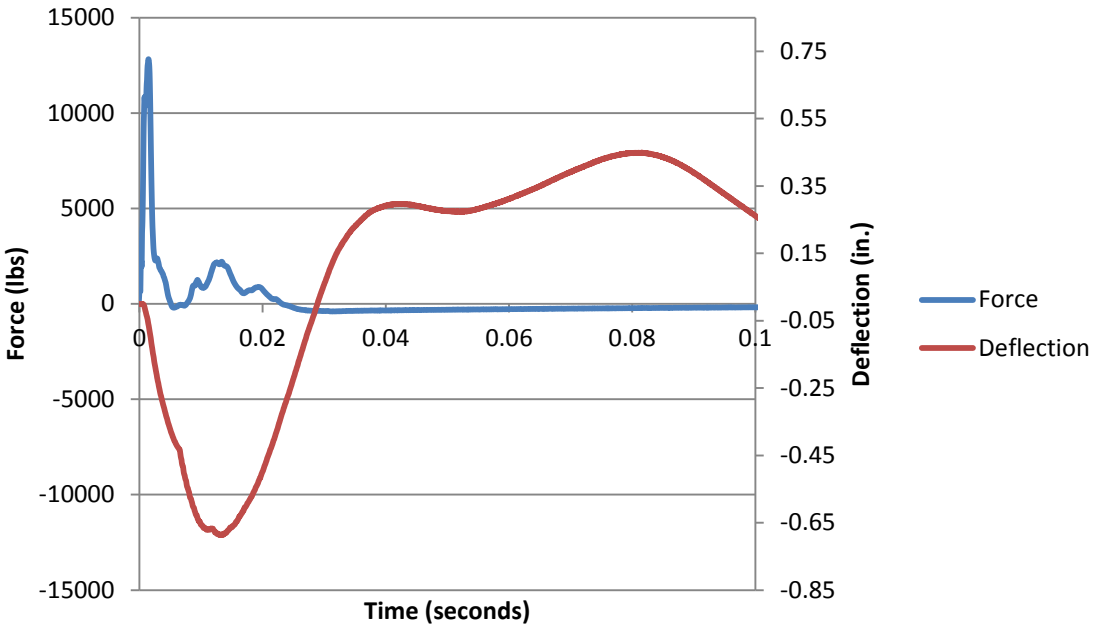

Figure B.25. Force and deflection vs. time for WWR 1 at 72 inches

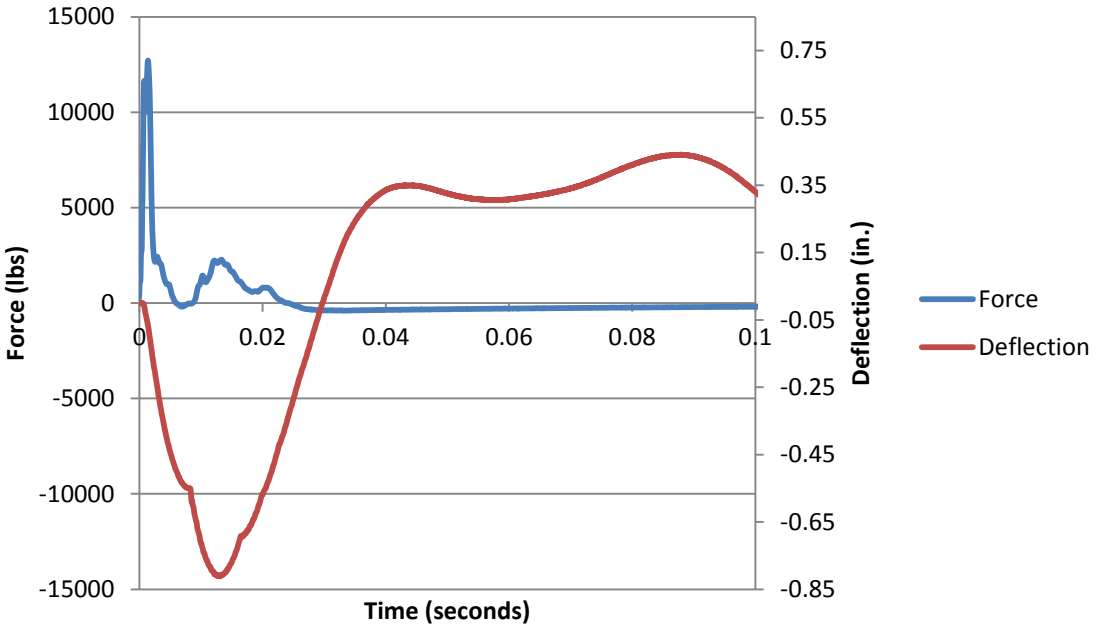

Figure B.26. Force and deflection vs. time for WWR 1 at 78 inches

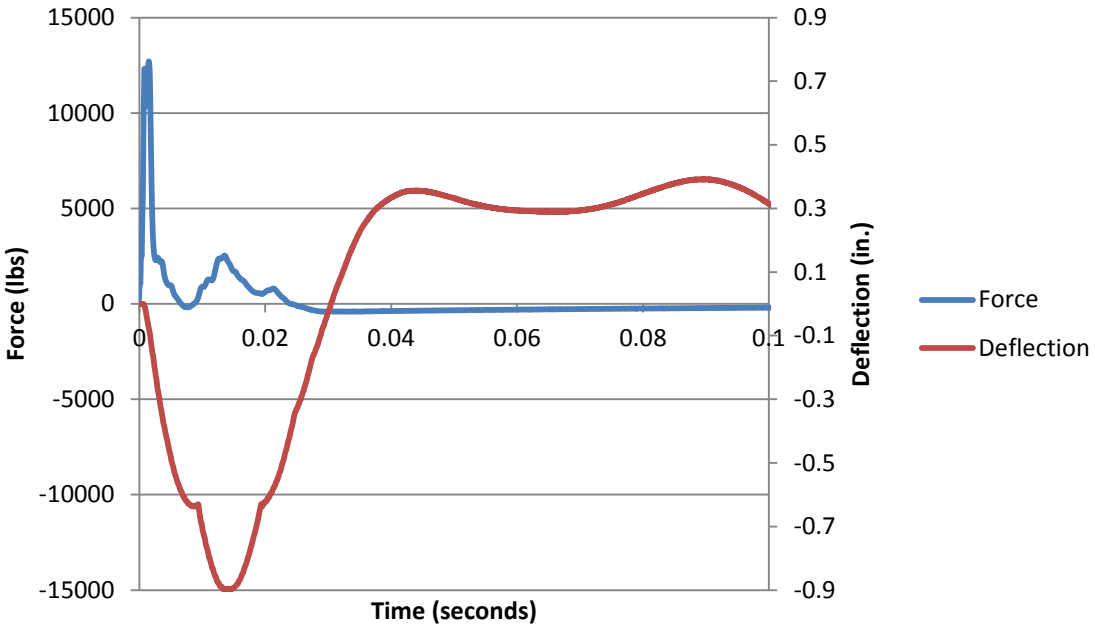

Figure B.27. Force and deflection vs. time for WWR 1 at 84 inches

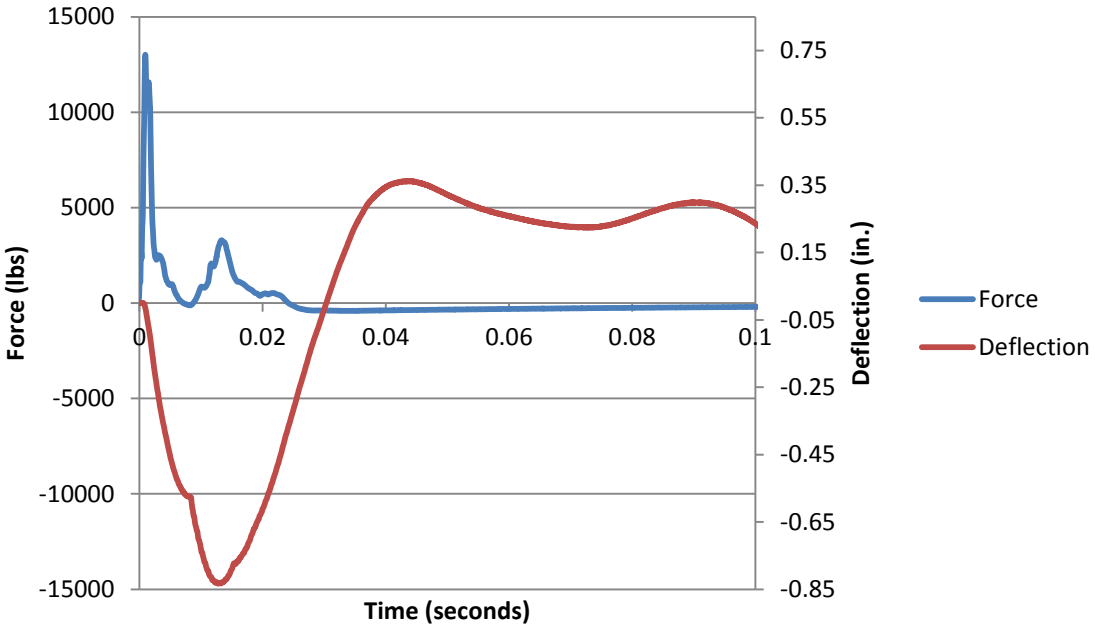

Figure B.28. Force and deflection vs. time for WWR 1 at 90 inches

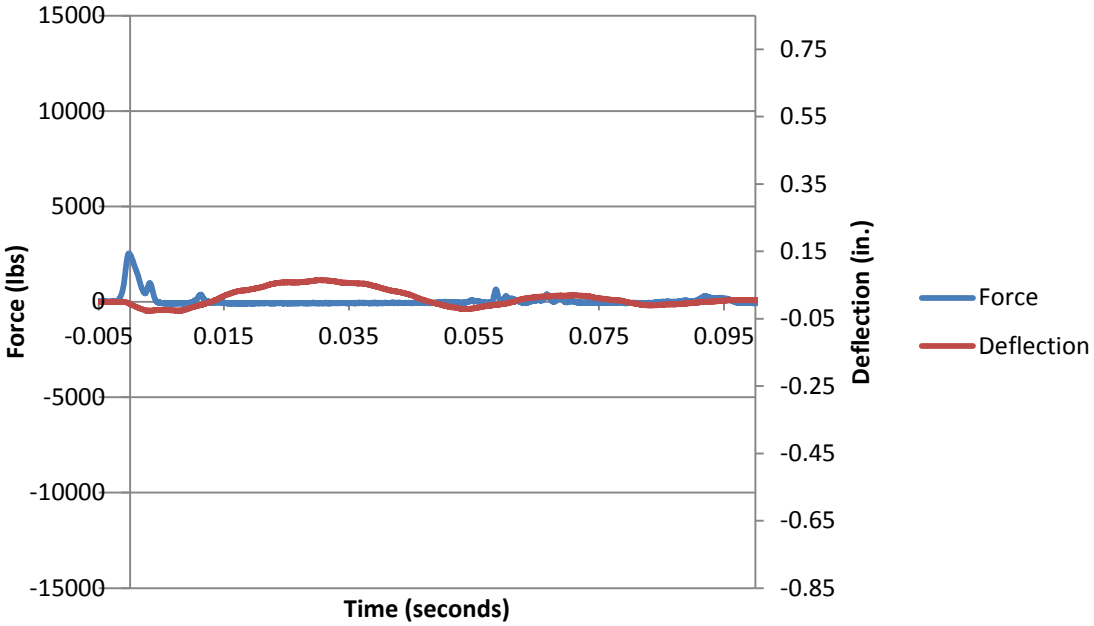

Figure B.29. Force and deflection vs. time for WWR 2 at 3 inches

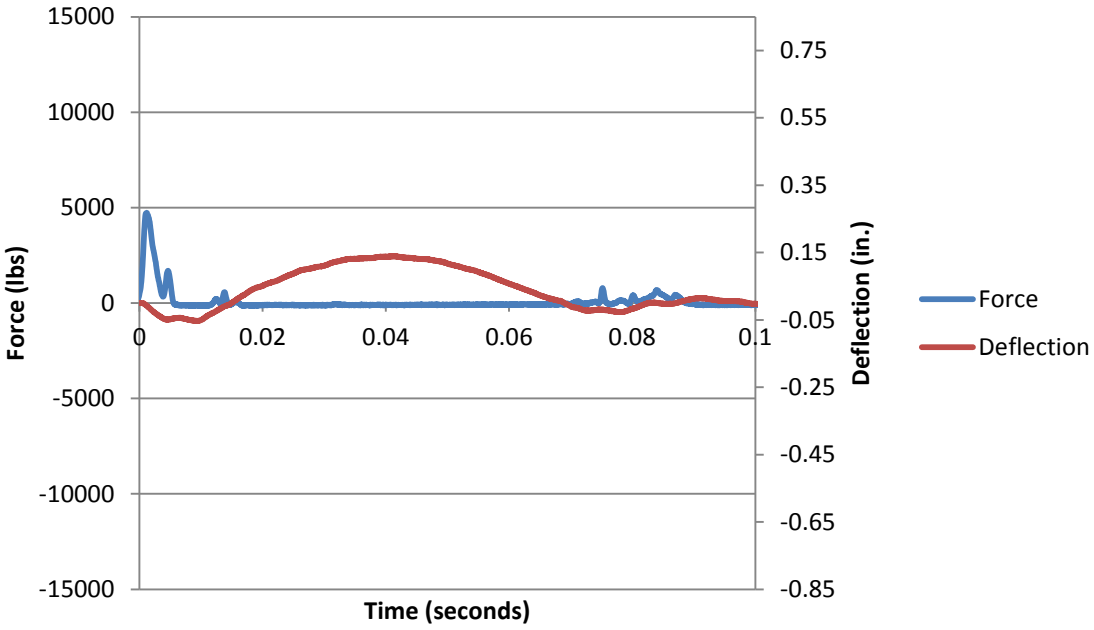

Figure B.30. Force and deflection vs. time for WWR 2 at 6 inches

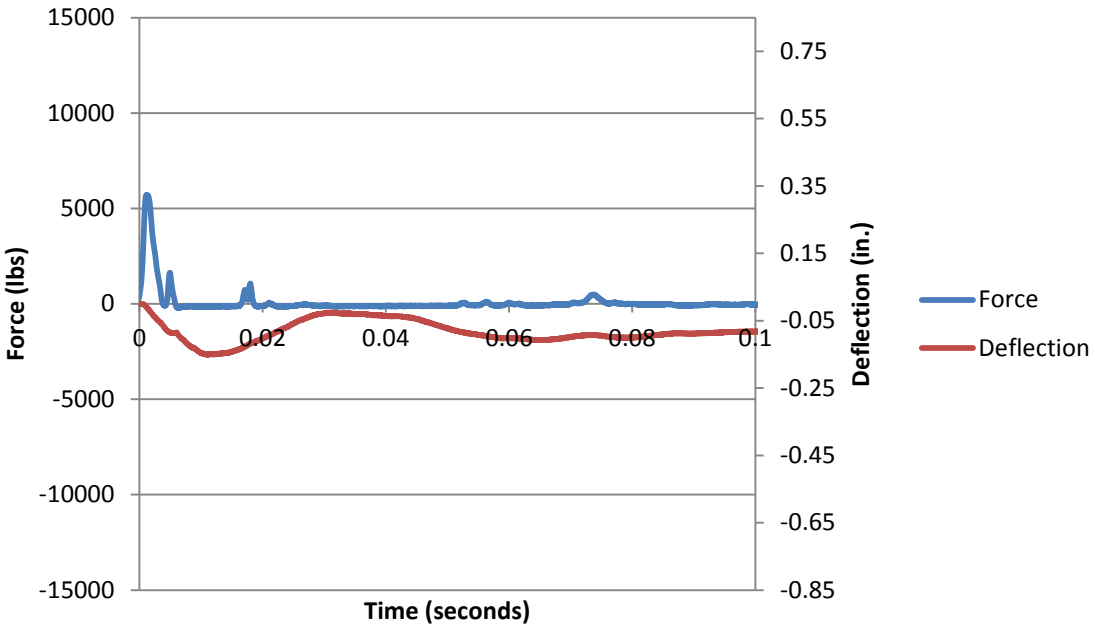

Figure B.31. Force and deflection vs. time for WWR 2 at 9 inches

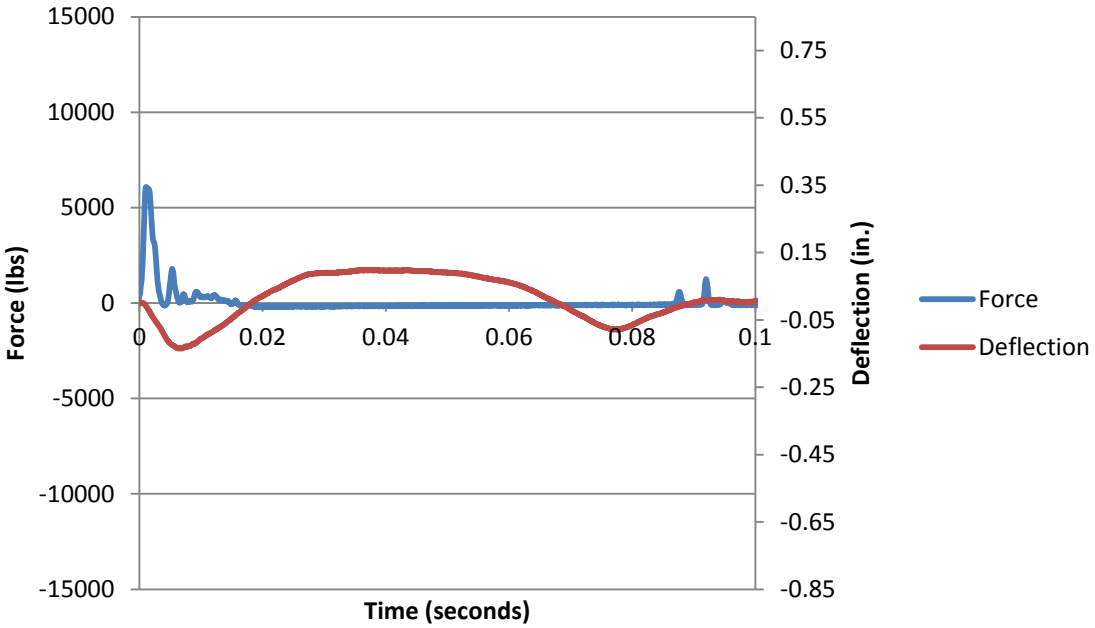

Figure B.32. Force and deflection vs. time for WWR 2 at 12 inches

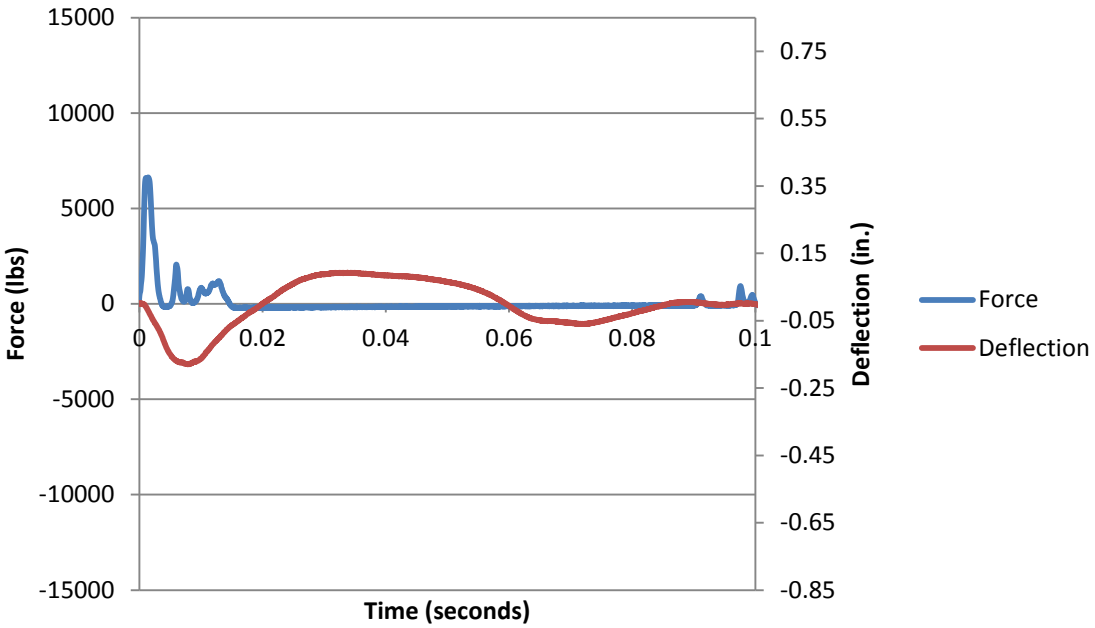

Figure B.33. Force and deflection vs. time for WWR 2 at 15 inches

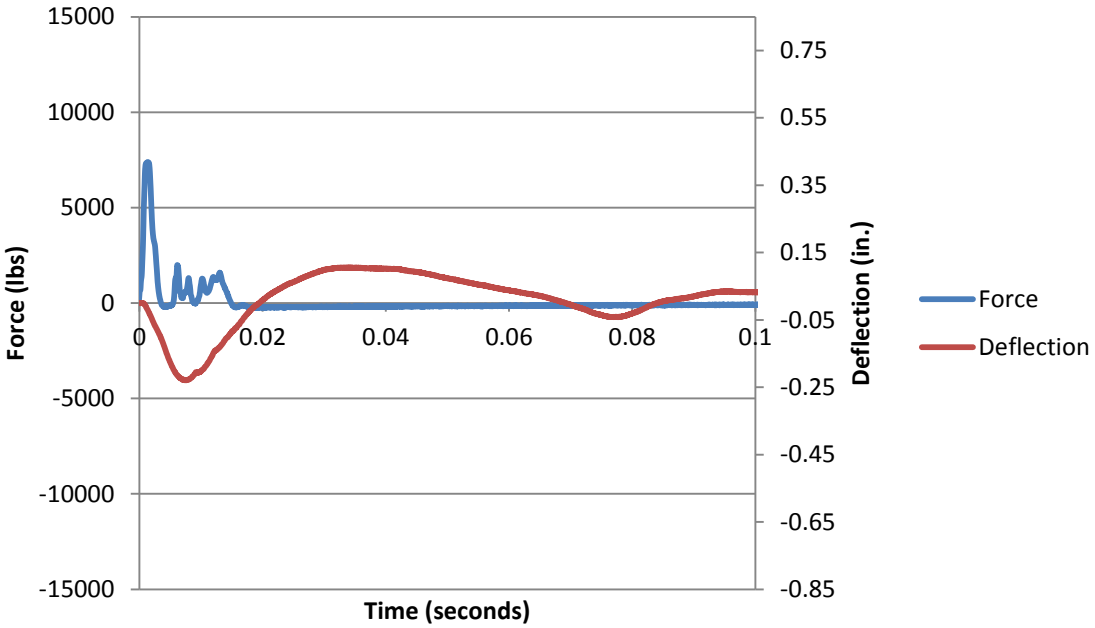

Figure B.34. Force and deflection vs. time for WWR 2 at 18 inches

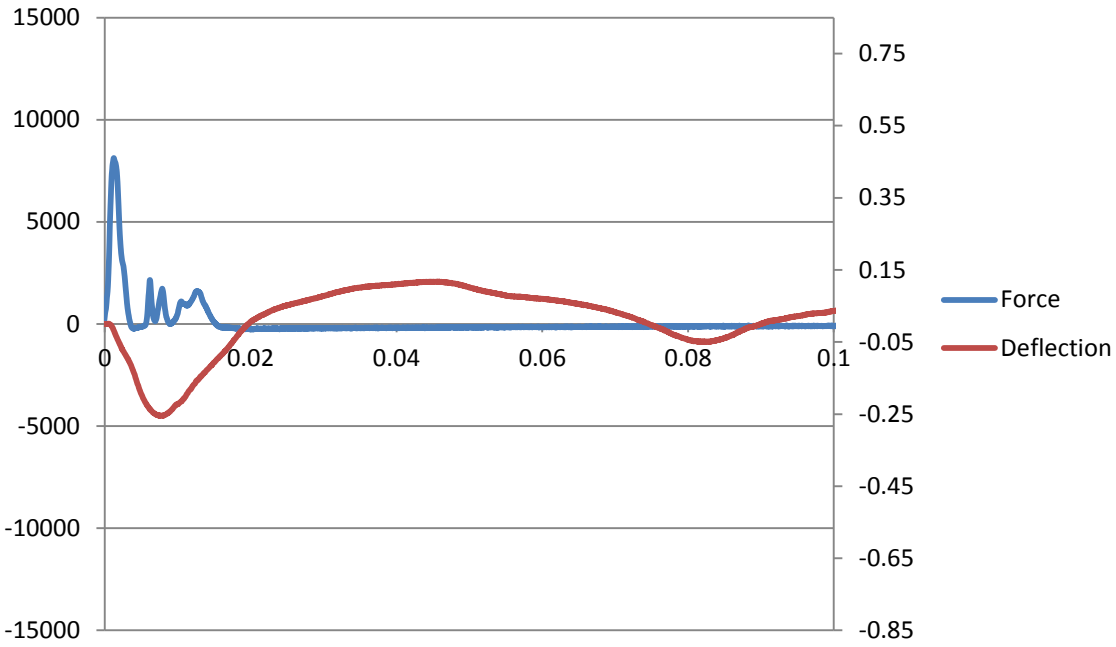

Figure B.35. Force and deflection vs. time for WWR 2 at 21 inches

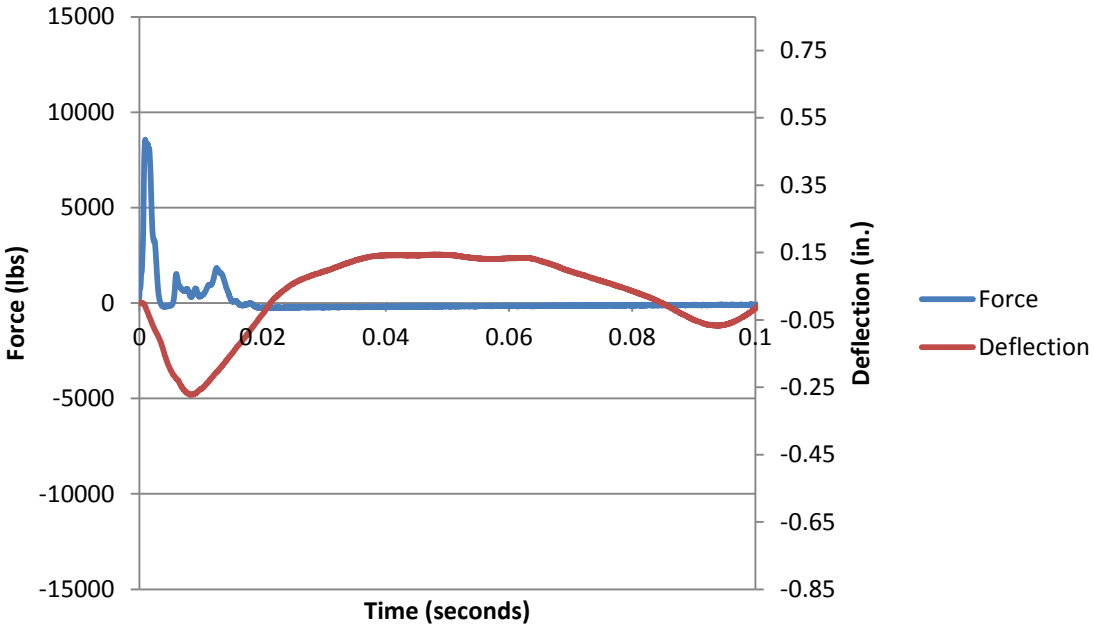

Figure B.36. Force and deflection vs. time for WWR 2 at 24 inches

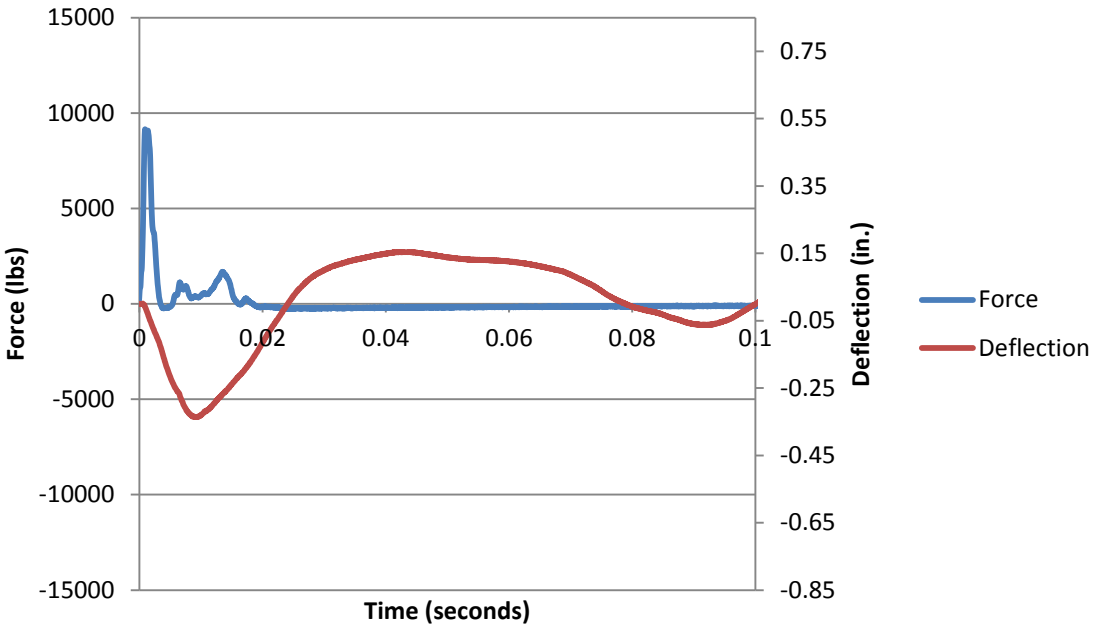

Figure B.37. Force and deflection vs. time for WWR 2 at 30 inches

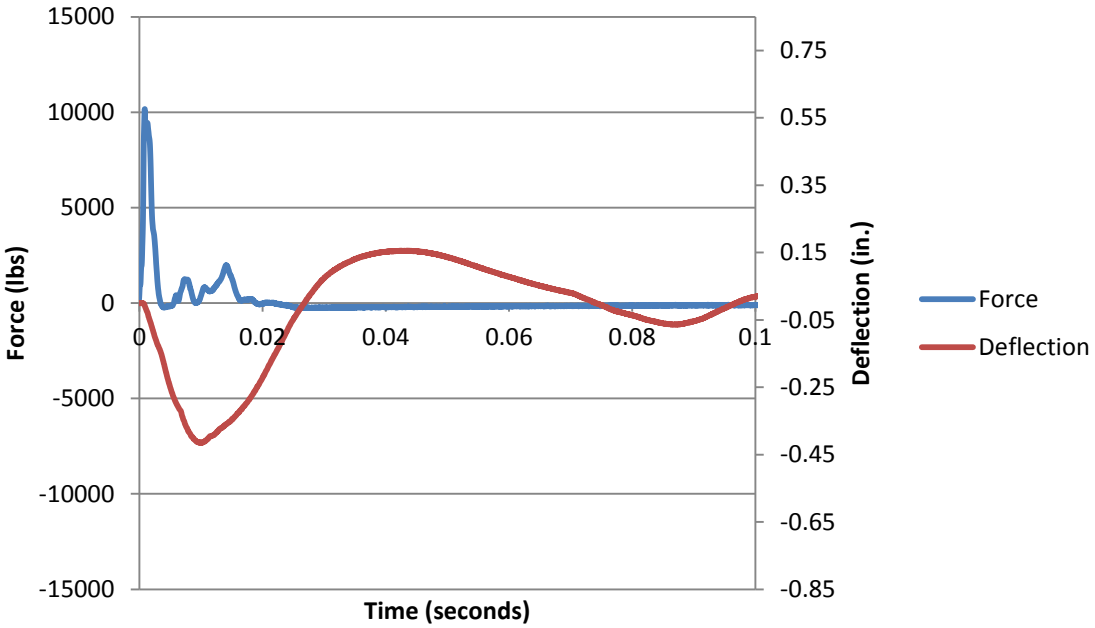

Figure B.38. Force and deflection vs. time for WWR 2 at 36 inches

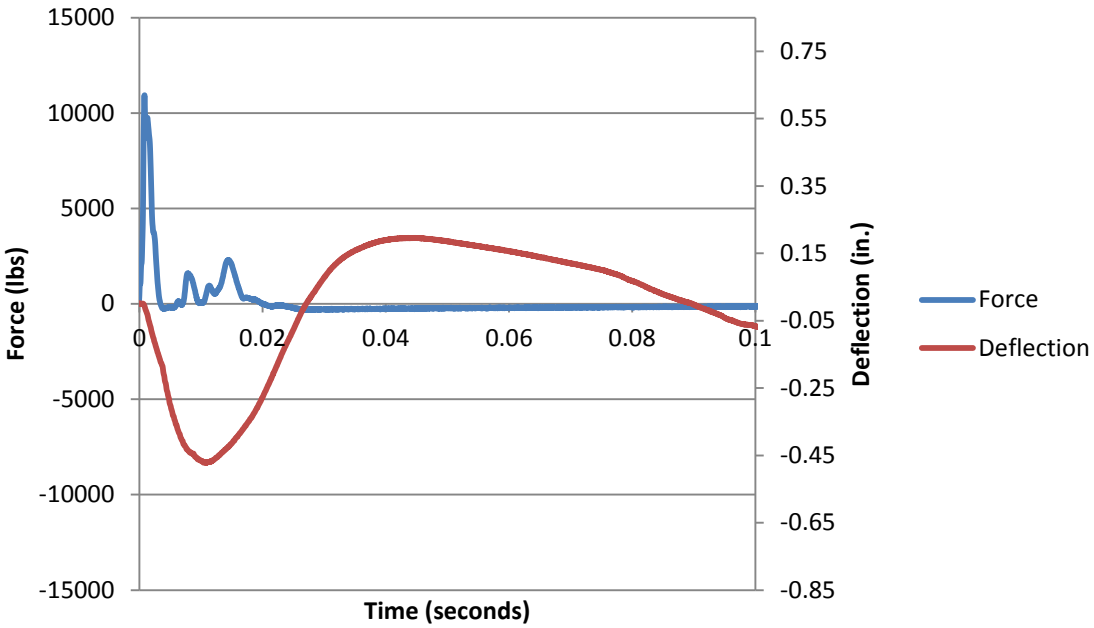

Figure B.39. Force and deflection vs. time for WWR 2 at 42 inches

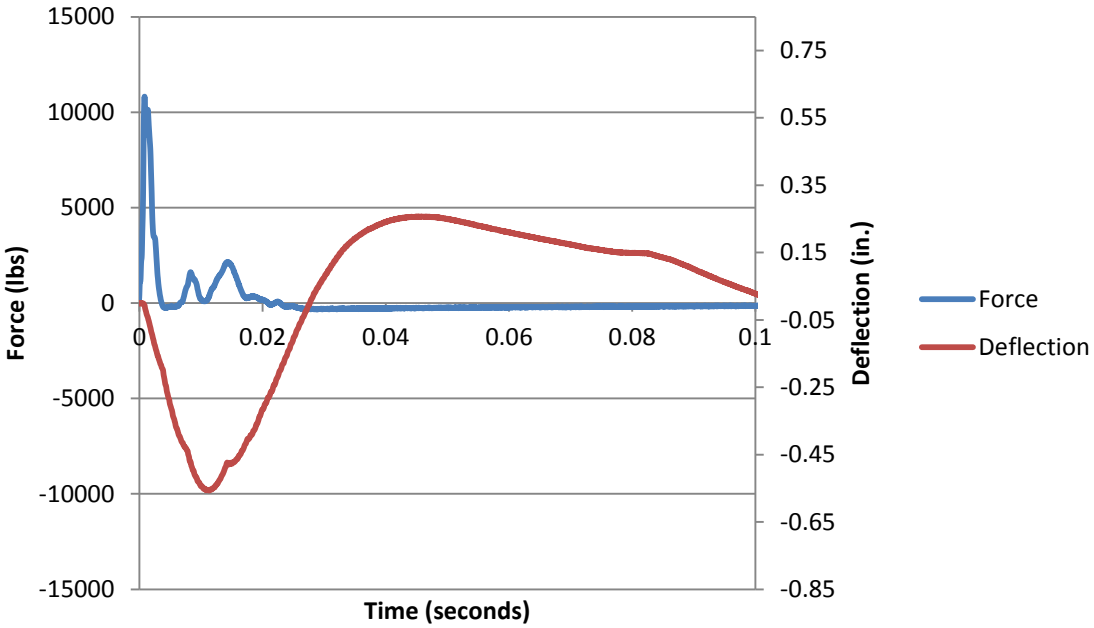

Figure B.40. Force and deflection vs. time for WWR 2 at 48 inches

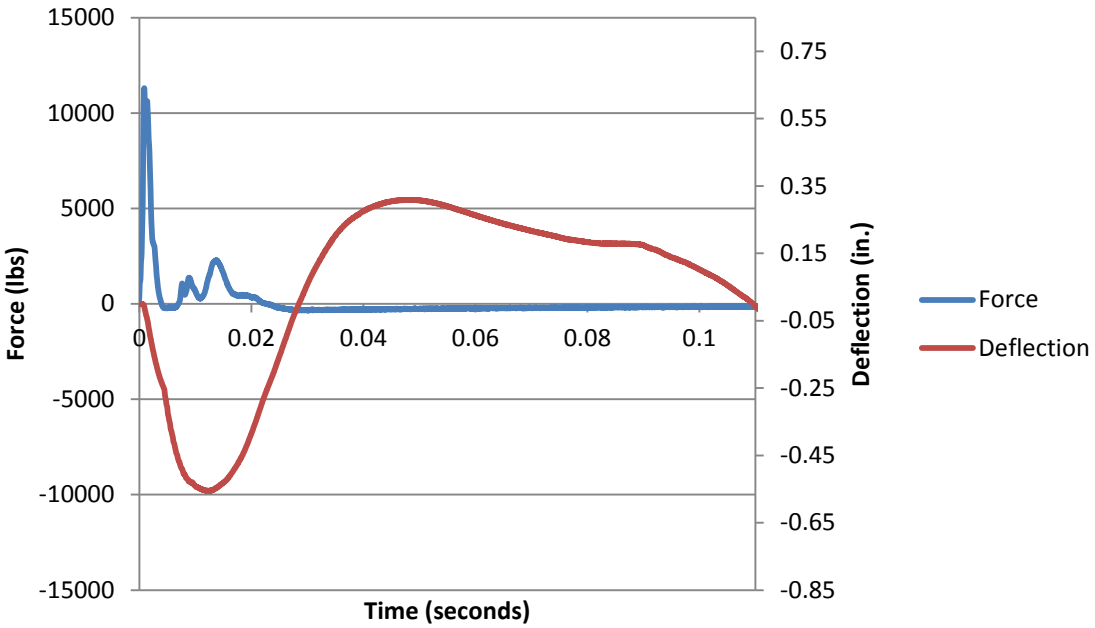

Figure B.41. Force and deflection vs. time for WWR 2 at 54 inches

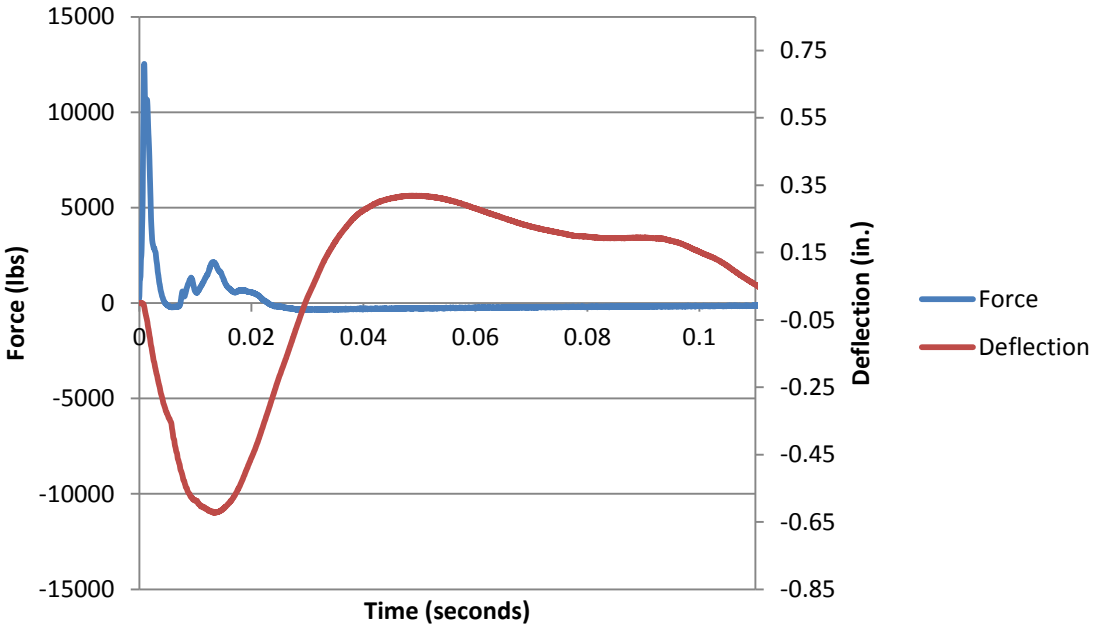

Figure B.42. Force and deflection vs. time for WWR 2 at 60 inches

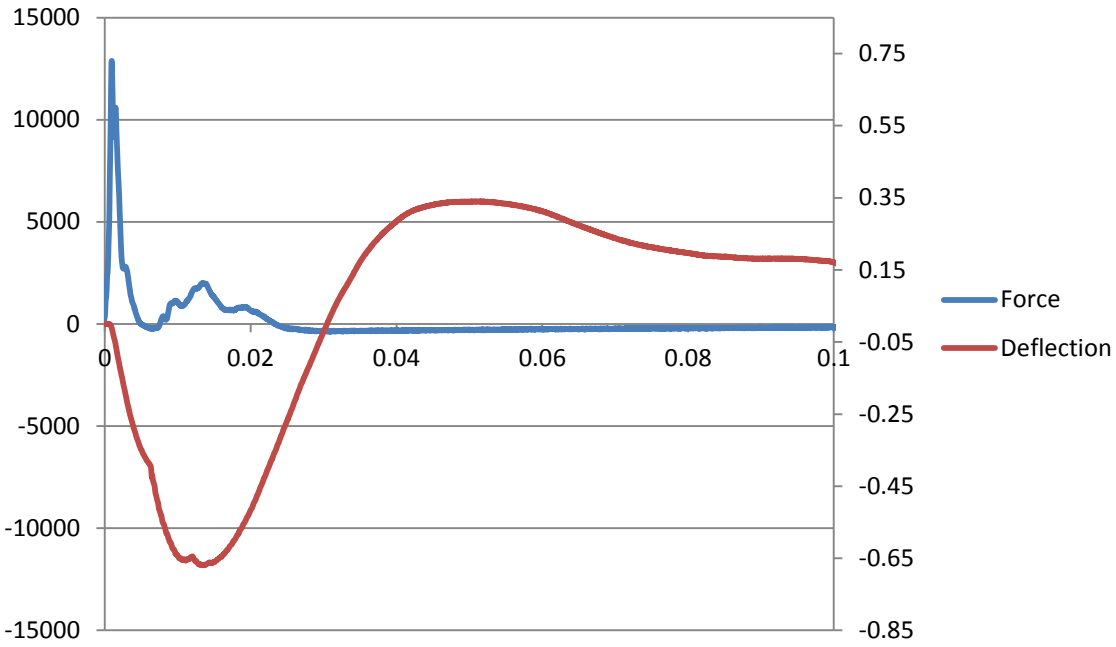

Figure B.43. Force and deflection vs. time for WWR 2 at 66 inches

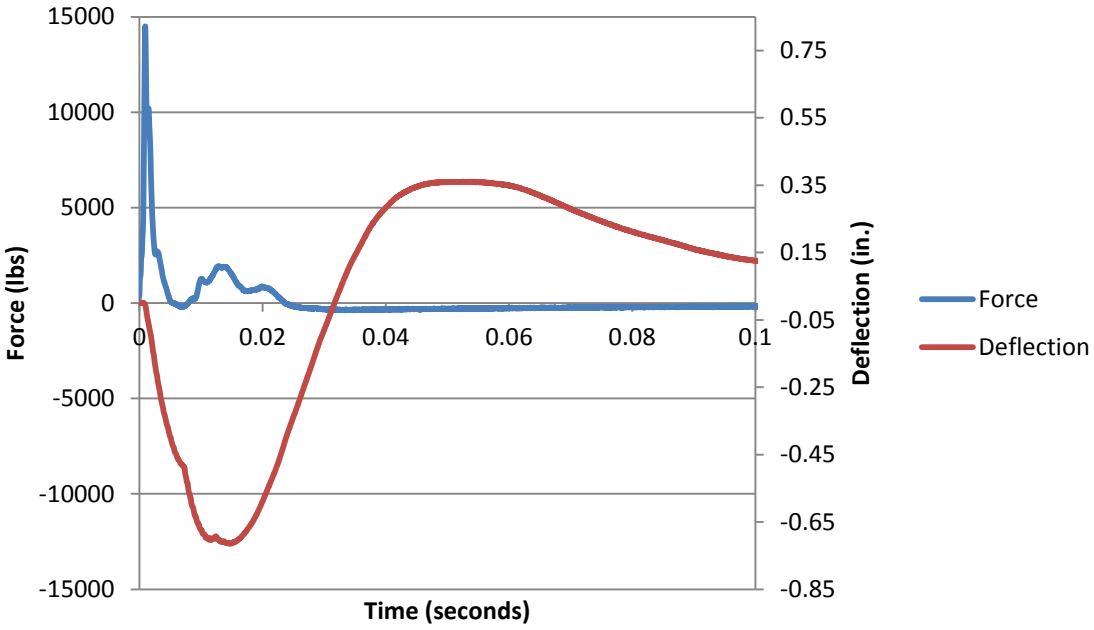

Figure B.44. Force and deflection vs. time for WWR 2 at 72 inches

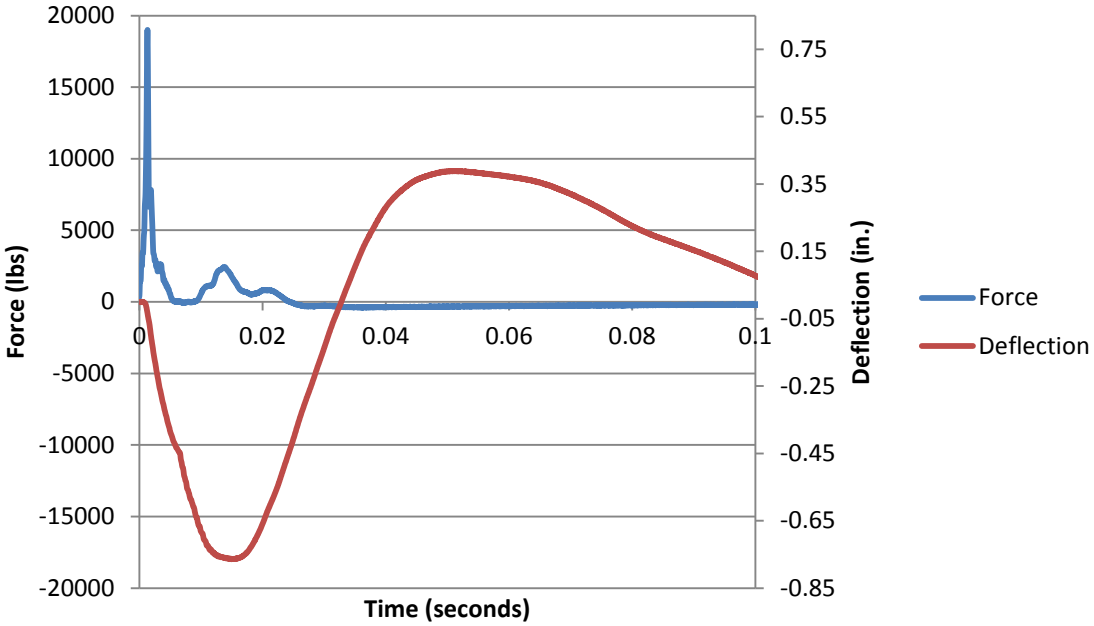

Figure B.45. Force and deflection vs. time for WWR 2 at 78 inches

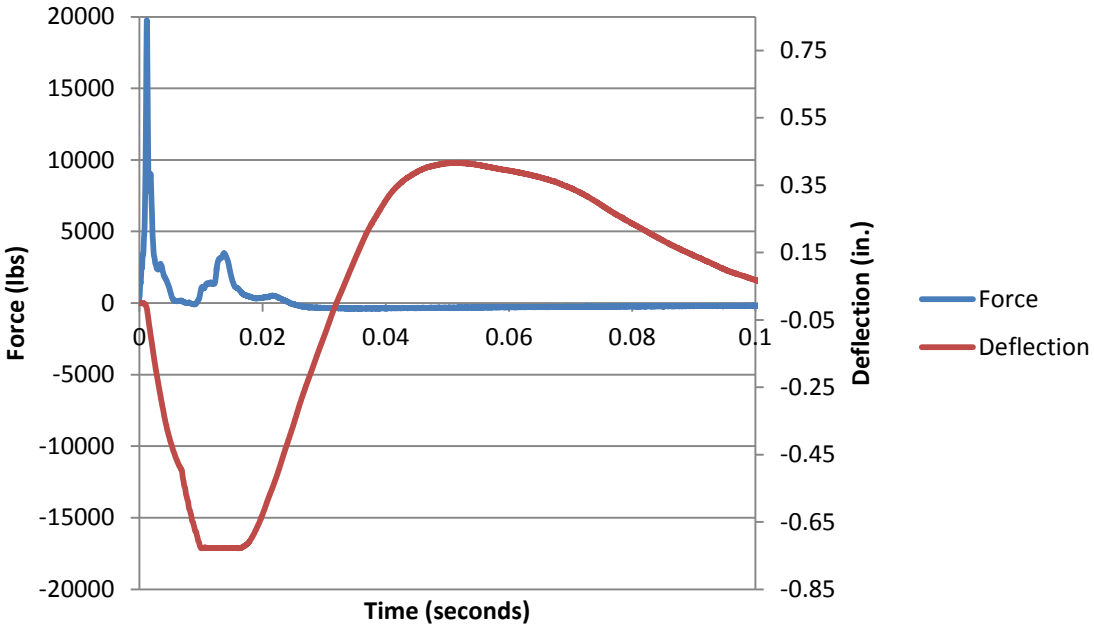

Figure B.46. Force and deflection vs. time for WWR 2 at 84 inches

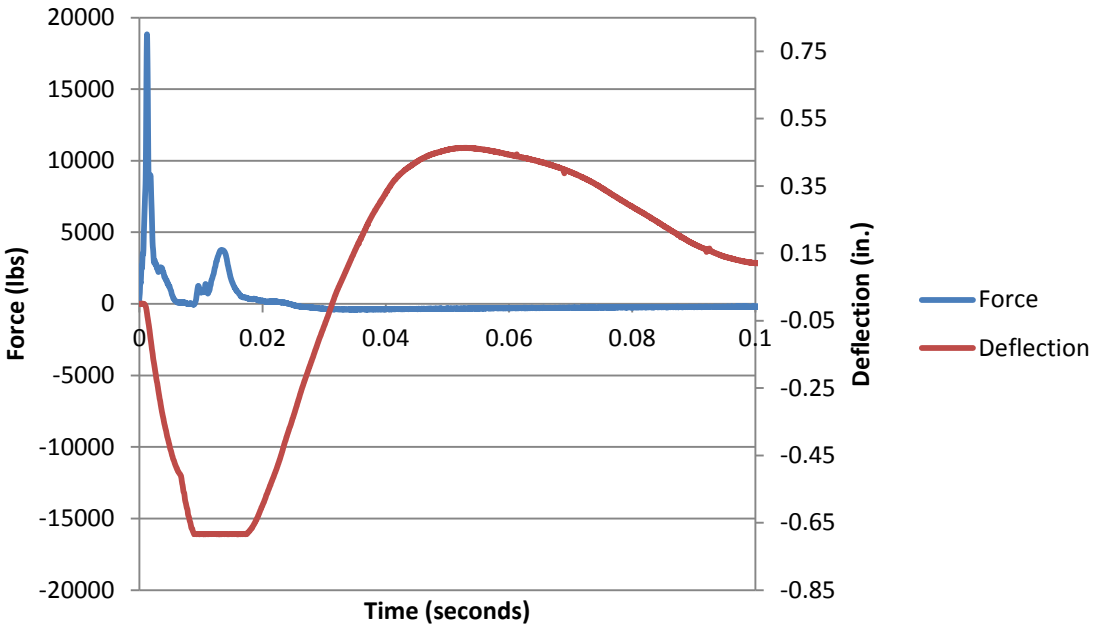

Figure B.47. Force and deflection vs. time for WWR 2 at 90 inches

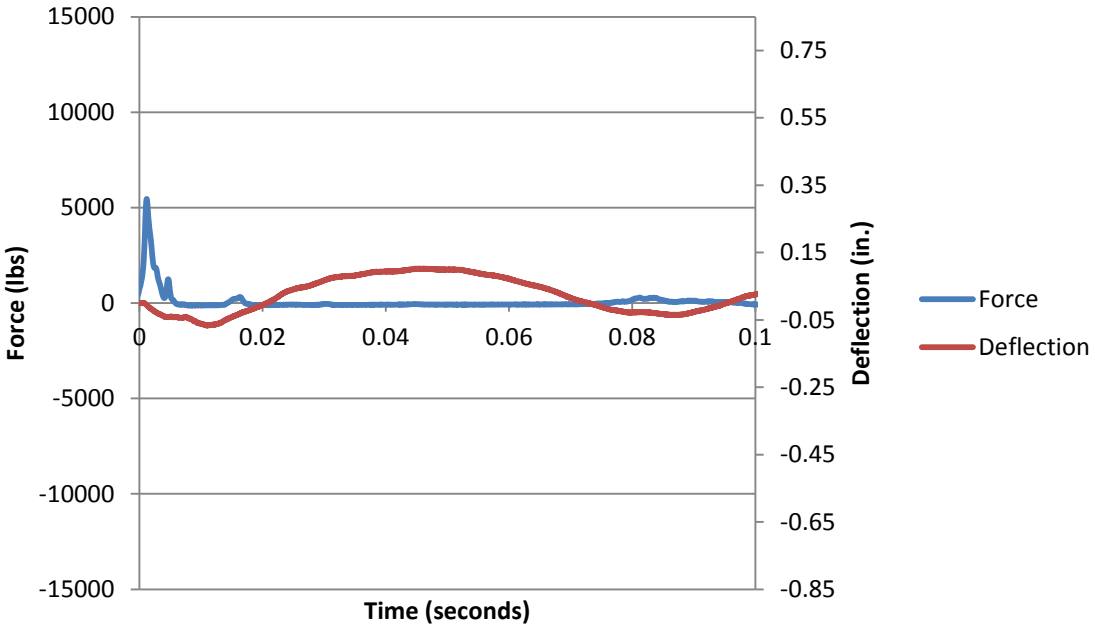

Figure B.48. Force and deflection vs. time for Fiber A1 at 3 inches

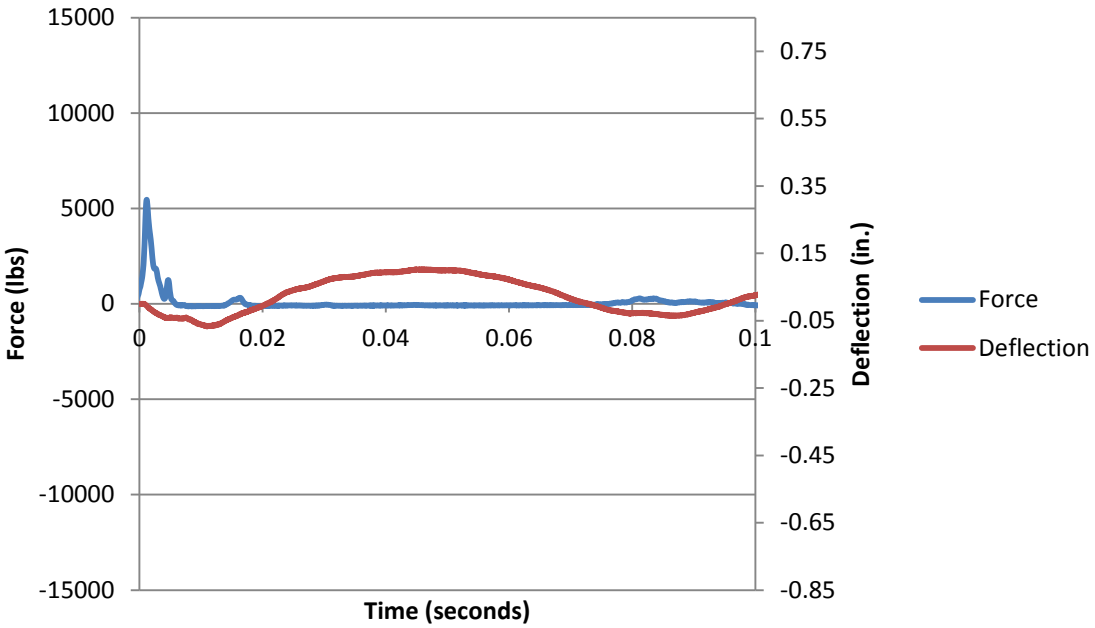

Figure B.49. Force and deflection vs. time for Fiber A1 at 6 inches

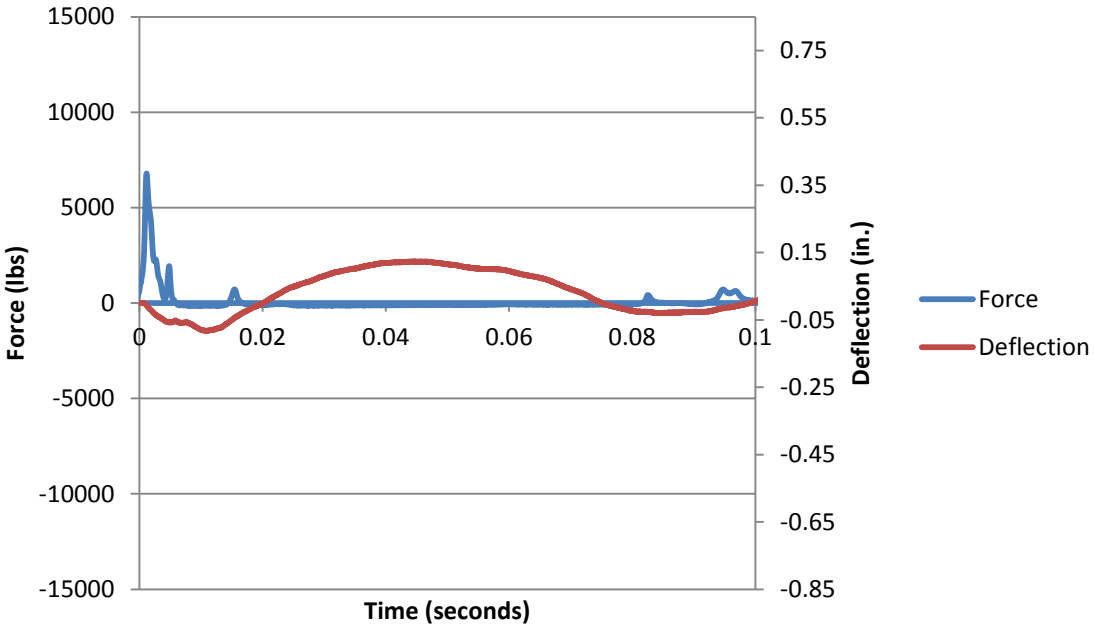

Figure B.50. Force and deflection vs. time for Fiber A1 at 9 inches

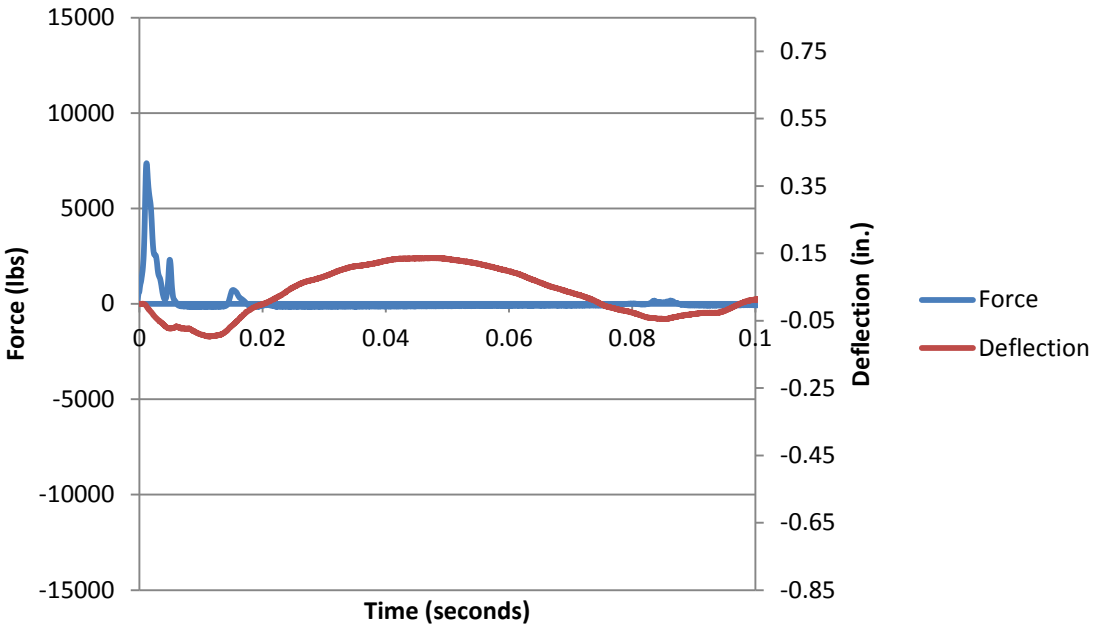

Figure B.51. Force and deflection vs. time for Fiber A1 at 12 inches

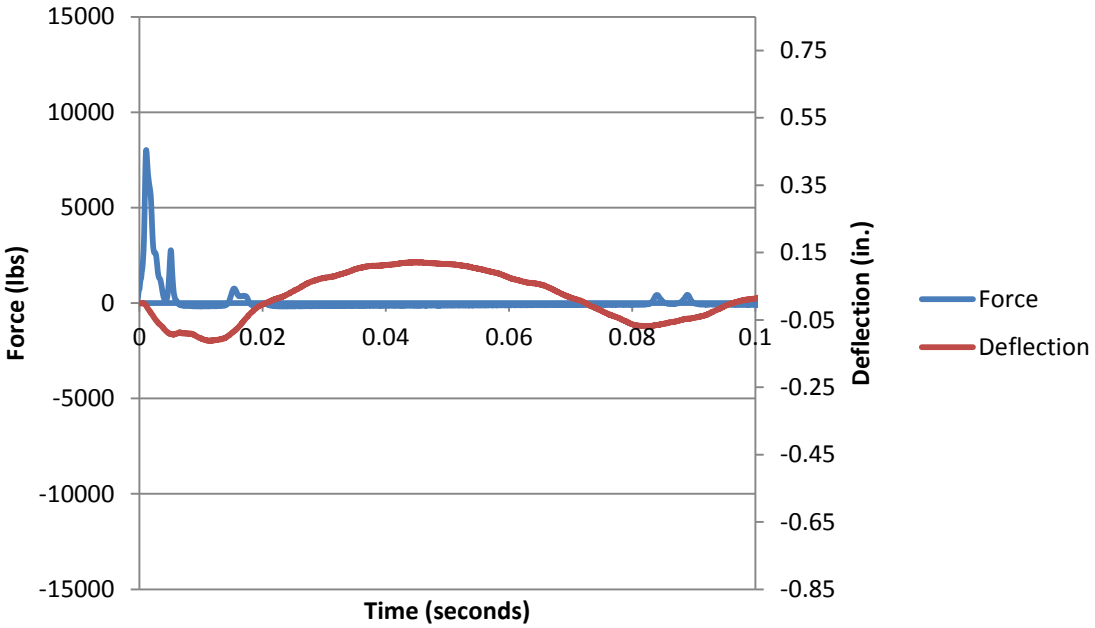

Figure B.52. Force and deflection vs. time for Fiber A1 at 15 inches

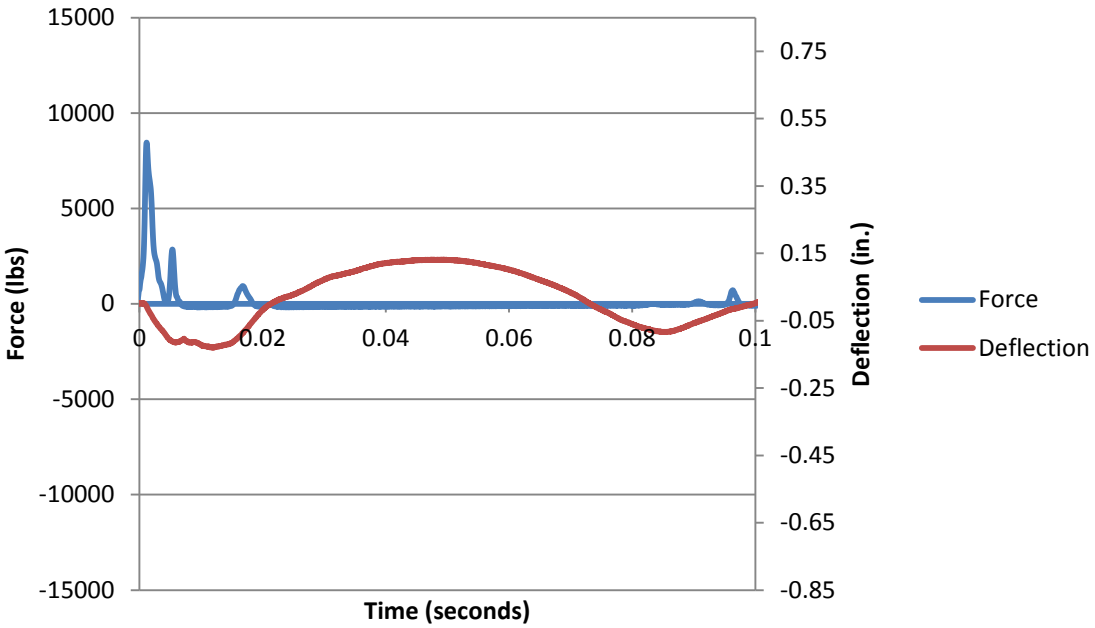

Figure B.53. Force and deflection vs. time for Fiber A1 at 18 inches

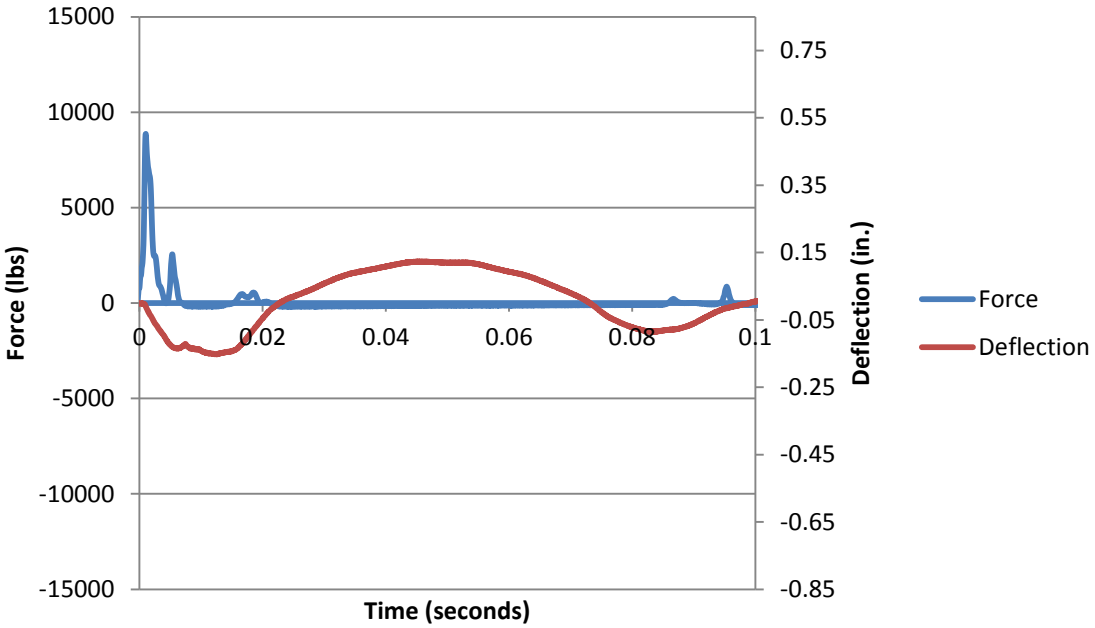

Figure B.54. Force and deflection vs. time for Fiber A1 at 21 inches

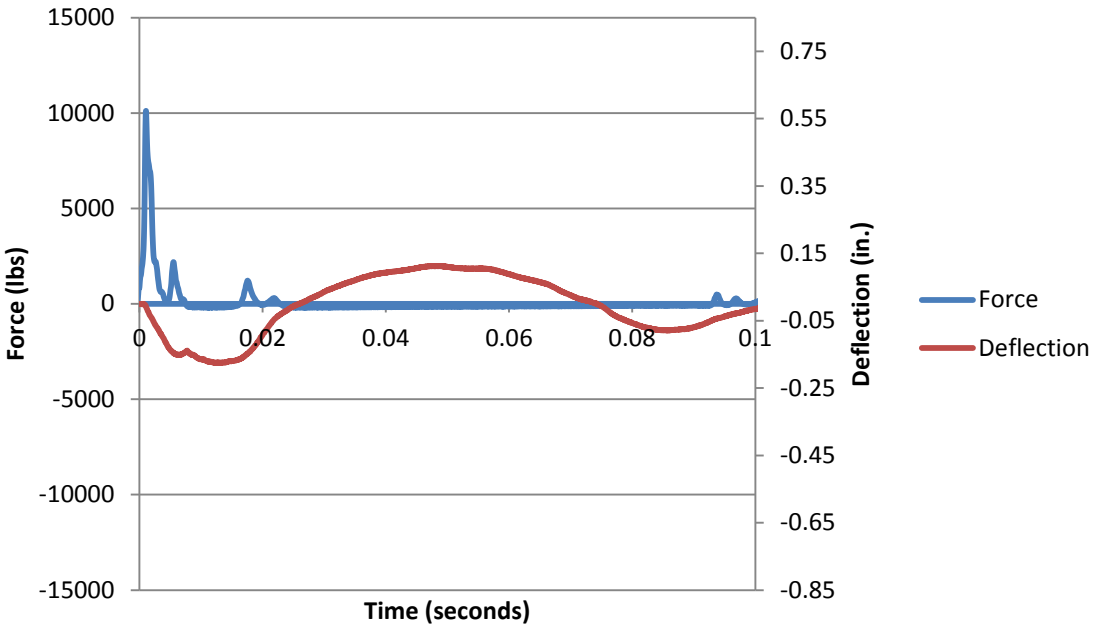

Figure B.55. Force and deflection vs. time for Fiber A1 at 24 inches

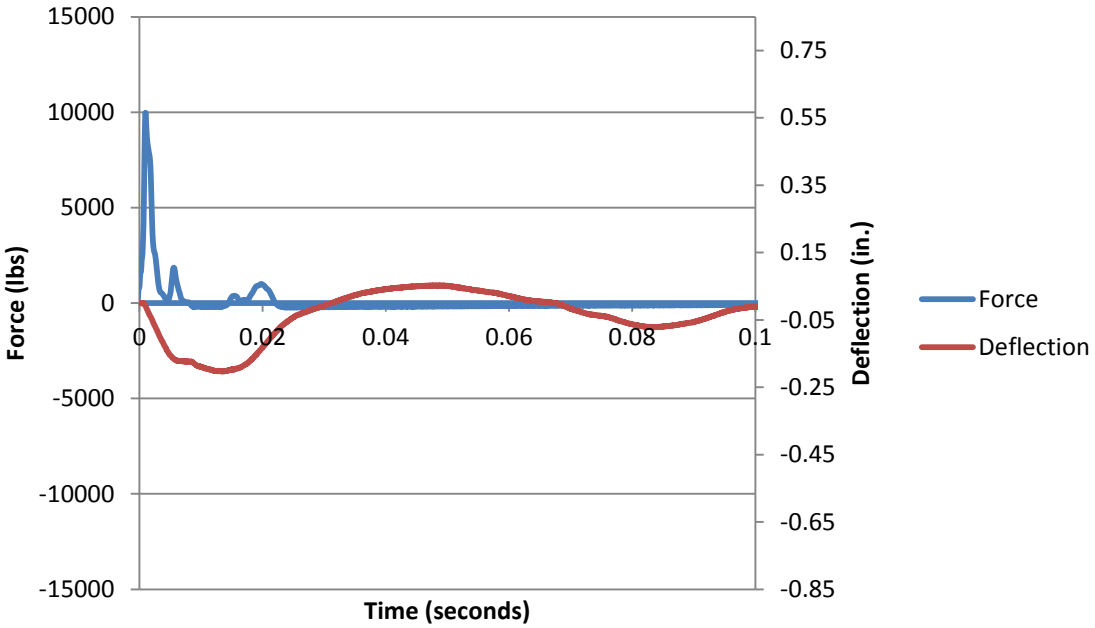

Figure B.56. Force and deflection vs. time for Fiber A1 at 30 inches

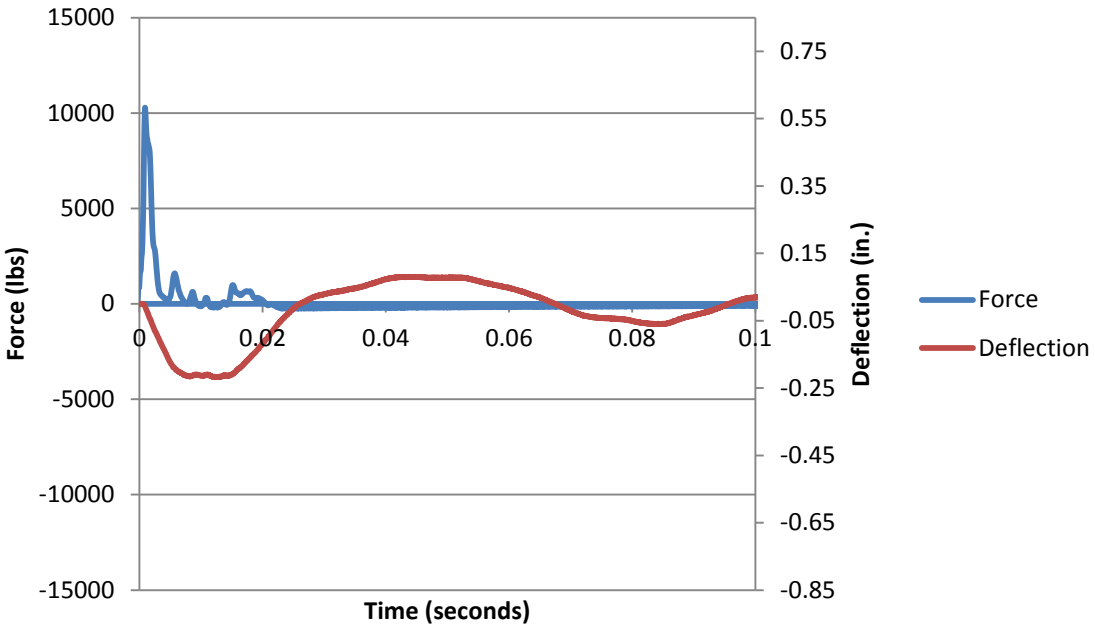

Figure B.57. Force and deflection vs. time for Fiber A1 at 36 inches

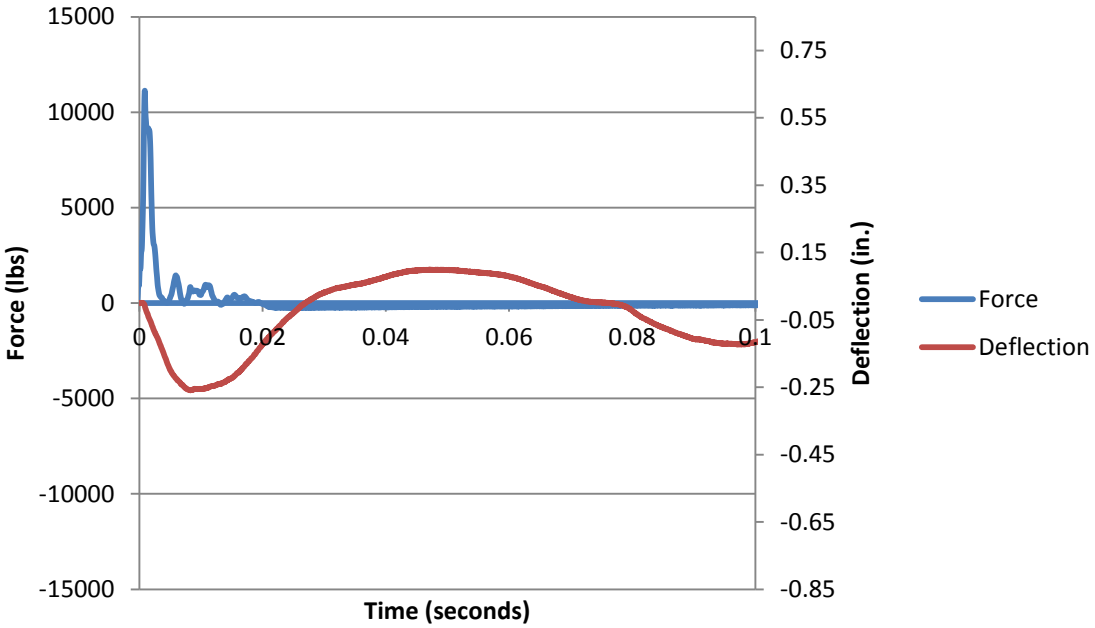

Figure B.58. Force and deflection vs. time for Fiber A1 at 42 inches

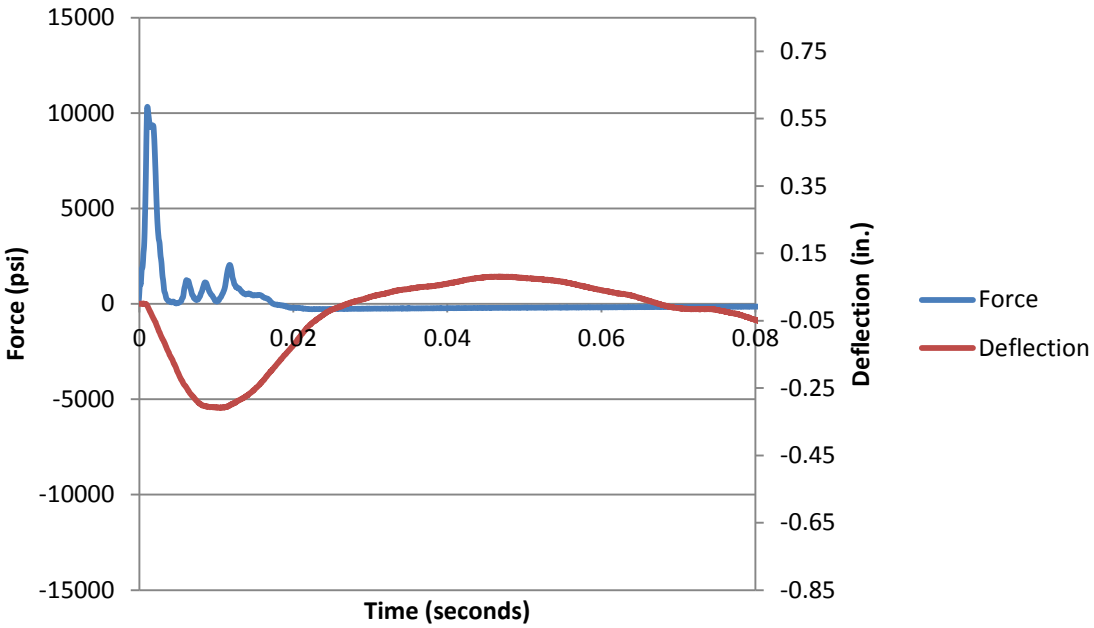

Figure B.59. Force and deflection vs. time for Fiber A1 at 48 inches

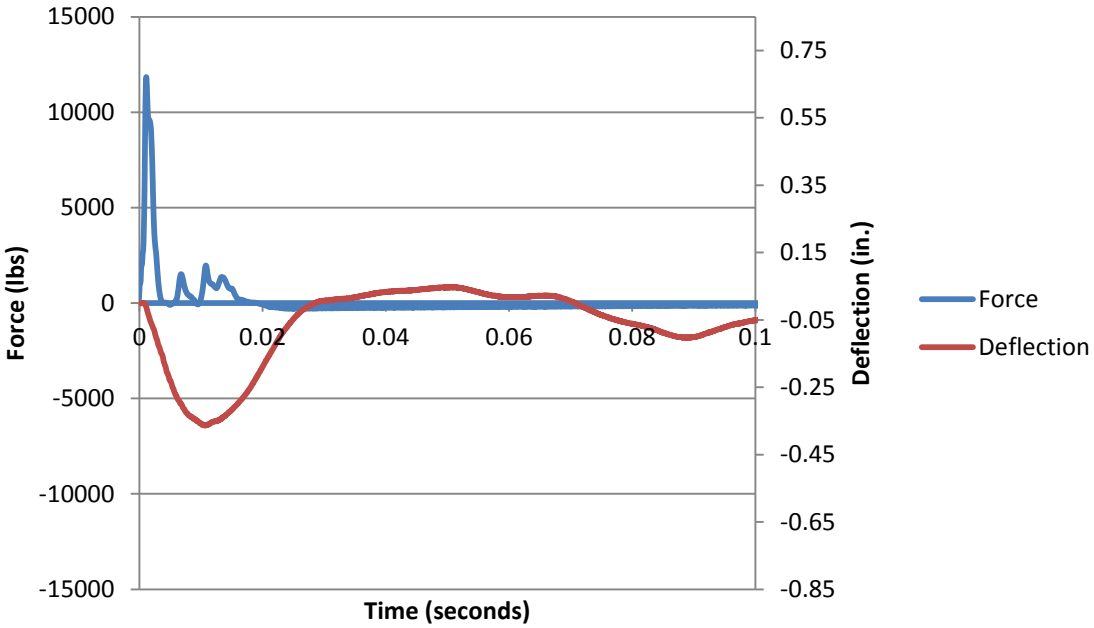

Figure B.60. Force and deflection vs. time for Fiber A1 at 54 inches

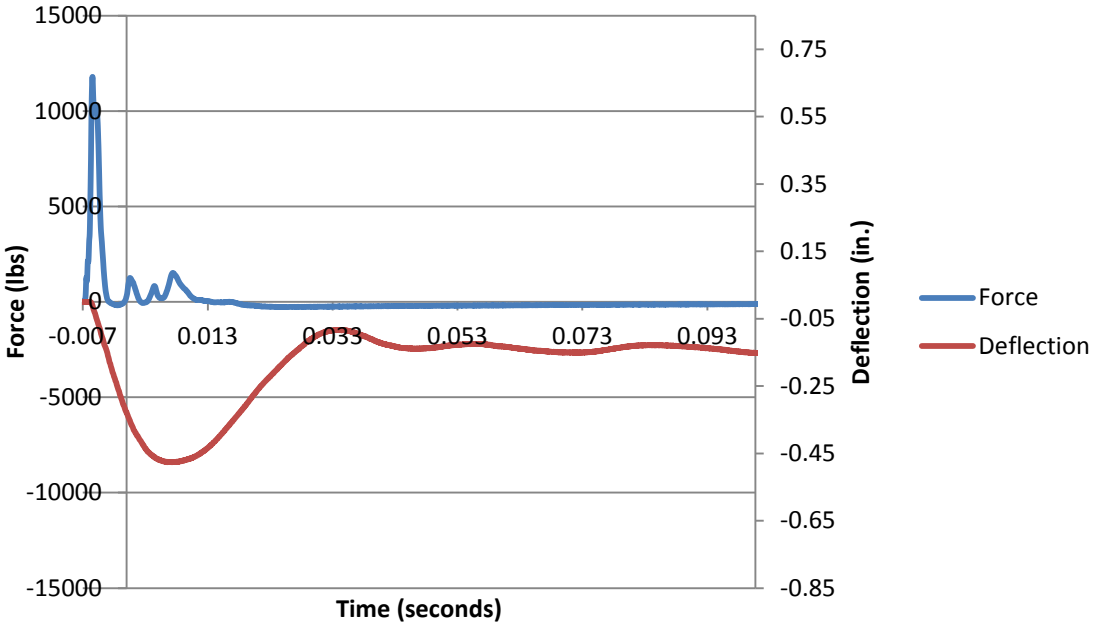

Figure B.61. Force and deflection vs. time for Fiber A1 at 60 inches

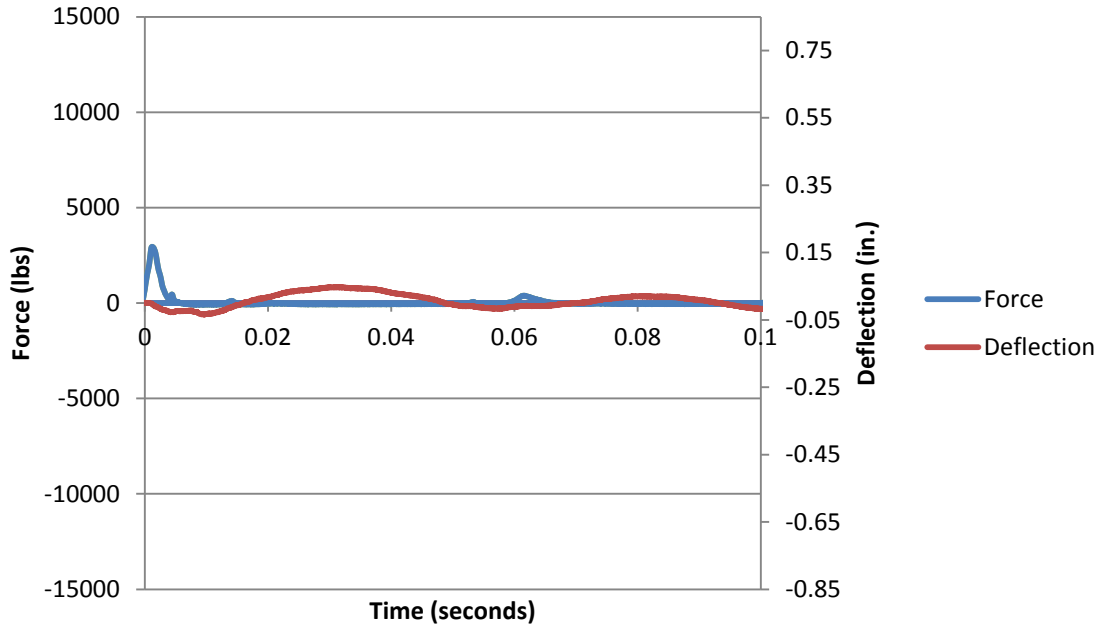

Figure B.62. Force and deflection vs. time for Fiber A2 at 3 inches

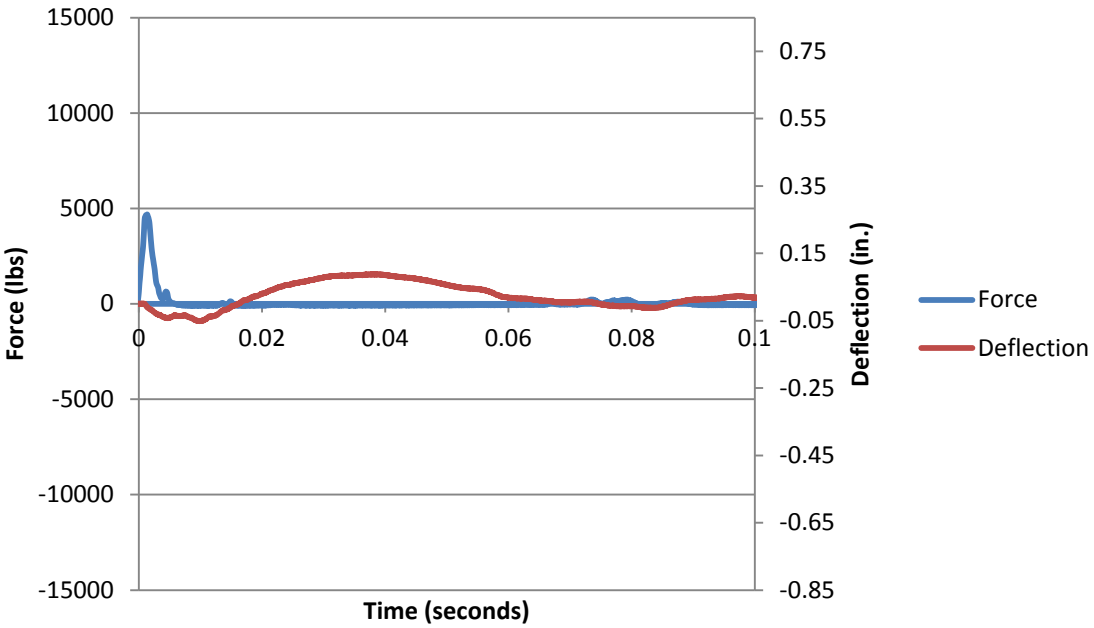

Figure B.63. Force and deflection vs. time for Fiber A2 at 6 inches

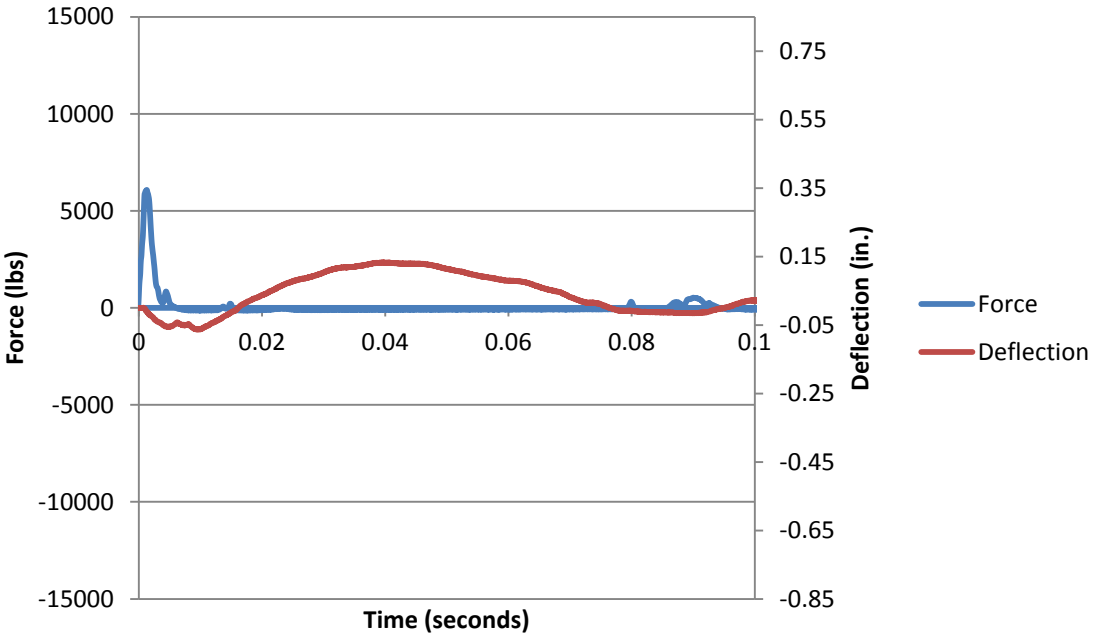

Figure B.64. Force and deflection vs. time for Fiber A2 at 9 inches

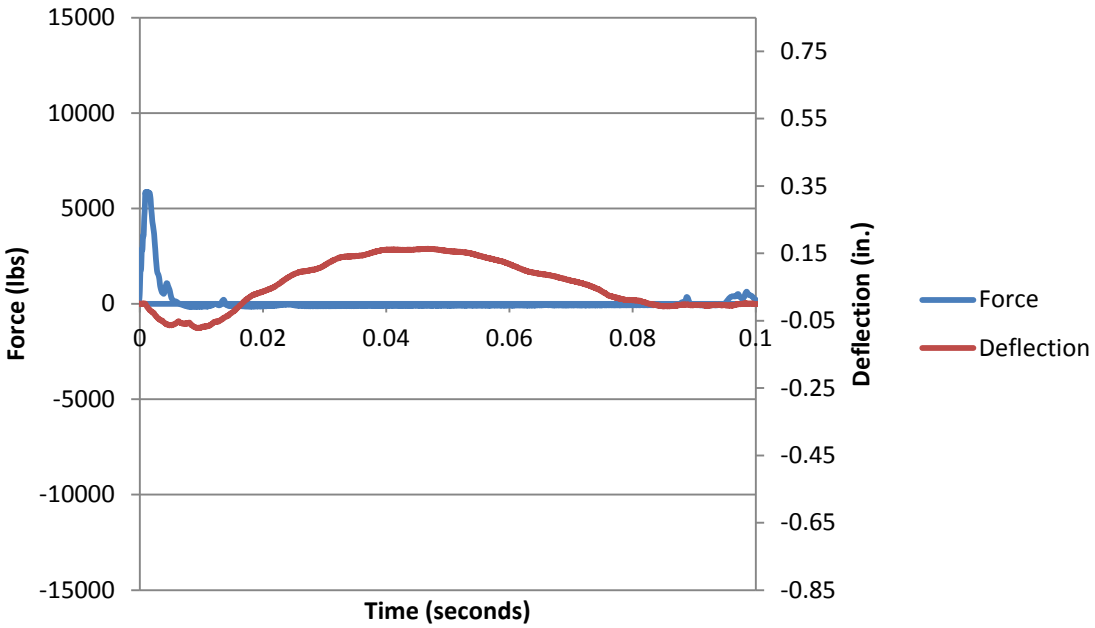

Figure B.65. Force and deflection vs. time for Fiber A2 at 12 inches

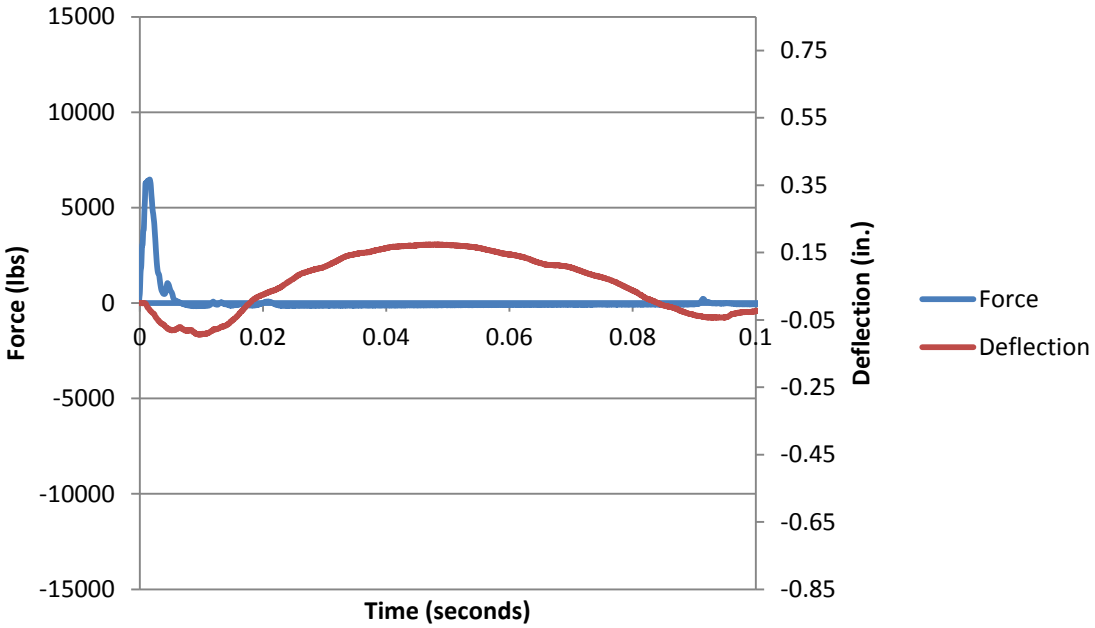

Figure B.66. Force and deflection vs. time for Fiber A2 at 15 inches

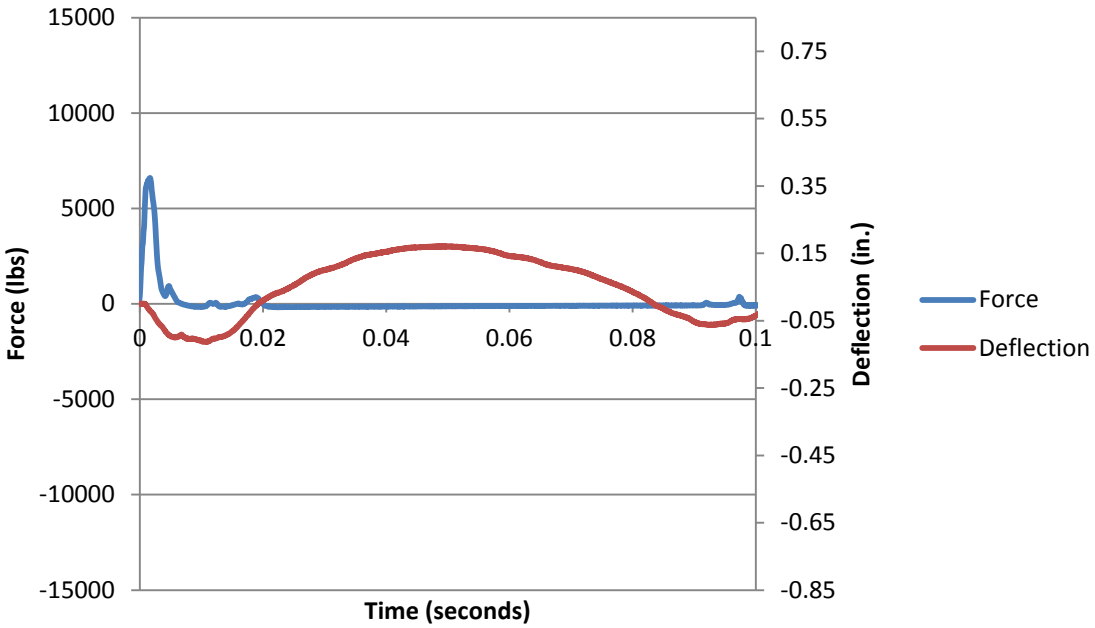

Figure B.67. Force and deflection vs. time for Fiber A2 at 18 inches

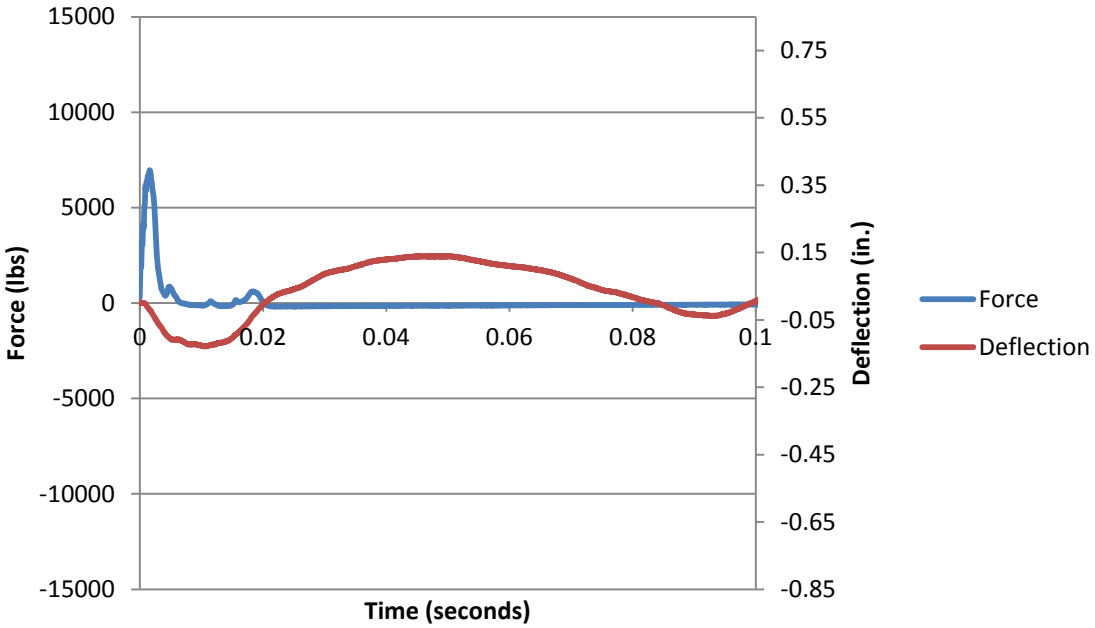

Figure B.68. Force and deflection vs. time for Fiber A2 at 21 inches

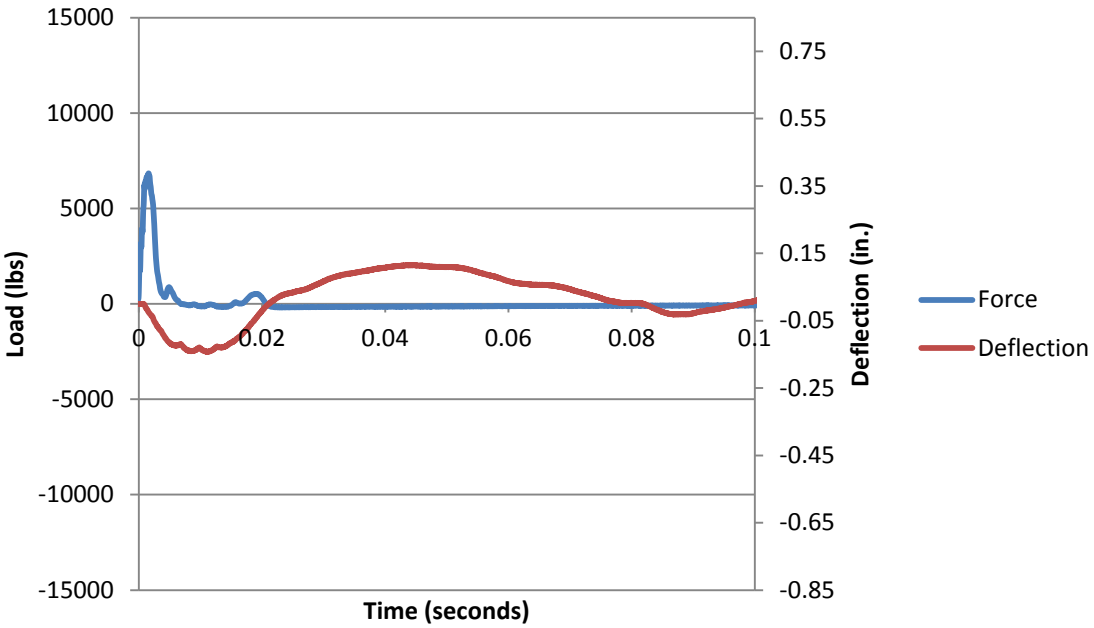

Figure B.69. Force and deflection vs. time for Fiber A2 at 24 inches

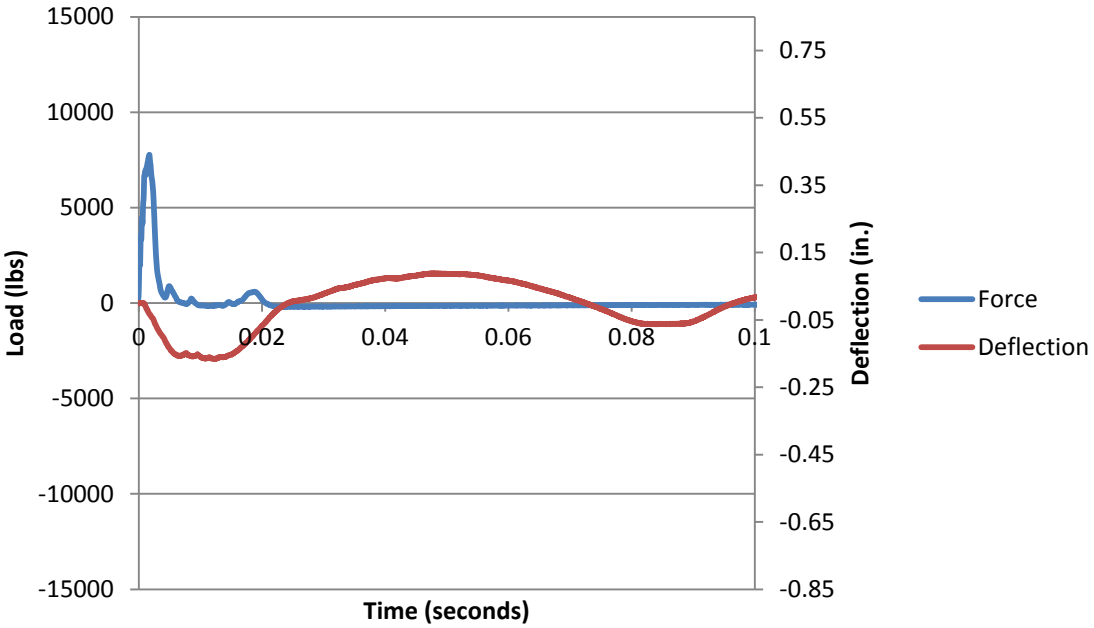

Figure B.70. Force and deflection vs. time for Fiber A2 at 30 inches

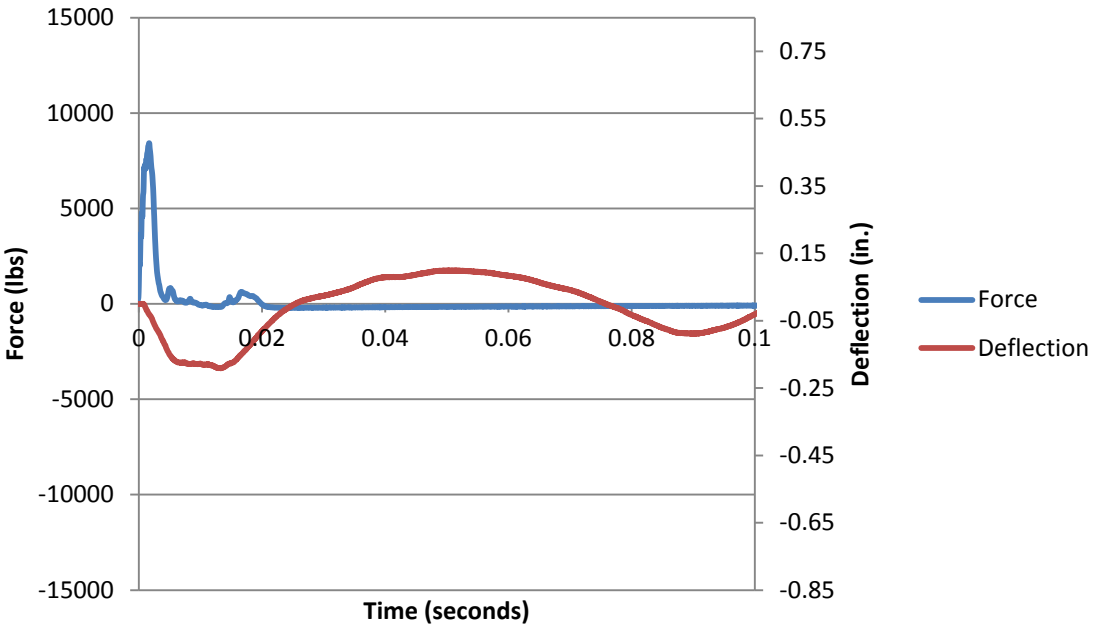

Figure B.71. Force and deflection vs. time for Fiber A2 at 36 inches

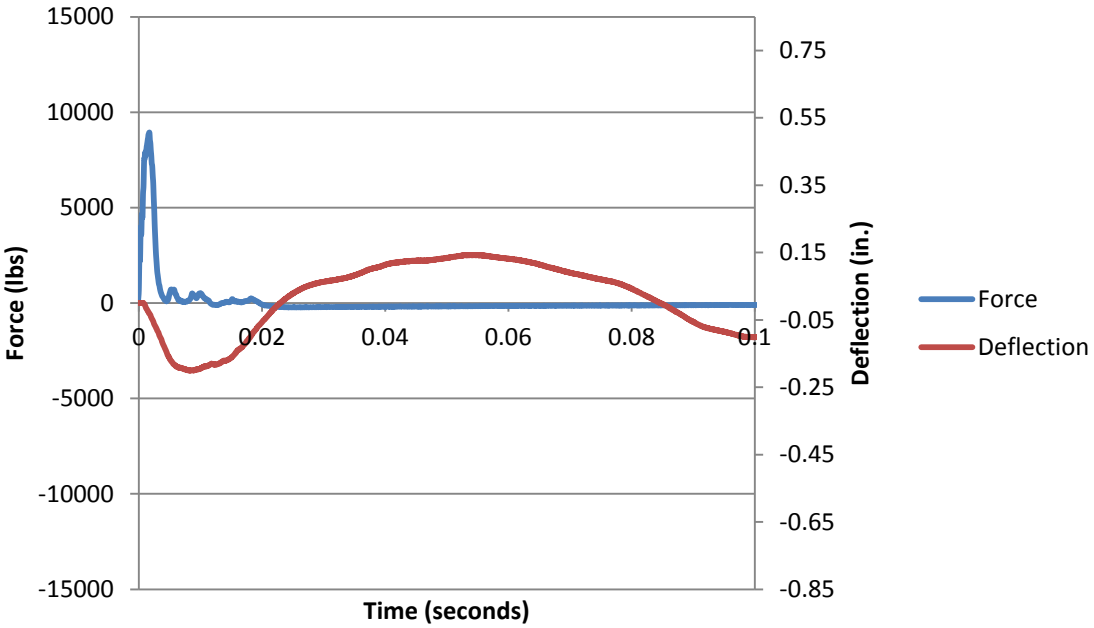

Figure B.72. Force and deflection vs. time for Fiber A2 at 42 inches

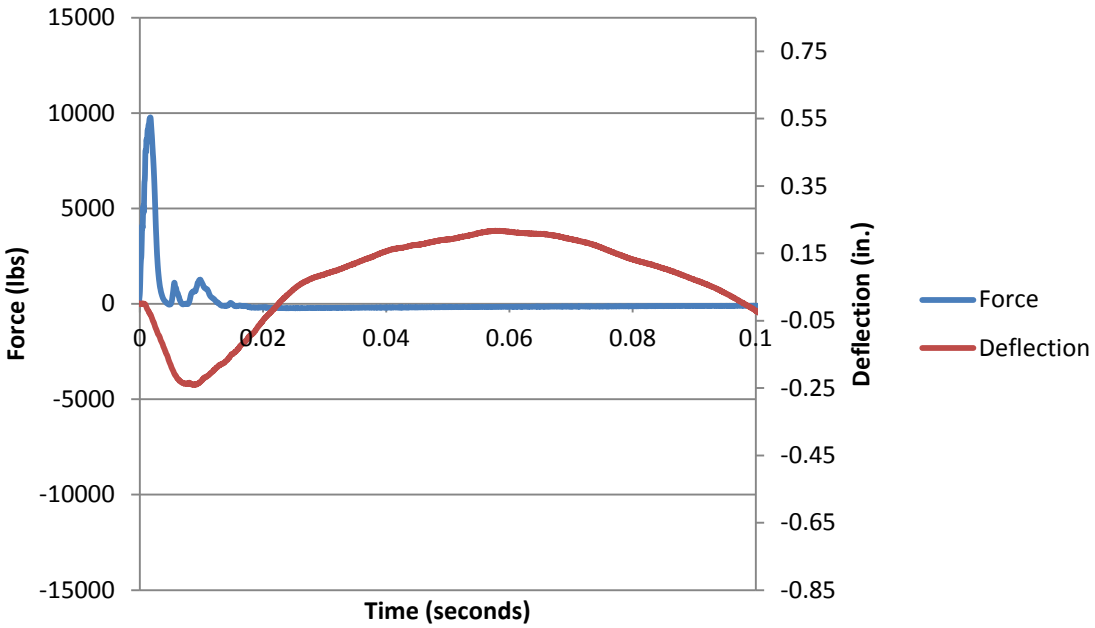

Figure B.73. Force and deflection vs. time for Fiber A2 at 48 inches

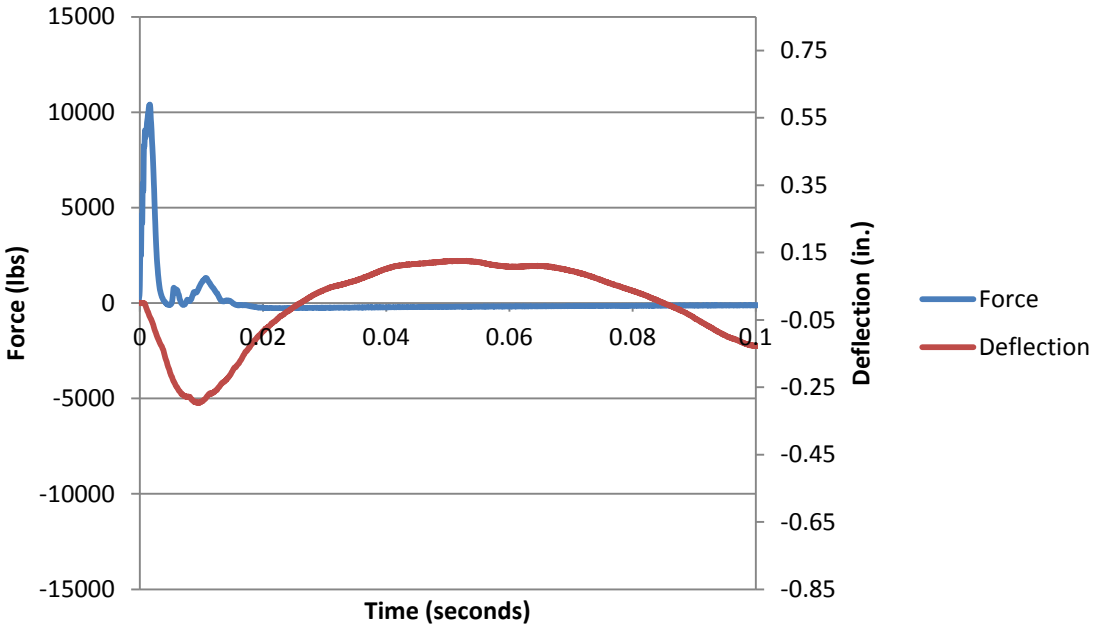

Figure B.74. Force and deflection vs. time for Fiber A2 at 54 inches

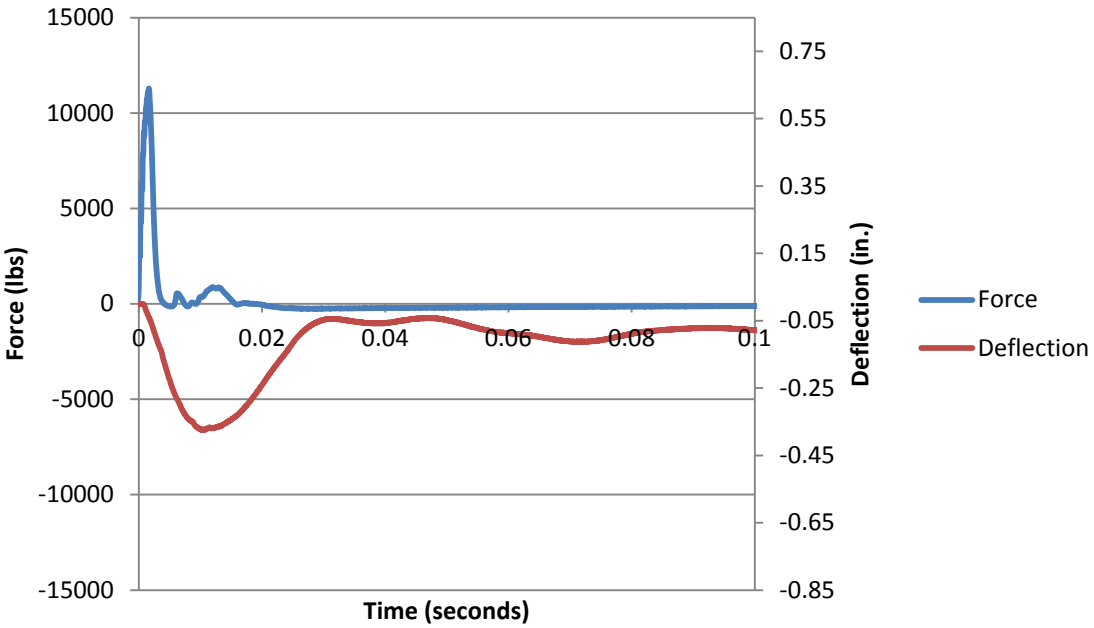

Figure B.75. Force and deflection vs. time for Fiber A2 at 60 inches

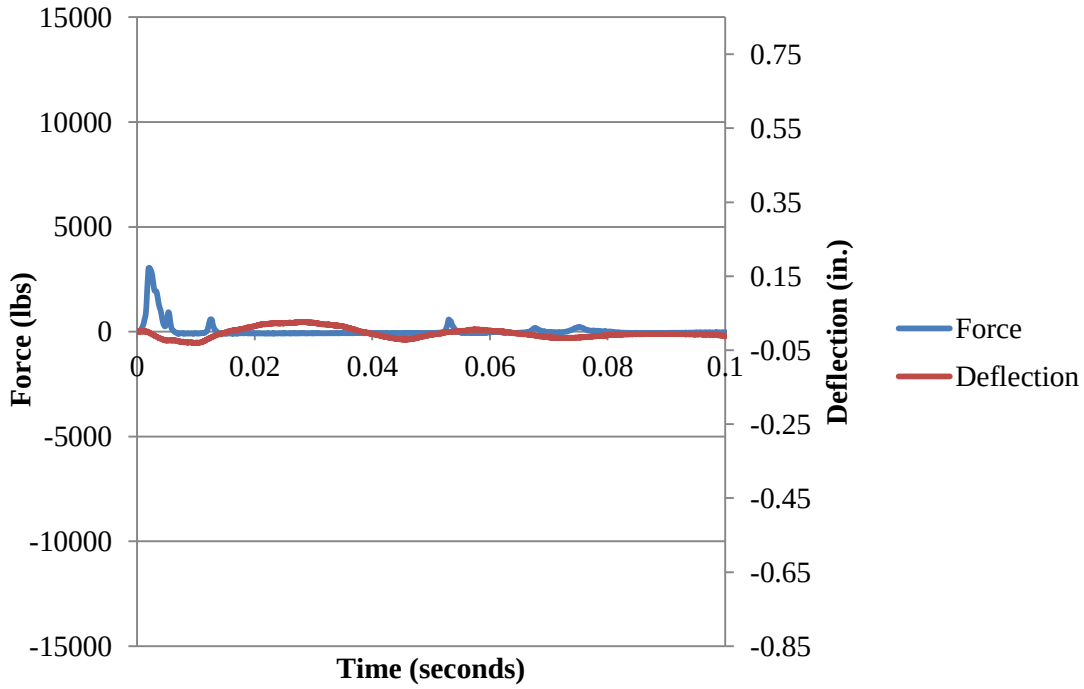

Figure B.76. Force and Deflection vs. Time for Fiber B1_1 at 3 in. (76 mm)

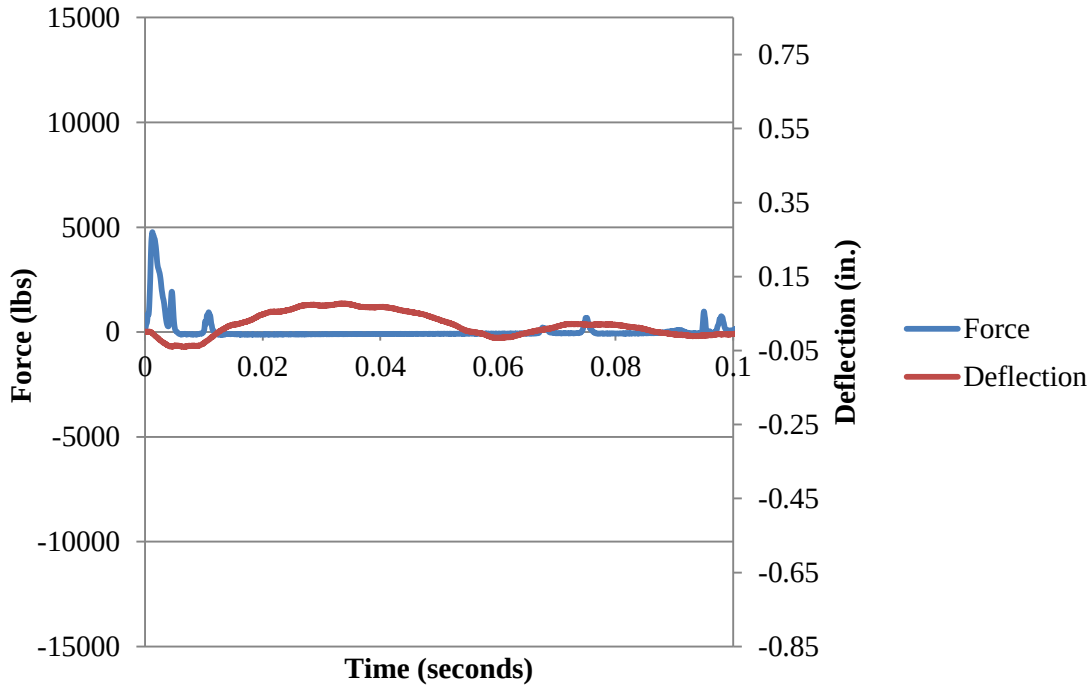

Figure B.77. Force and Deflection vs. Time for Fiber B1_1 at 6 in. (152 mm)

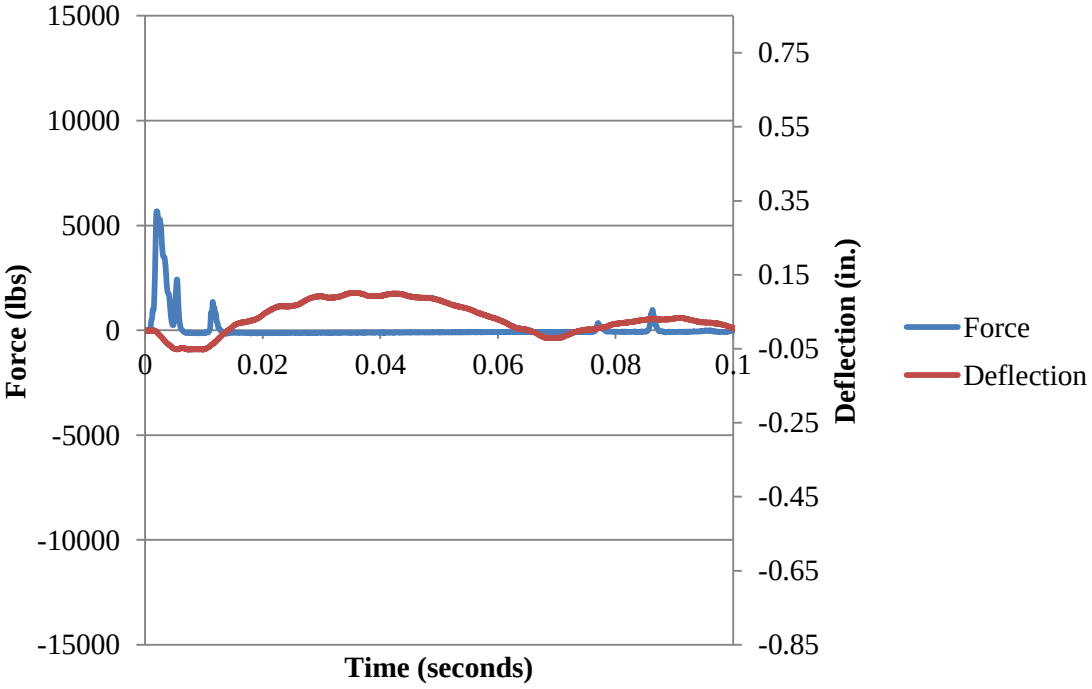

Figure B.78. Force and Deflection vs. Time for Fiber B1_1 at 9 in. (228 mm)

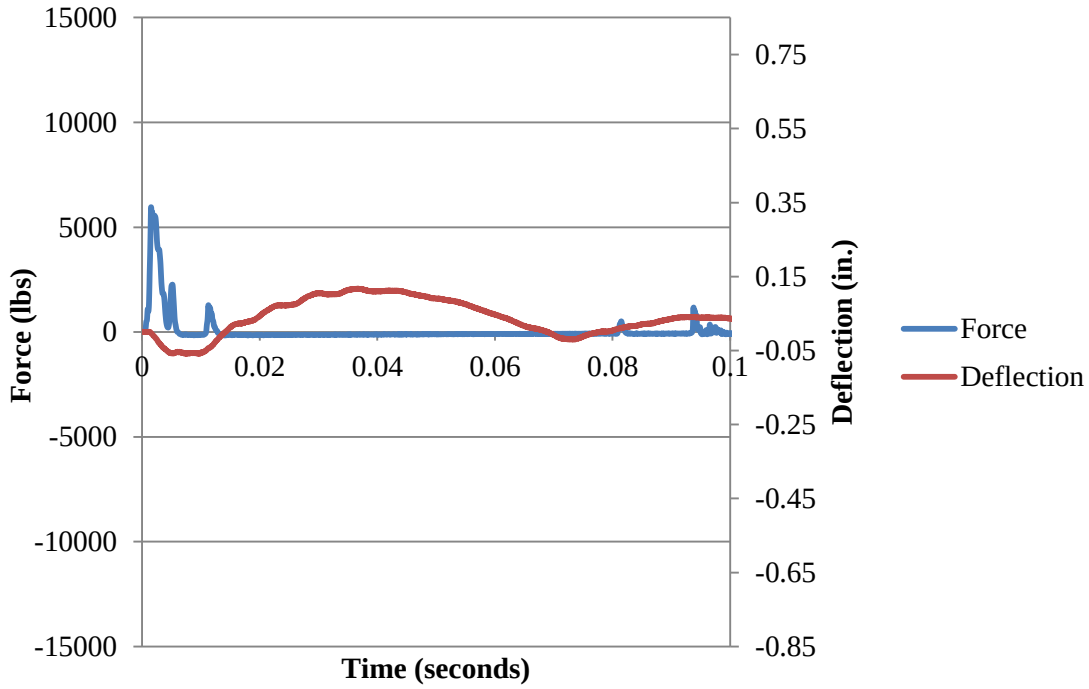

Figure B.79. Force and Deflection vs. Time for Fiber B1_1 at 12 in. (305 mm)

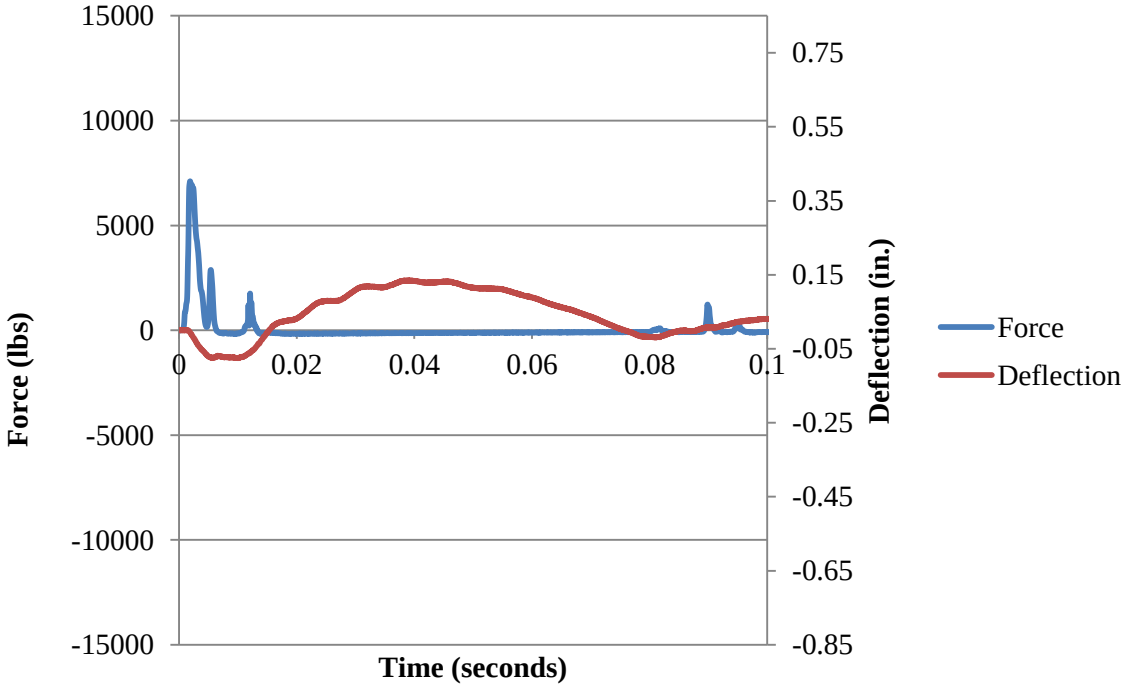

Figure B.80. Force and Deflection vs. Time for Fiber B1_1 at 15 in. (381 mm)

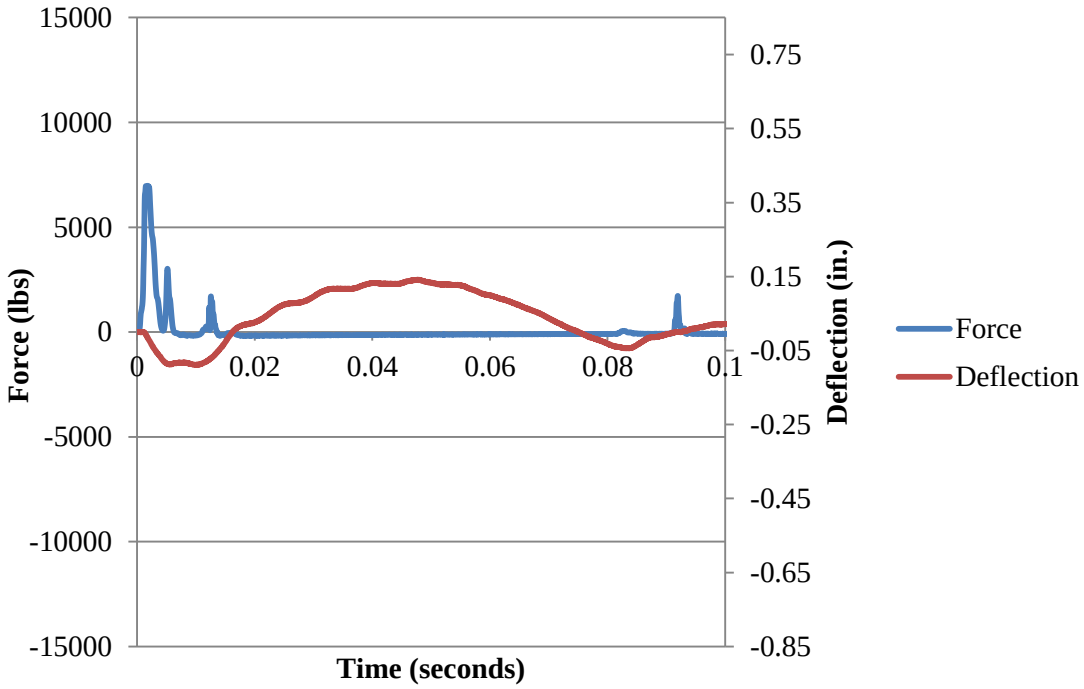

Figure B.81. Force and Deflection vs. Time for Fiber B1_1 at 18 in. (457 mm)

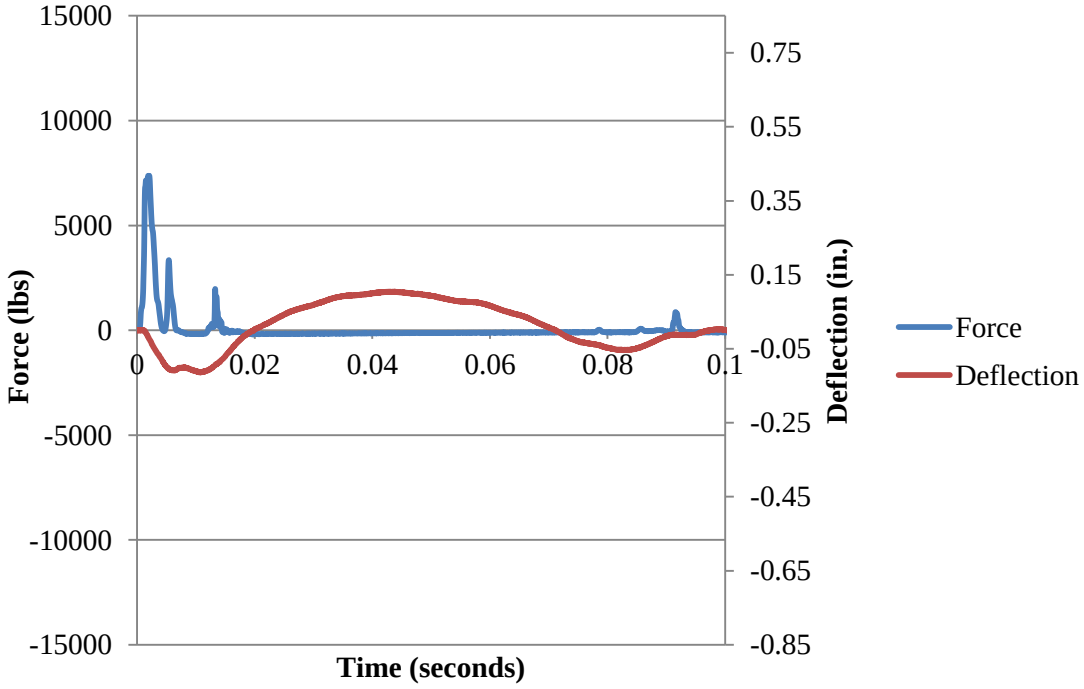

Figure B.82. Force and Deflection vs. Time for Fiber B1_1 at 21 in. (533 mm)

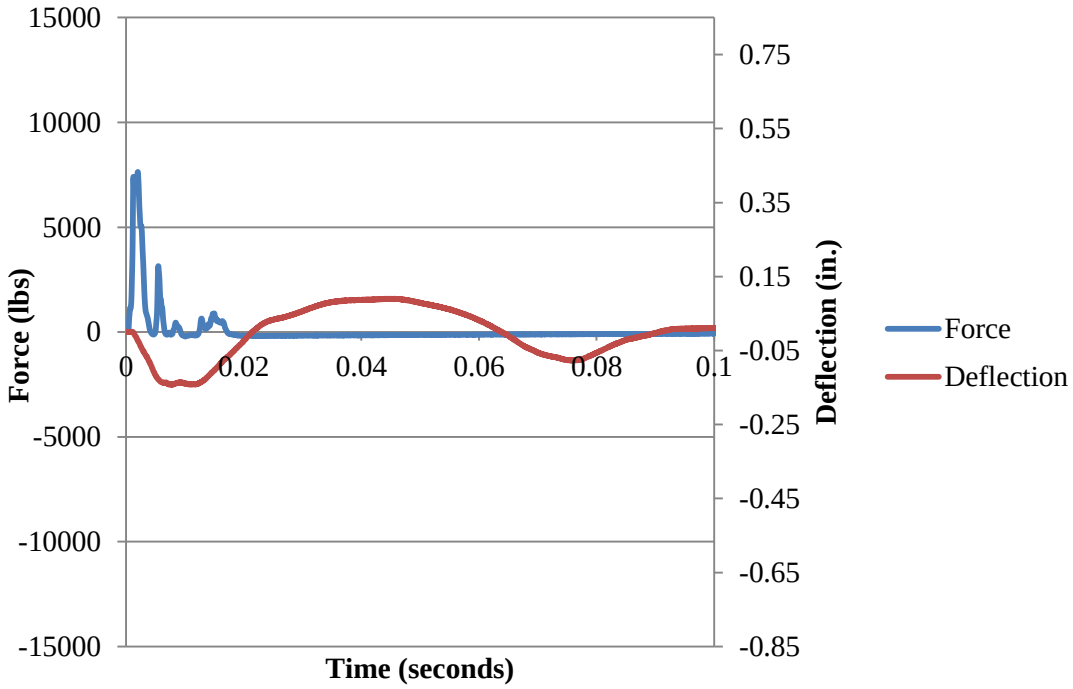

Figure B.83. Force and Deflection vs. Time for Fiber B1_1 at 24 in. (610 mm)

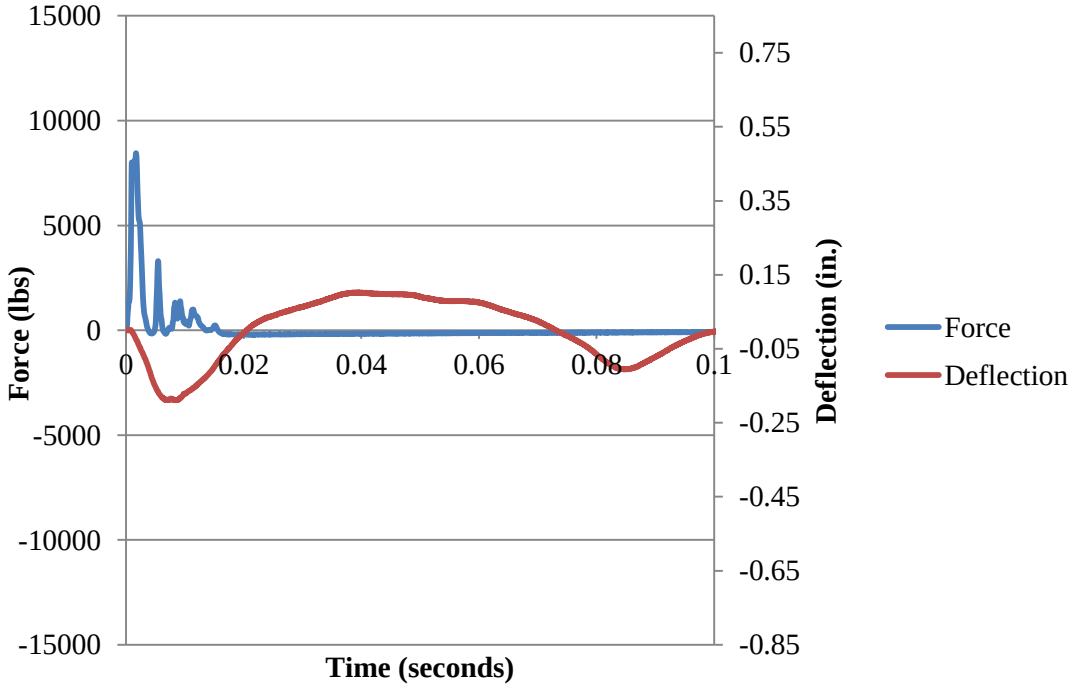

Figure B.84. Force and Deflection vs. Time for Fiber B1_1 at 30 in. (762 mm)

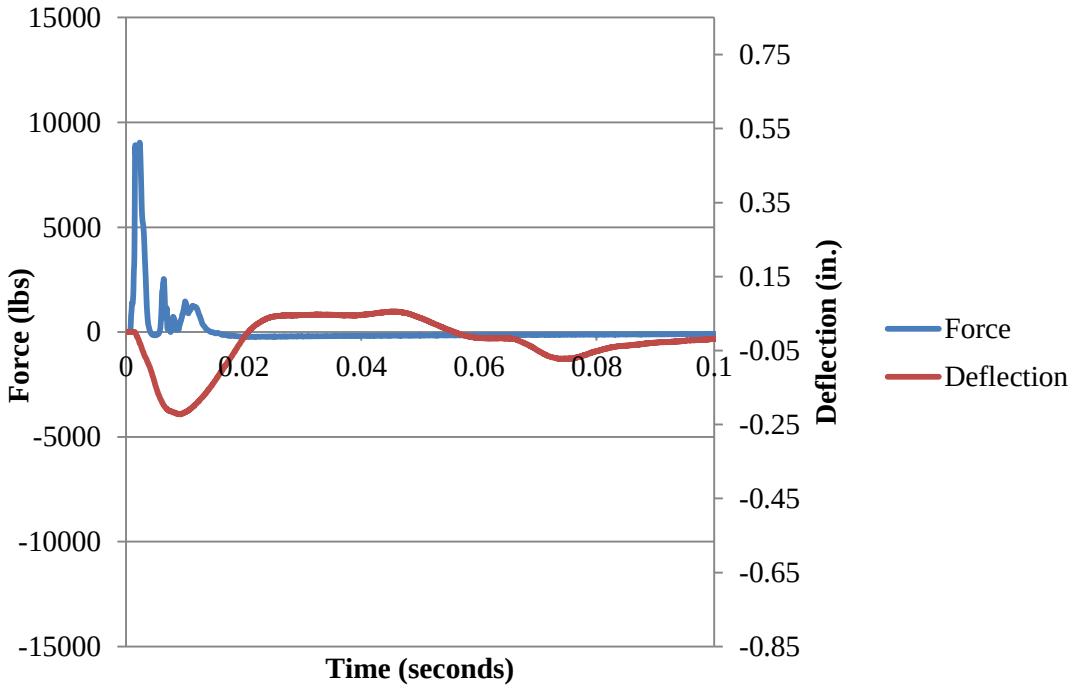

Figure B. 85. Force and Deflection vs. Time for Fiber B1_1 at 36 in. (914 mm)

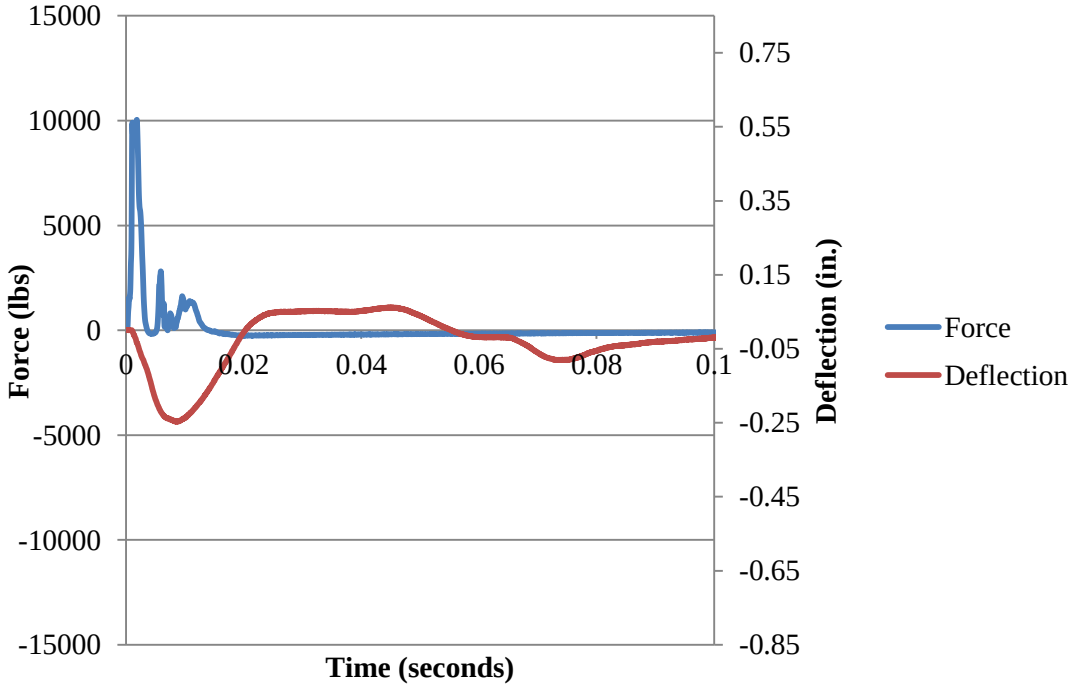

Figure B.86. Force and Deflection vs. Time for Fiber B1_1 at 42 in. (1067 mm)

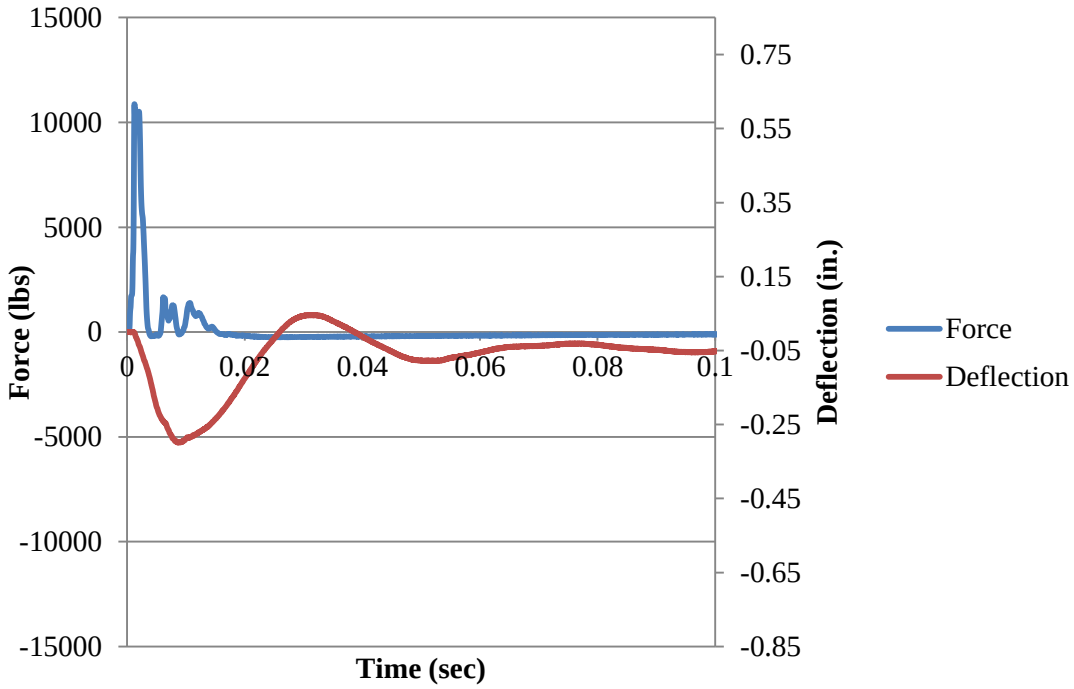

Figure B.87. Force and Deflection vs. Time for Fiber B1_1 at 48 in. (1219 mm)

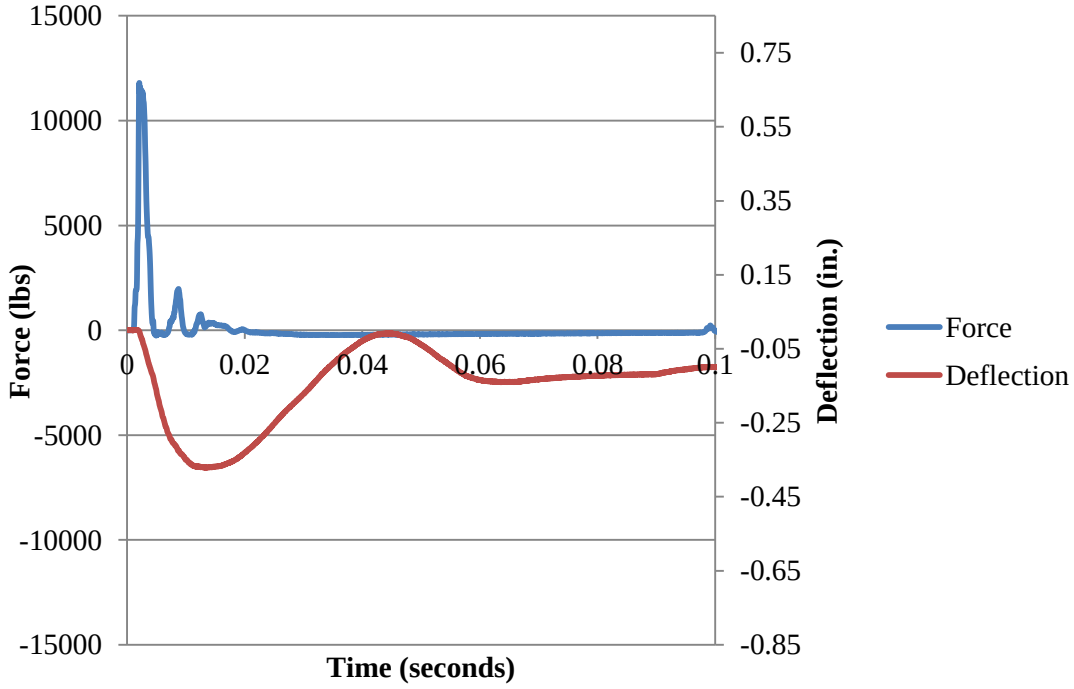

Figure B.88. Force and Deflection vs. Time for Fiber B1_1 at 54 in. (1372 mm)

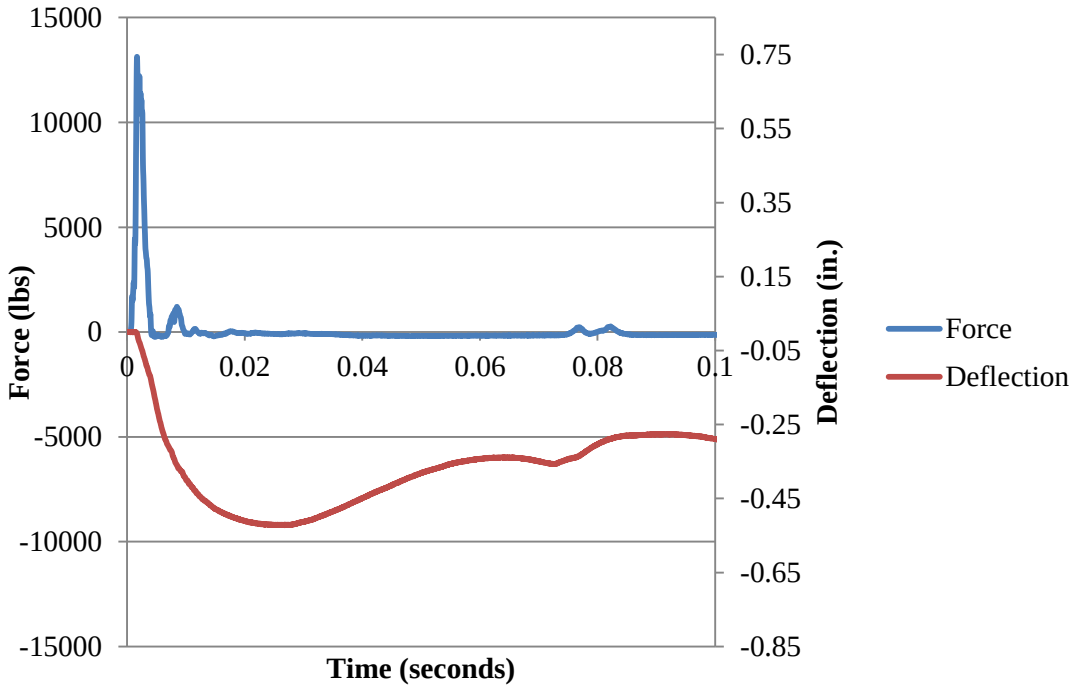

Figure B.89. Force and Deflection vs. Time for Fiber B1_1 at 60 in. (1524 mm)

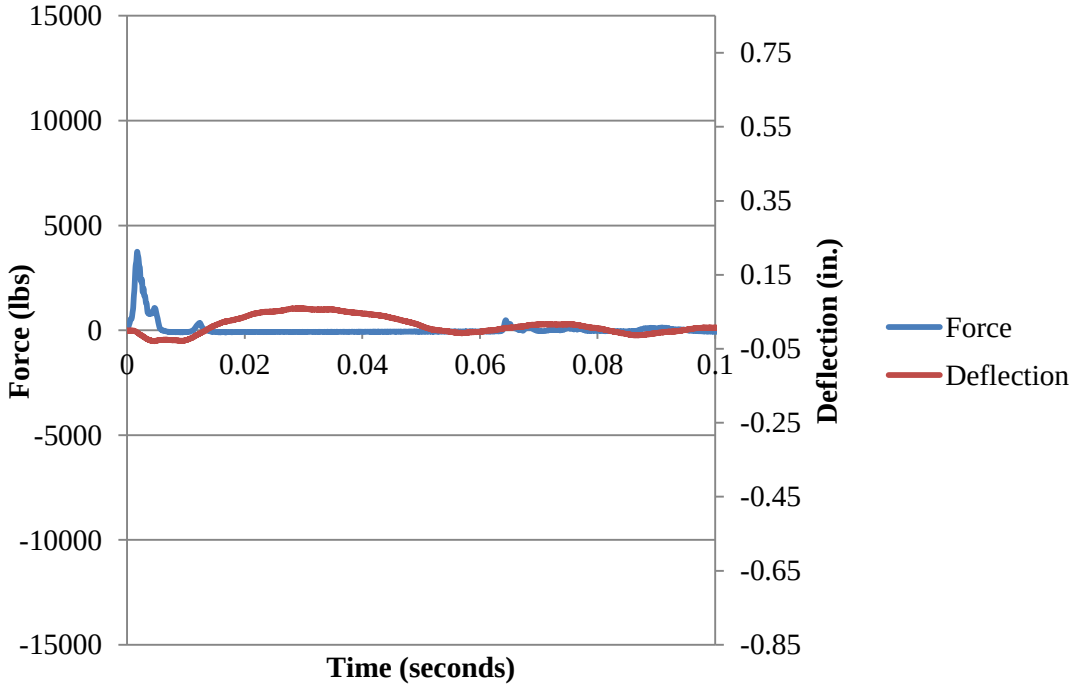

Figure B.90. Force and Deflection vs. Time for Fiber B1_2 at 3 in. (76 mm)

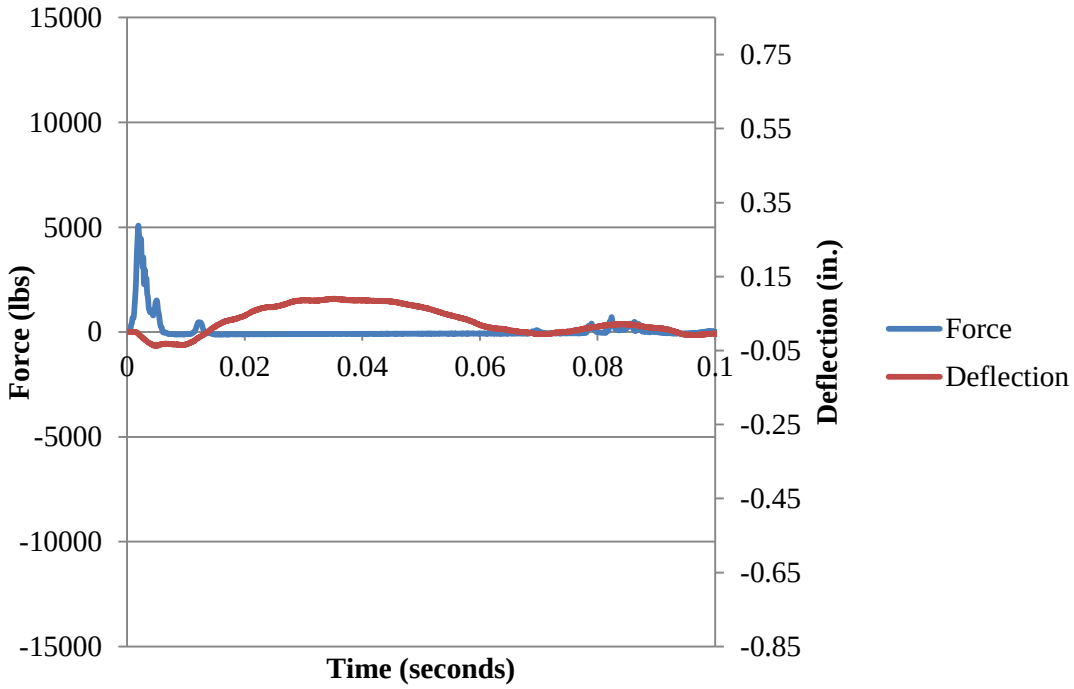

Figure B.91. Force and Deflection vs. Time for Fiber B1_2 at 6 in. (152 mm)

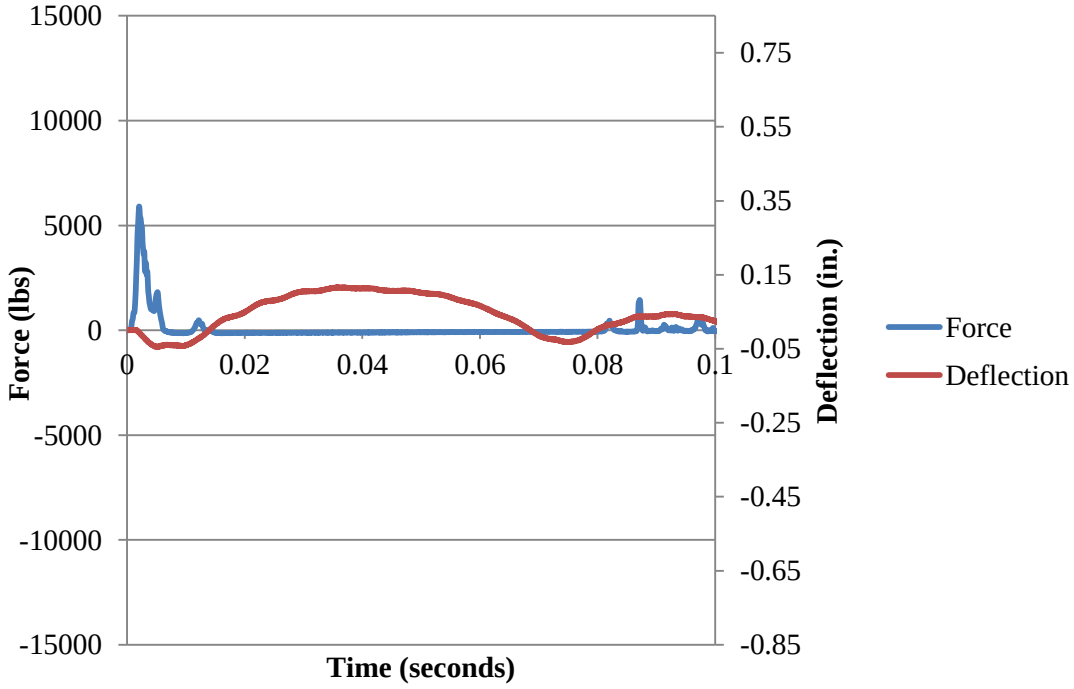

Figure B.92. Force and Deflection vs. Time for Fiber B1_2 at 9 in. (229 mm)

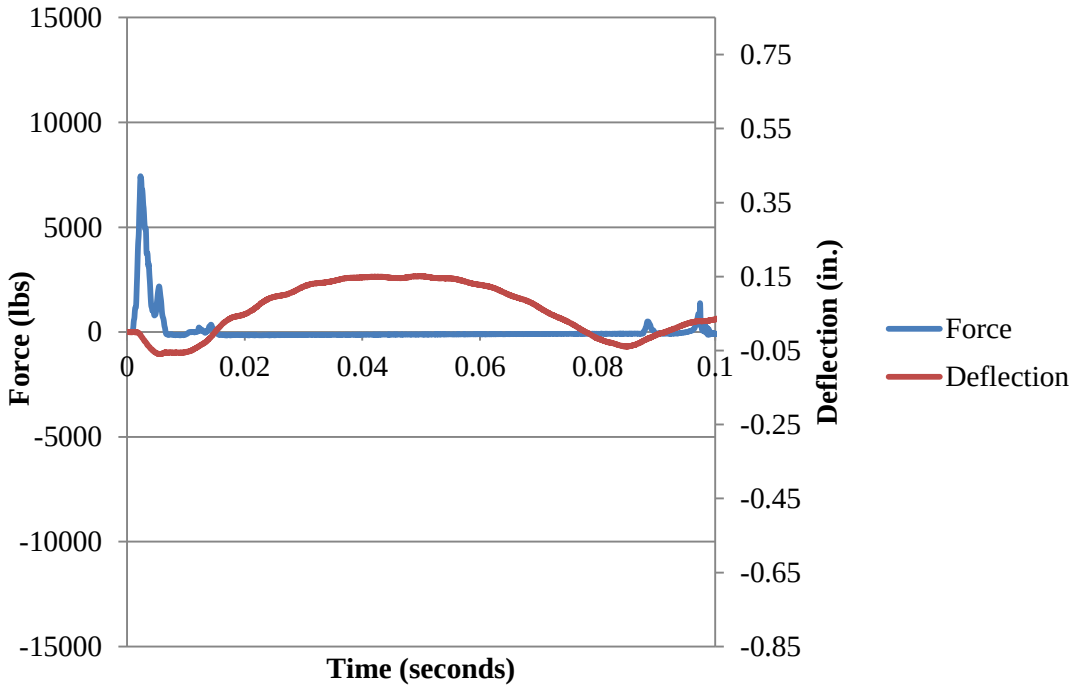

Figure B.93. Force and Deflection vs. Time for Fiber B1_2 at 12 in. (305 mm)

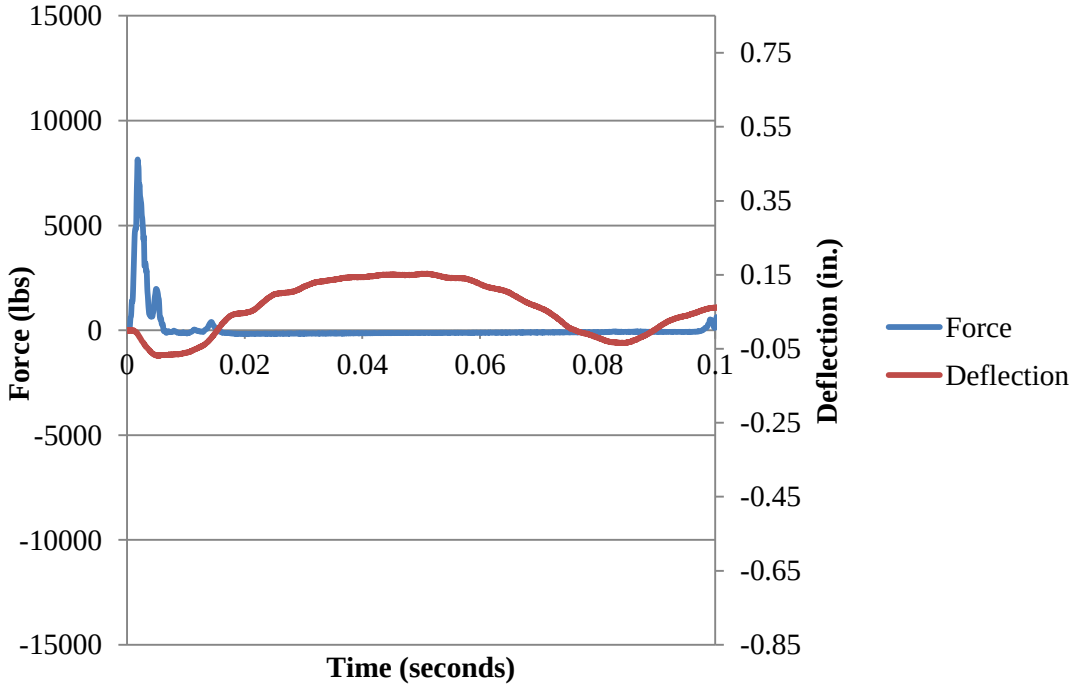

Figure B.94. Force and Deflection vs. Time for Fiber B1_2 at 15 in. (381 mm)

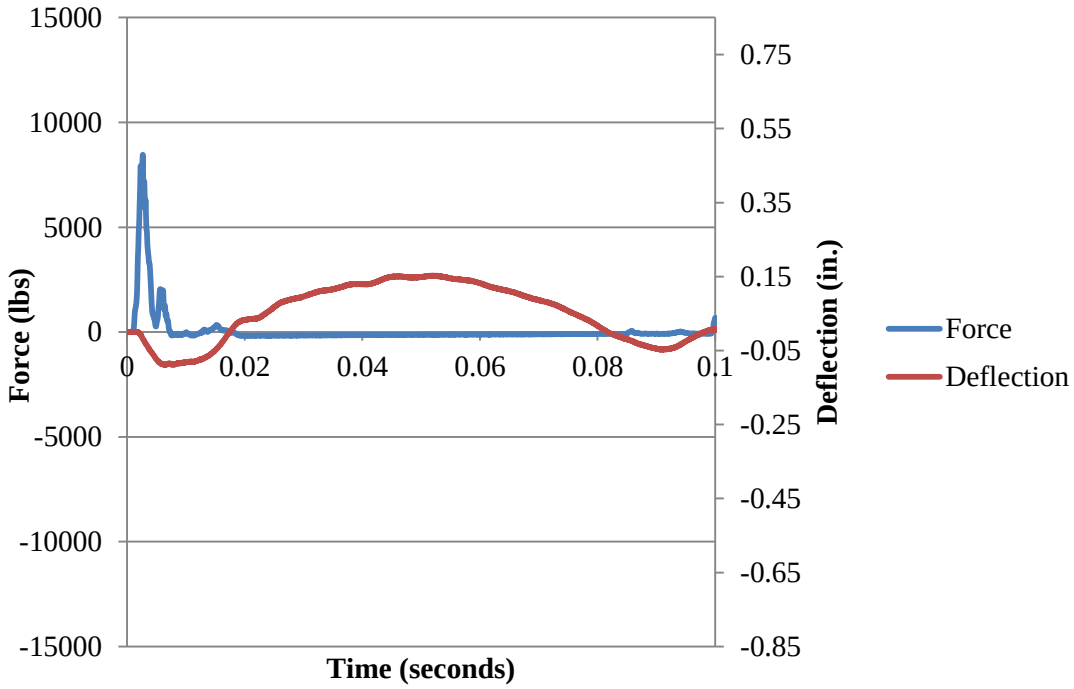

Figure B.95. Force and Deflection vs. Time for Fiber B1_2 at 18 in. (457 mm)

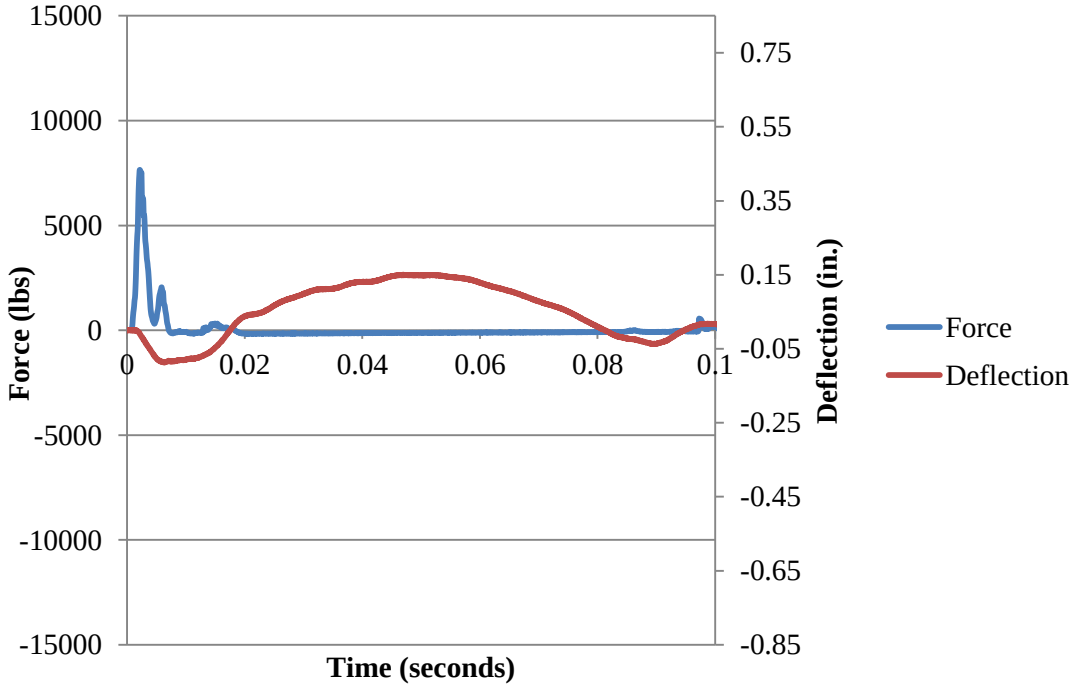

Figure B.96. Force and Deflection vs. Time for Fiber B1_2 at 21 in. (533 mm)

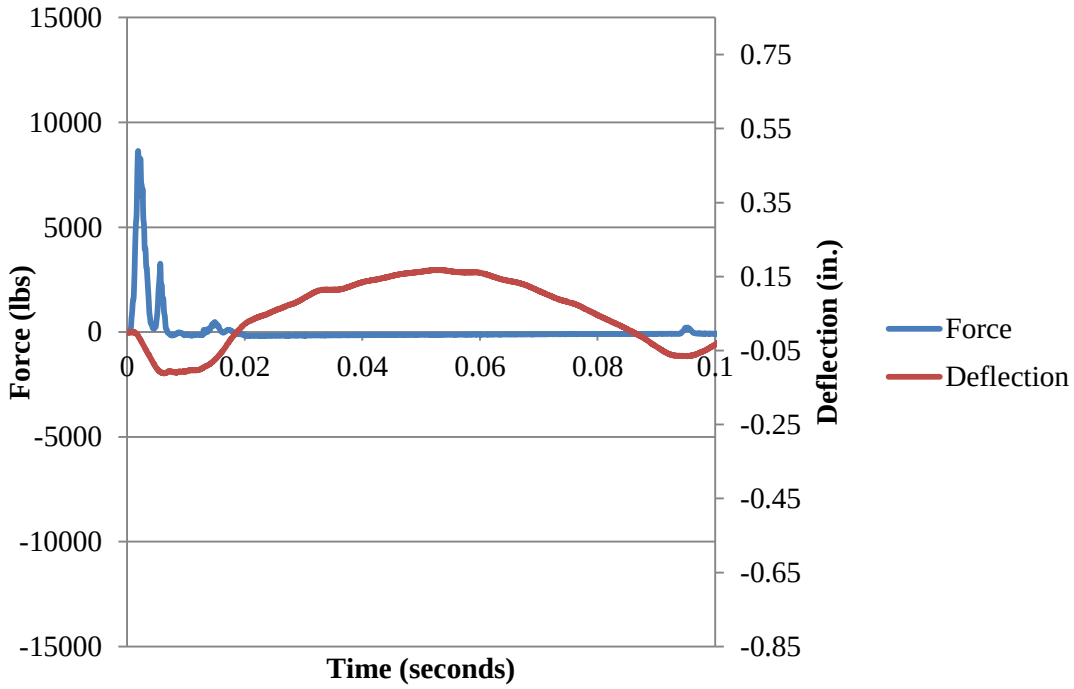

Figure B.97. Force and Deflection vs. Time for Fiber B1_2 at 24 in. (610 mm)

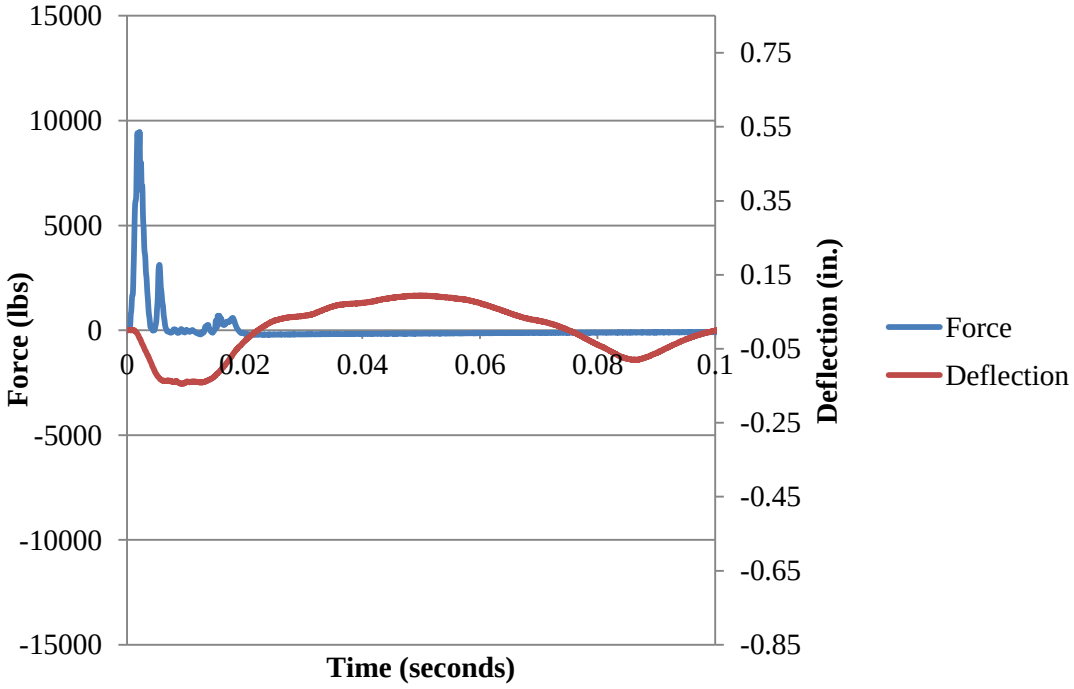

Figure B.98. Force and Deflection vs. Time for Fiber B1_2 at 30 in. (762 mm)

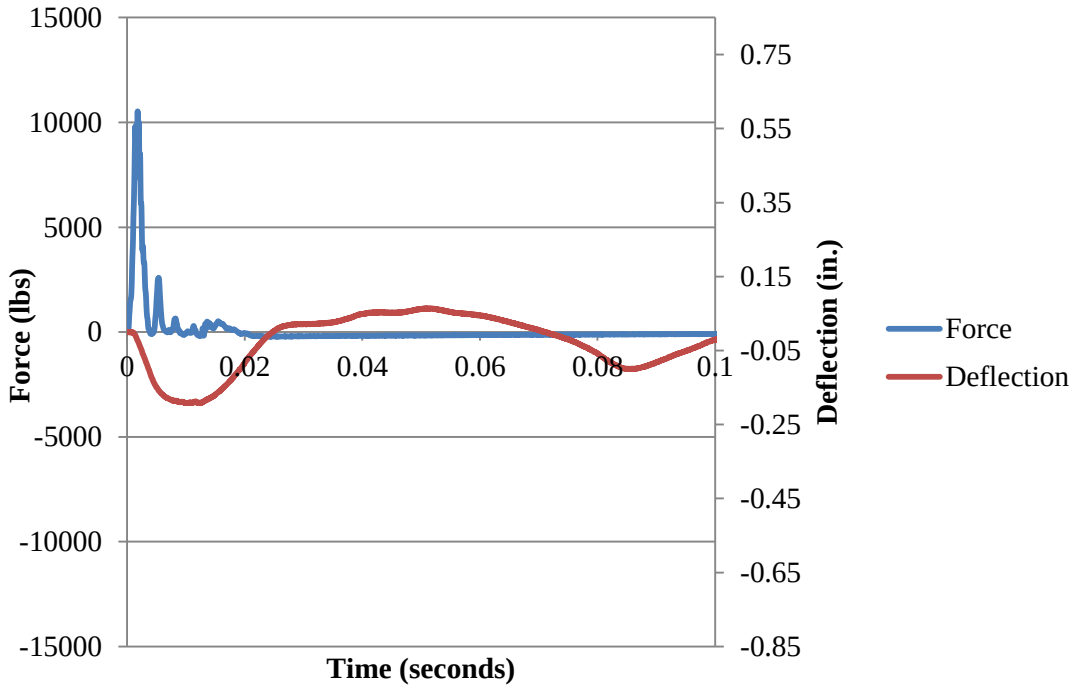

Figure B.99. Force and Deflection vs. Time for Fiber B1_2 at 36 in. (914 mm)

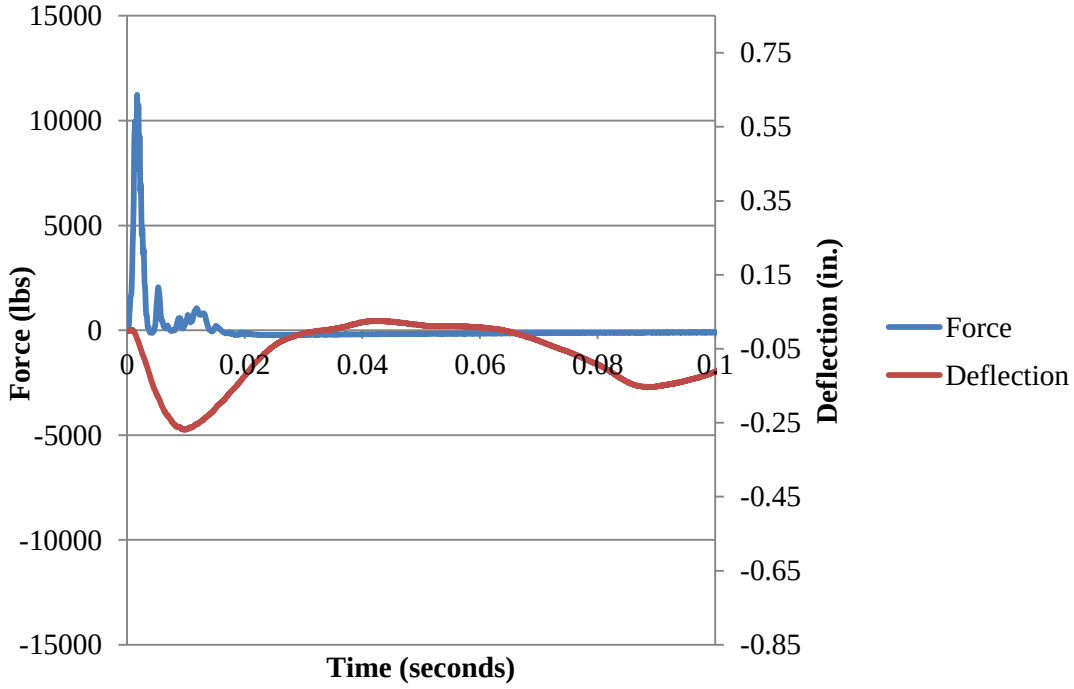

Figure B.100. Force and Deflection vs. Time for Fiber B1_2 at 42 in. (1067 mm)

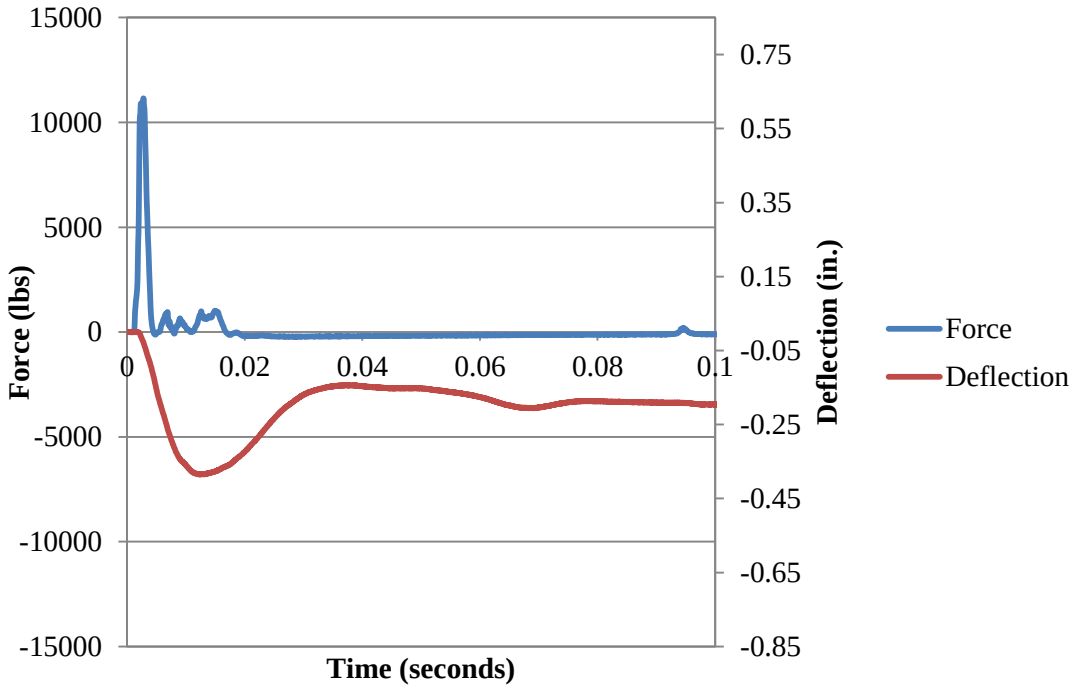

Figure B.101. Force and Deflection vs. Time for Fiber B1_2 at 48 in. (1219 mm)

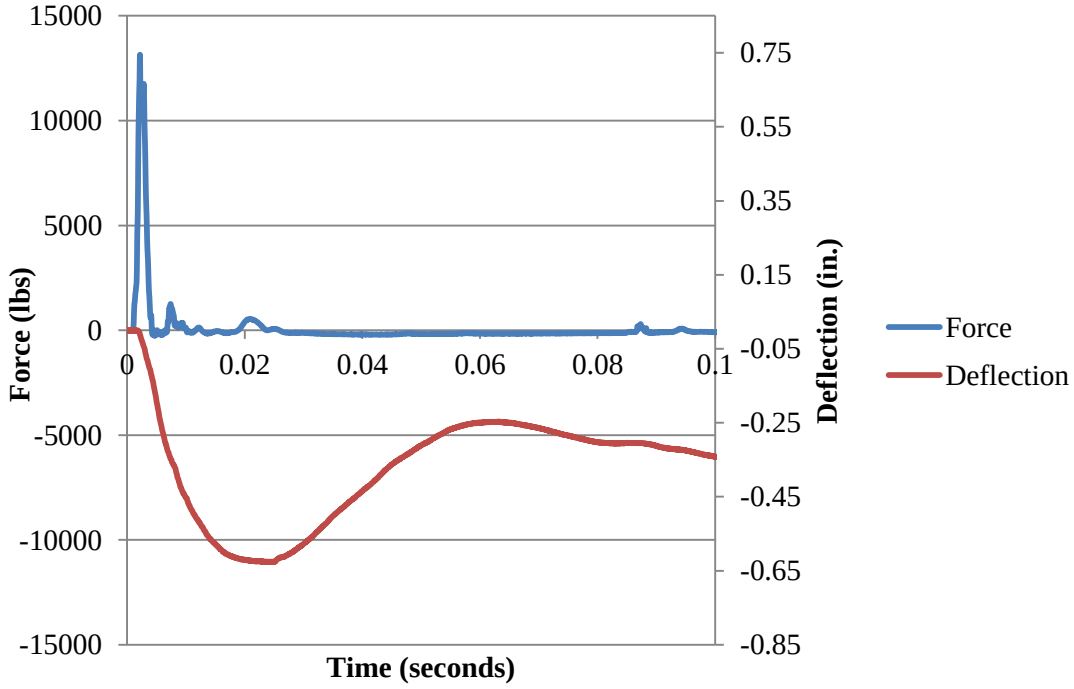

Figure B.102. Force and Deflection vs. Time for Fiber B1_2 at 54 in. (1372 mm)

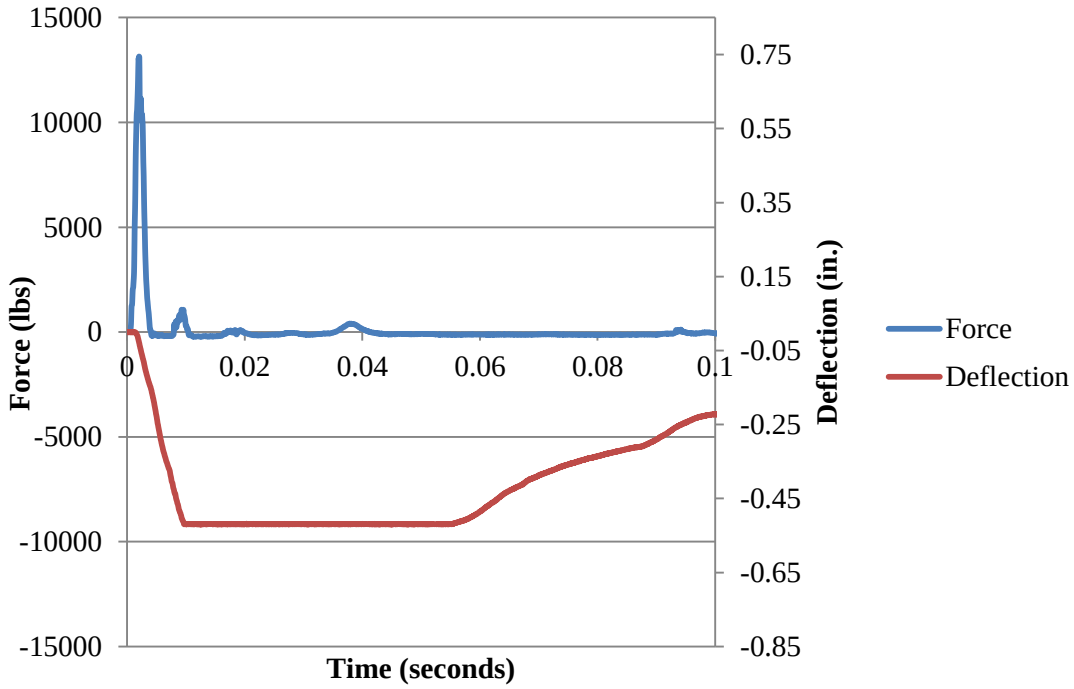

Figure B.103. Force and Deflection vs. Time for Fiber B1_2 at 60 in. (1524 mm)

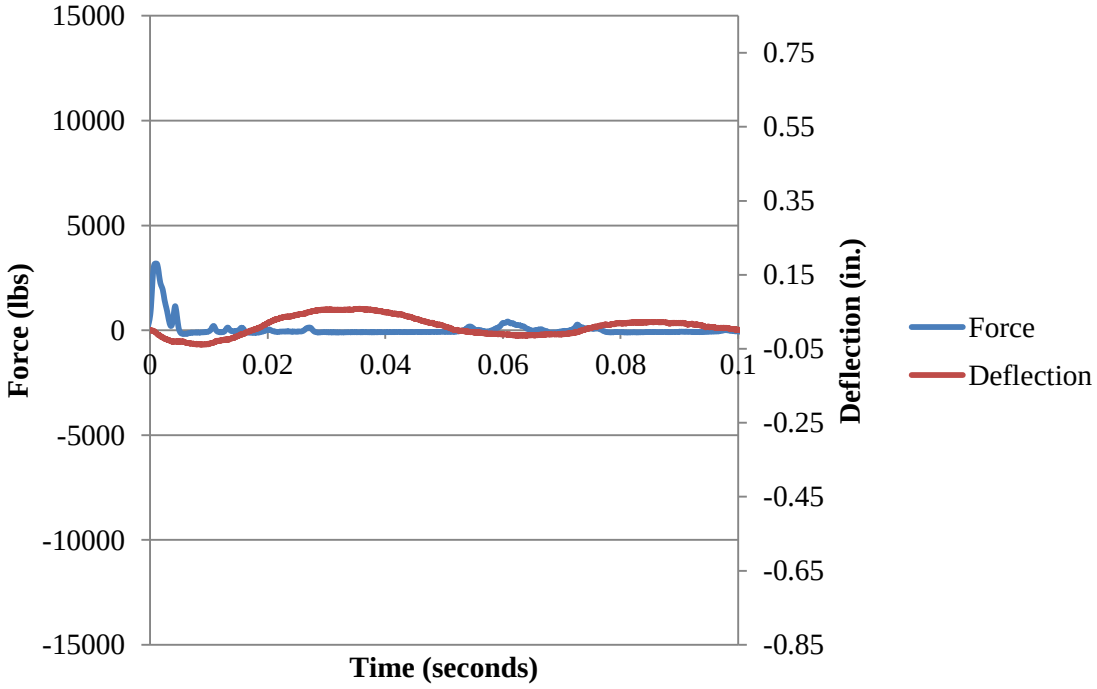

Figure B.104. Force and Deflection vs. Time for Fiber B2_1 at 3 in. (76 mm)

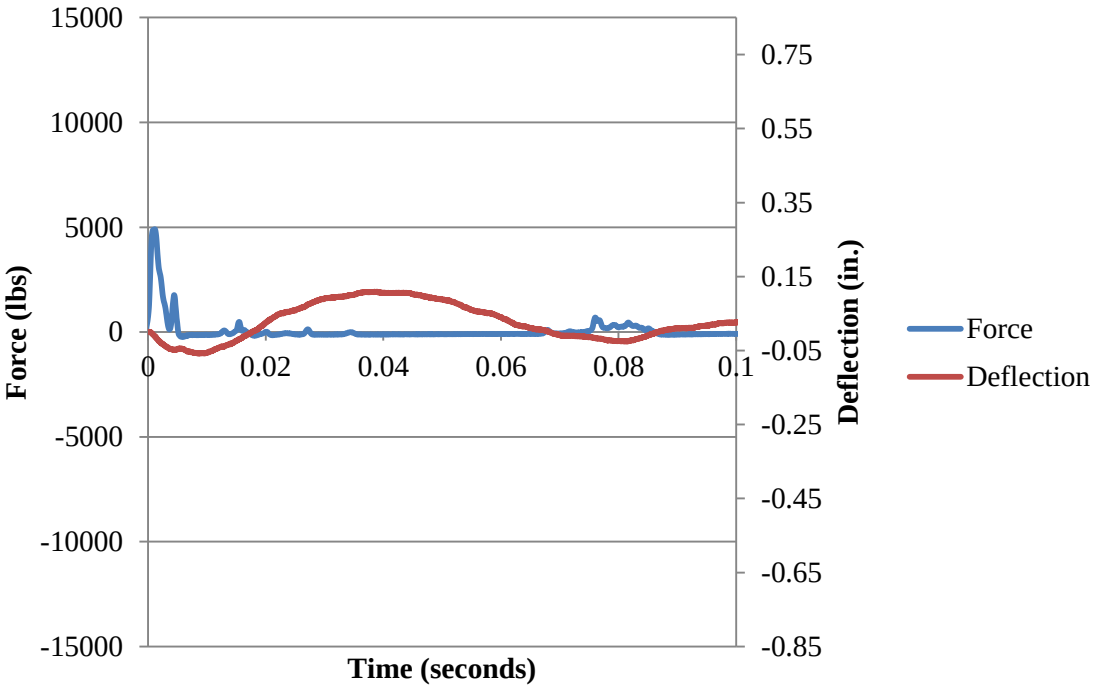

Figure B.105. Force and Deflection vs. Time for Fiber B2_1 at 6 in. (152 mm)

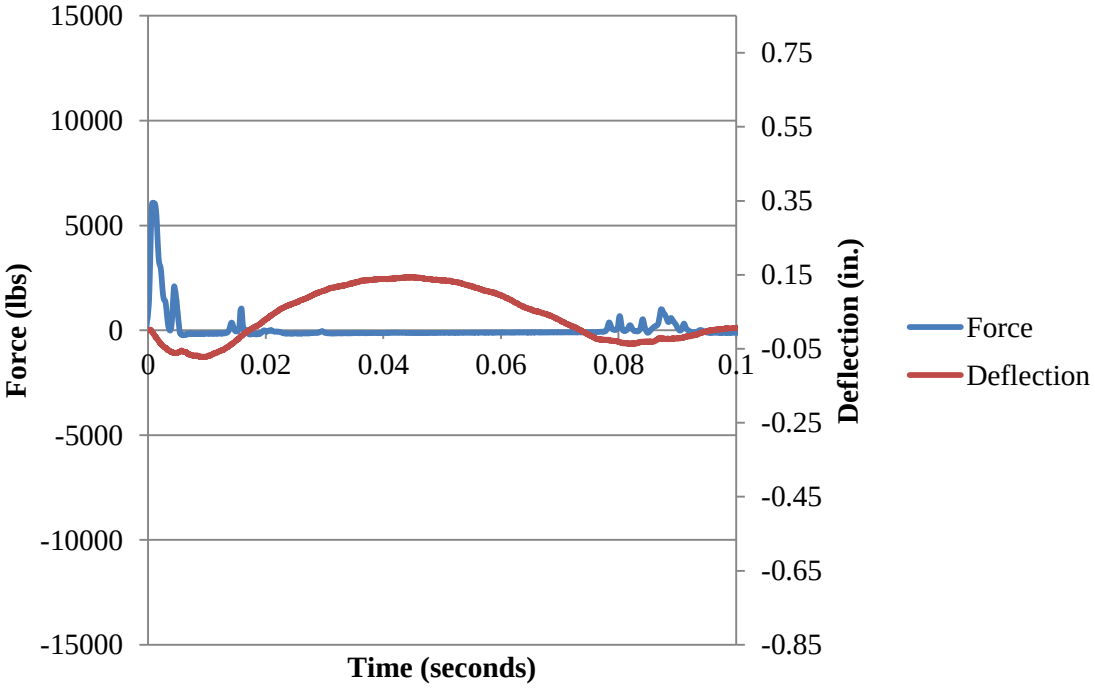

Figure B.106. Force and Deflection vs. Time for Fiber B2_1 at 9 in. (229 mm)

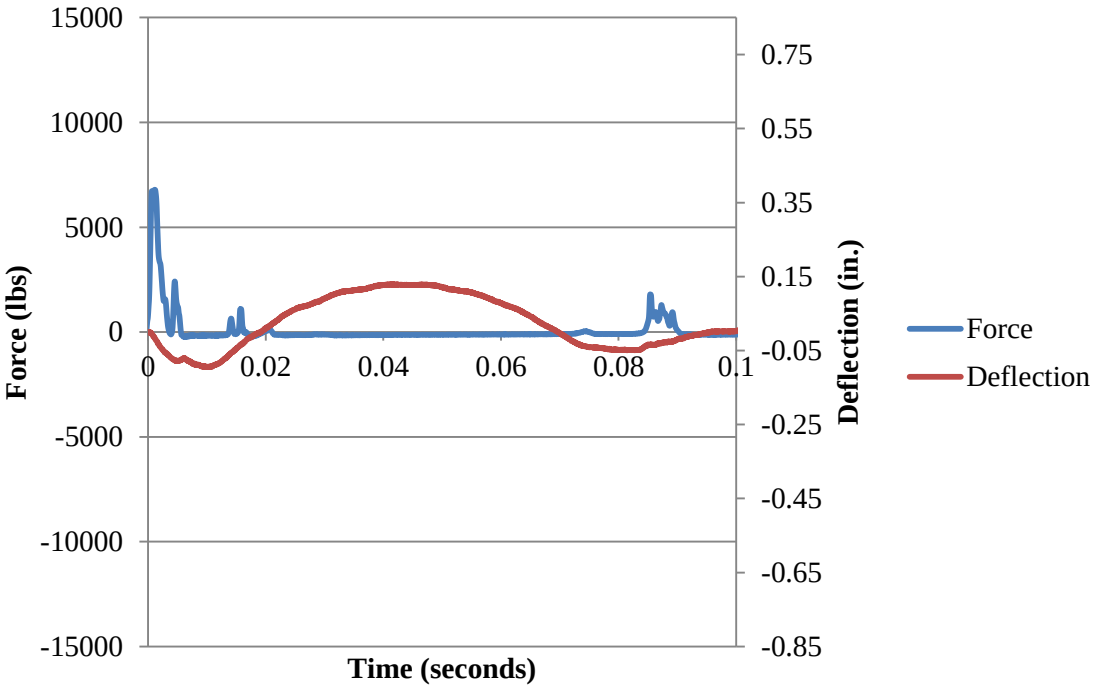

Figure B.107. Force and Deflection vs. Time for Fiber B2_1 at 12 in. (305 mm)

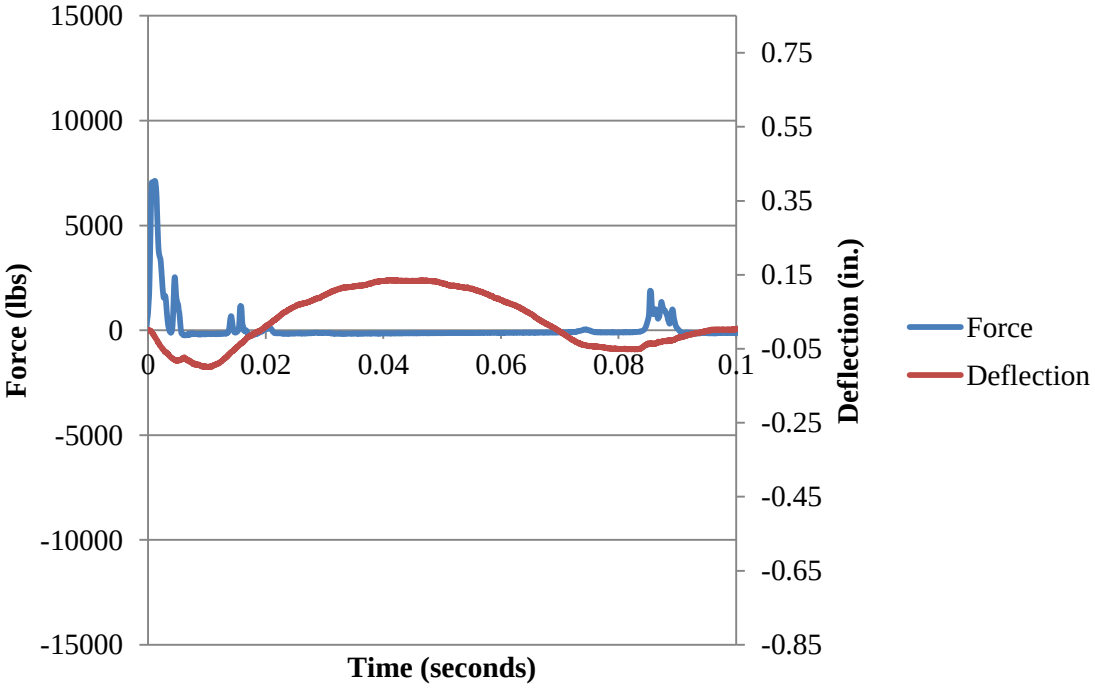

Figure B.108. Force and Deflection vs. Time for Fiber B2_1 at 15 in. (381 mm)

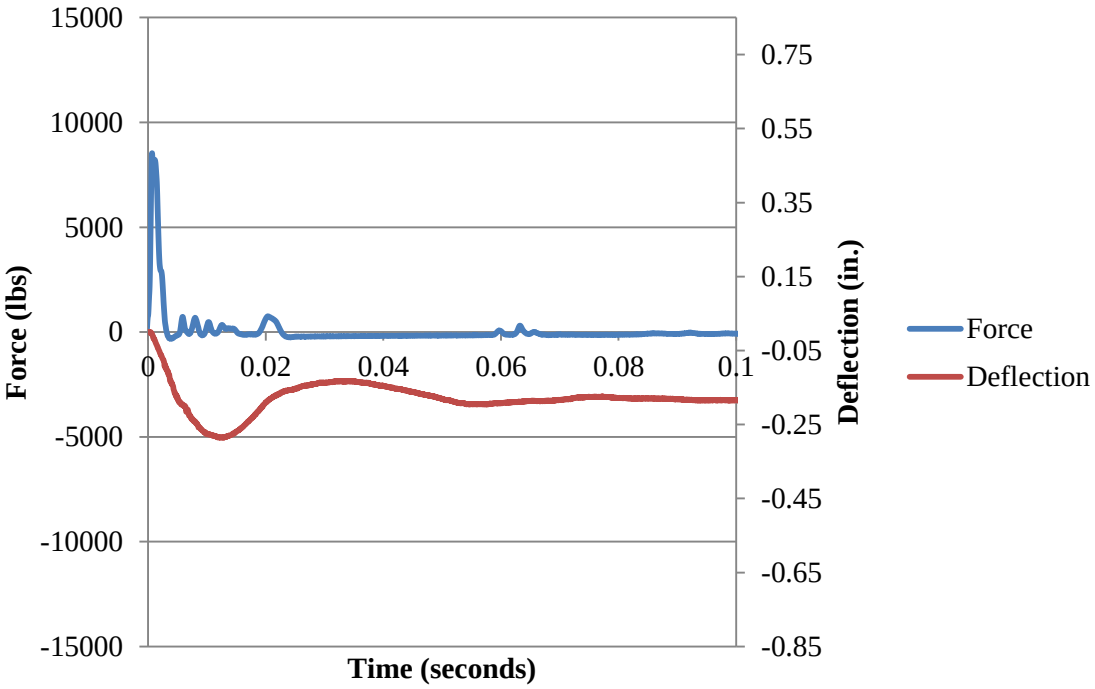

Figure B.109. Force and Deflection vs. Time for Fiber B2_1 at 18 in. (457 mm)

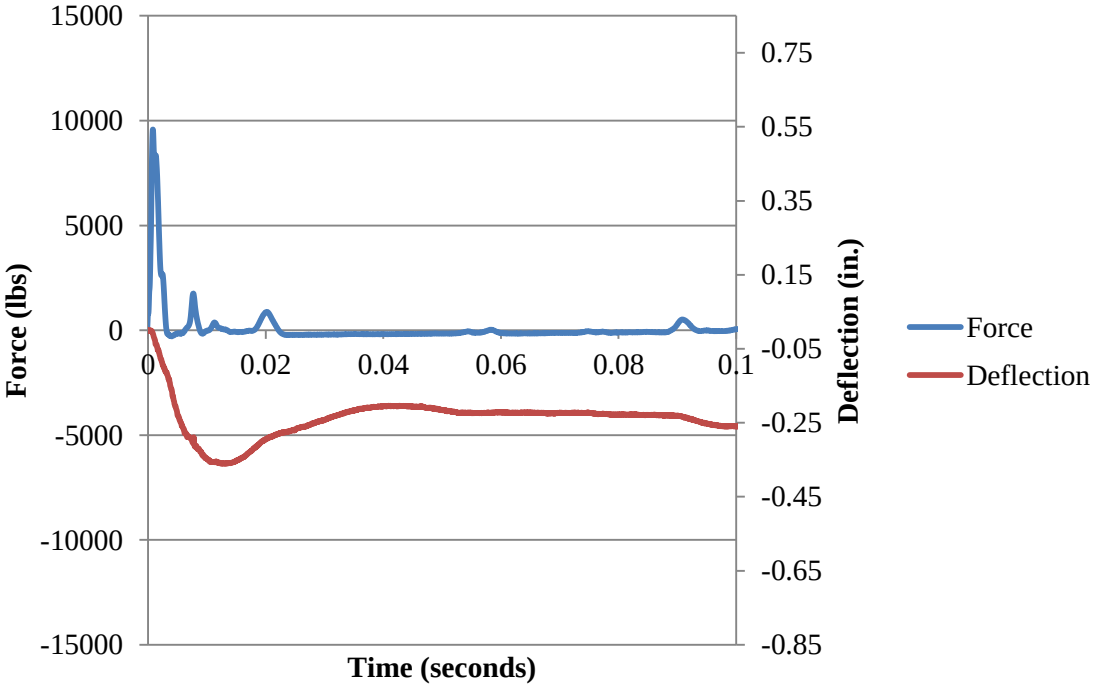

Figure B.110. Force and Deflection vs. Time for Fiber B2_1 at 21 in. (533 mm)

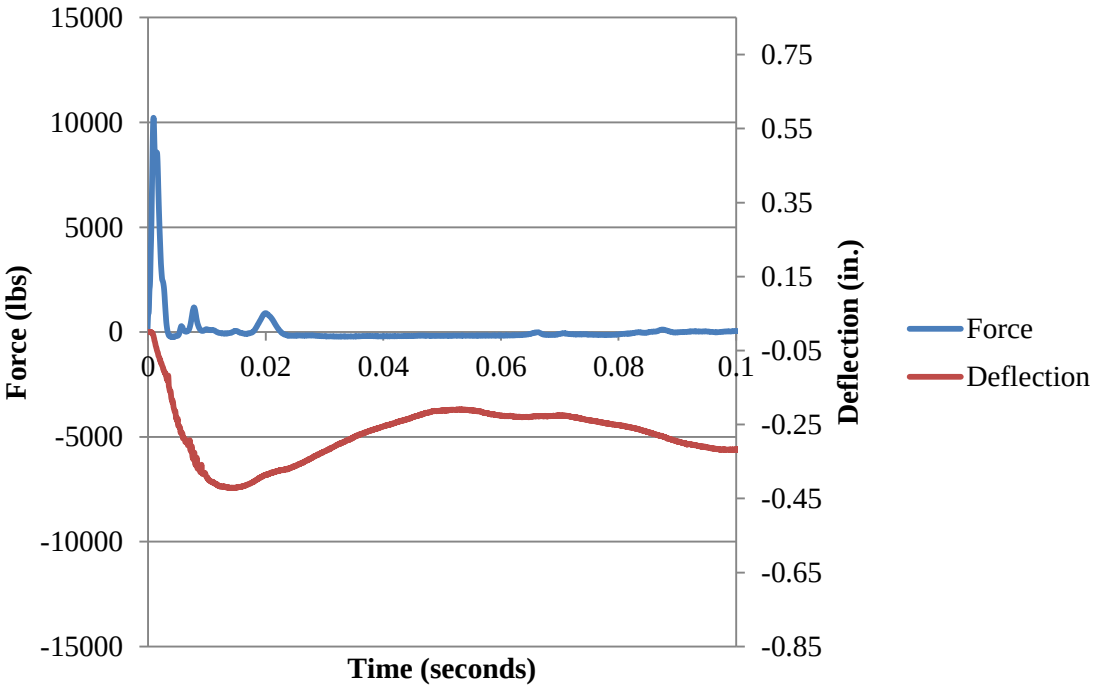

Figure B.111. Force and Deflection vs. Time for Fiber B2_1 at 24 in. (610 mm)

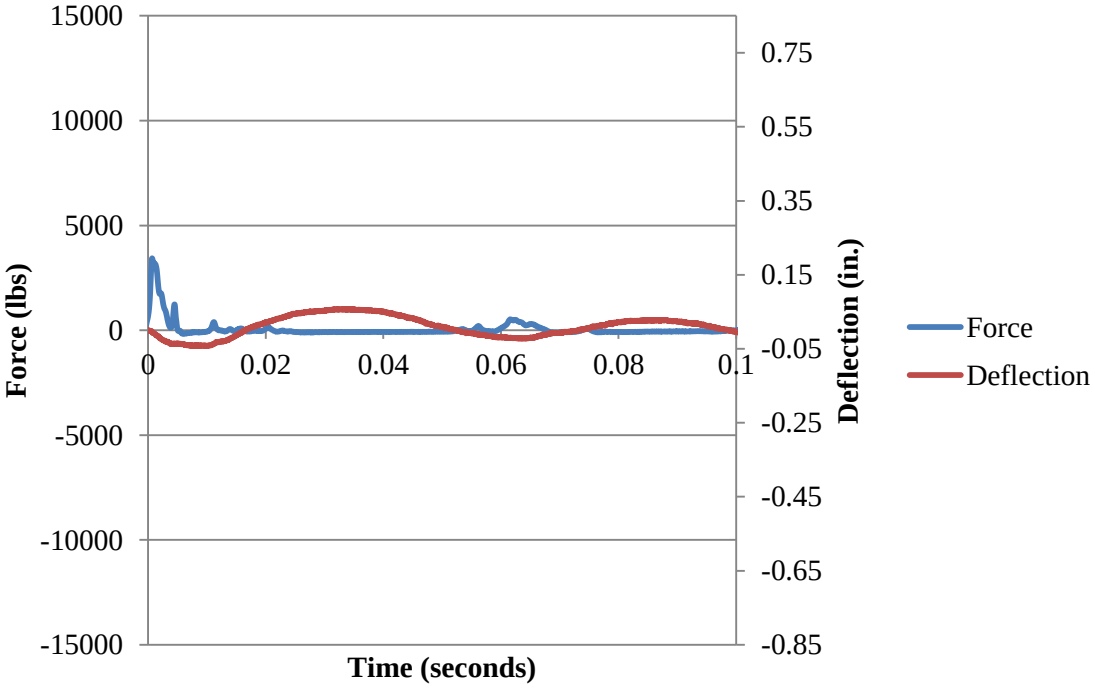

Figure B.112. Force and Deflection vs. Time for Fiber B2_2 at 3 in. (76 mm)

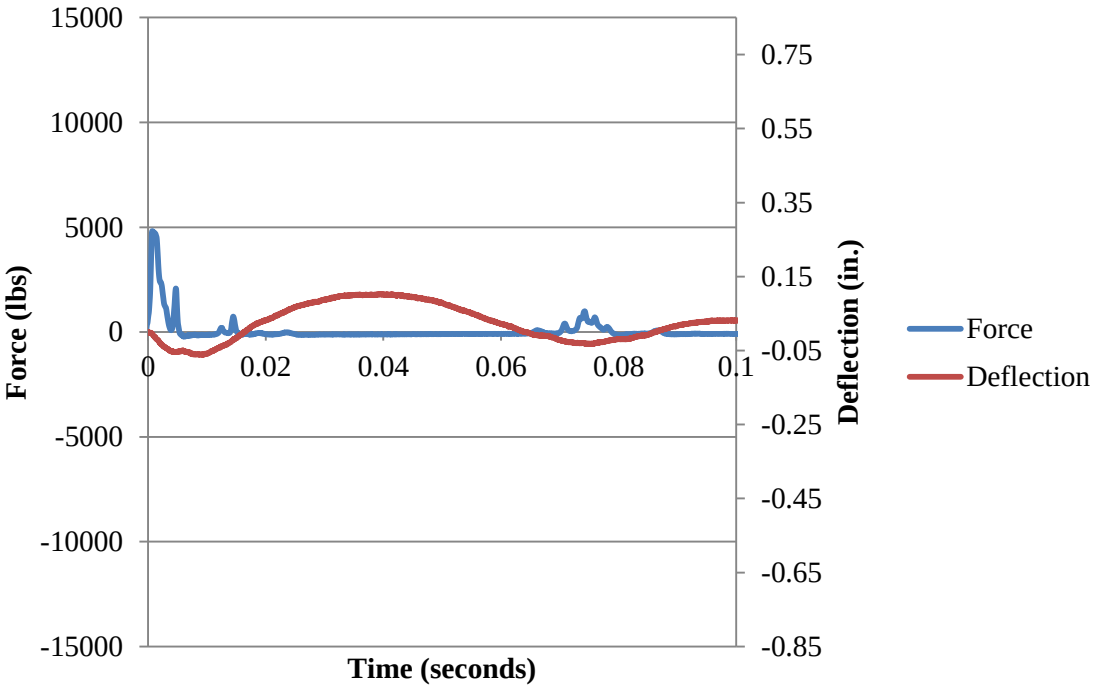

Figure B.113. Force and Deflection vs. Time for Fiber B2_2 at 6 in. (152 mm)

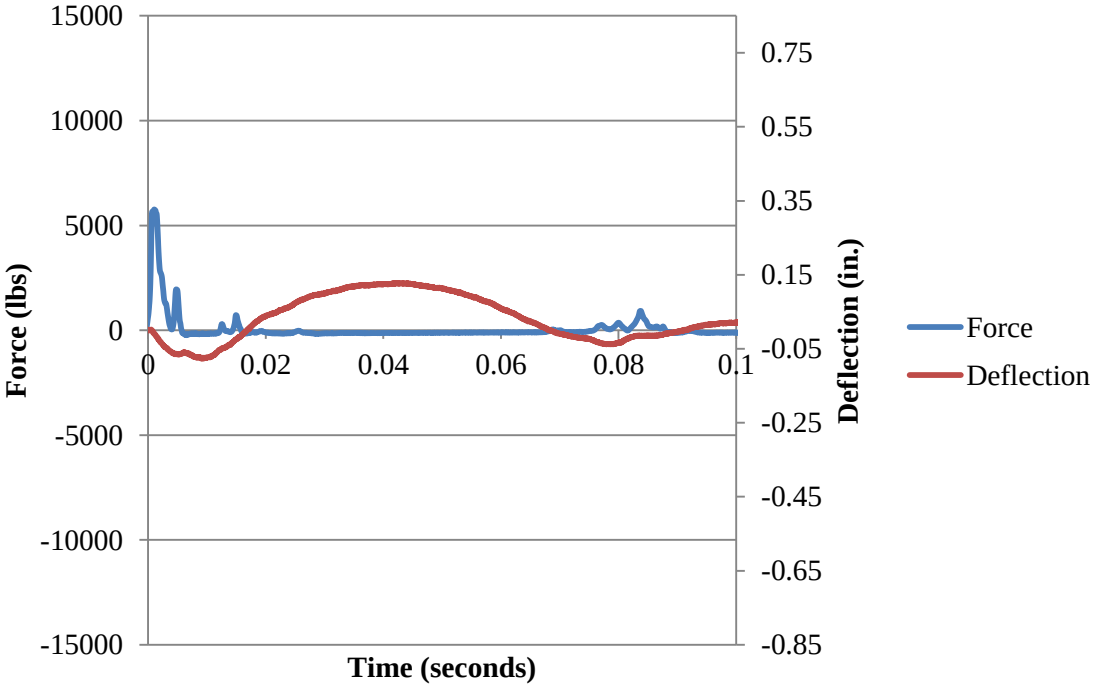

Figure B.114. Force and Deflection vs. Time for Fiber B2_2 at 9 in. (229 mm)

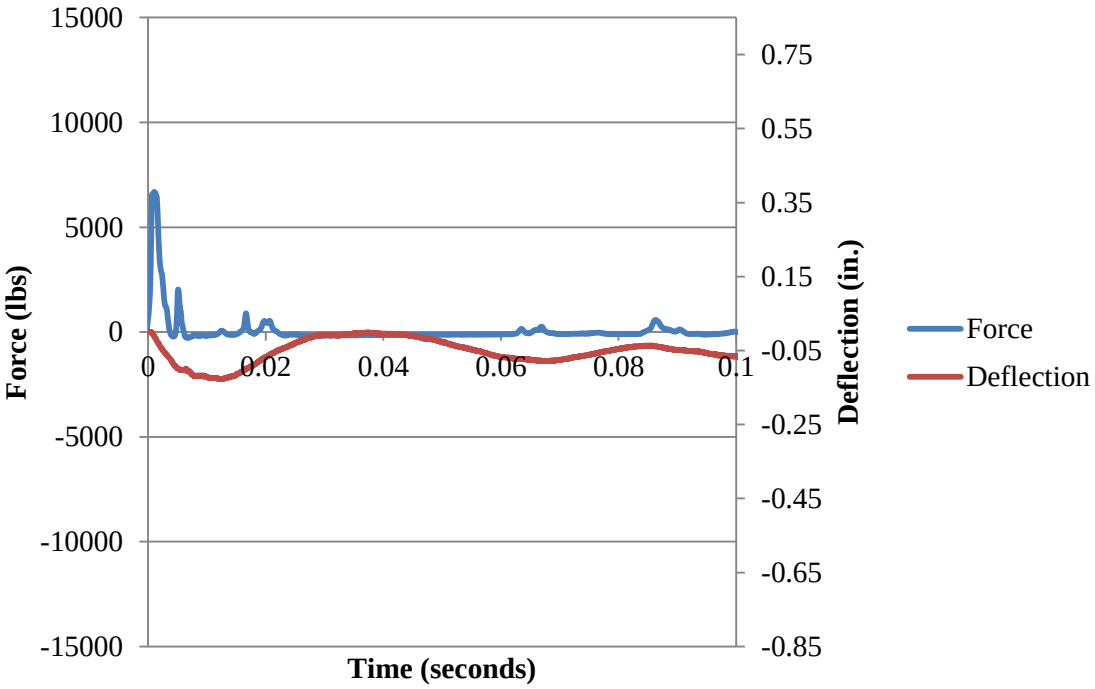

Figure B.115. Force and Deflection vs. Time for Fiber B2_2 at 12 in. (305 mm)

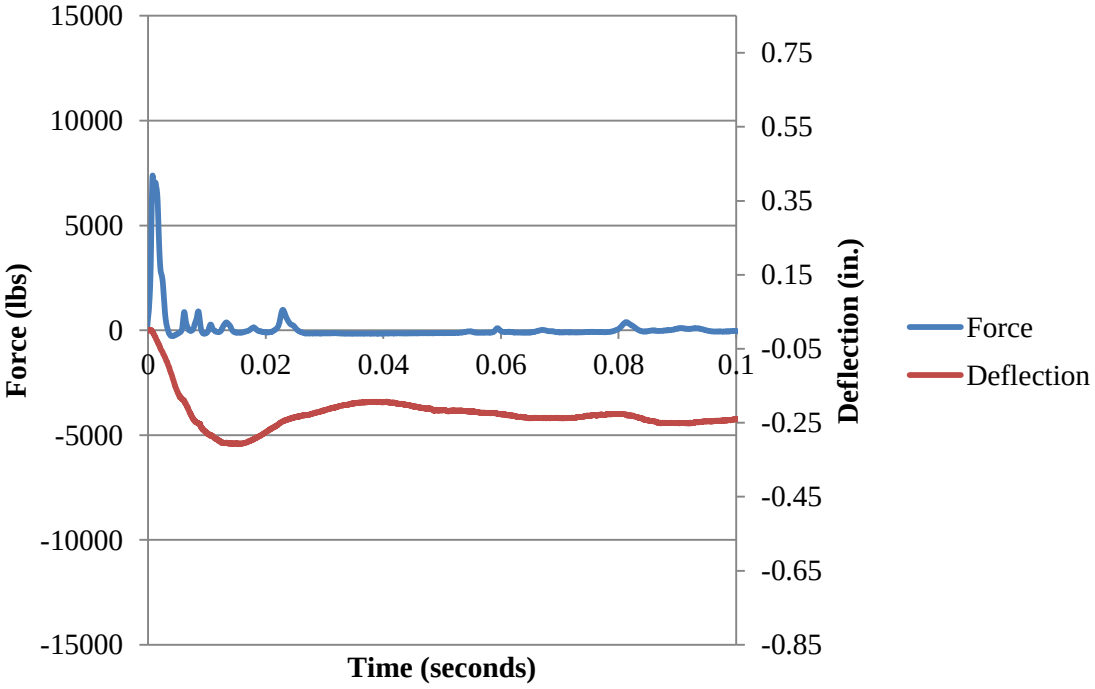

Figure B.116. Force and Deflection vs. Time for Fiber B2_2 at 15 in. (381 mm)

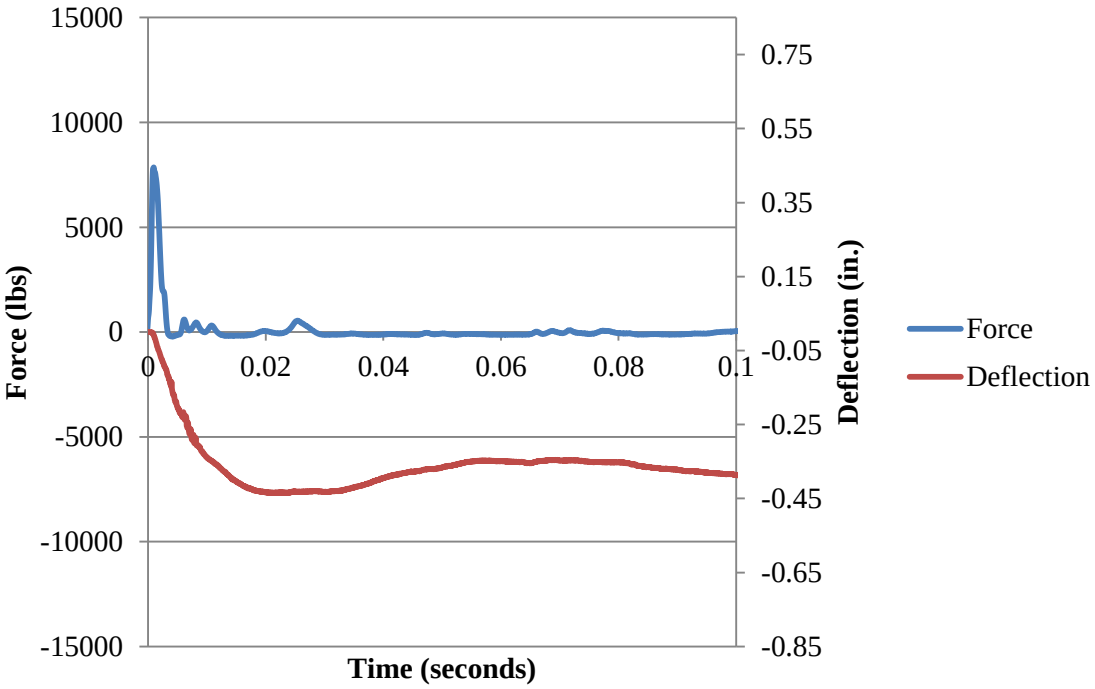

Figure B.117. Force and Deflection vs. Time for Fiber B2_2 at 18 in. (457 mm)

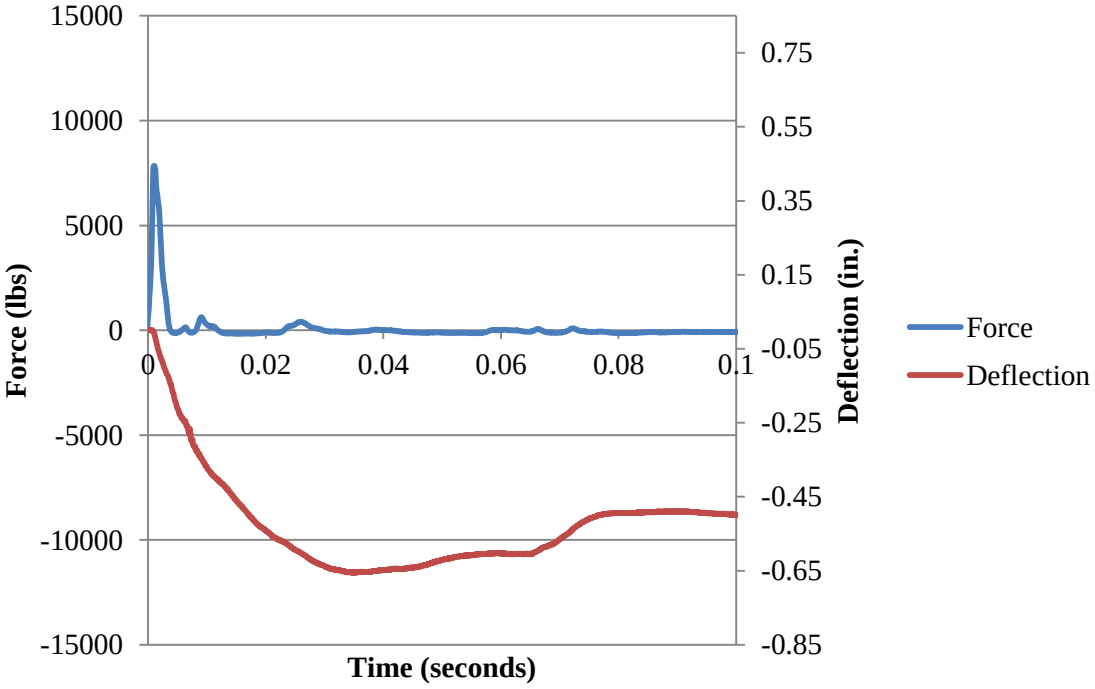

Figure B.118. Force and Deflection vs. Time for Fiber B2_2 at 21 in. (533 mm)

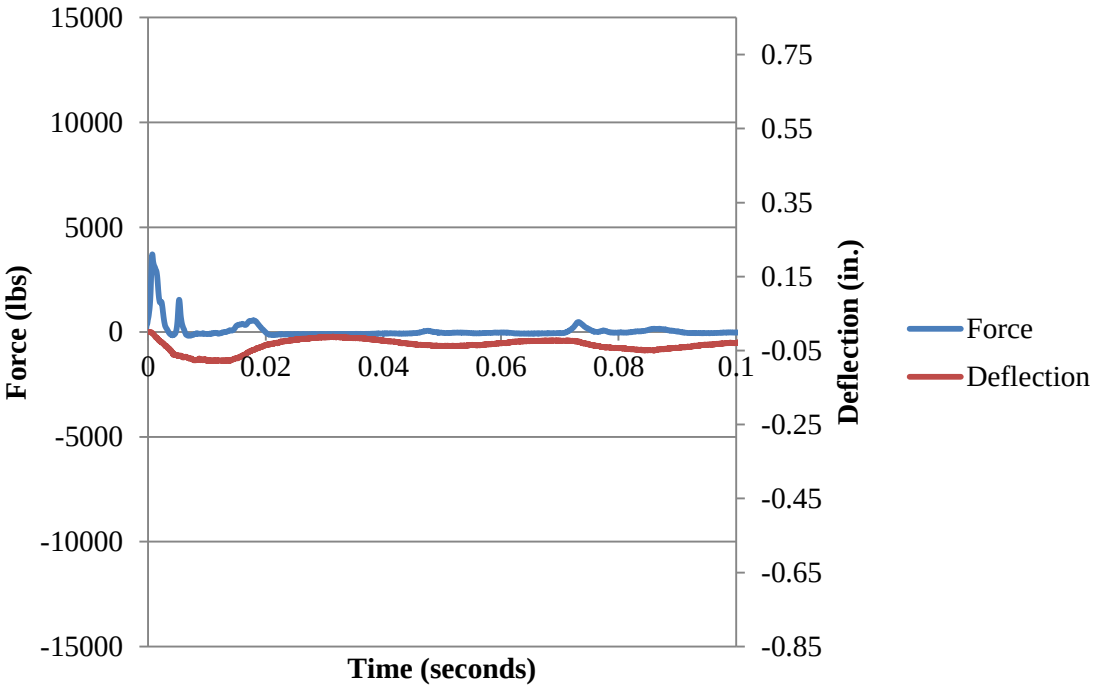

Figure B.119. Force and Deflection vs. Time for Fiber B2_3 at 3 in. (76 mm)

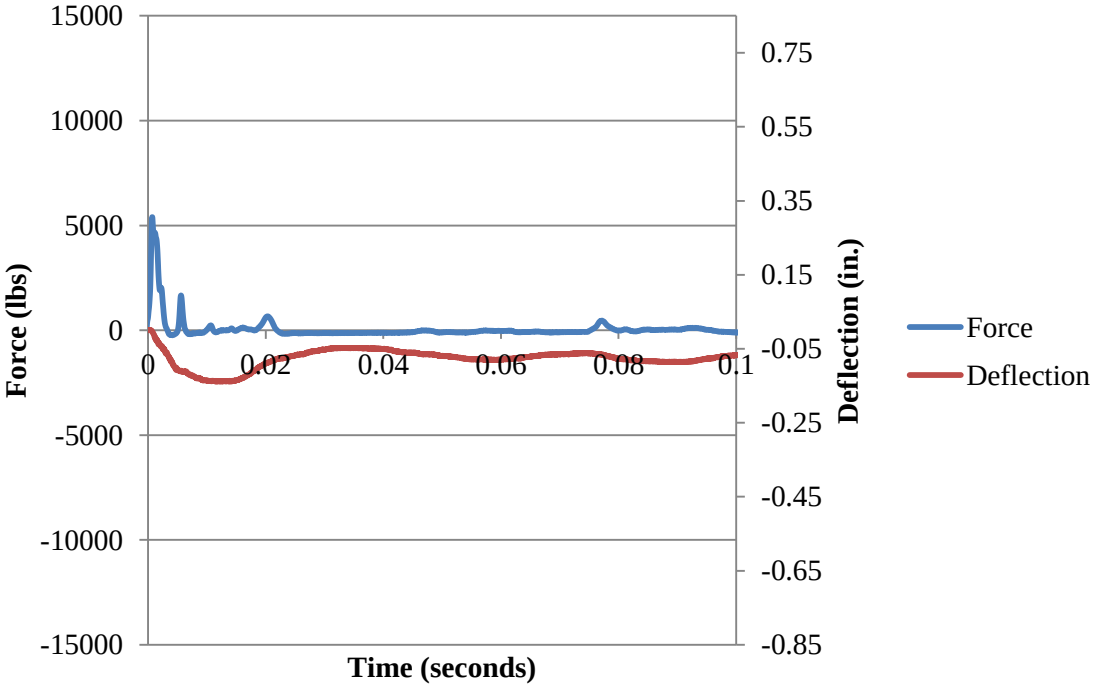

Figure B.120. Force and Deflection vs. Time for Fiber B2_3 at 6 in. (152 mm)

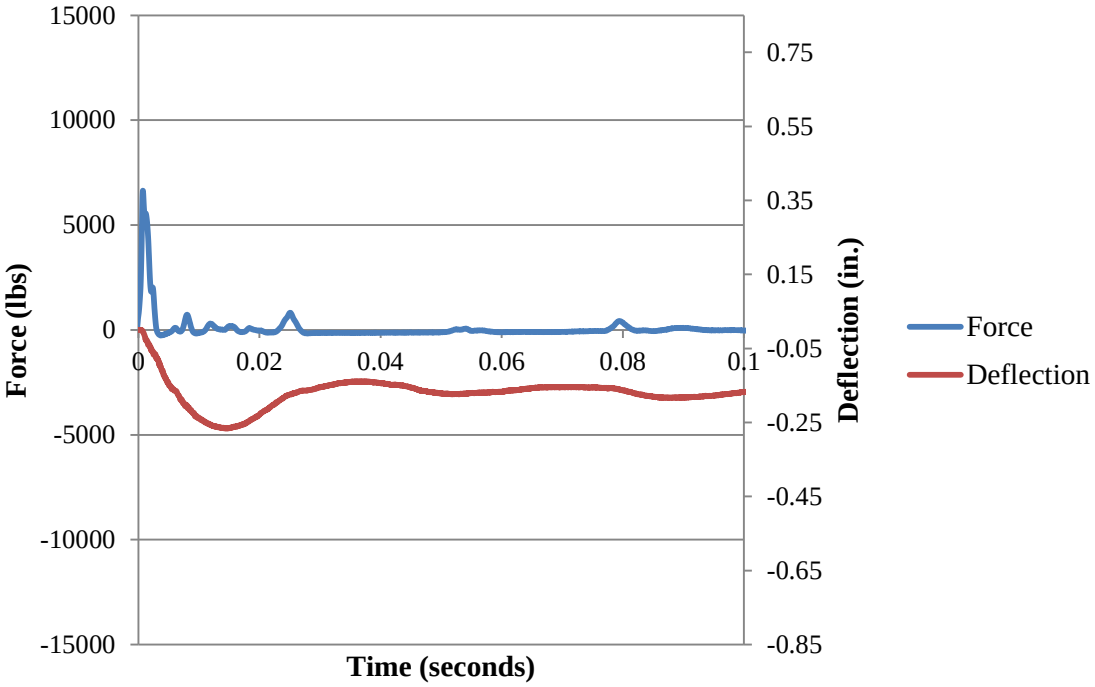

Figure B.121. Force and Deflection vs. Time for Fiber B2_3 at 9 in. (229 mm)

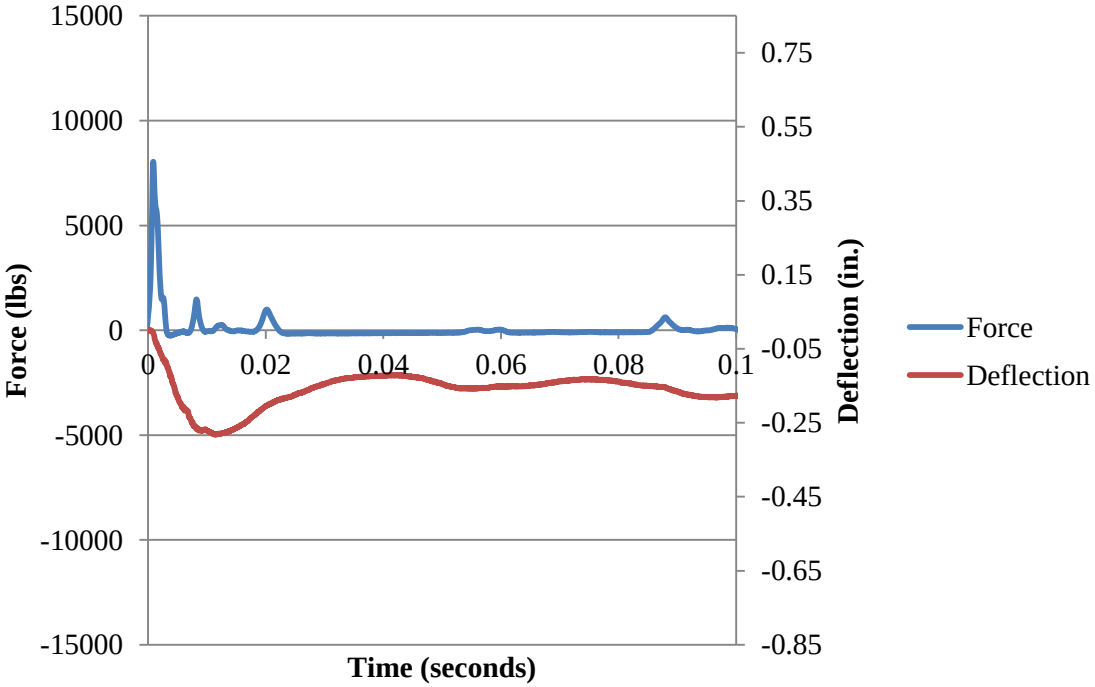

Figure B.122. Force and Deflection vs. Time for Fiber B2_3 at 12 in. (305 mm)

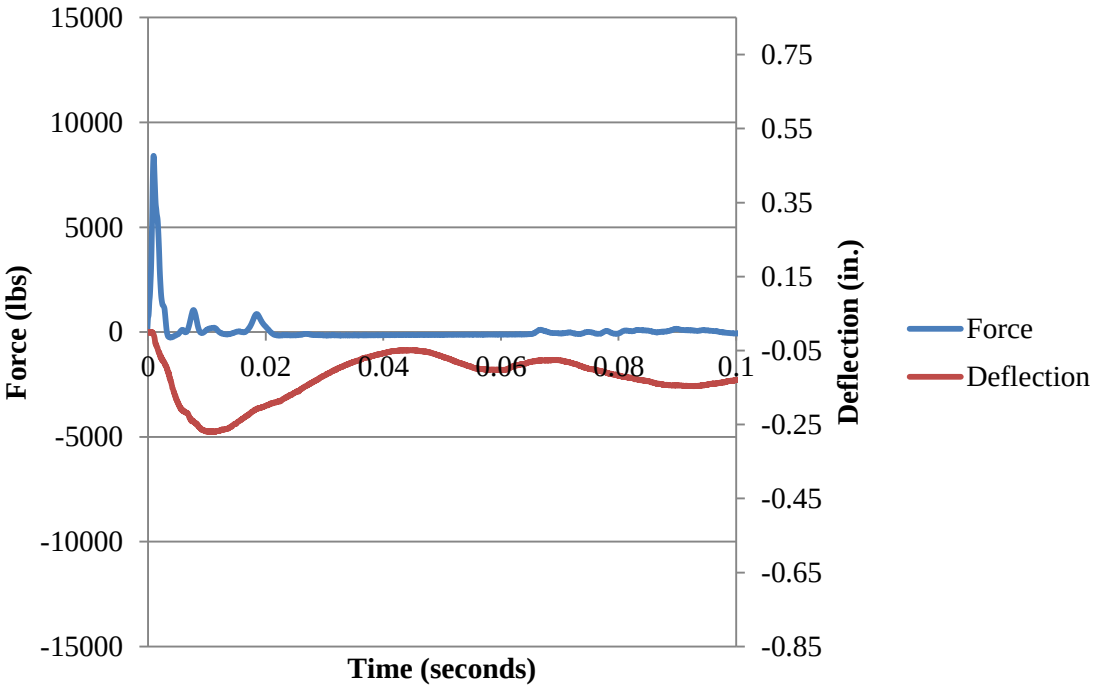

Figure B.123. Force and Deflection vs. Time for Fiber B2_3 at 15 in. (381 mm)

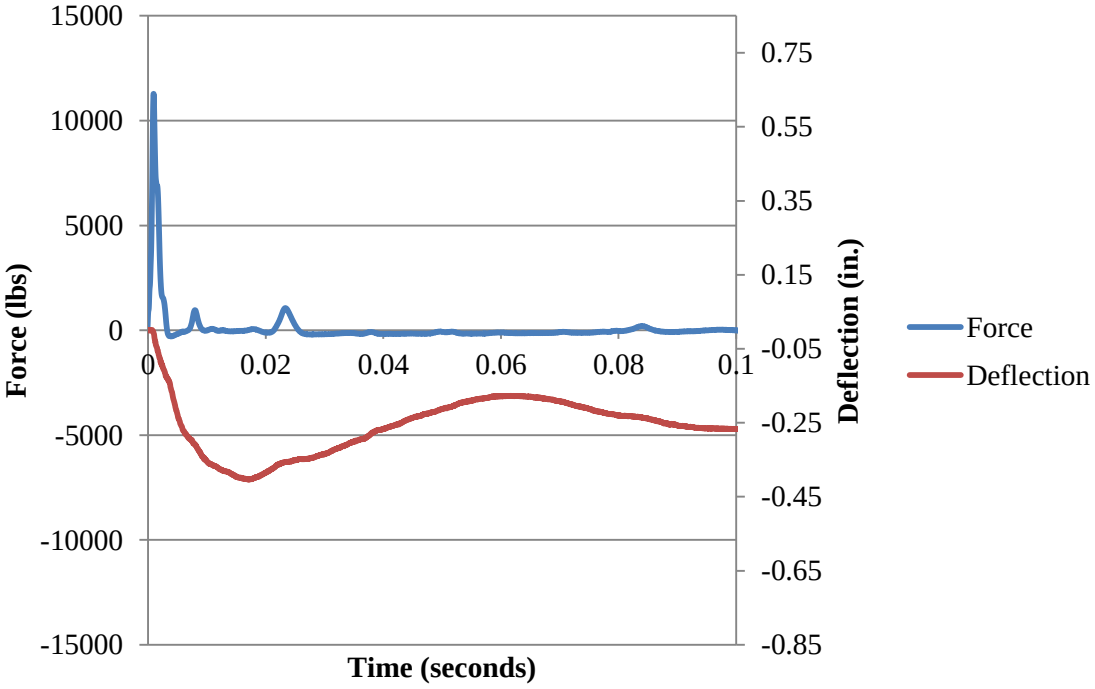

Figure B.124. Force and Deflection vs. Time for Fiber B2_3 at 18 in. (457 mm)

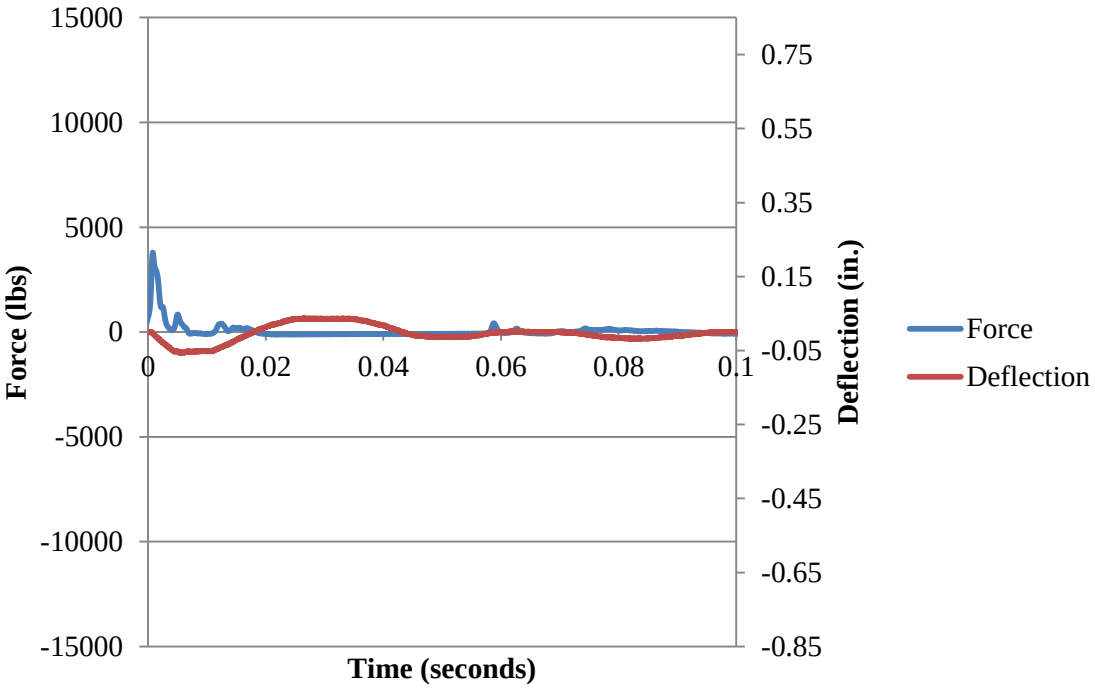

Figure B.125. Force and Deflection vs. Time for Fiber B2_4 at 3 in. (76 mm)

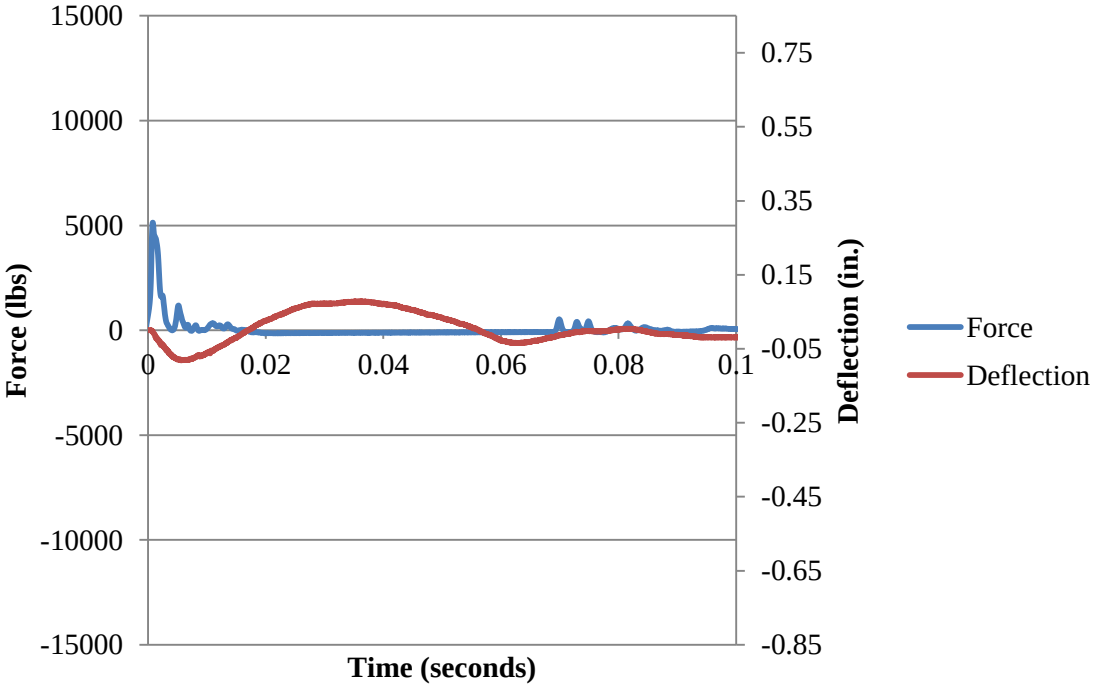

Figure B.126. Force and Deflection vs. Time for Fiber B2_4 at 6 in. (152 mm)

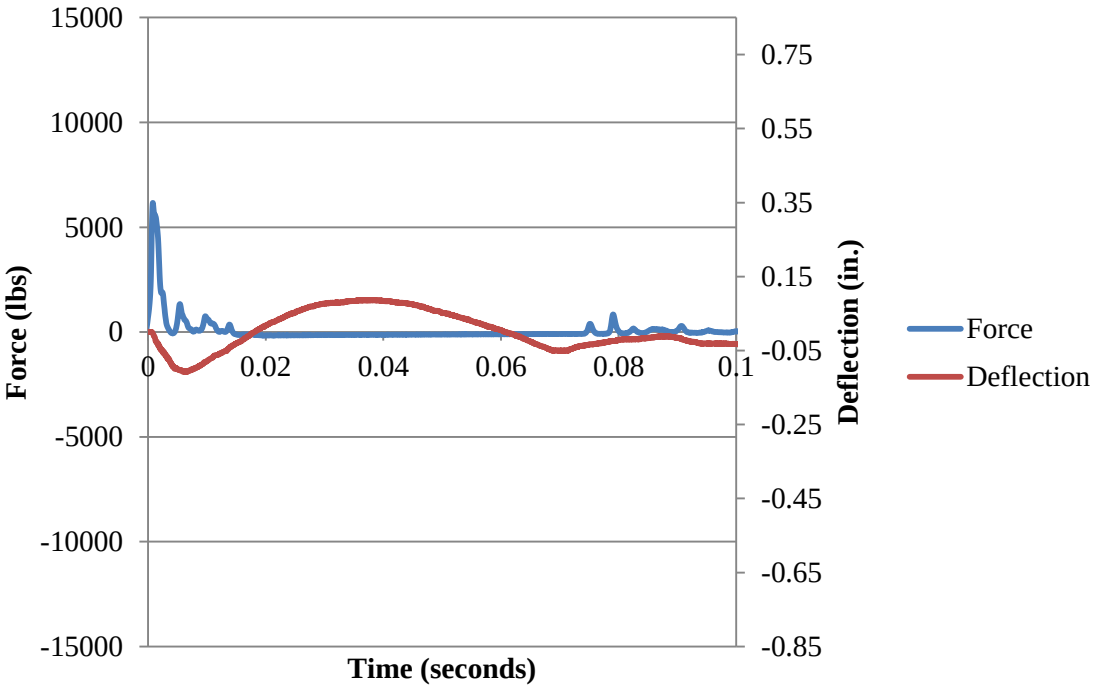

Figure B.127. Force and Deflection vs. Time for Fiber B2_4 at 9 in. (229 mm)

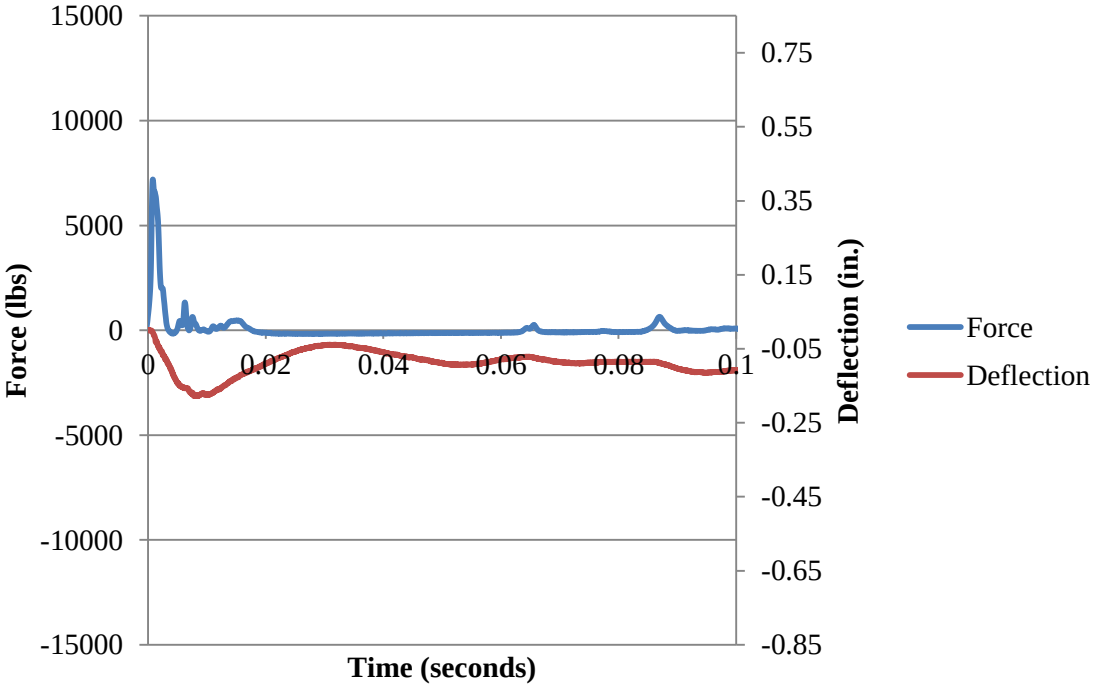

Figure B.128. Force and Deflection vs. Time for Fiber B2_4 at 12 in. (305 mm)

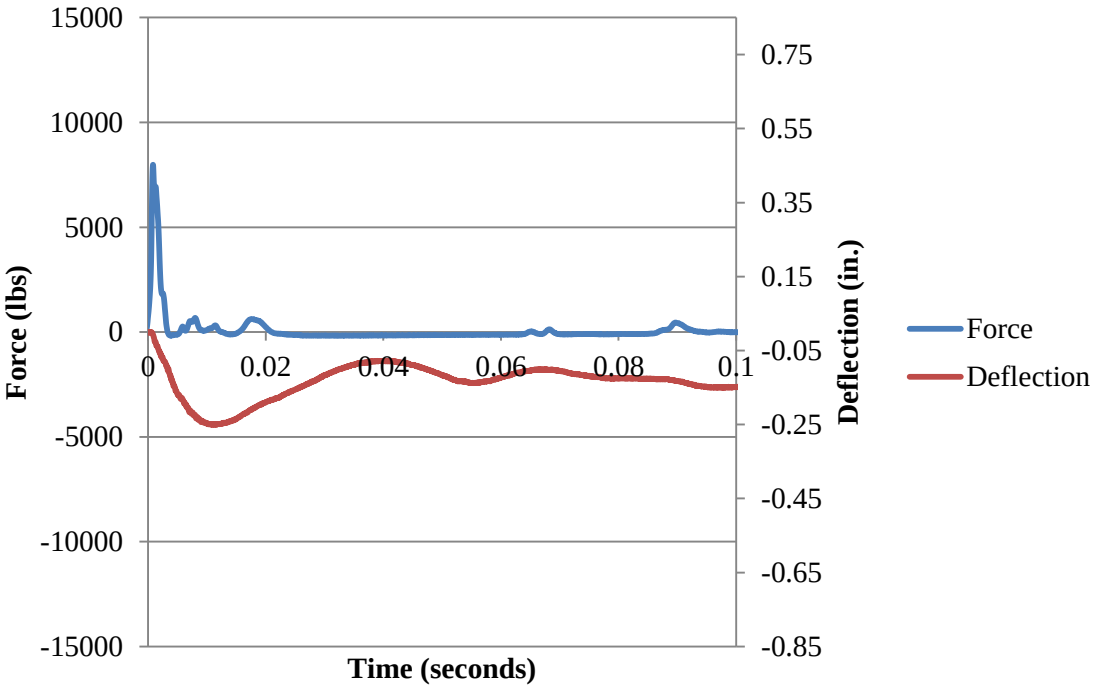

Figure B.129. Force and Deflection vs. Time for Fiber B2_4 at 15 in. (381 mm)

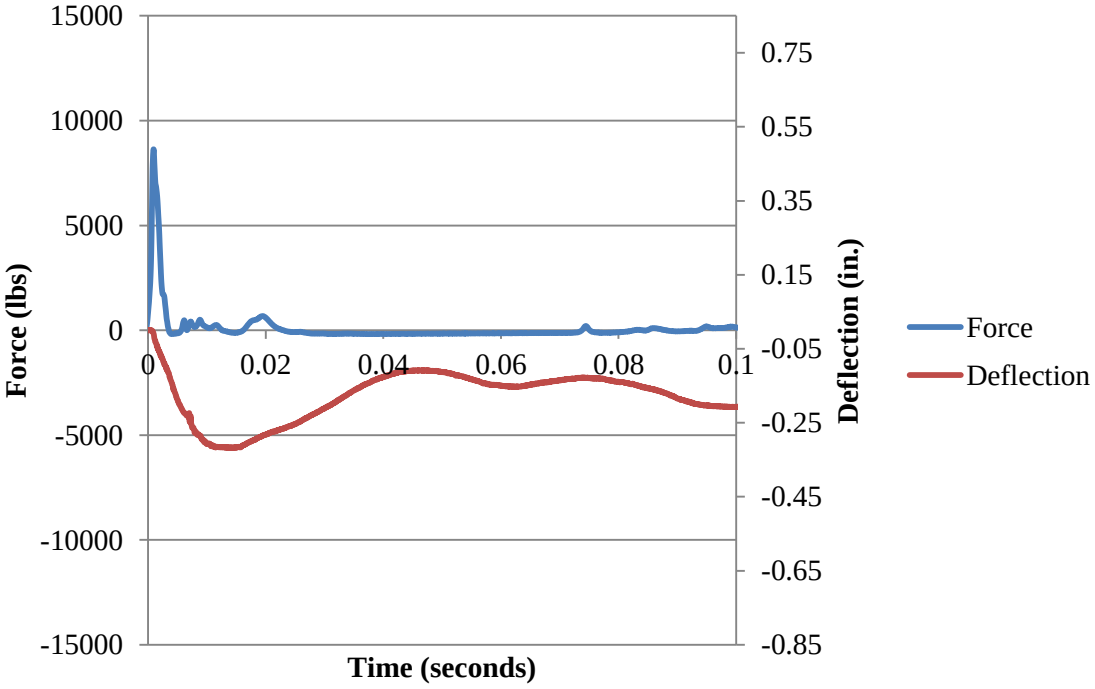

Figure B.130. Force and Deflection vs. Time for Fiber B2_4 at 18 in. (457 mm)

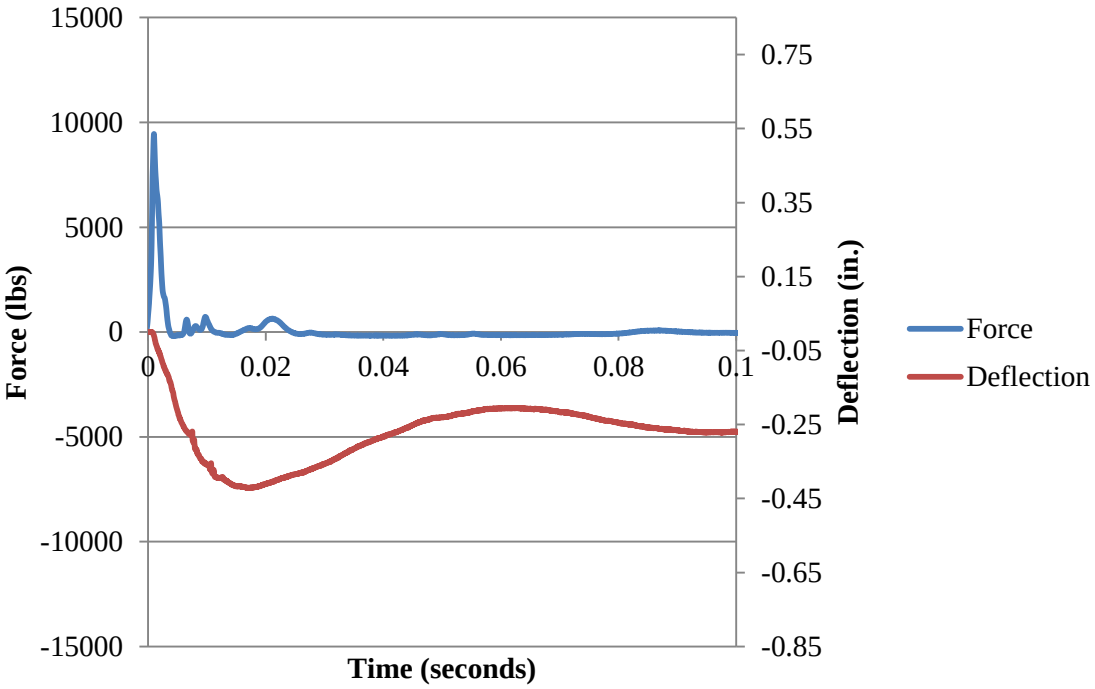

Figure B.131. Force and Deflection vs. Time for Fiber B2_4 at 21 in. (533 mm)

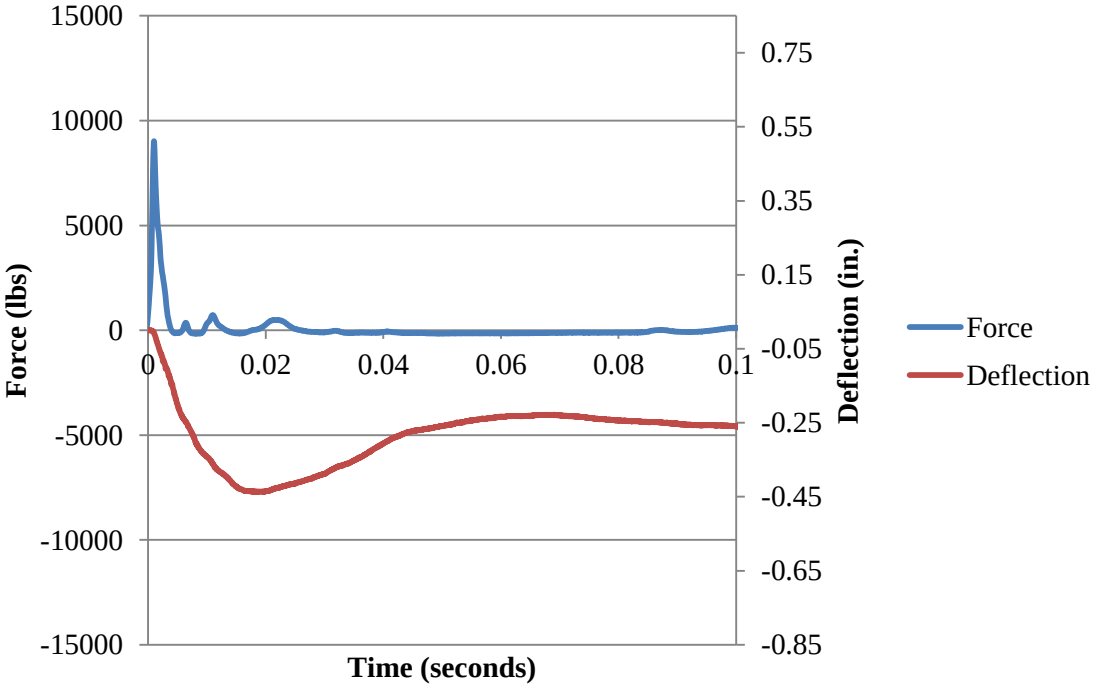

Figure B.132. Force and Deflection vs. Time for Fiber B2_4 at 24 in. (610 mm)

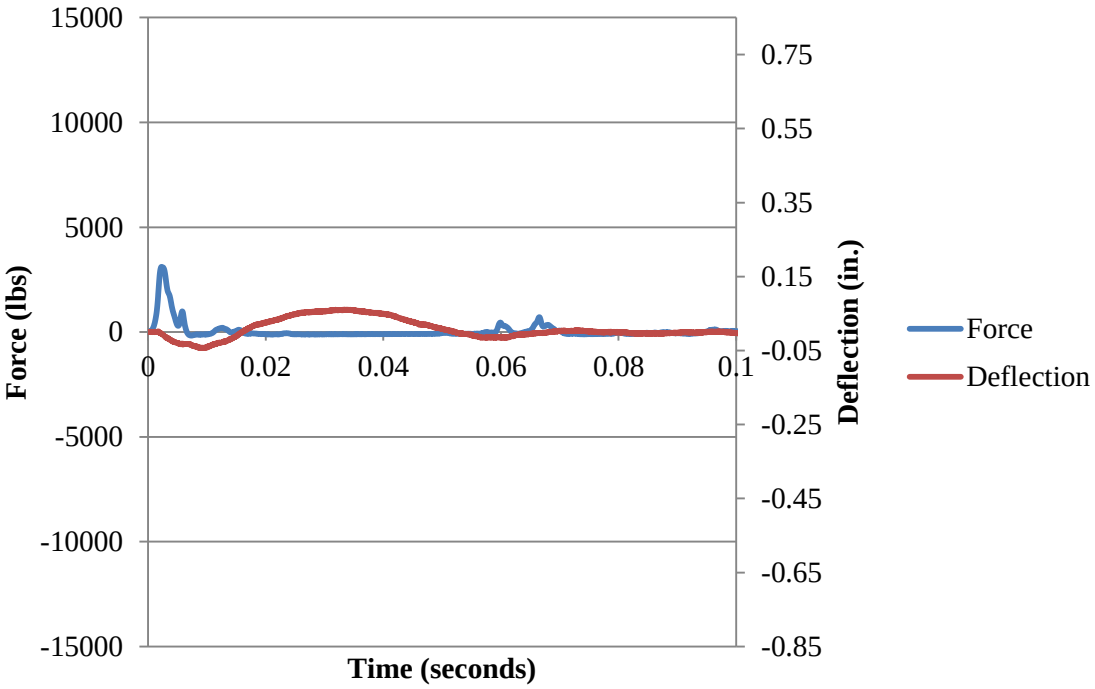

Figure B.133. Force and Deflection vs. Time for Fiber B3_1 at 3 in. (76 mm)

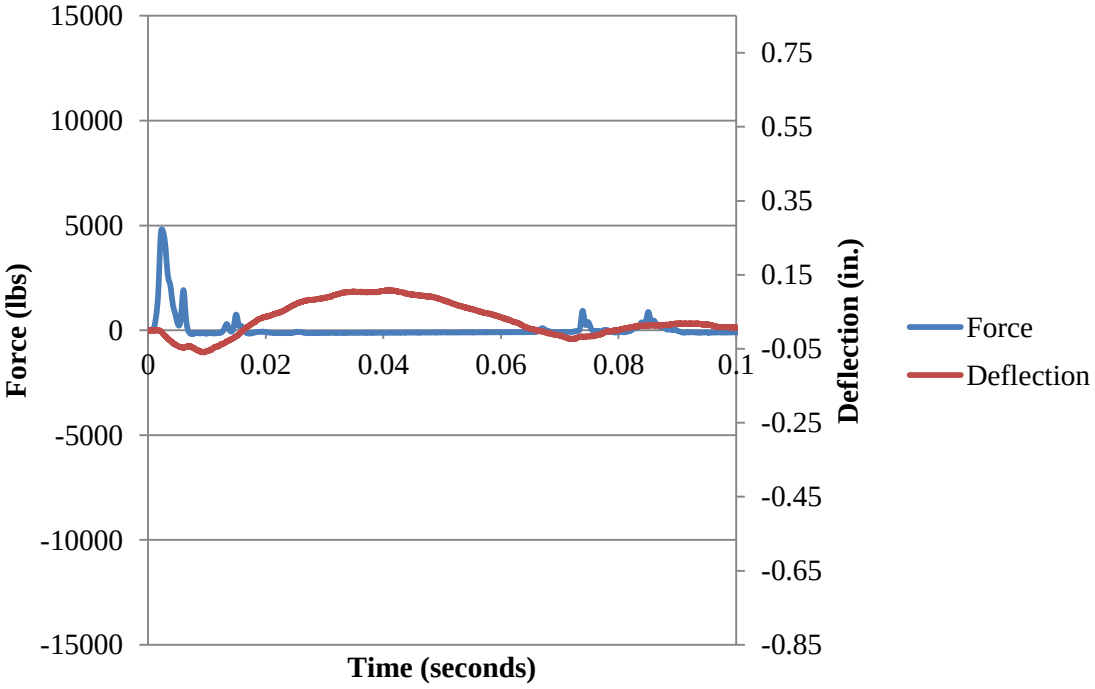

Figure B.134. Force and Deflection vs. Time for Fiber B3_1 at 6 in. (152 mm)

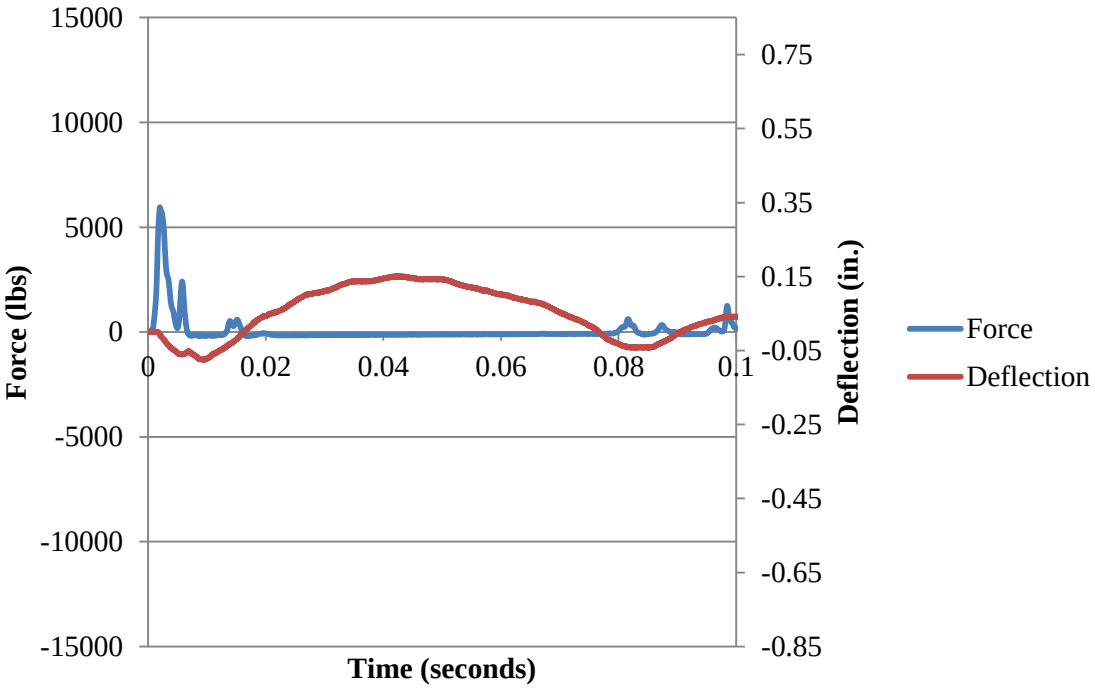

Figure B.135. Force and Deflection vs. Time for Fiber B3_1 at 9 in. (229 mm)

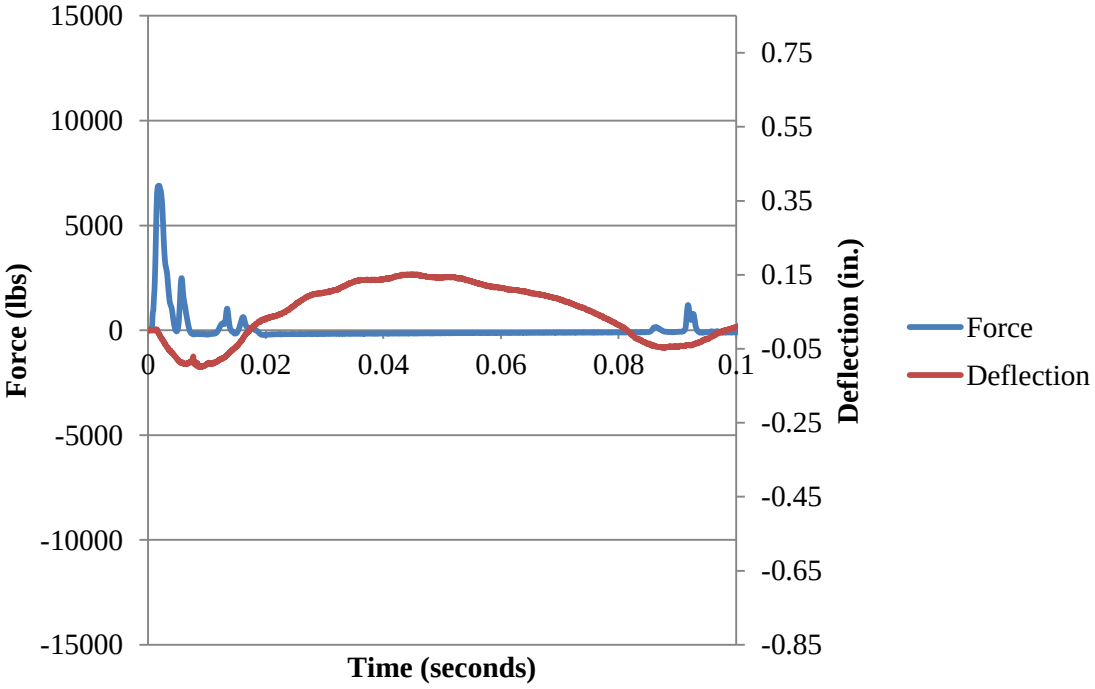

Figure B.136. Force and Deflection vs. Time for Fiber B3_1 at 12 in. (305 mm)

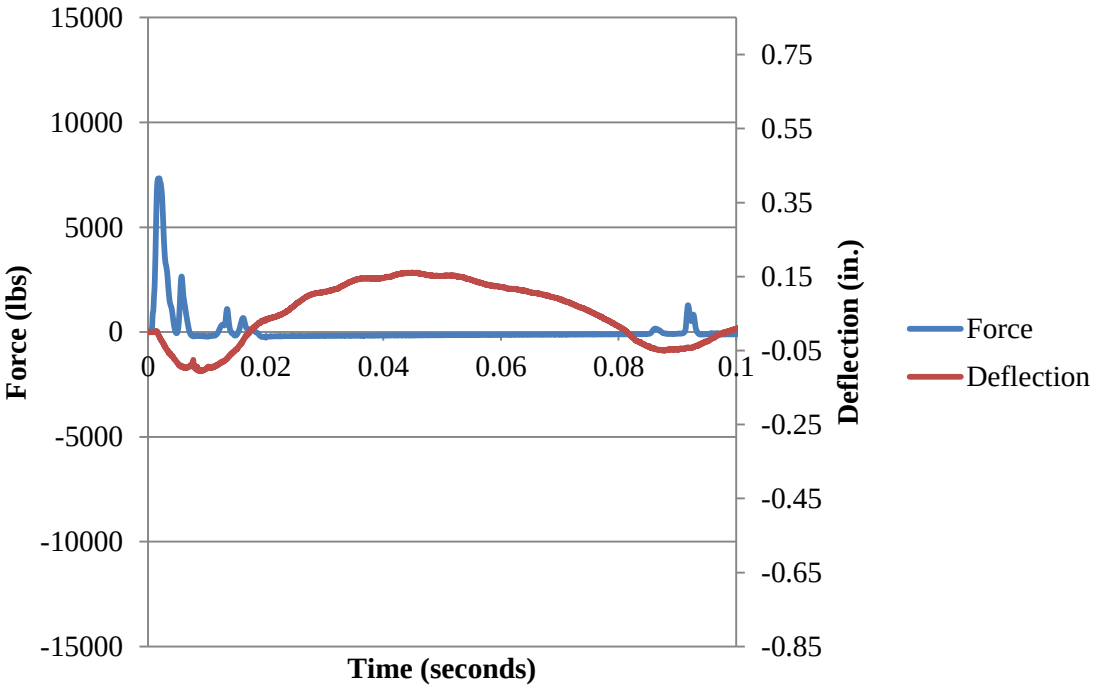

Figure B.137. Force and Deflection vs. Time for Fiber B3_1 at 15 in. (381 mm)

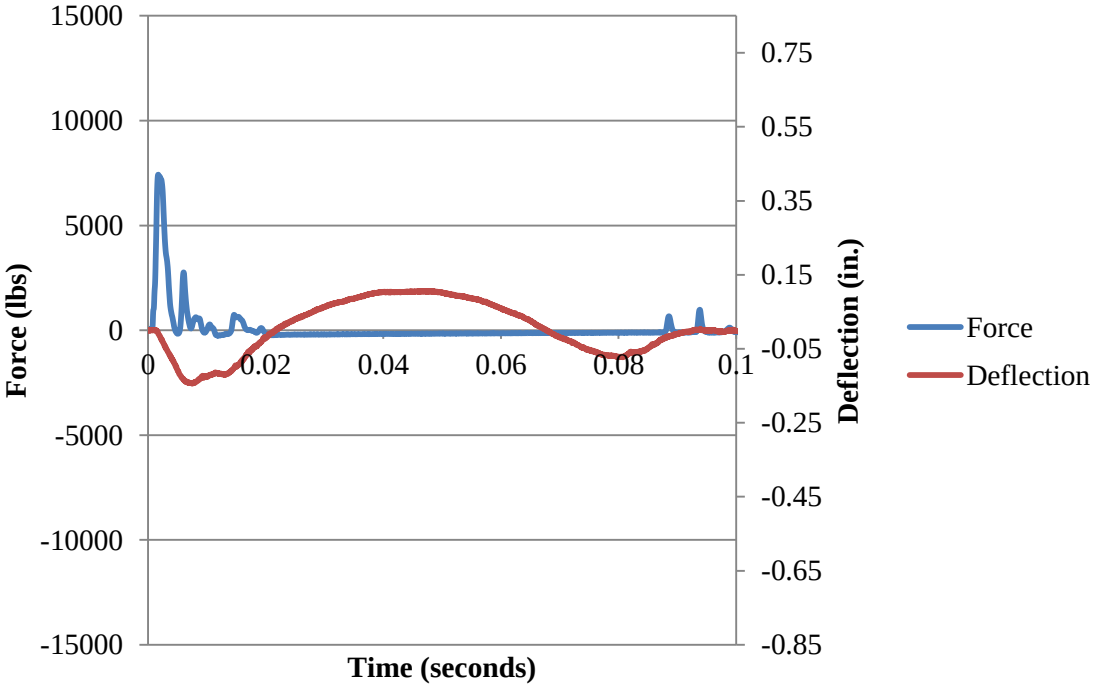

Figure B.138. Force and Deflection vs. Time for Fiber B3_1 at 18 in. (457 mm)

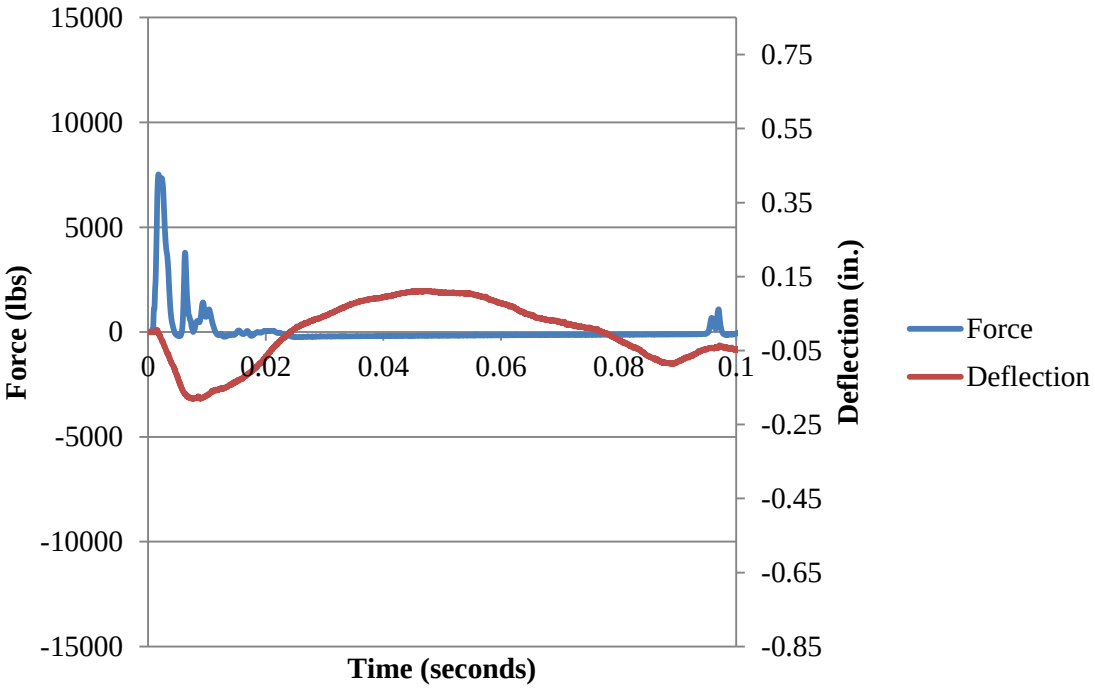

Figure B.139. Force and Deflection vs. Time for Fiber B3_1 at 21 in. (533 mm)

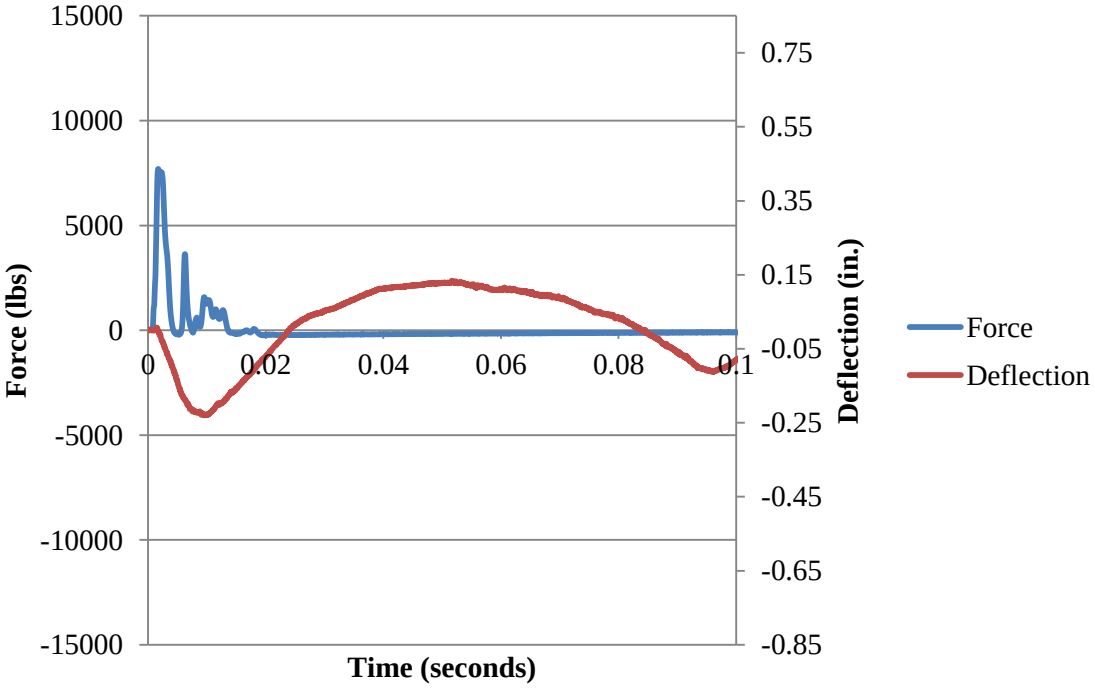

Figure B.140. Force and Deflection vs. Time for Fiber B3_1 at 24 in. (610 mm)

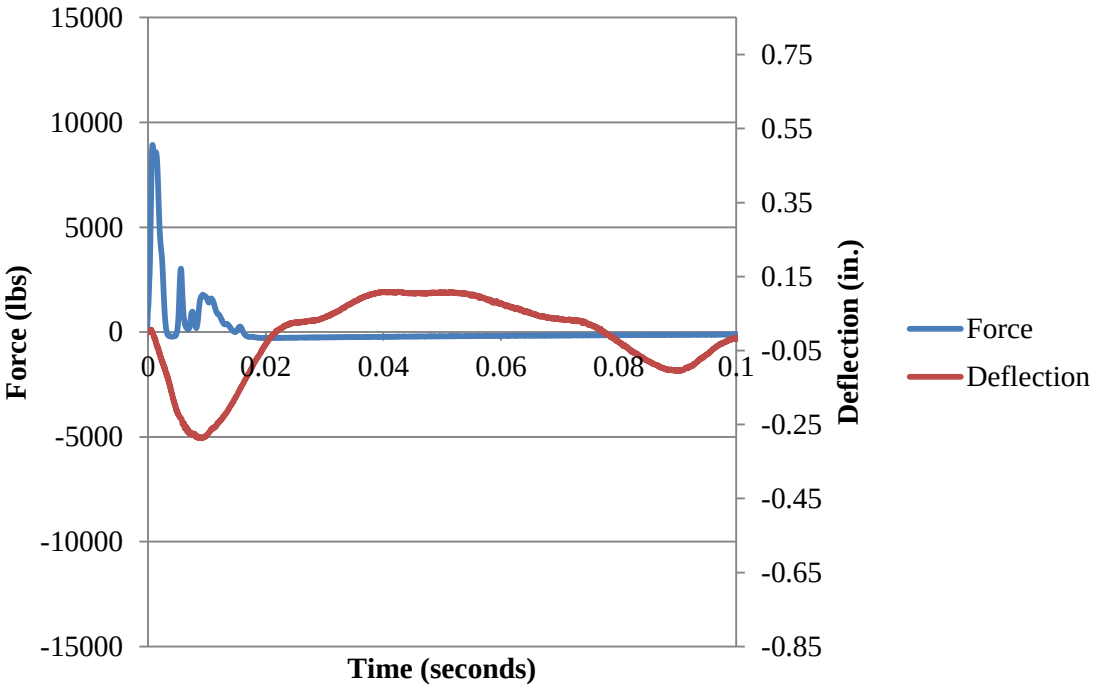

Figure B.141. Force and Deflection vs. Time for Fiber B3_1 at 30 in. (762 mm)

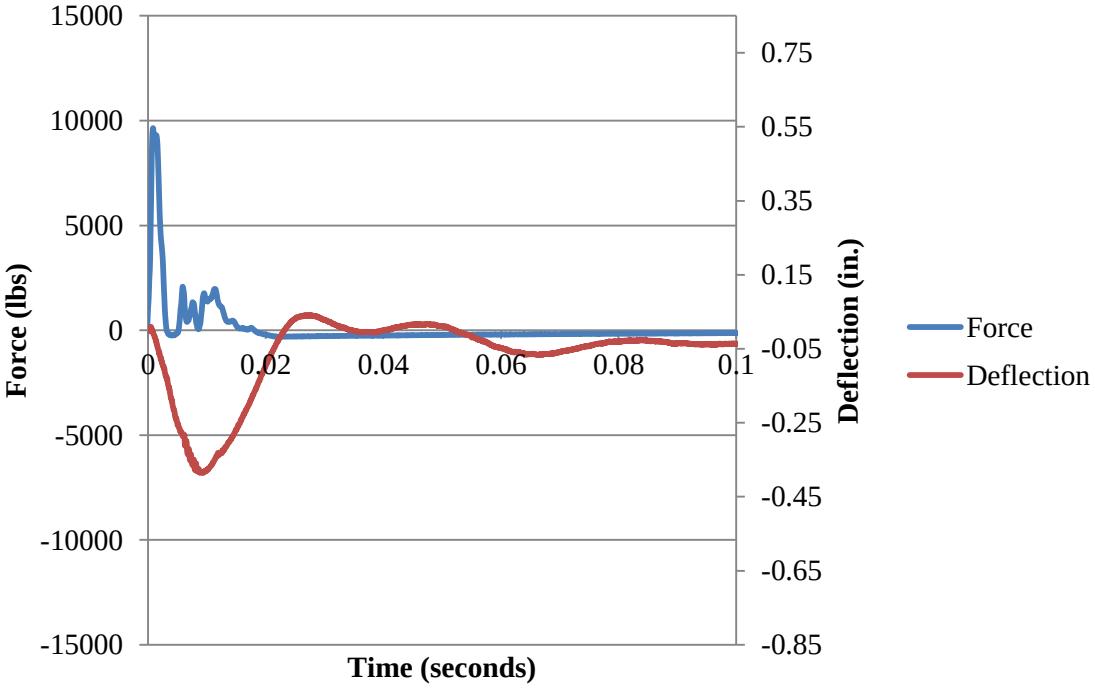

Figure B.142. Force and Deflection vs. Time for Fiber B3_1 at 36 in. (914 mm)

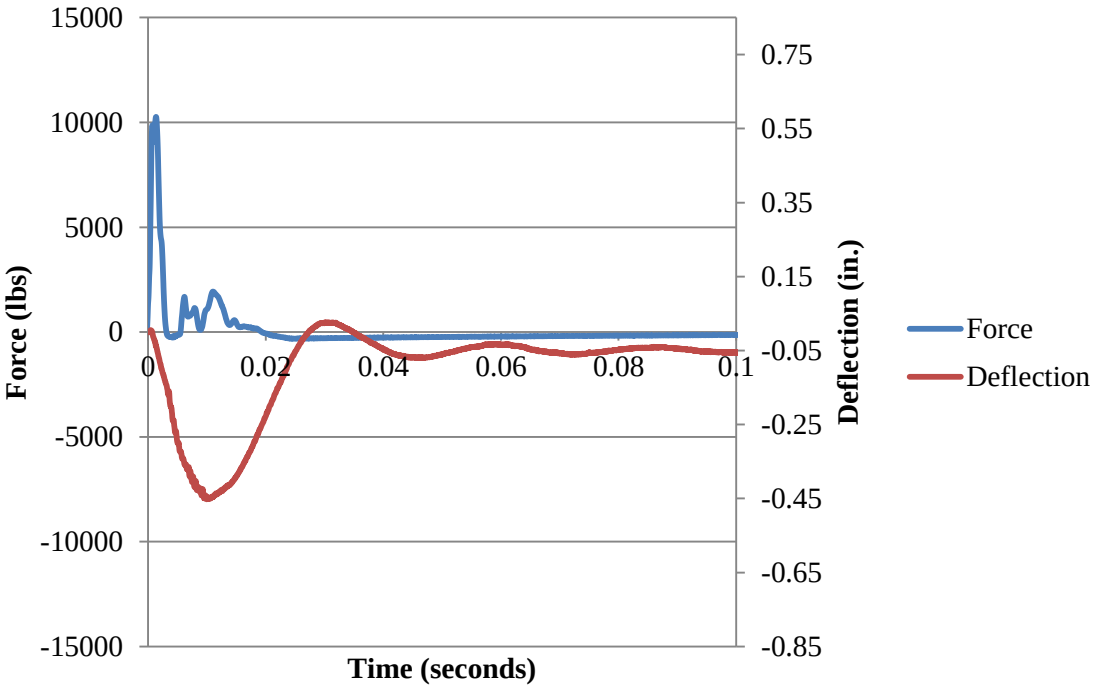

Figure B.143. Force and Deflection vs. Time for Fiber B3_1 at 42 in. (1067 mm)

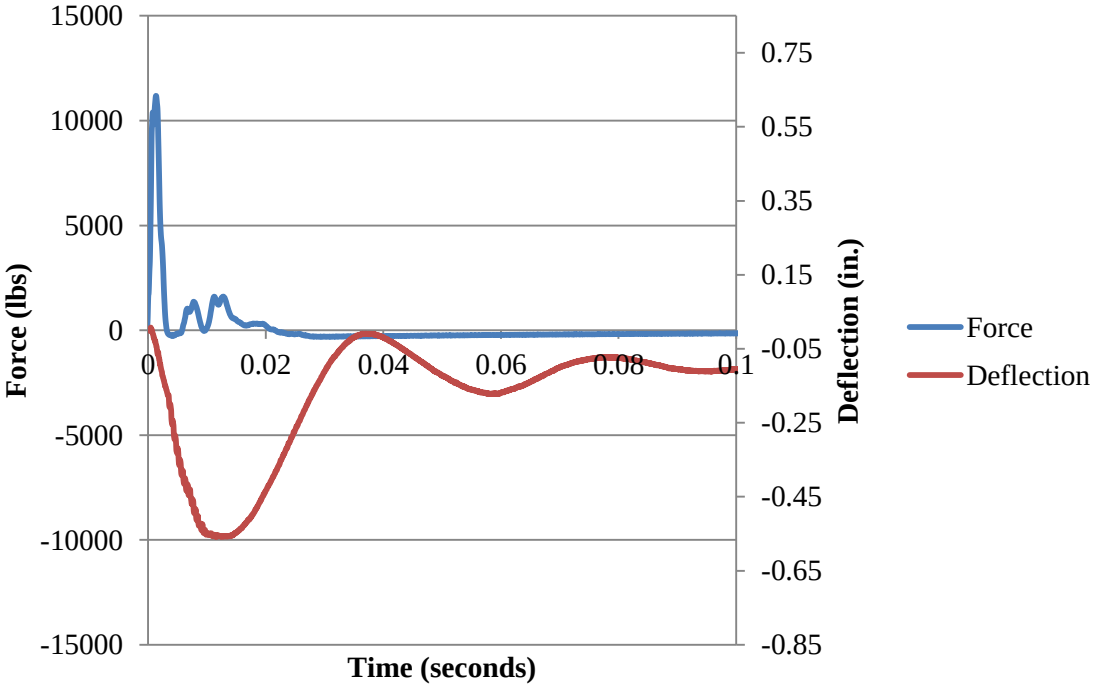

Figure B.144. Force and Deflection vs. Time for Fiber B3_1 at 48 in. (1219 mm)

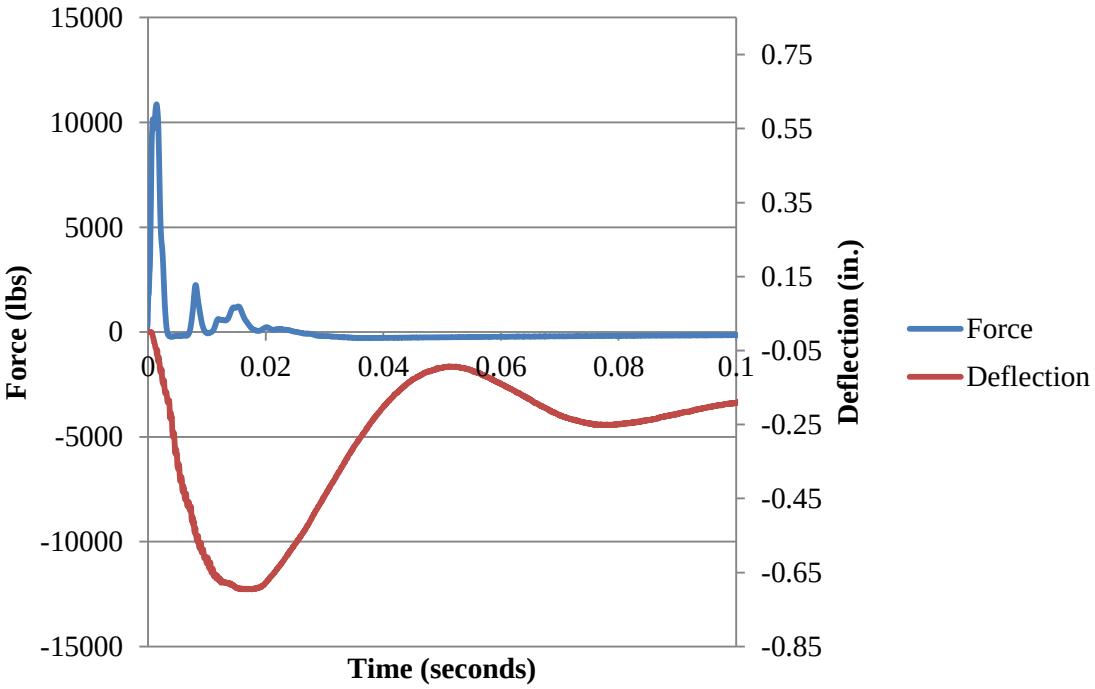

Figure B.145. Force and Deflection vs. Time for Fiber B3_1 at 54 in. (1372 mm)

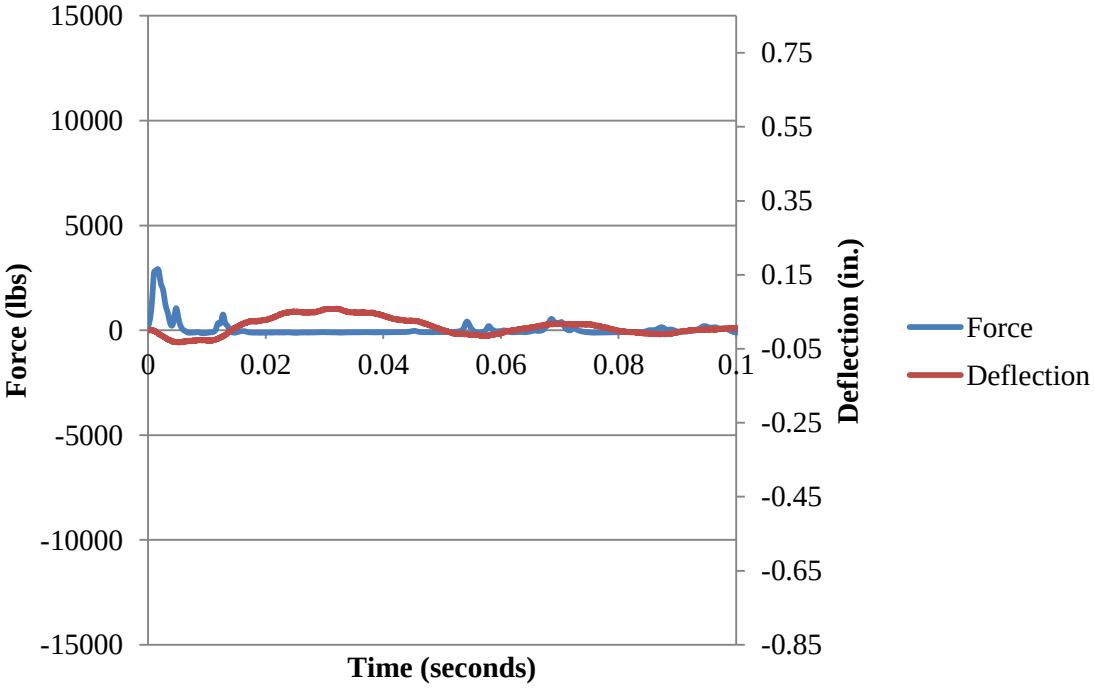

Figure B.146. Force and Deflection vs. Time for Fiber B3_2 at 3 in. (76 mm)

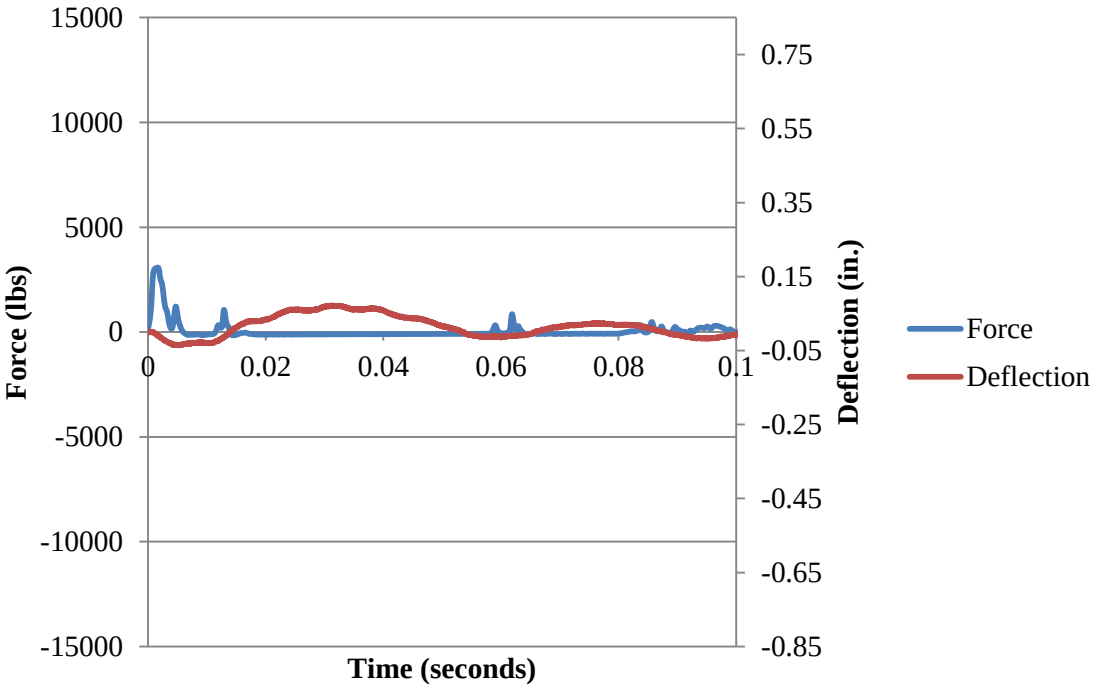

Figure B.147. Force and Deflection vs. Time for Fiber B3_2 at 6 in. (152 mm)

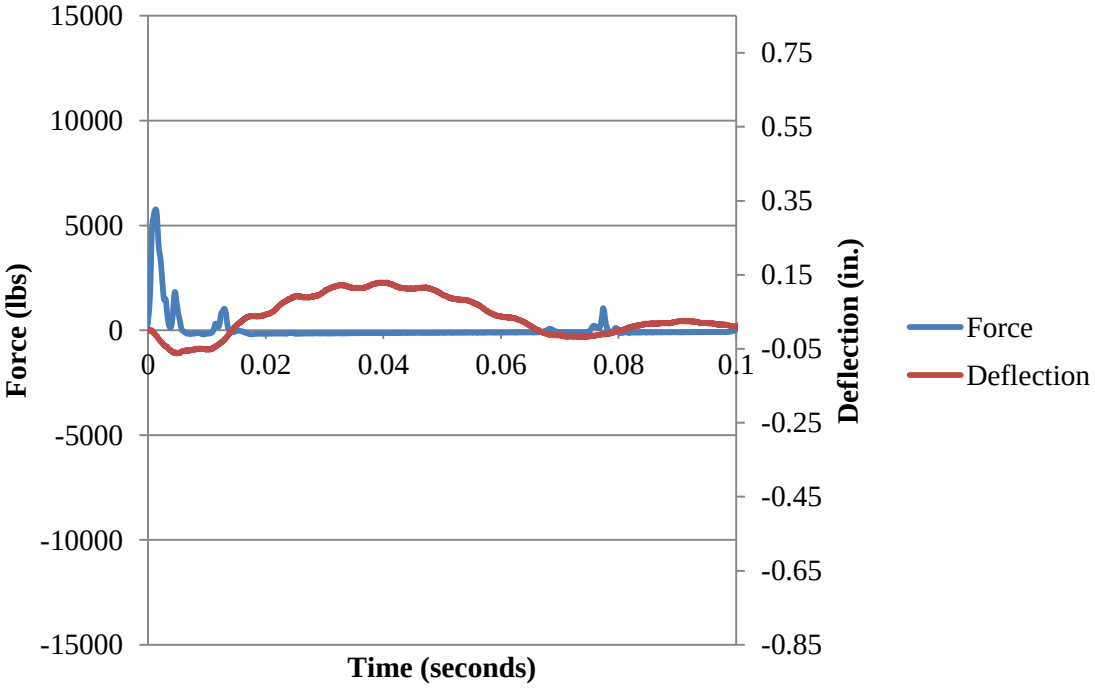

Figure B.148. Force and Deflection vs. Time for Fiber B3_2 at 9 in. (229 mm)

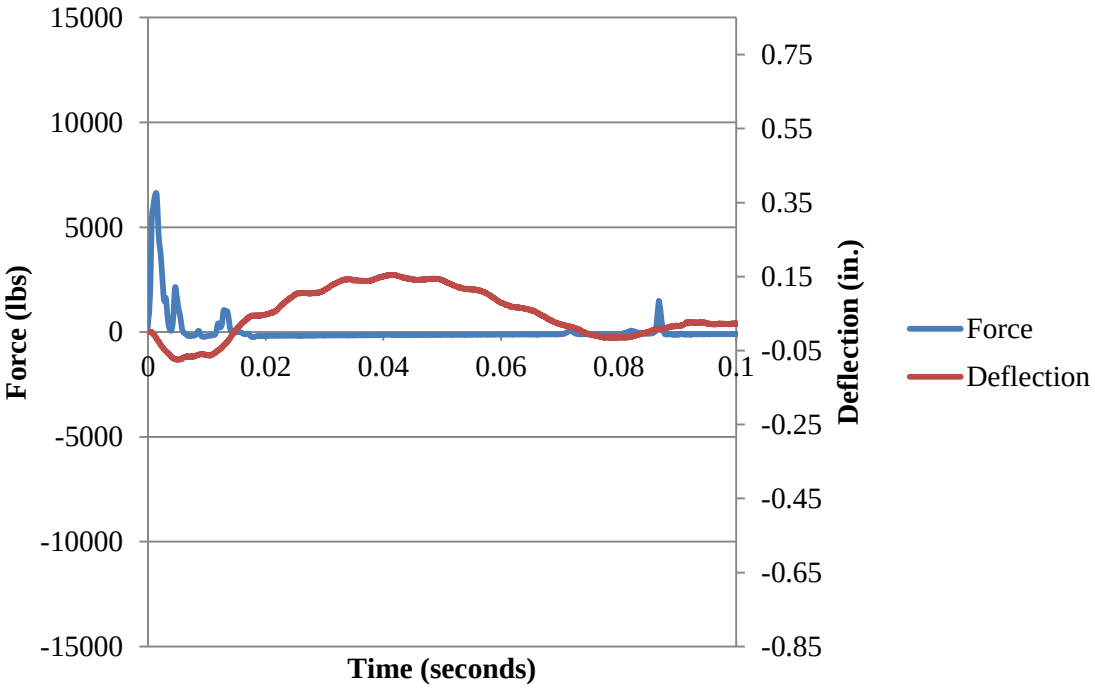

Figure B.149. Force and Deflection vs. Time for Fiber B3_2 at 12 in. (305 mm)

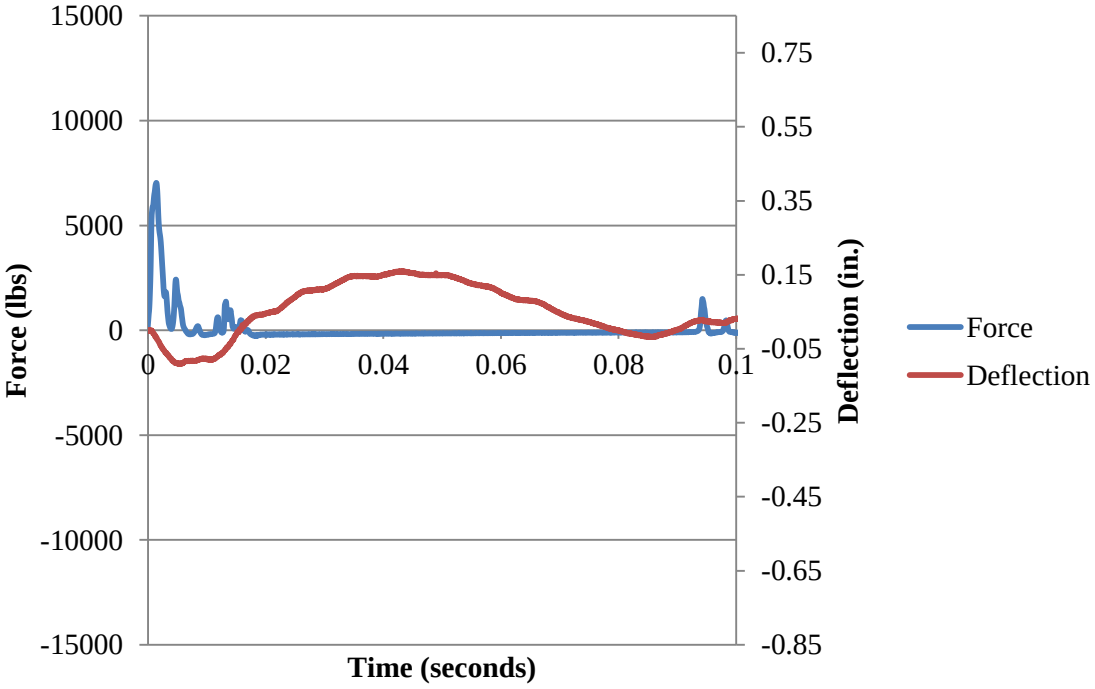

Figure B.150. Force and Deflection vs. Time for Fiber B3_2 at 15 in. (381 mm)

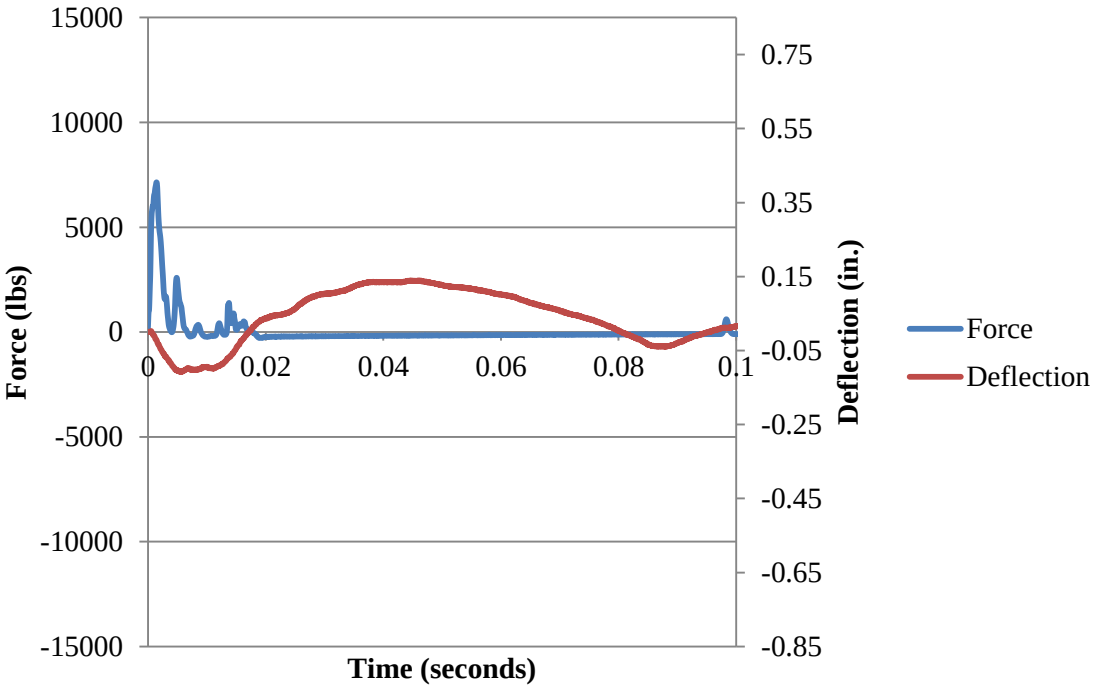

Figure B.151. Force and Deflection vs. Time for Fiber B3_2 at 18 in. (457 mm)

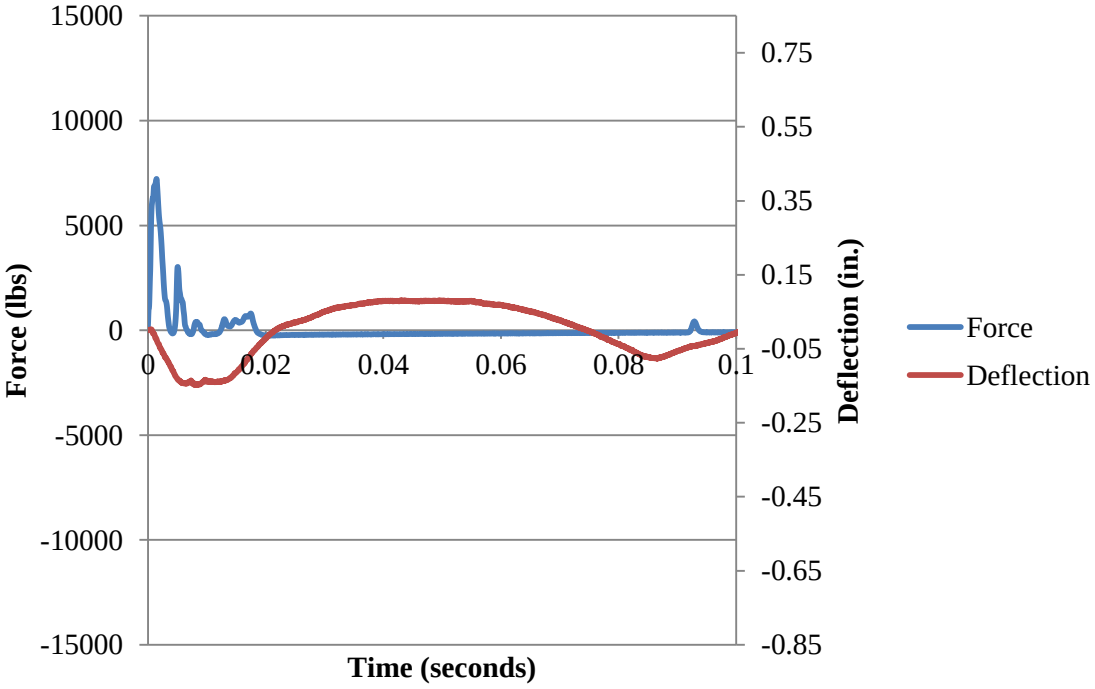

Figure B.152. Force and Deflection vs. Time for Fiber B3_2 at 21 in. (533 mm)

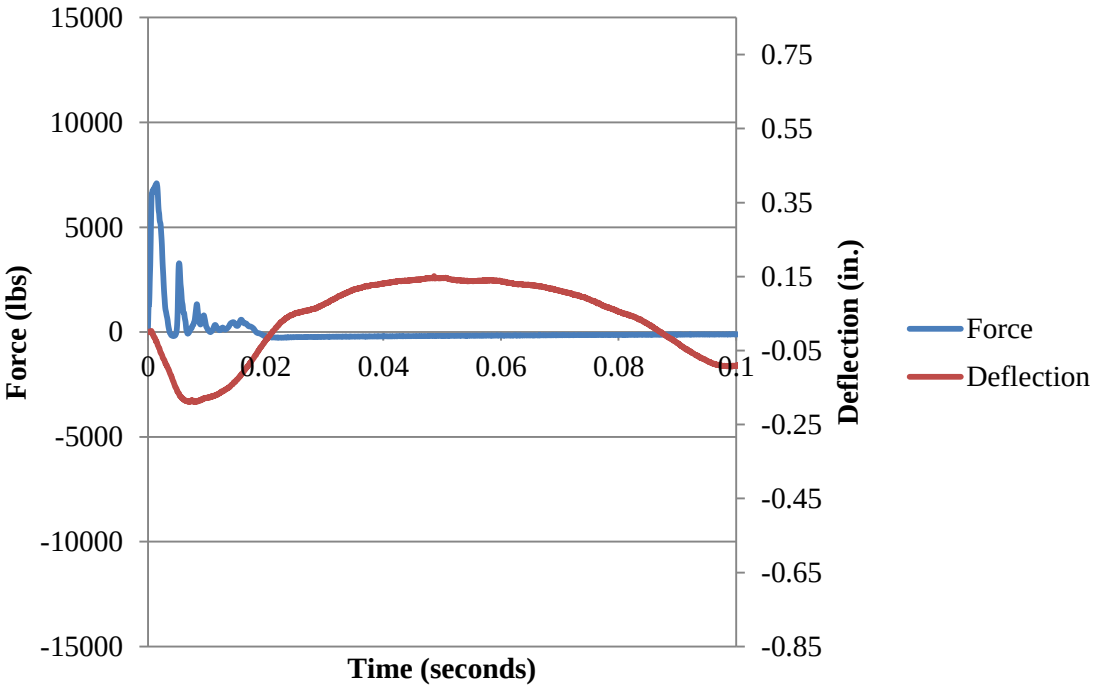

Figure B.153. Force and Deflection vs. Time for Fiber B3_2 at 24 in. (610 mm)

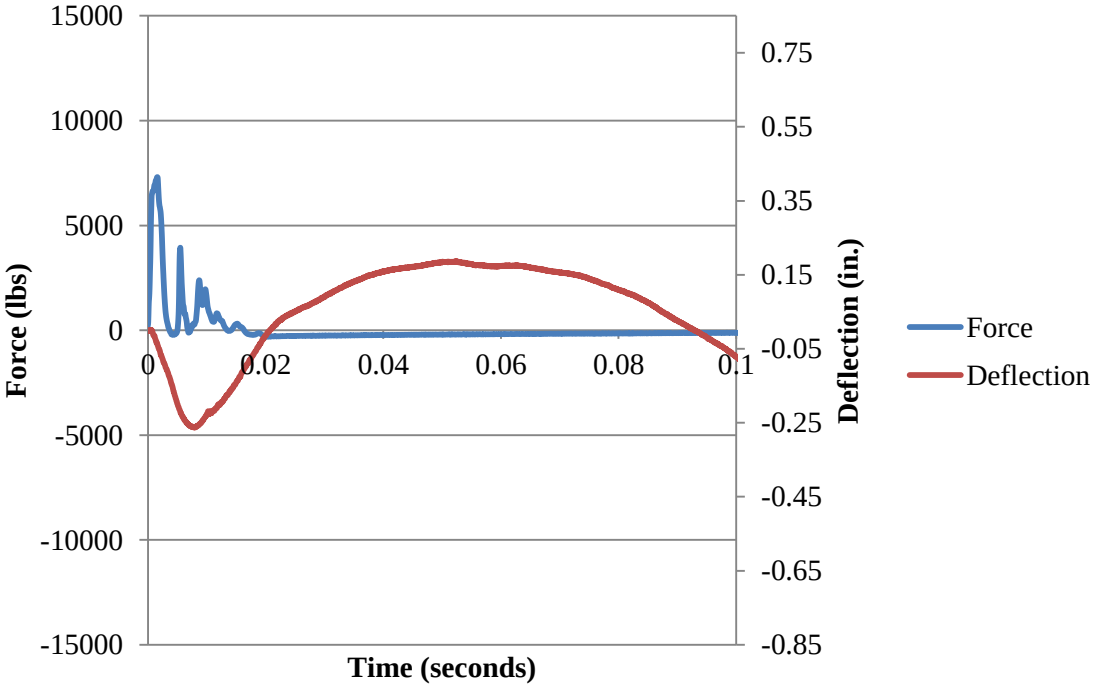

Figure B.154. Force and Deflection vs. Time for Fiber B3_2 at 30 in. (762 mm)

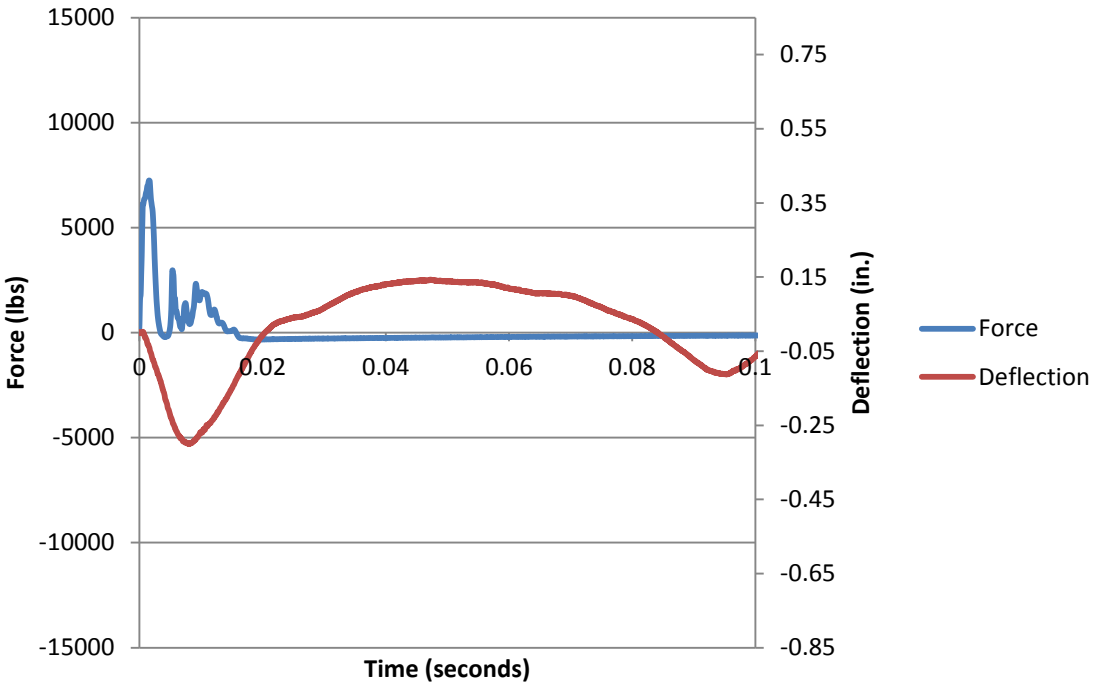

Figure B.155. Force and Deflection vs. Time for Fiber B3_2 at 36 in. (914 mm)

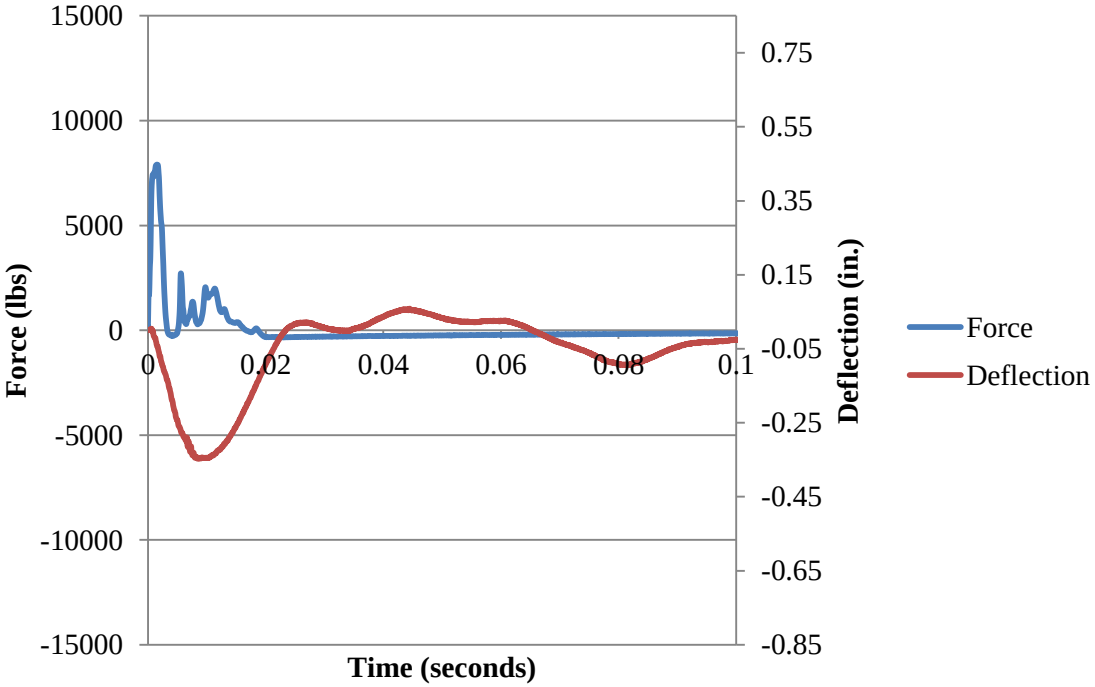

Figure B.156. Force and Deflection vs. Time for Fiber B3_2 at 42 in. (1067 mm)

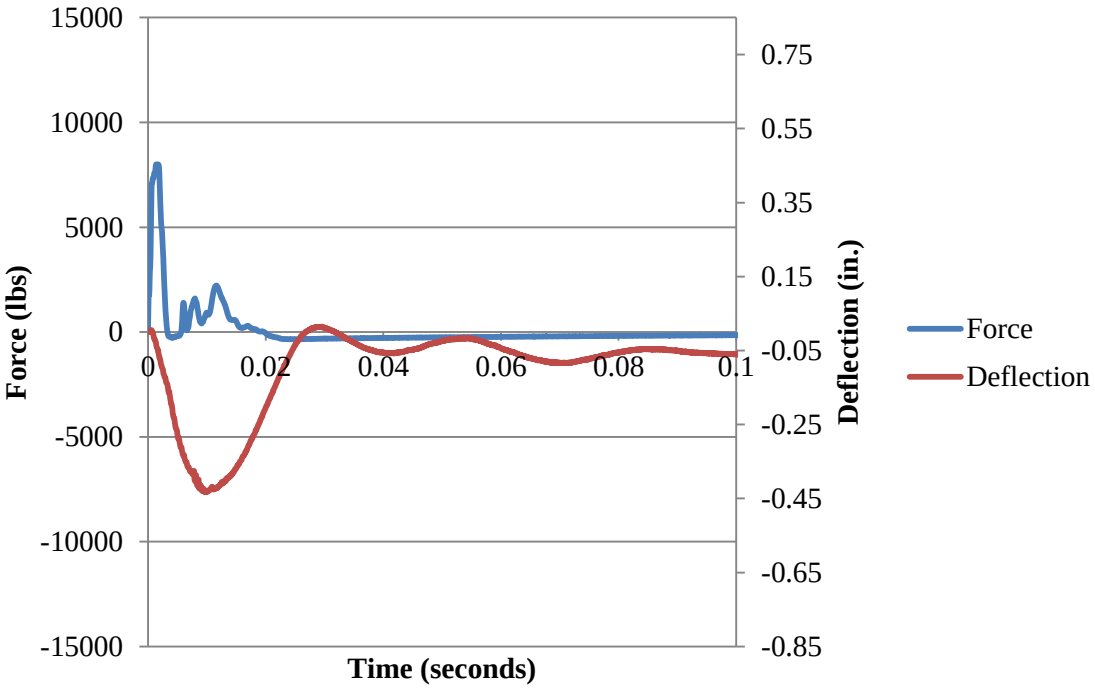

Figure B.157. Force and Deflection vs. Time for Fiber B3_2 at 48 in. (1219 mm)

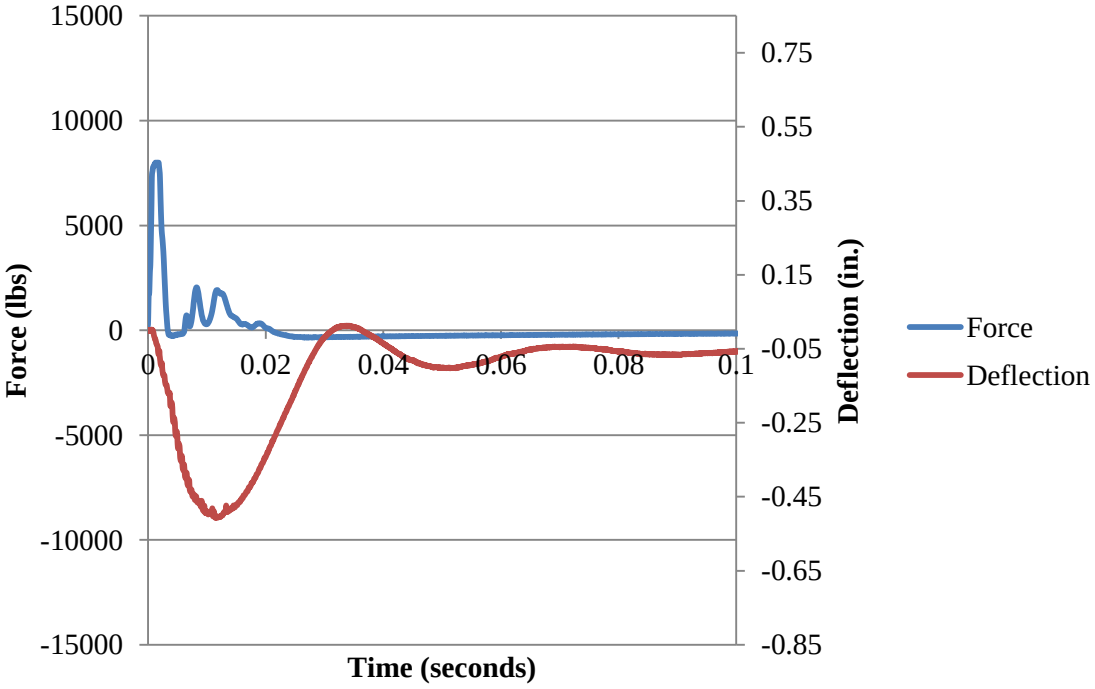

Figure B.158. Force and Deflection vs. Time for Fiber B3_2 at 54 in. (1372 mm)

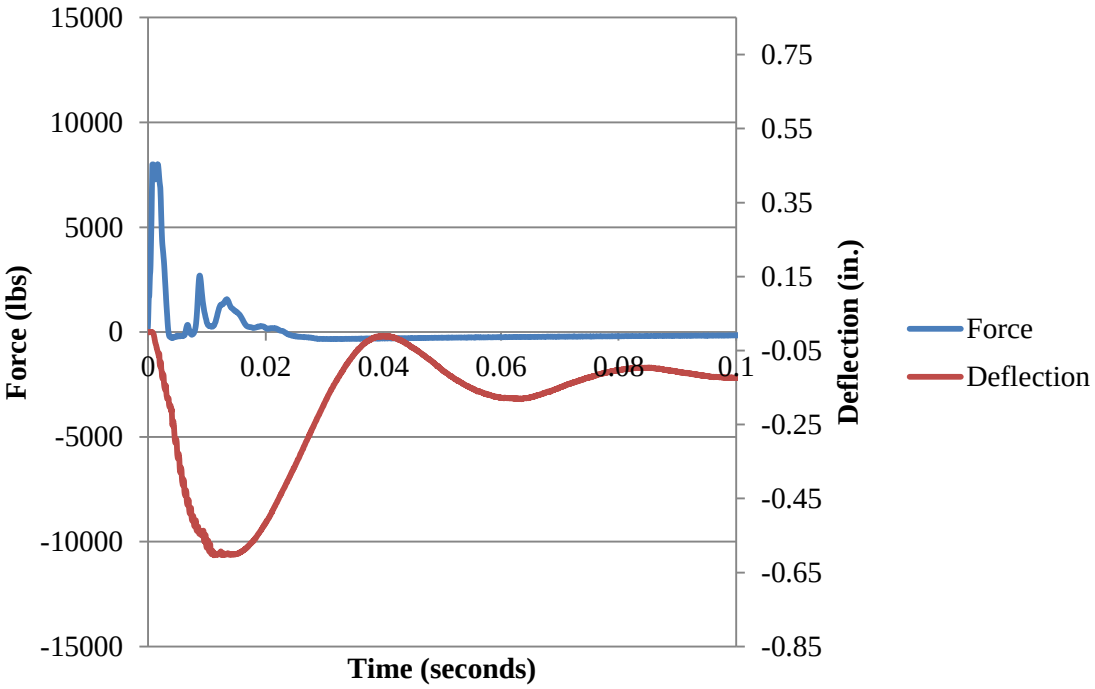

Figure B.159. Force and Deflection vs. Time for Fiber B3_2 at 60 in. (1524 mm)

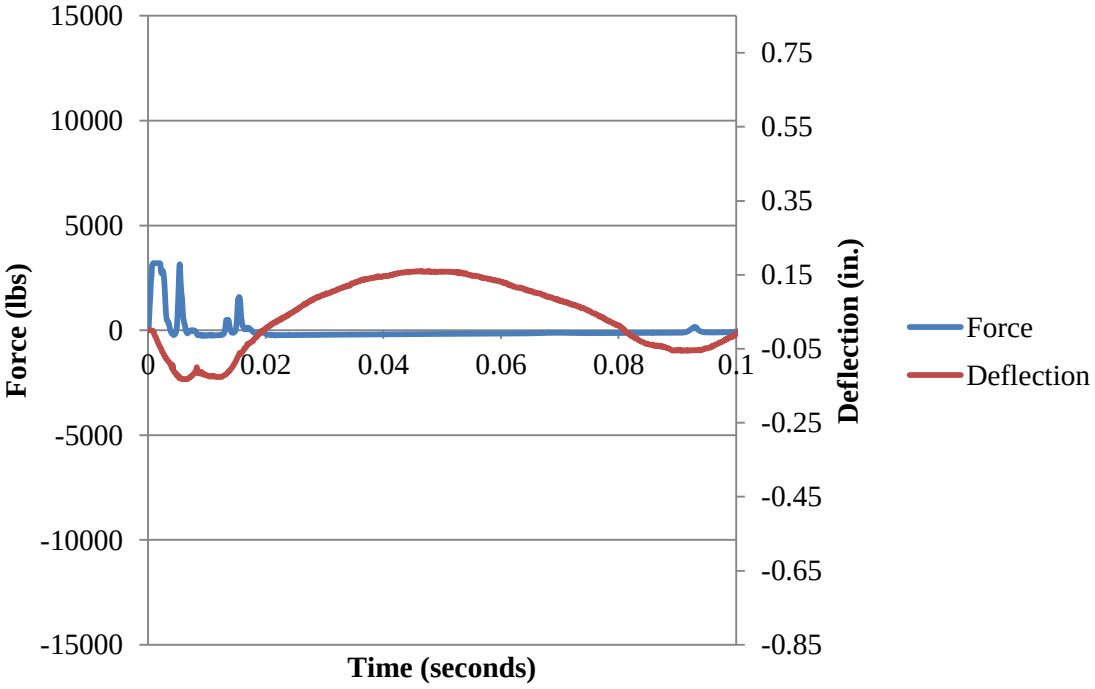

Figure B.160. Force and Deflection vs. Time for Fiber B3_3 at 21 in. (533 mm)

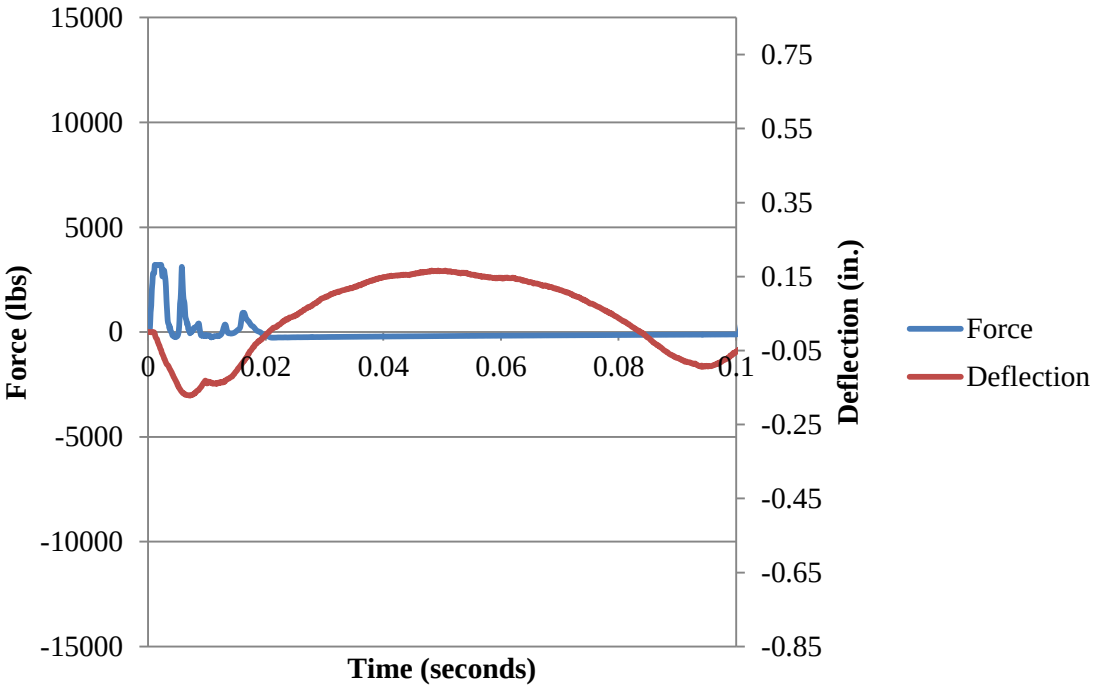

Figure B.161. Force and Deflection vs. Time for Fiber B3_3 at 24 in. (610 mm)

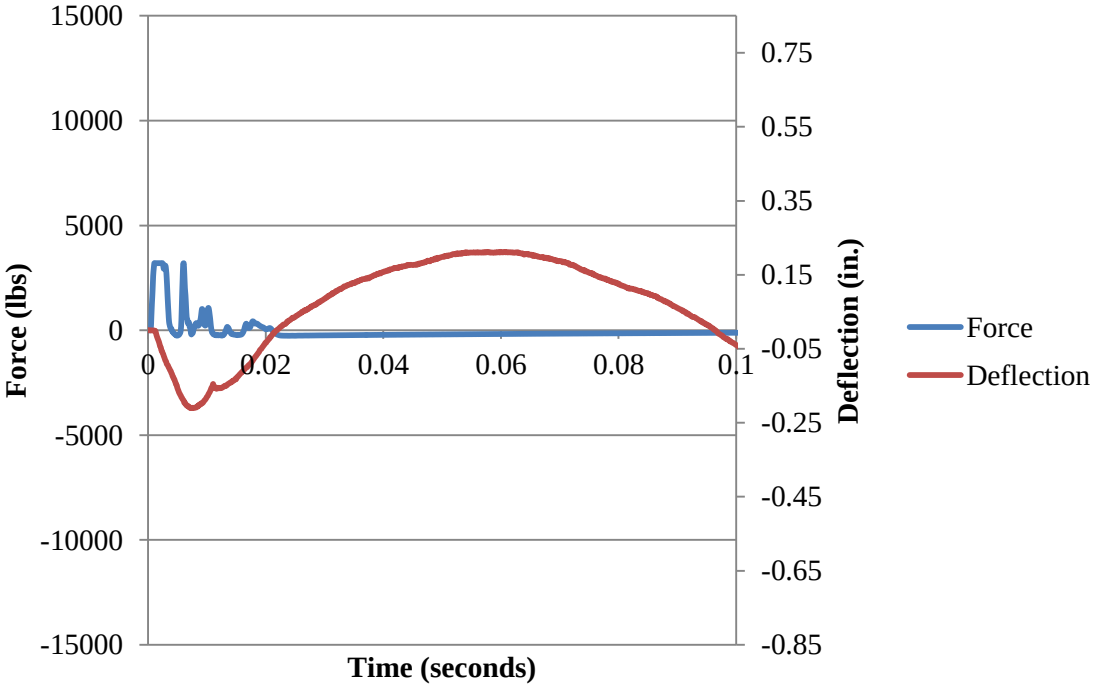

Figure B.162. Force and Deflection vs. Time for Fiber B3_3 at 30 in. (762 mm)

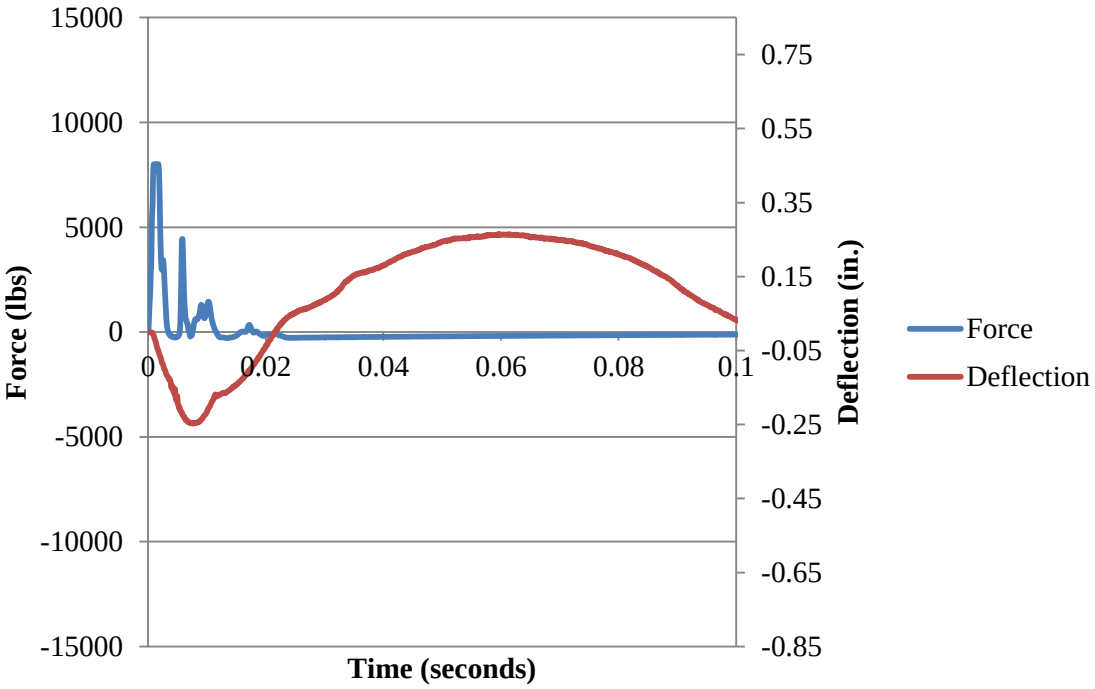

Figure B.163. Force and Deflection vs. Time for Fiber B3_3 at 36 in. (914 mm)

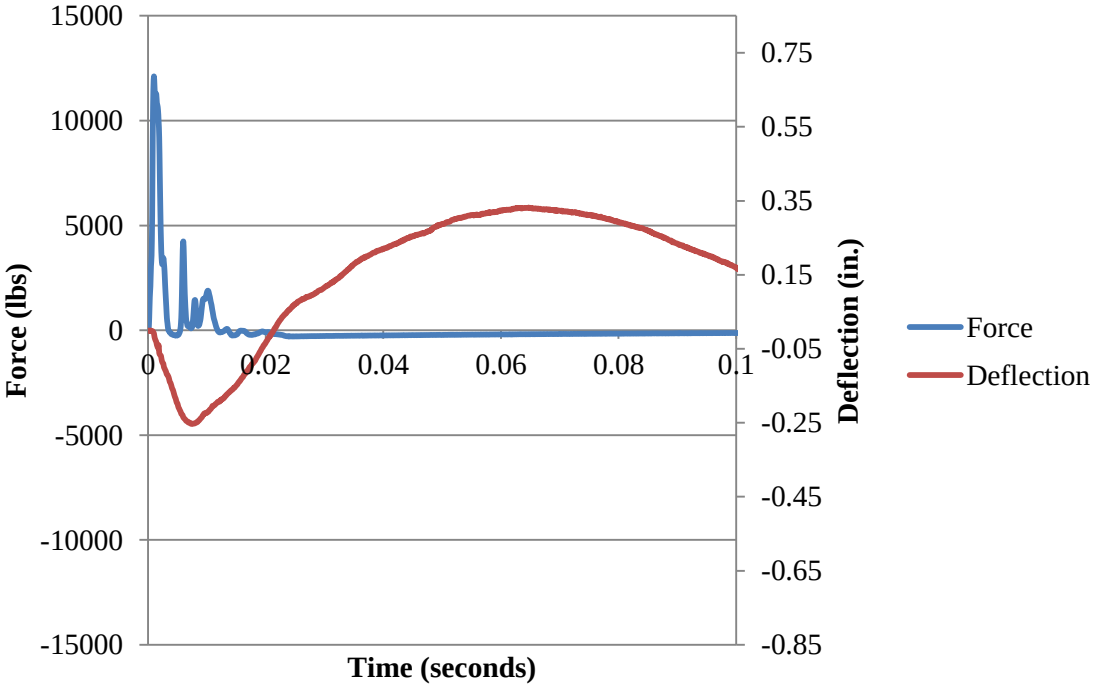

Figure B.164. Force and Deflection vs. Time for Fiber B3_3 at 42 in. (1067 mm)

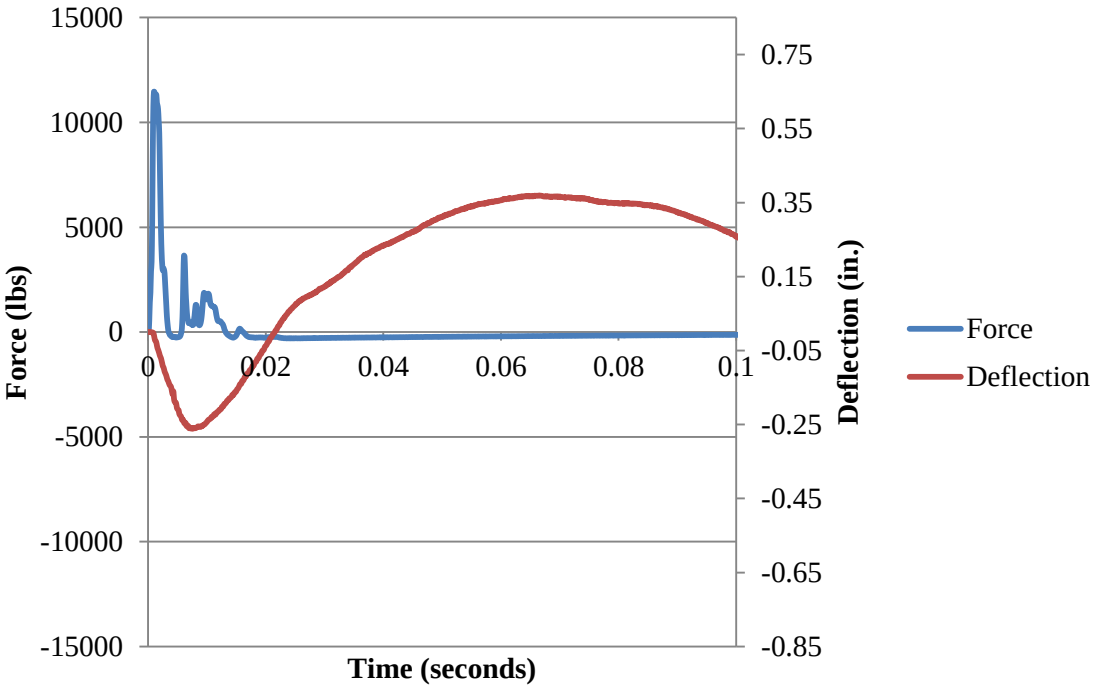

Figure B.165. Force and Deflection vs. Time for Fiber B3_3 at 48 in. (1219 mm)

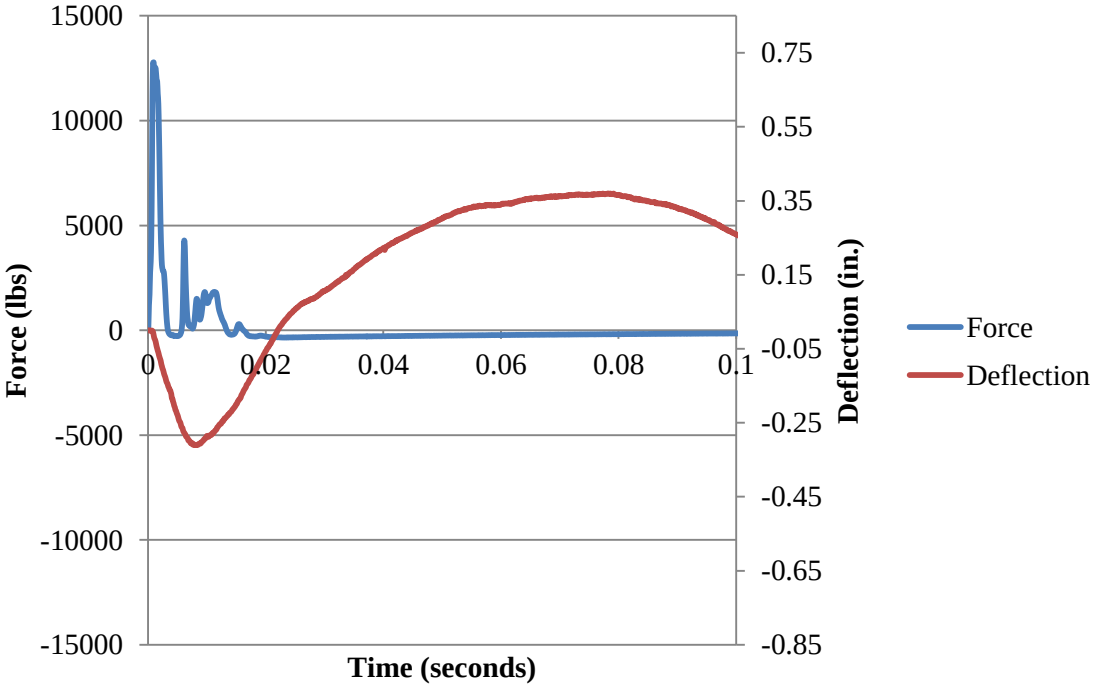

Figure B.166. Force and Deflection vs. Time for Fiber B3_3 at 54 in. (1372 mm)

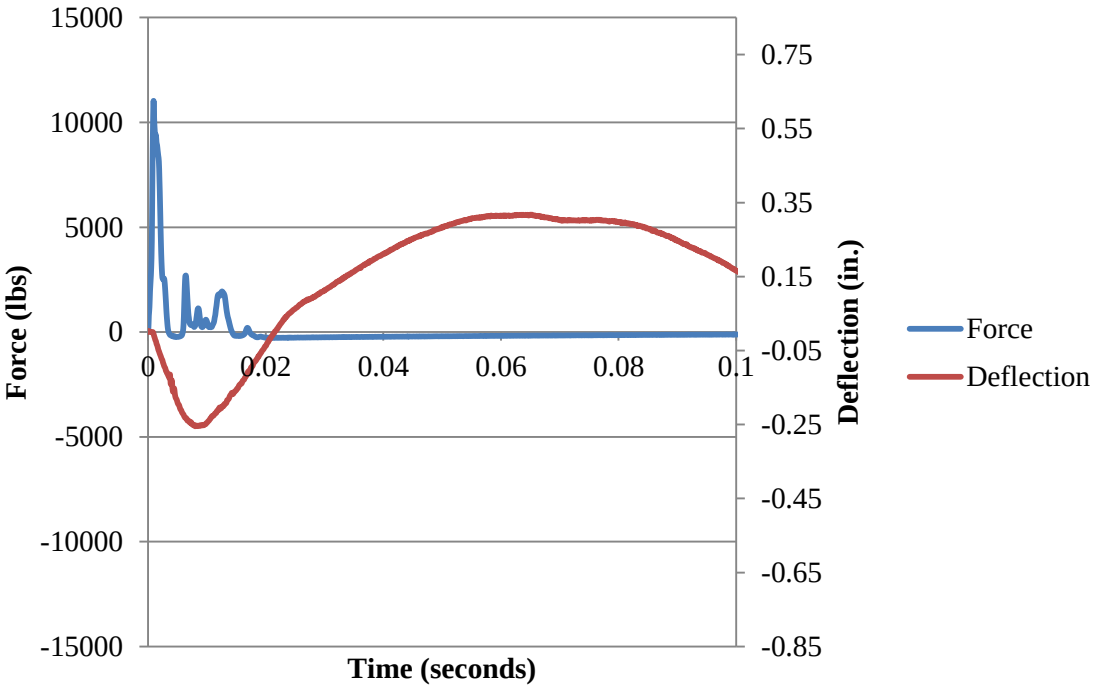

Figure B.167. Force and Deflection vs. Time for Fiber B3_3 at 60 in. (1524 mm)

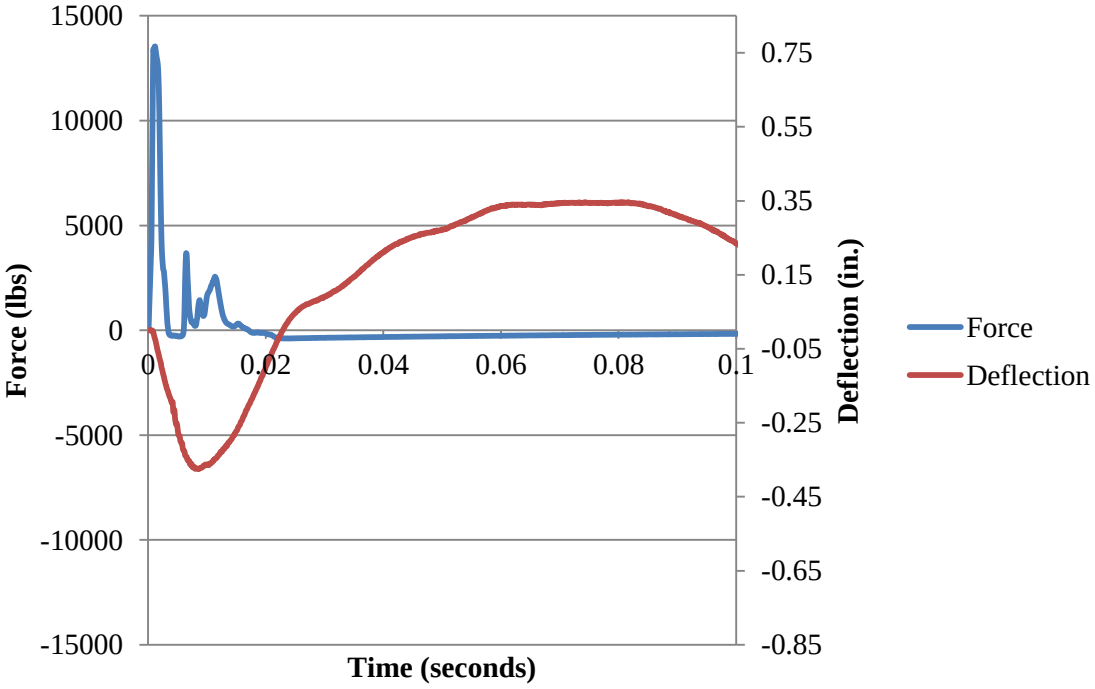

Figure B.168. Force and Deflection vs. Time for Fiber B3_3 at 66 in. (1676 mm)

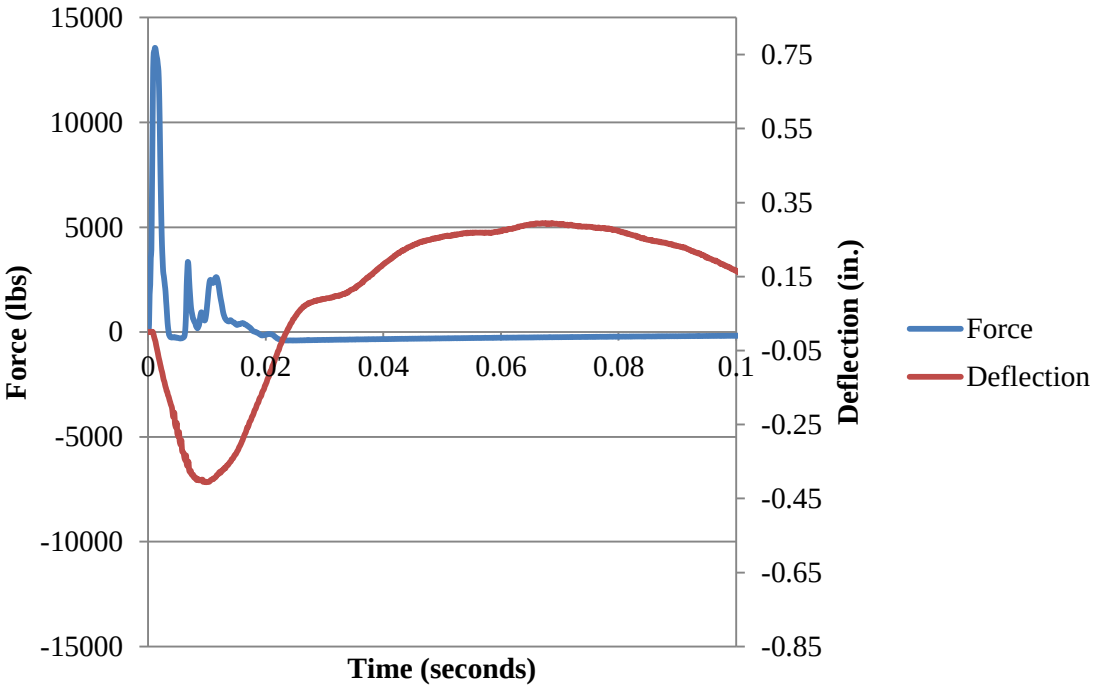

Figure B.169. Force and Deflection vs. Time for Fiber B3_3 at 72 in. (1829 mm)

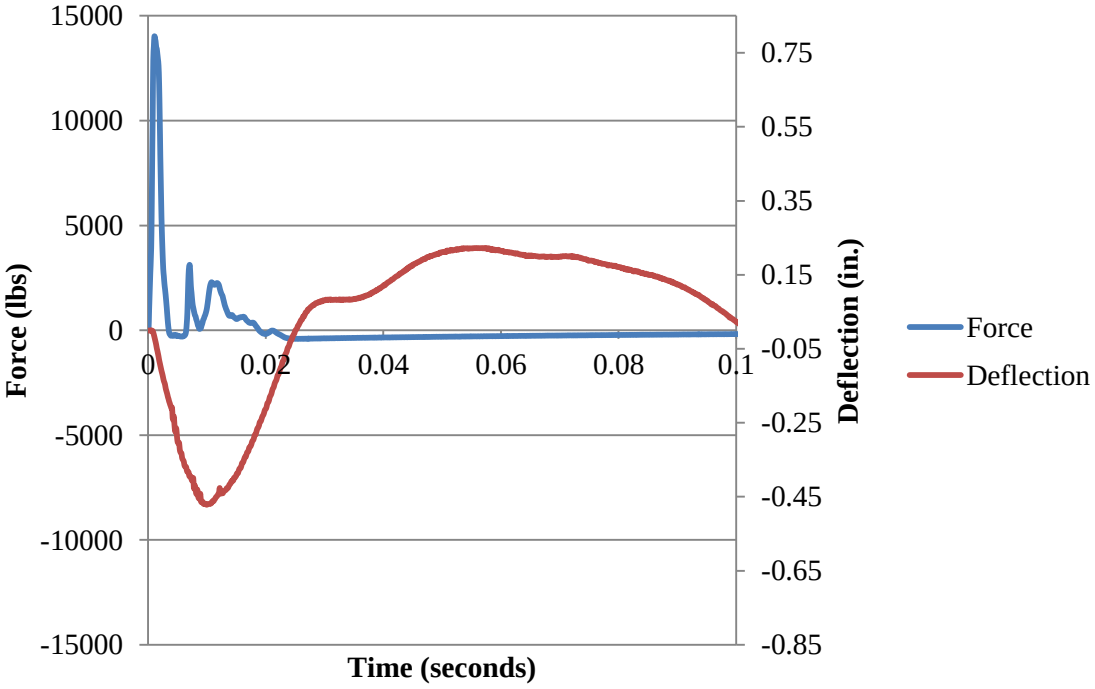

Figure B.170. Force and Deflection vs. Time for Fiber B3_3 at 78 in. (1981 mm)

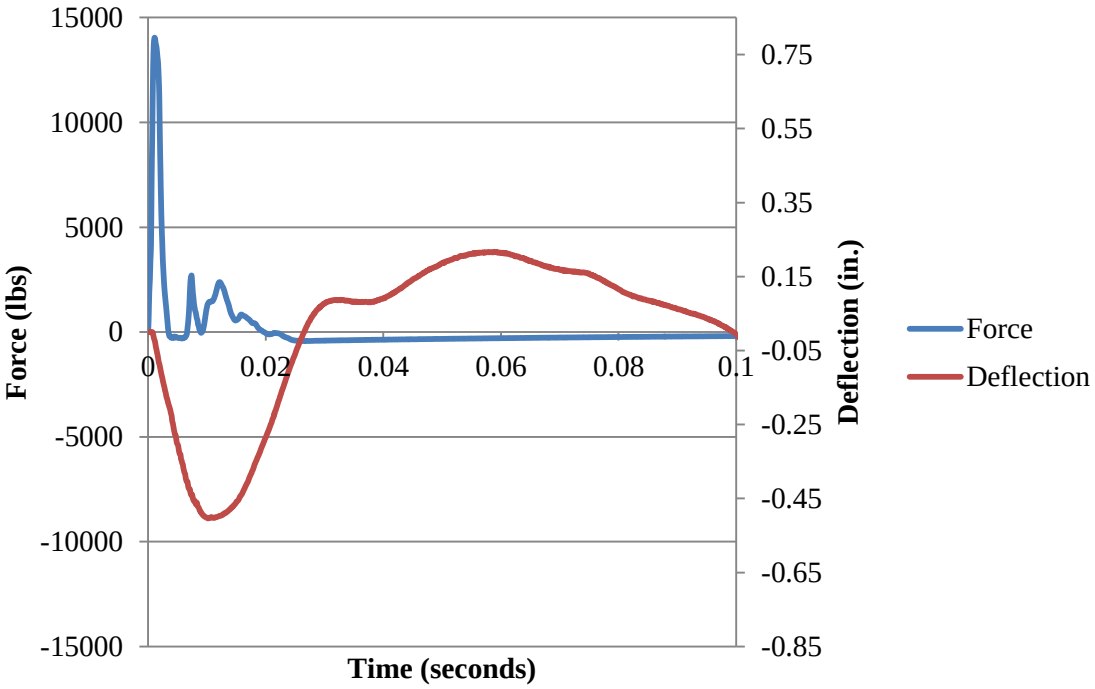

Figure B.171. Force and Deflection vs. Time for Fiber B3_3 at 84 in. (2134 mm)

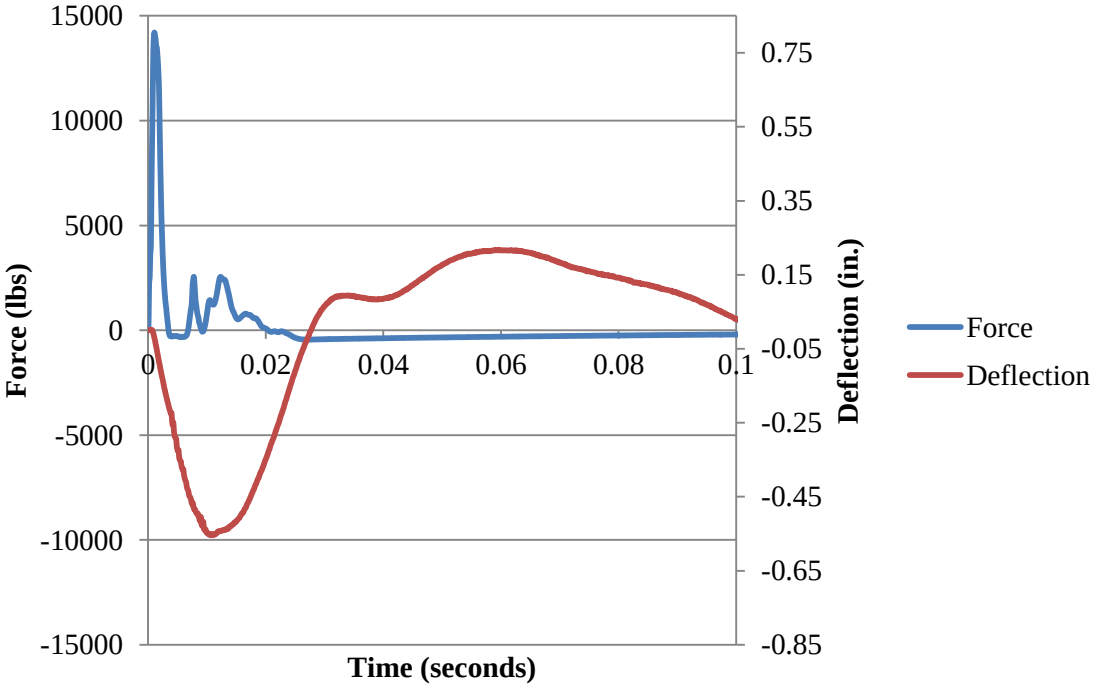

Figure B.172. Force and Deflection vs. Time for Fiber B3_3 at 90 in. (2286 mm)

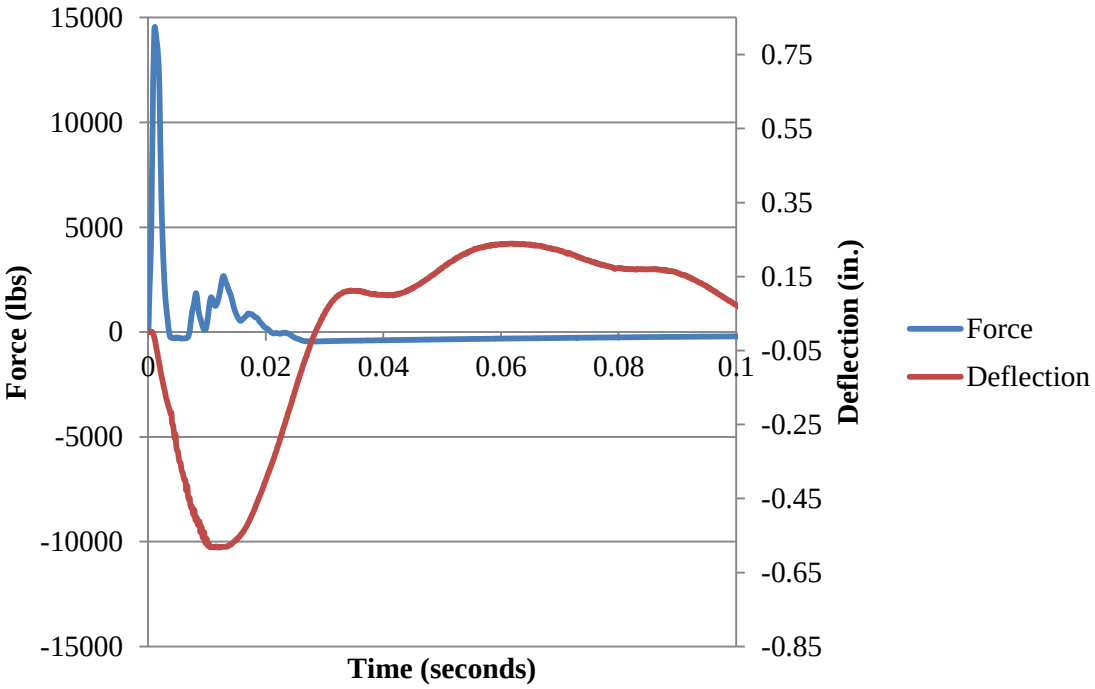

Figure B.173. Force and Deflection vs. Time for Fiber B3_3 at 96 in. (2438 mm)

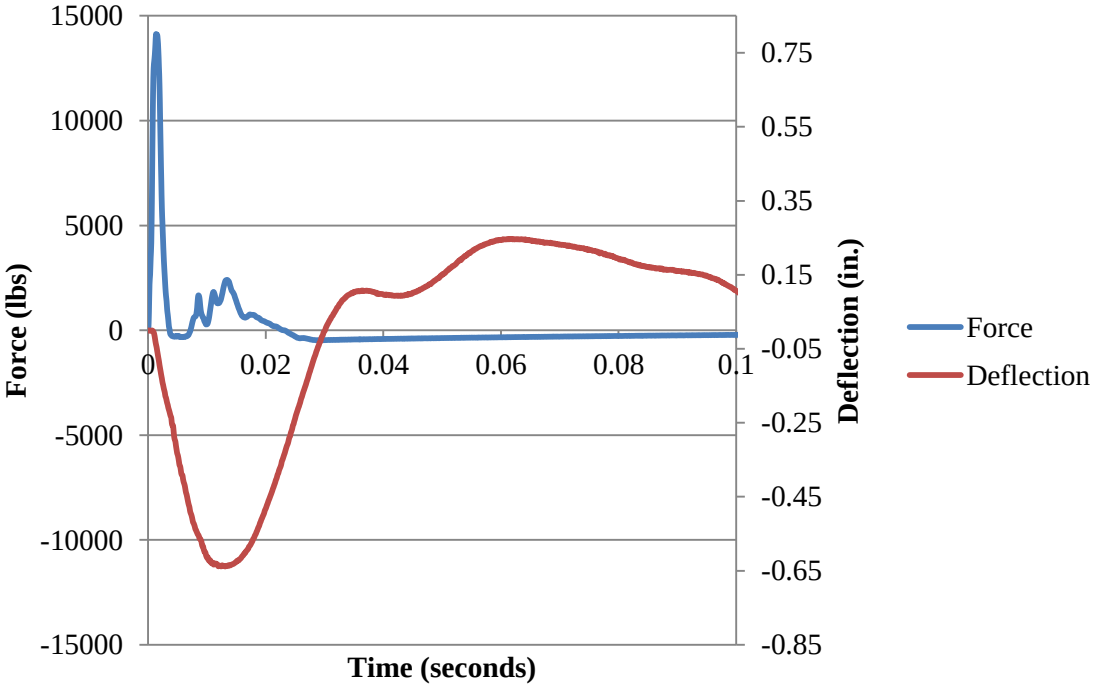

Figure B.174. Force and Deflection vs. Time for Fiber B3_3 at 102 in. (2591 mm)

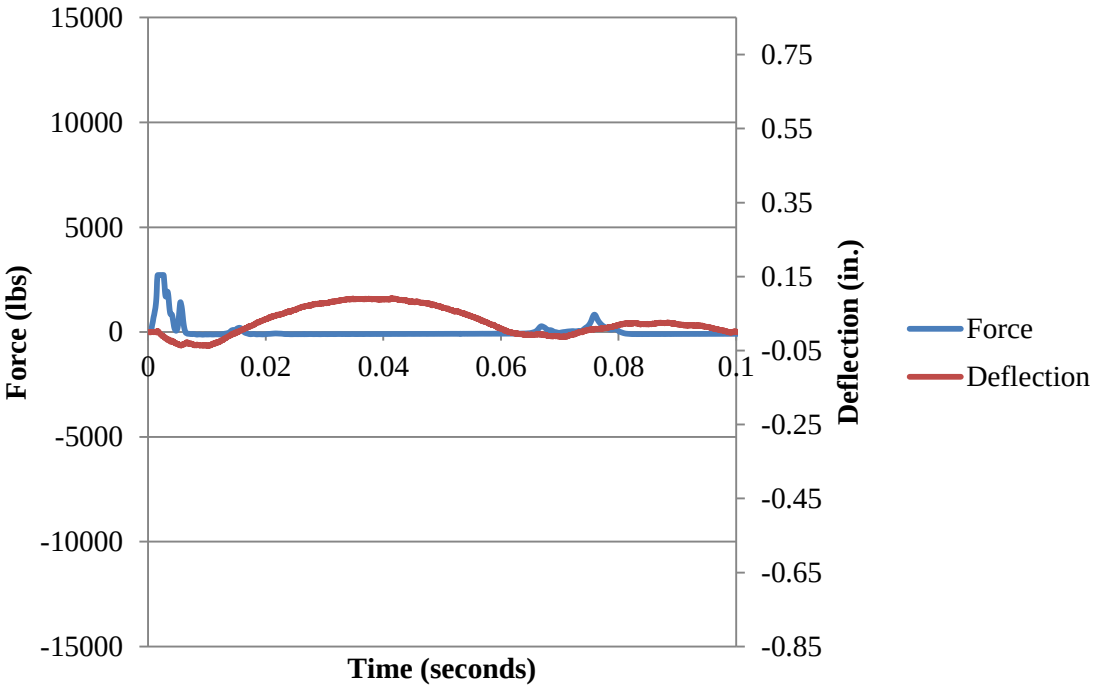

Figure B.175. Force and Deflection vs. Time for Fiber B3_4 at 3 in. (76 mm)

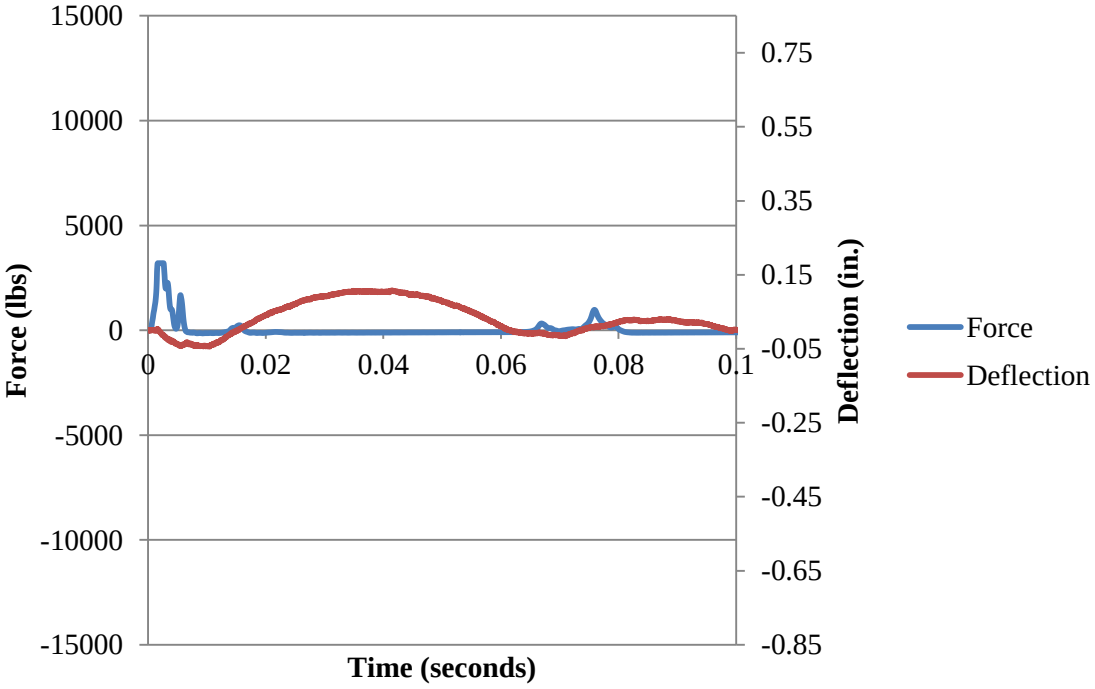

Figure B.176. Force and Deflection vs. Time for Fiber B3_4 at 6 in. (152 mm)

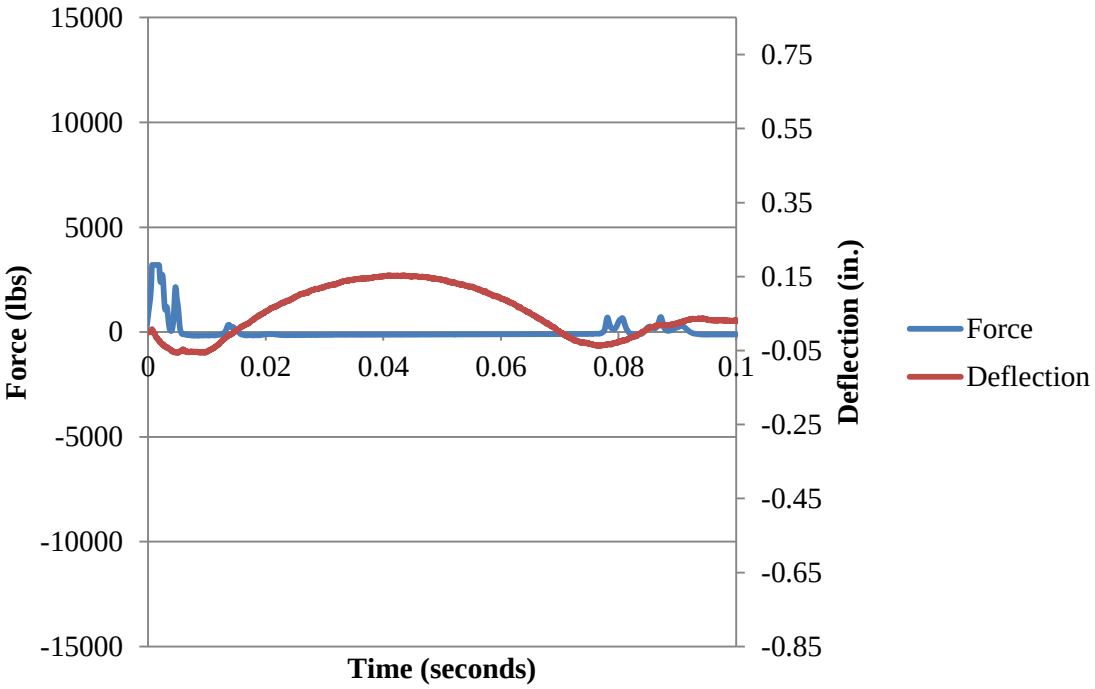

Figure B.177. Force and Deflection vs. Time for Fiber B3_4 at 9 in. (229 mm)

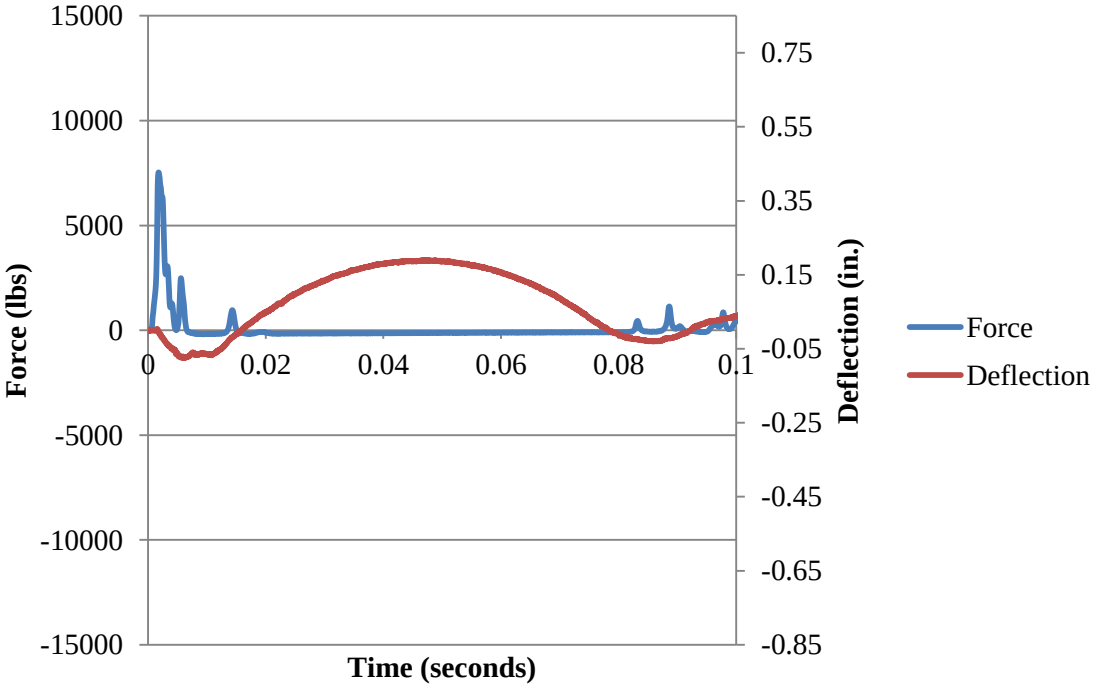

Figure B.178. Force and Deflection vs. Time for Fiber B3_4 at 12 in. (305 mm)

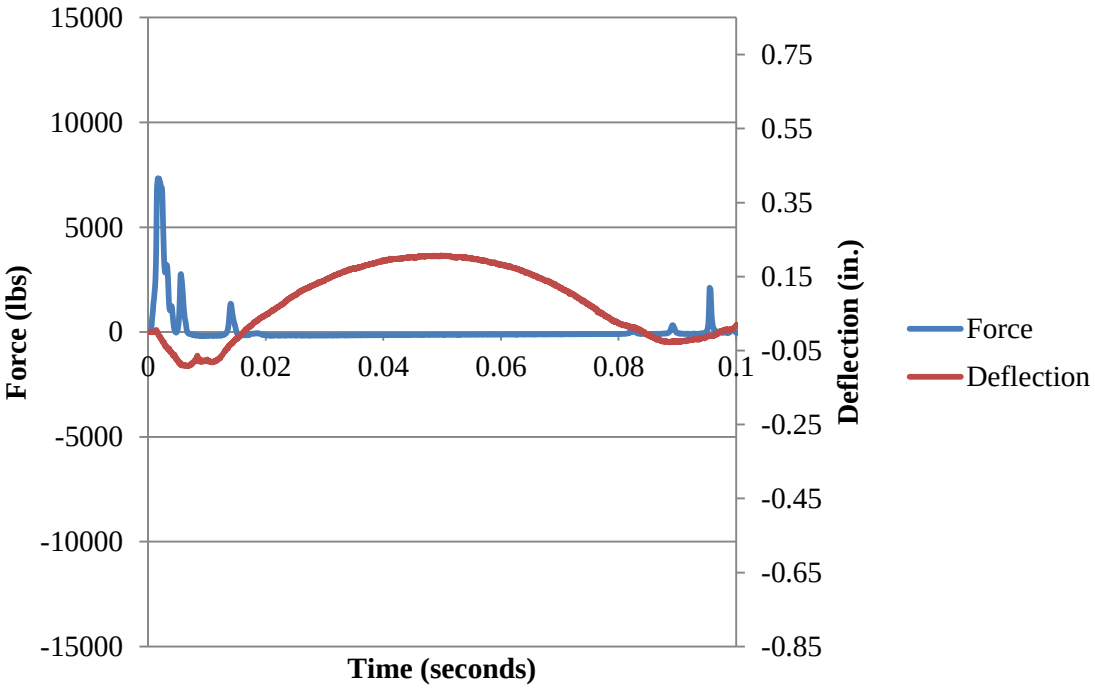

Figure B.179. Force and Deflection vs. Time for Fiber B3_4 at 15 in. (381 mm)

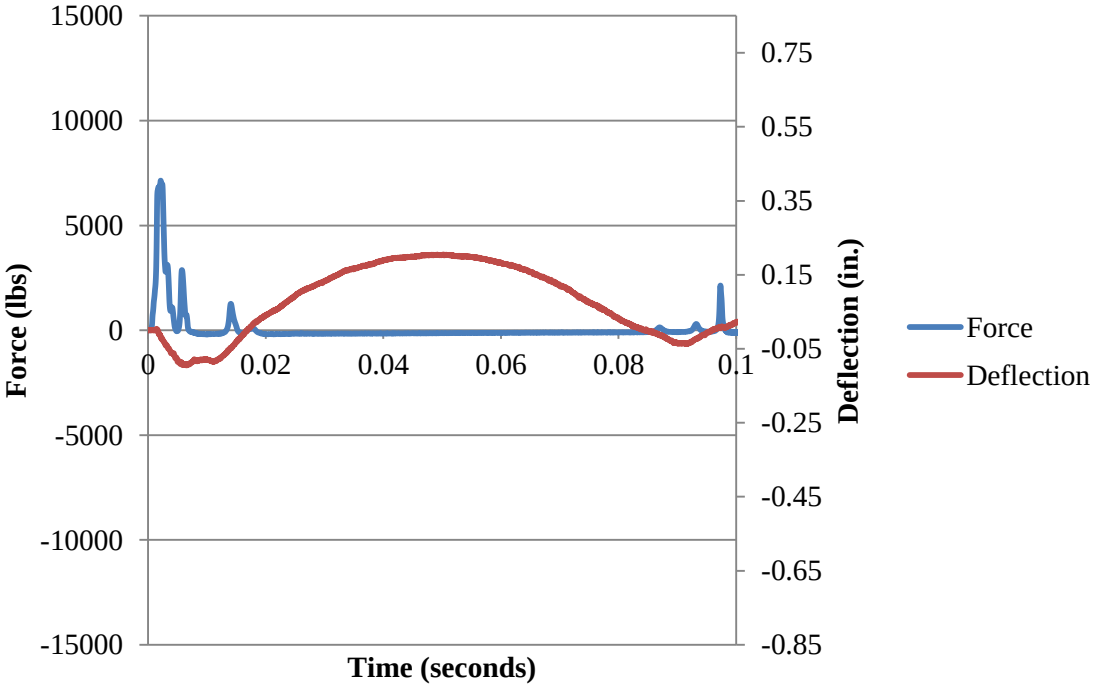

Figure B.180. Force and Deflection vs. Time for Fiber B3_4 at 18 in. (457 mm)

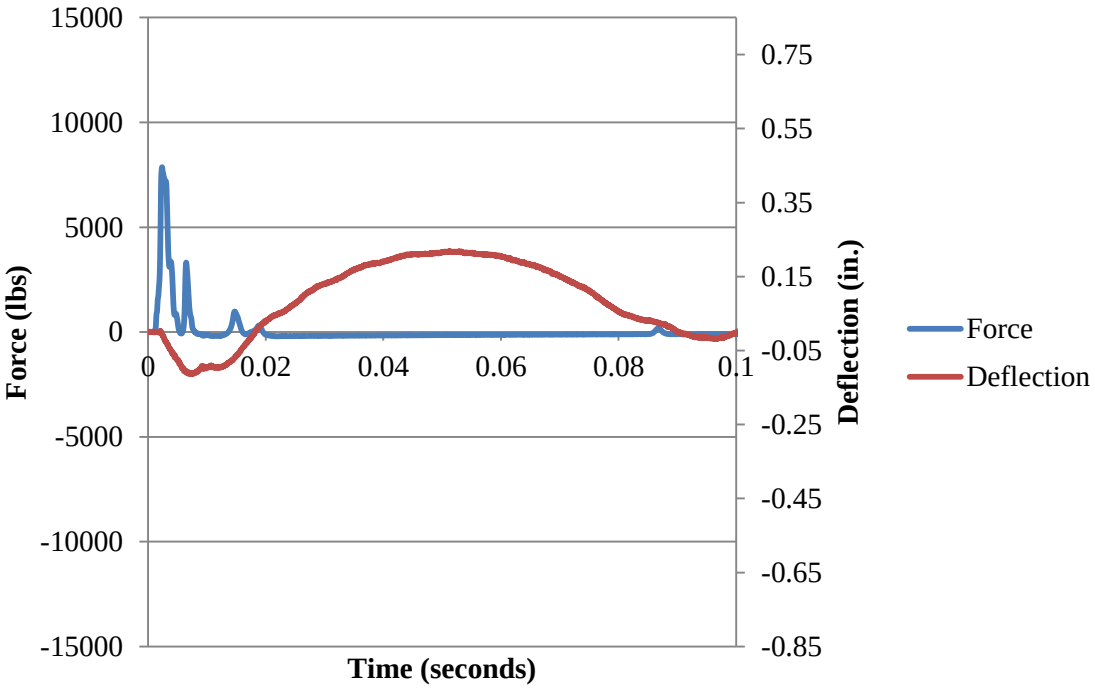

Figure B.181. Force and Deflection vs. Time for Fiber B3_4 at 21 in. (533 mm)

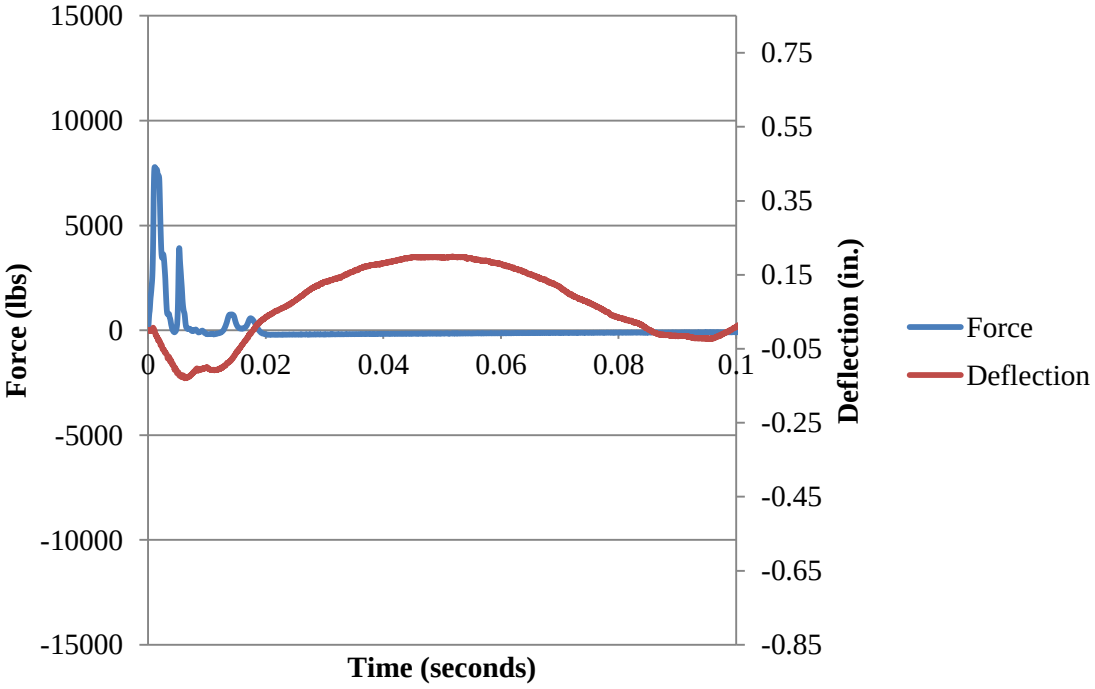

Figure B.182. Force and Deflection vs. Time for Fiber B3_4 at 24 in. (610 mm)

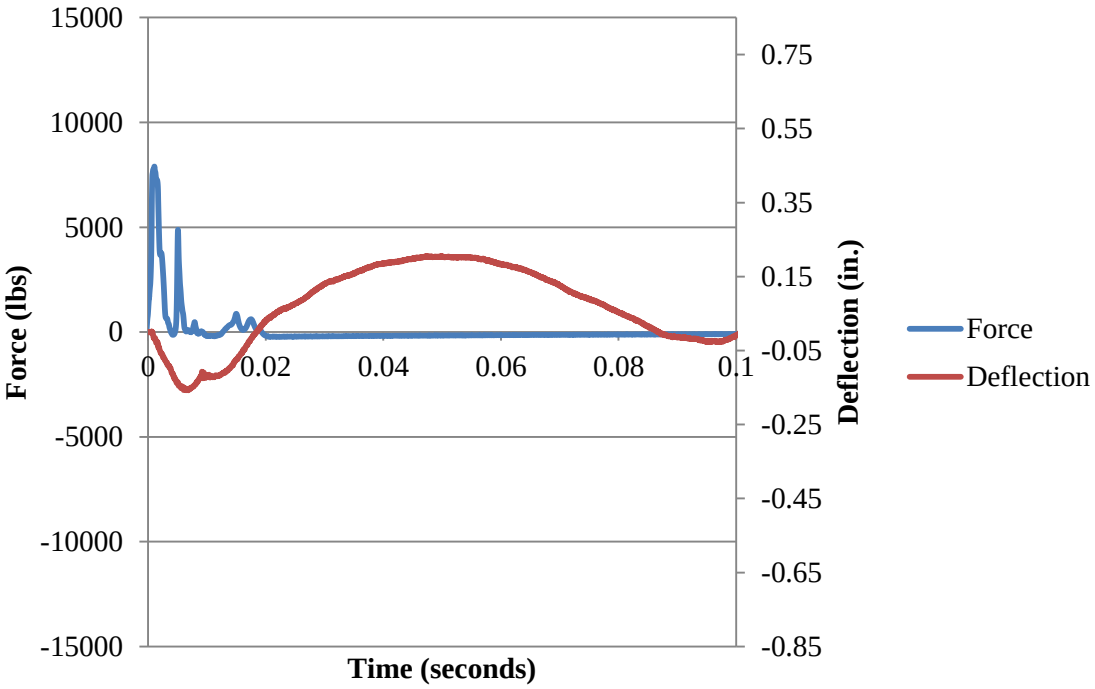

Figure B.183. Force and Deflection vs. Time for Fiber B3_4 at 30 in. (762 mm)

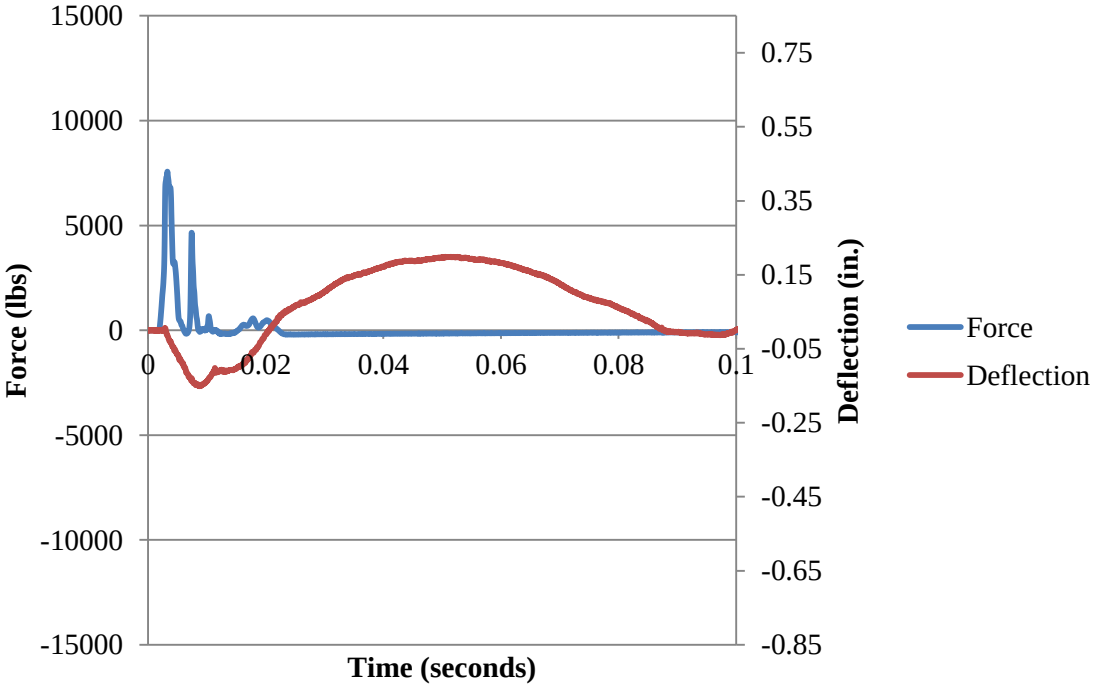

Figure B.184. Force and Deflection vs. Time for Fiber B3_4 at 36 in. (914 mm)

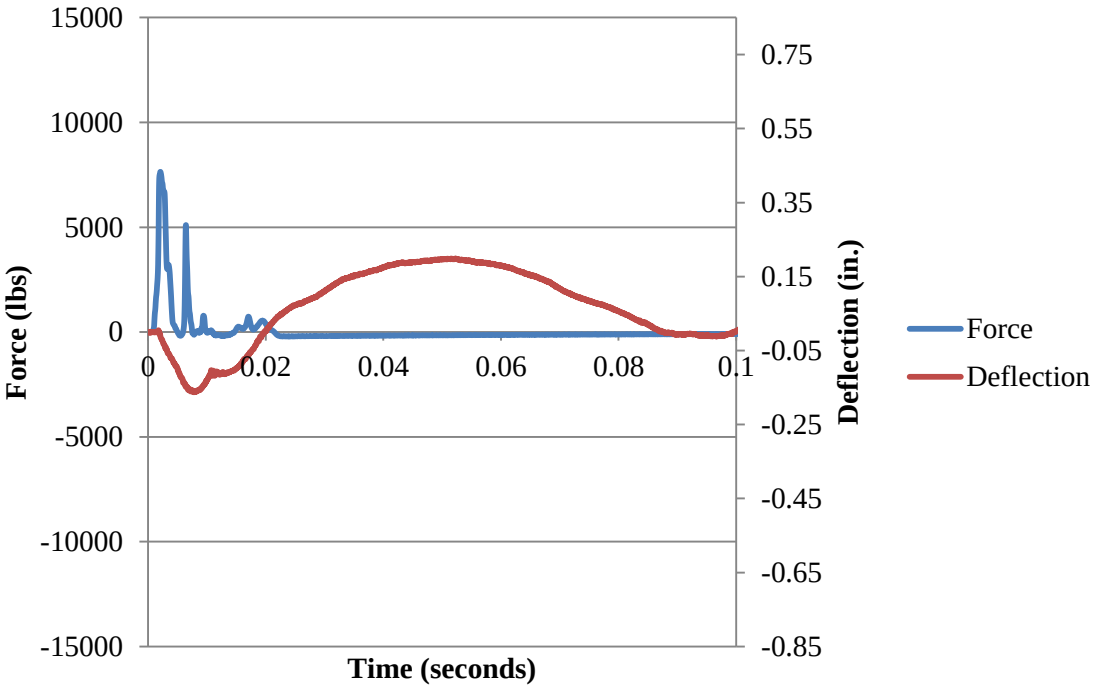

Figure B.185. Force and Deflection vs. Time for Fiber B3_4 at 42 in. (1067 mm)

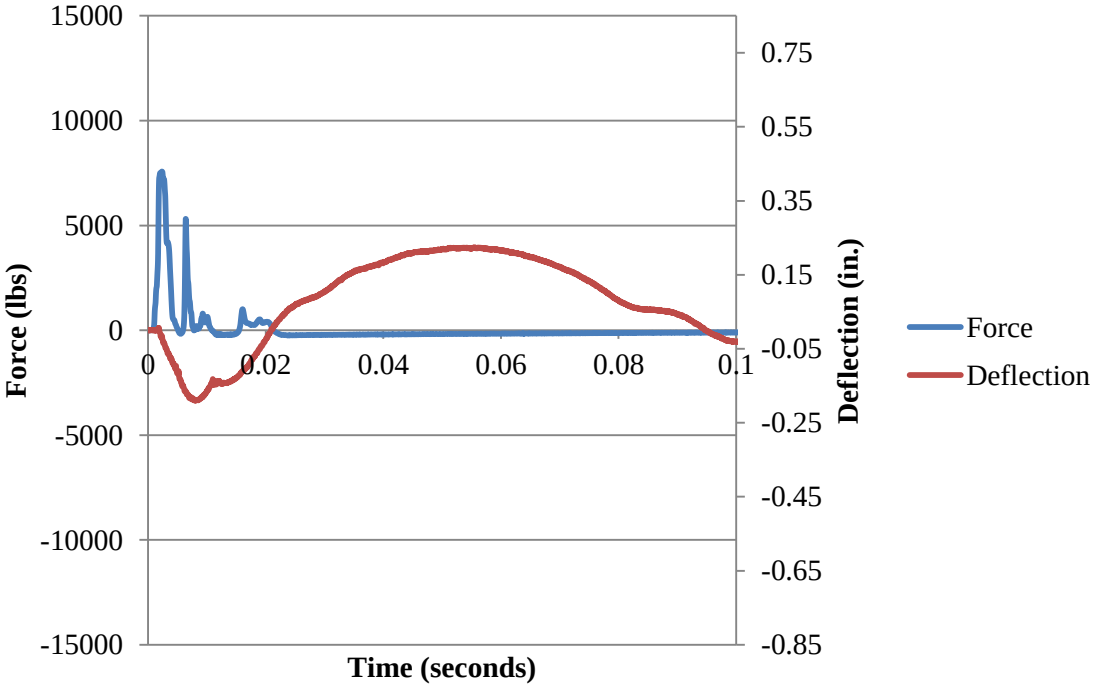

Figure B.186. Force and Deflection vs. Time for Fiber B3_4 at 48 in. (1219 mm)

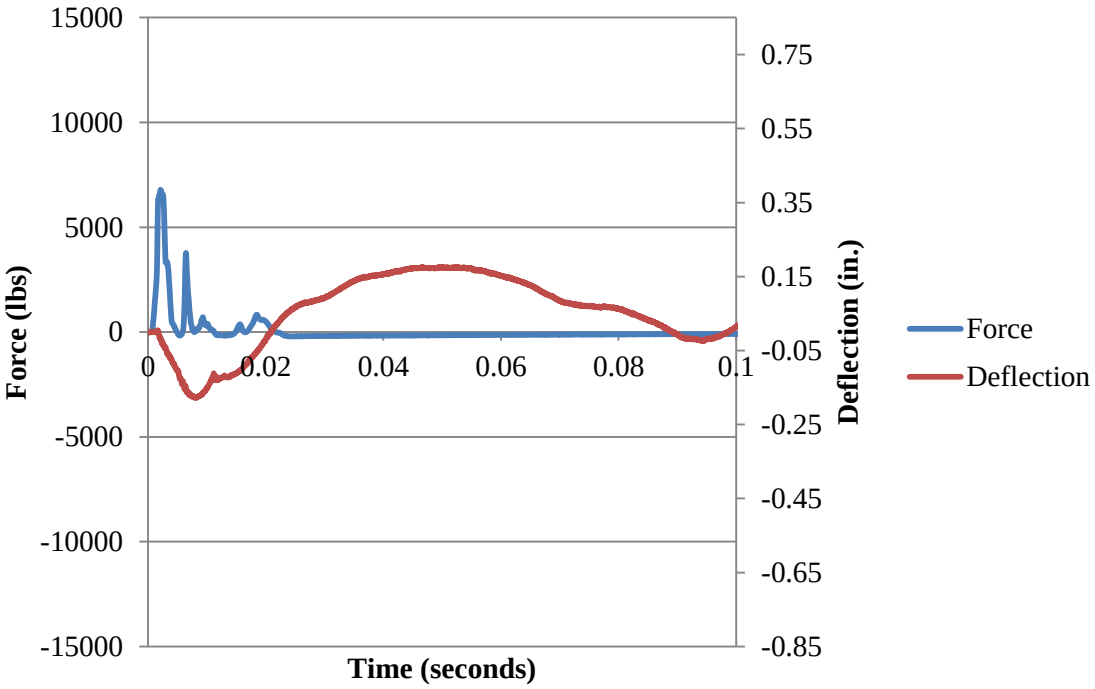

Figure B.187. Force and Deflection vs. Time for Fiber B3_4 at 54 in. (1372 mm)

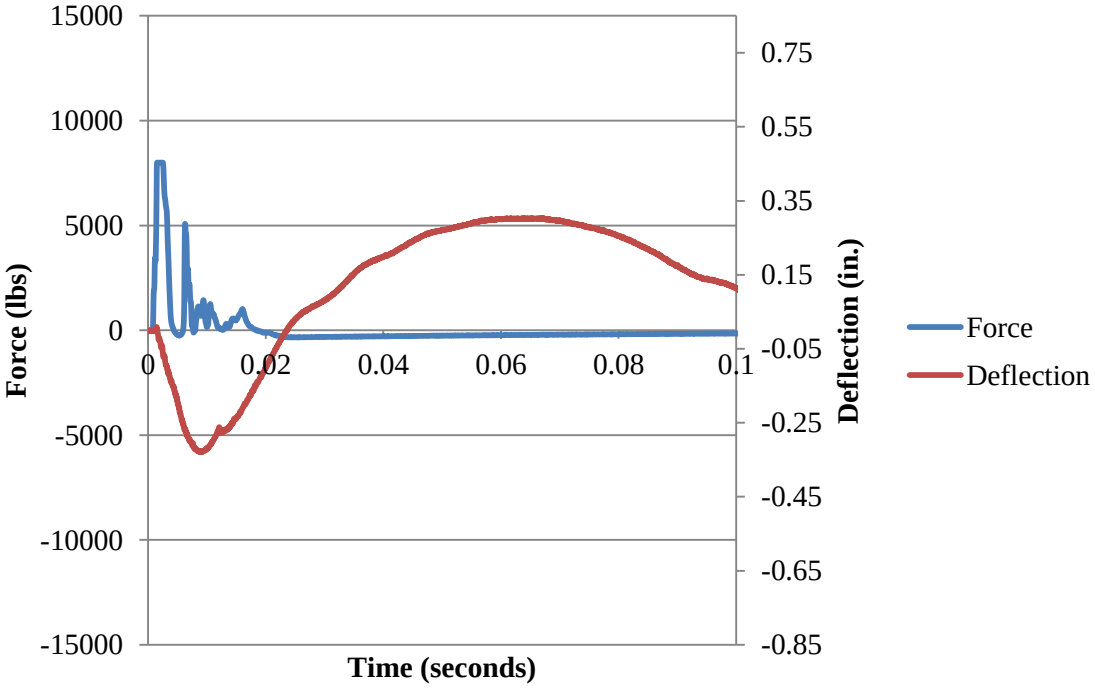

Figure B.188. Force and Deflection vs. Time for Fiber B3_4 at 60 in. (1524 mm)

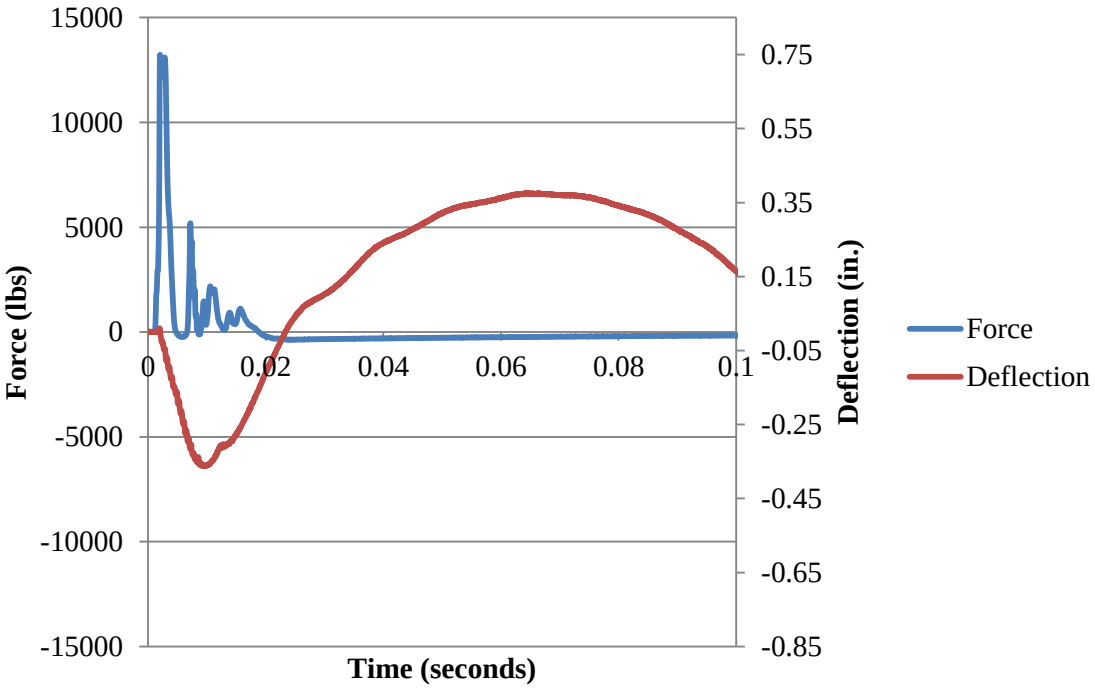

Figure B.189. Force and Deflection vs. Time for Fiber B3_4 at 66 in. (1676 mm)

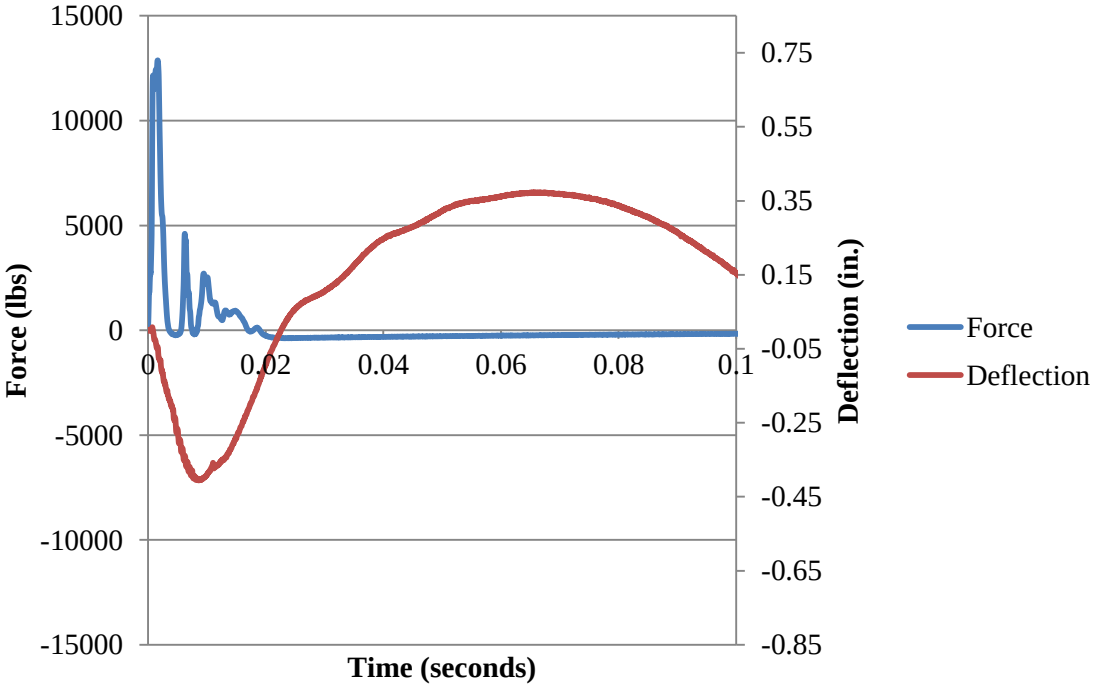

Figure B.190. Force and Deflection vs. Time for Fiber B3_4 at 72 in. (1829 mm)

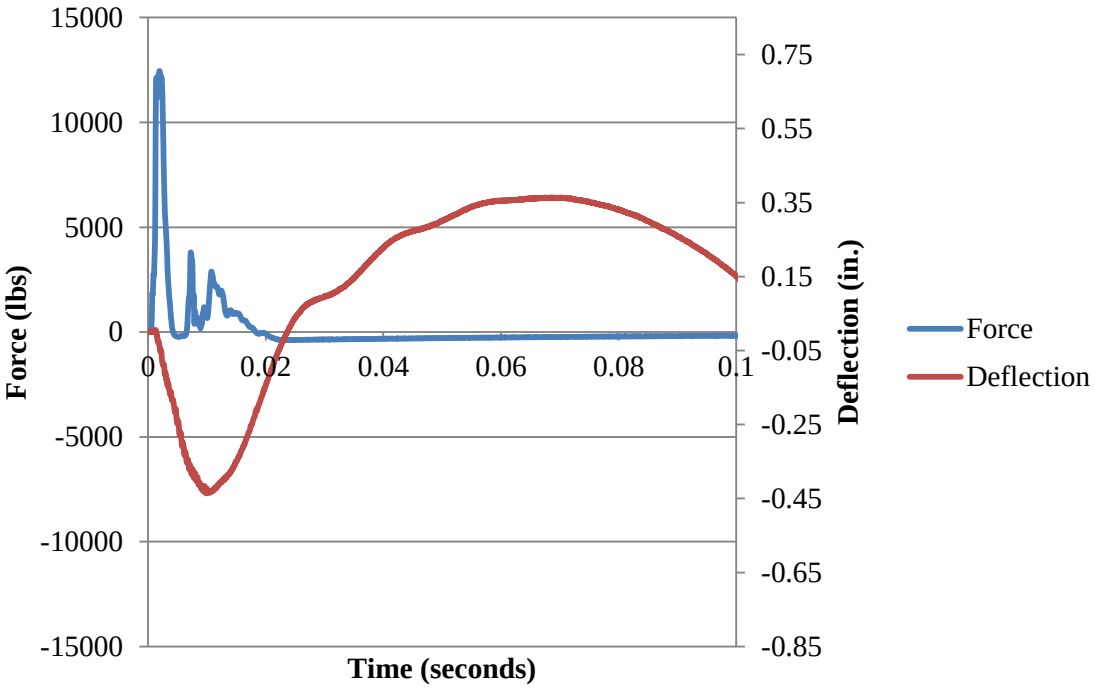

Figure B.191. Force and Deflection vs. Time for Fiber B3_4 at 78 in. (1981 mm)

APPENDIX C.
CONWEP ANALYSES

This appendix includes all pertinent data and graphs generated from the CONWEP analyses for the 3.5-foot (1067 mm) and 5.5-foot (1676 mm) standoff distances. The smaller standoff distance stems from the work done by Schokker and Musselman (2006), while the data for a 5.5-foot (1676 mm) standoff distance was run to aid the researchers if there was a need for shot refinement during field-testing.

UNCLASSIFIED

Pressure Distribution on a Wall	
Charge weight	74.99 pounds TNT
Standoff distance from target	3.5 feet
Peak pressure	9990 psi
at X =	0 feet
Y =	0 feet
Minimum pressure	3114 psi
at X =	-3 feet
Y =	-3 feet
Peak impulse	1284 psi-msec
at X =	0 feet
Y =	0 feet
Average impulse	656.2 psi-msec
Equivalent uniform load	
Supports fixed on all sides	
Equivalent uniform peak pressure	6929 psi
Equivalent uniform impulse	865.9 psi-msec
Decay coefficient of equivalent uniform pressure, α	8.003

Figure C.1. CONWEP analysis for 3.5-foot (1067 mm) standoff distance; peak pressures

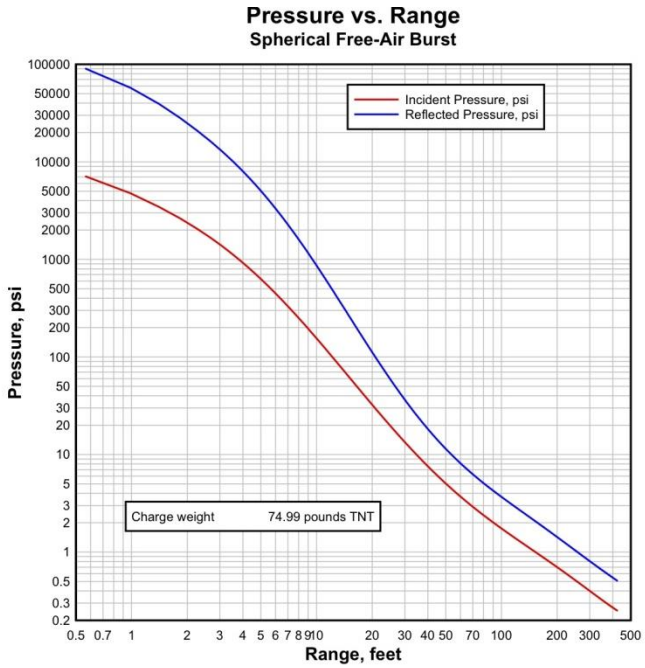

Figure C.2. CONWEP analysis for 3.5-foot (1067 mm) standoff distance; pressure vs. range

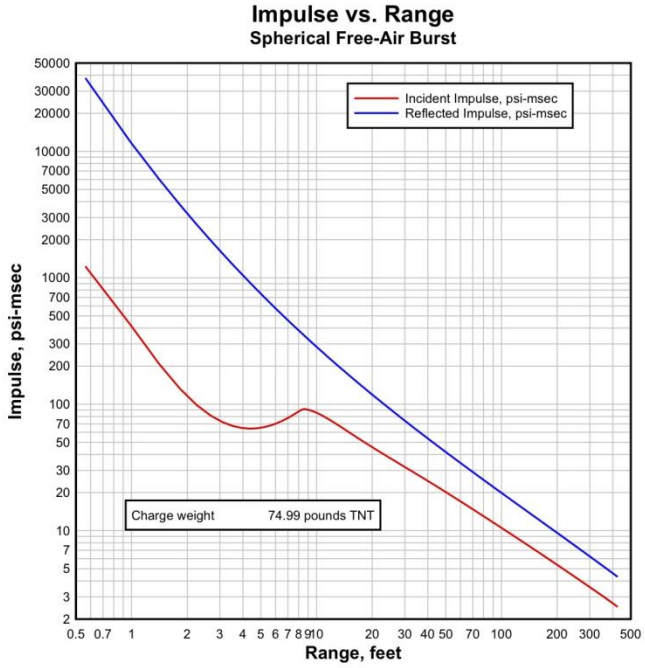

Figure C.3. CONWEP analysis for 3.5-foot (1067 mm) standoff distance; impulse vs. range

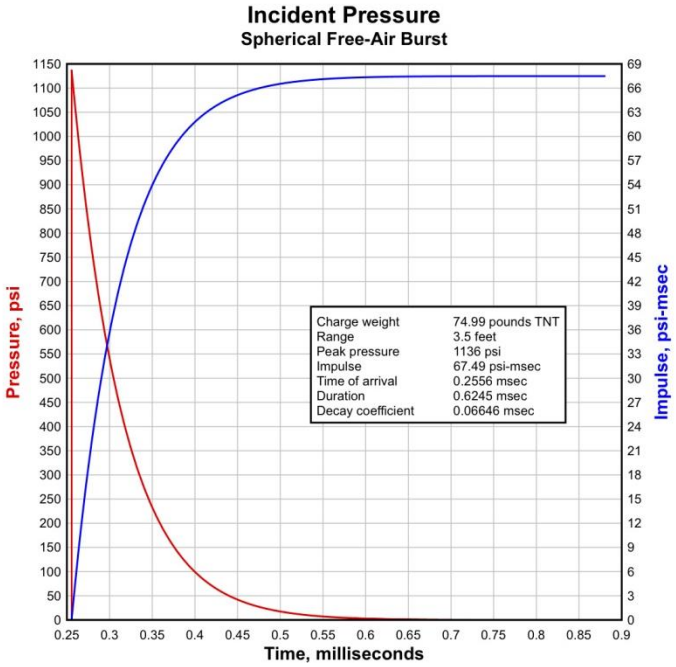

Figure C.4. CONWEP analysis for 3.5-foot (1067 mm) standoff distance; incident pressure vs. time

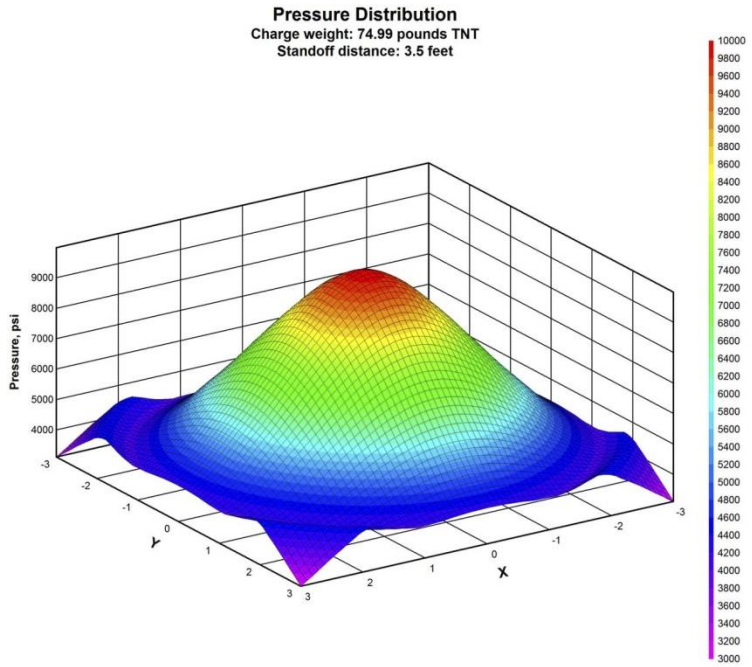

Figure C.5. CONWEP analysis for 3.5-foot (1067 mm) standoff distance; pressure distribution

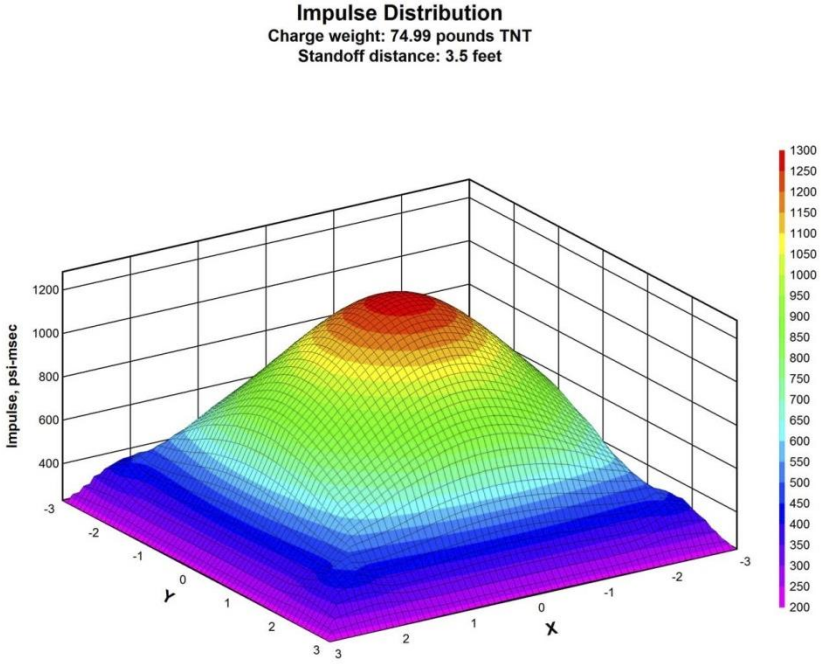

Figure C.6. CONWEP analysis for 3.5-foot (1067 mm) standoff distance; impulse distribution

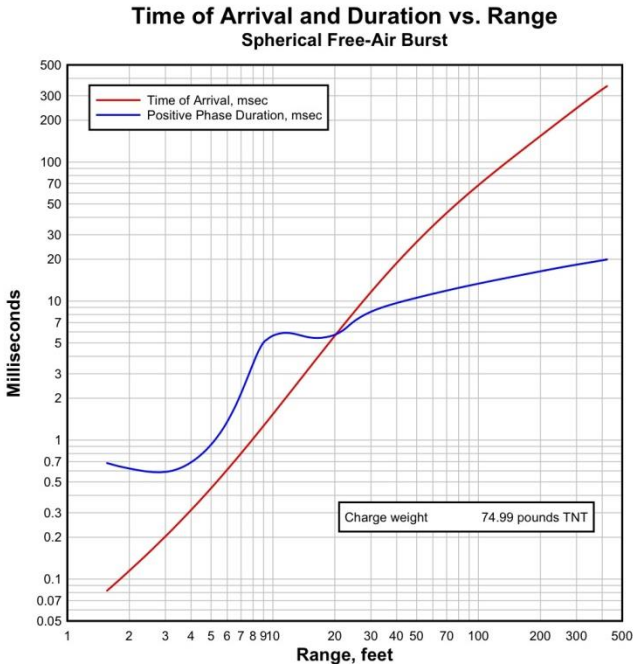

Figure C.7. CONWEP analysis for 3.5-foot (1067 mm) standoff distance; time of arrival and duration vs. range

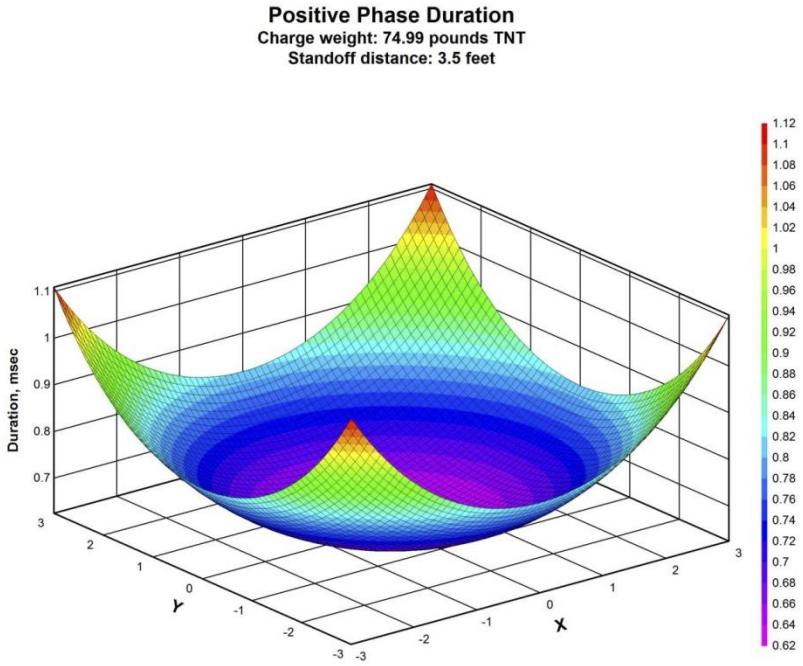

Figure C.8. CONWEP analysis for 3.5-foot (1067 mm) standoff distance; positive phase duration

UNCLASSIFIED

Pressure Distribution on a Wall	
Charge weight	74.99 pounds TNT
Standoff distance from target	5.5 feet
Peak pressure	4150 psi
at X =	0 feet
Y =	0 feet
Minimum pressure	1799 psi
at X =	-3 feet
Y =	-3 feet
Peak impulse	650.2 psi-msec
at X =	0 feet
Y =	0 feet
Average impulse	467.3 psi-msec
Equivalent uniform load	
Supports fixed on all sides	
Equivalent uniform peak pressure	3367 psi
Equivalent uniform impulse	546.5 psi-msec
Decay coefficient of equivalent uniform pressure, α	6.161

Figure C.9. CONWEP analysis for 5.5-foot (1676 mm) standoff distance; peak pressures

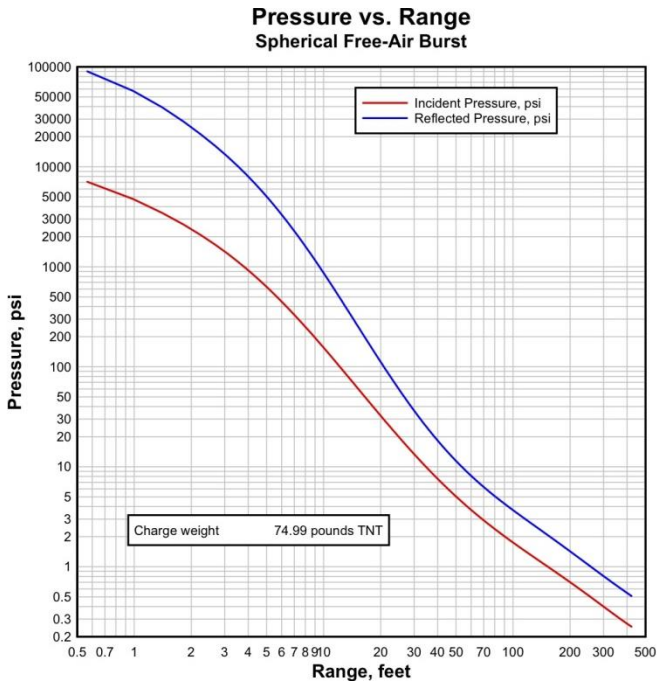

Figure C.10. CONWEP analysis for 5.5-foot (1676 mm) standoff distance; pressure vs. range

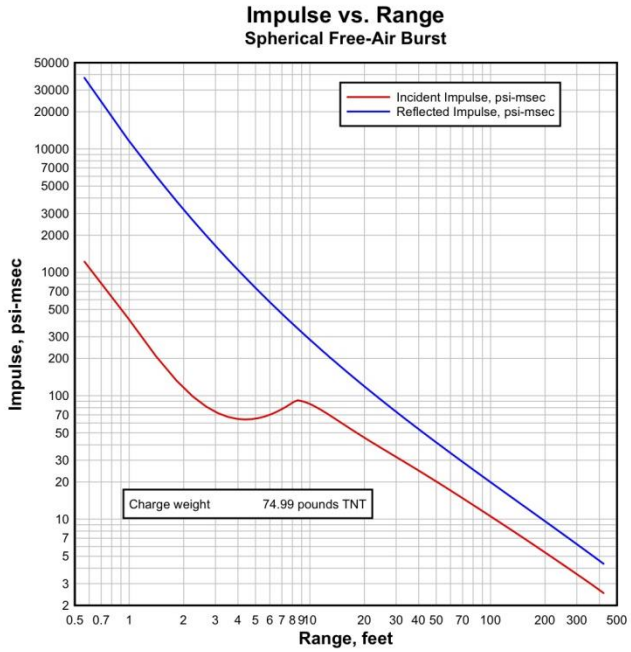

Figure C.11. CONWEP analysis for 5.5-foot (1676 mm) standoff distance; impulse vs. range

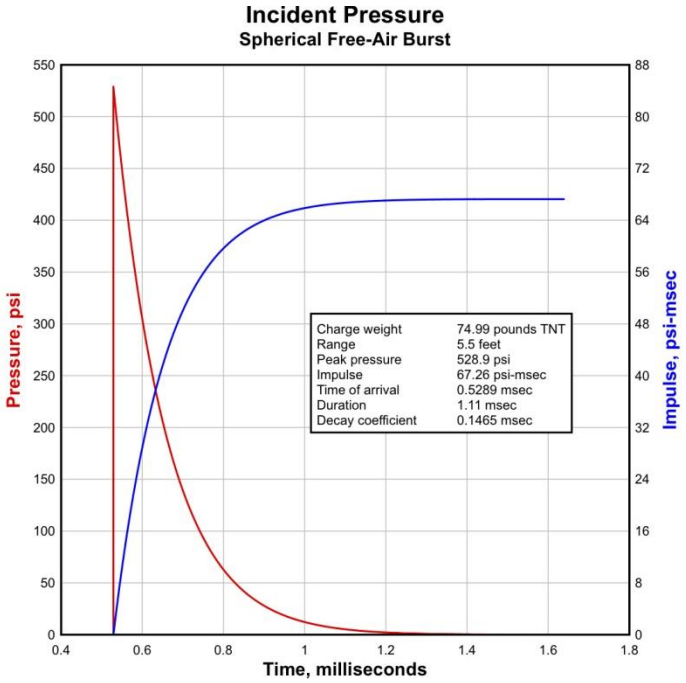

Figure C.12. CONWEP analysis for 5.5-foot (1676 mm) standoff distance; incident pressure

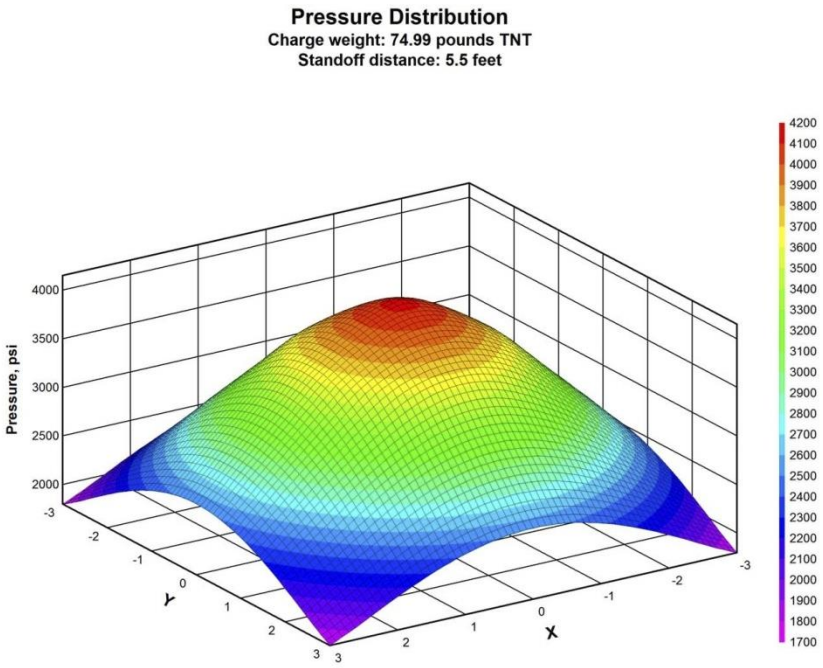

Figure C.13. CONWEP analysis for 5.5-foot (1676 mm) standoff distance; pressure distribution

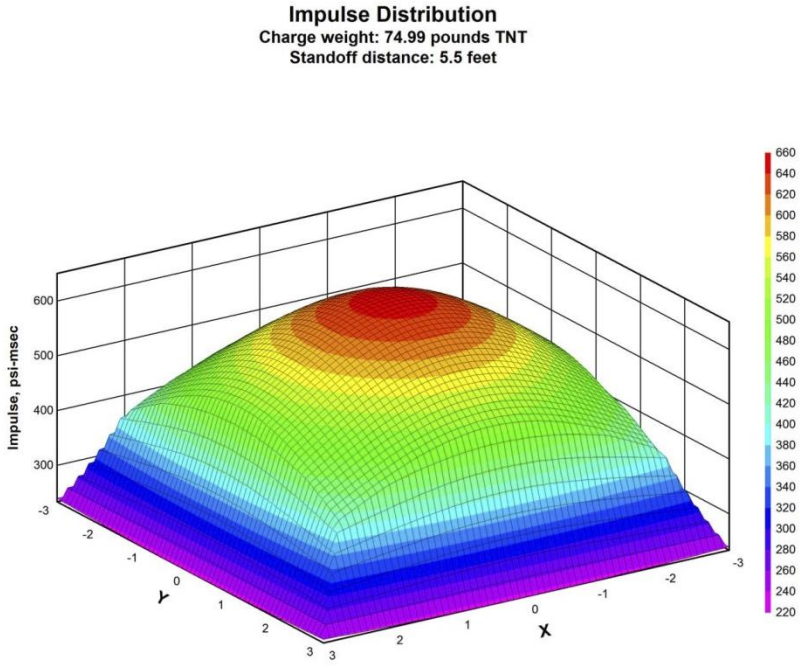

Figure C.14. CONWEP analysis for 5.5-foot (1676 mm) standoff distance; impulse distribution

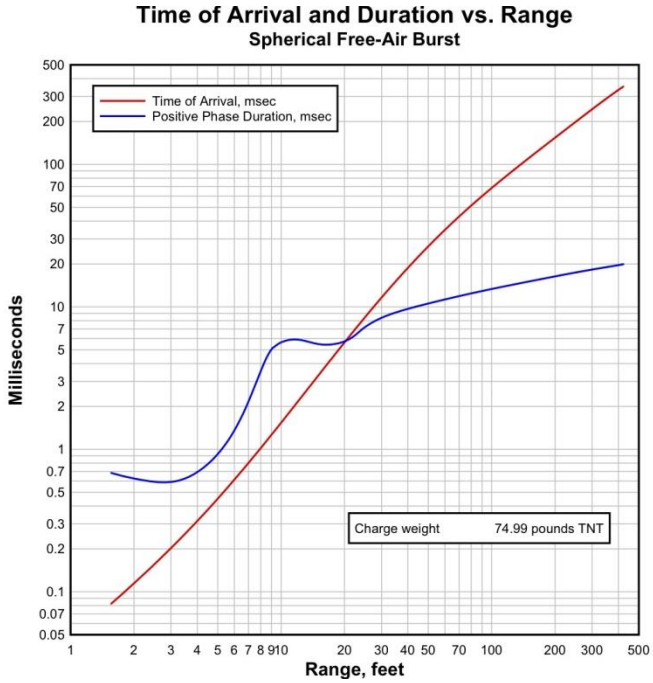

Figure C.15. CONWEP analysis for 5.5-foot (1676 mm) standoff distance; time of arrival and duration vs. range

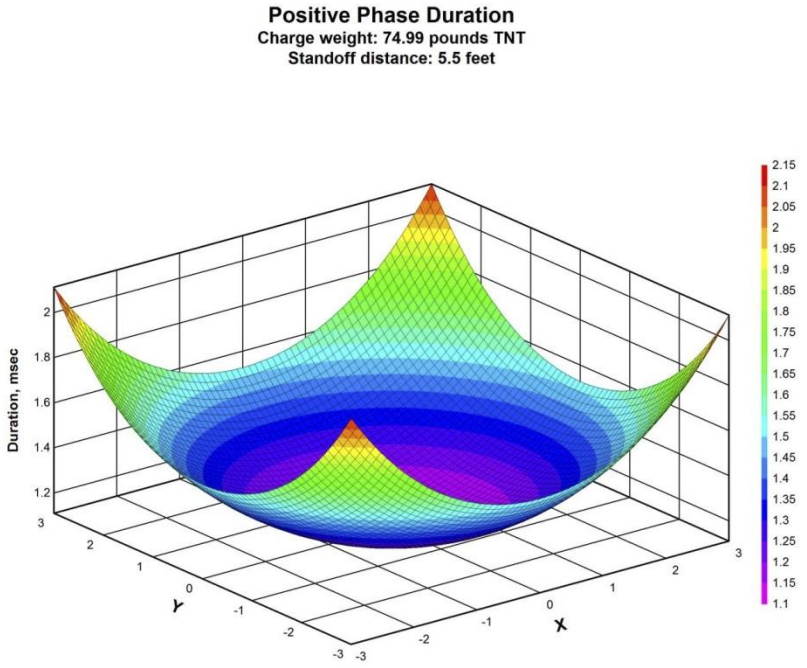

Figure C.16. CONWEP analysis for 5.5-foot (1676 mm) standoff distance; positive phase distribution

APPENDIX D.
BLAST DATA

This appendix includes the results of the blast test from Paper V which was removed from the paper based on the reviewer's comment. This data is reflected pressure from the sensor on top of the panel. The removed part from the paper is as below:

"Figure D.1is a typical plot of the panel's reflected pressure at the sensor nearest the LCFRC-A1, PS3. The pressure is shown at time zero with a positive duration of 0.4 ms. As shown in the plot, the peak pressure during the blast exceeded 138 MPa. This value surpassed the readable range of both the sensor and the data acquisition system. Within the readable range, however, the plot followed a typical air blast reflected pressure reading characterized by an exponential decay over time, with an initial positive phase followed by a negative phase. Background noise (shown in the graph) was caused by the structure's vibration. The reflected pressure was determined to be the average value within the measured range of data. It was used to show the approximate blast pressure shape."

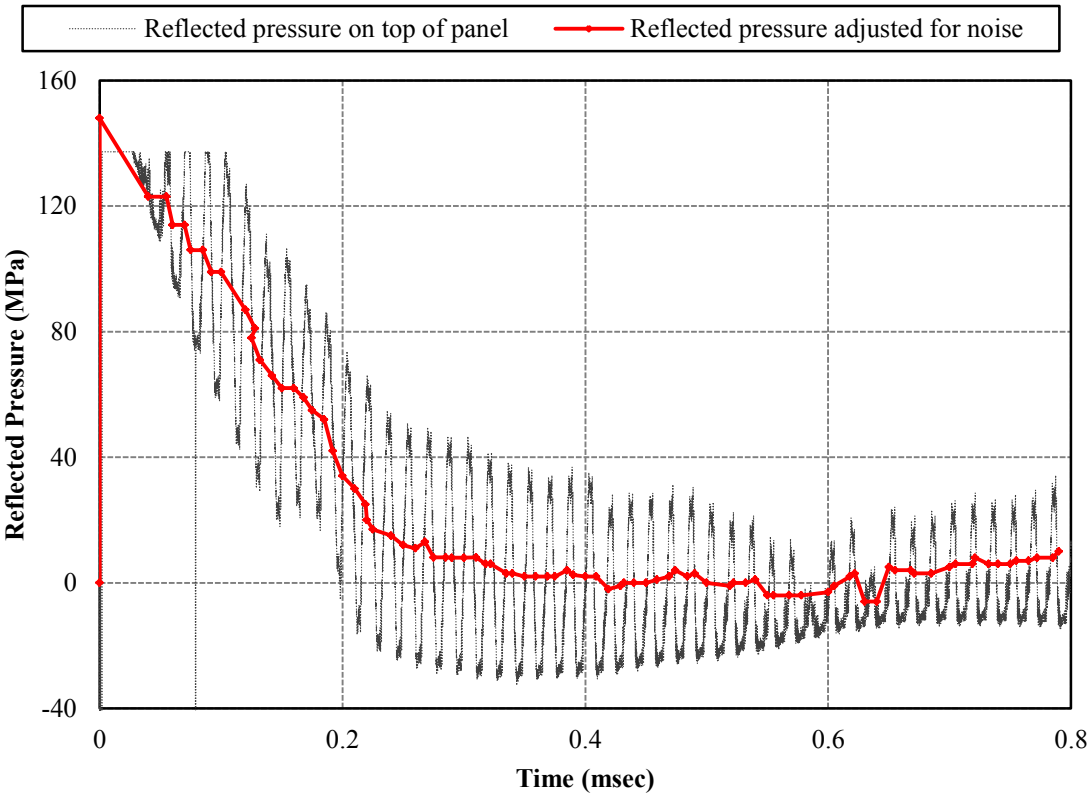

Figure D.1. Time history of reflected pressure on LCFRC-A1 during experiment at PS3

VITA

Zahra Sadat "Sara" Tabatabaei was born in Iran. She graduated from International University of Imam Khomeini, Ghazvin in 2004 with a Bachelor's Degree. She started her graduate study at the same year and graduated with a Master's Degree in Earthquake Engineering in 2007. She started her PhD in January 2009 at University of Missouri Rolla, later renamed Missouri University of Science and Technology. Her PhD research focused on the numerical analysis of carbon fiber reinforced concrete. She had five presentations at different conferences and published four papers in journals. She received her PhD from Missouri University of Science and Technology in Civil Engineering in December 2013.